PART I: MICROMECHANICS OF DENSE SUSPENSIONS: MICROSCOPIC INTERACTIONS TO MACROSCOPIC RHEOLOGY

&

PART II: MOTION IN A STRATIFIED FLUID: SWIMMERS AND ANISOTROPIC PARTICLES

by

Rishabh V. More

A Dissertation

Submitted to the Faculty of Purdue University

In Partial Fulfillment of the Requirements for the degree of

Doctor of Philosophy

School of Mechanical Engineering

West Lafayette, Indiana

May 2022

THE PURDUE UNIVERSITY GRADUATE SCHOOL
STATEMENT OF COMMITTEE APPROVAL

Dr. Arezoo Ardekani, Chair

School of Mechanical Engineering

Dr. Osman Basaran

School of Chemical Engineering

Dr. Ivan Christov

School of Mechanical Engineering

Dr. Jun Chen

School of Mechanical Engineering

Approved by:

Dr. Nicole Key

To *Mummy*, *Pappa*, *Appa* and *Yukta*

ACKNOWLEDGMENTS

I begin by thanking my advisor Dr. Arezoo Ardekani for providing me with an opportunity to pursue PhD and for guiding me in my research work. I am very grateful for the freedom she offered me while deciding and working on my thesis research projects and otherwise. I also appreciate her patience with my progress and providing crucial advice to excel in my career. Prof. Ardekani has a keen sense of when to give insight and guidance versus letting a student tussle as an independent researcher, which has been invaluable to my personal growth. I could not have imagined having a better advisor and mentor for my PhD.

I am thankful to Dr. Osman Basaran, Dr. Ivan Christov, and Dr. Jun Chen for agreeing to be on my Doctoral Advisory Committee and taking time out of their schedules for my defense.

I want to thank all Professors who taught me at Purdue University. In particular, I am incredibly grateful to Prof. Basaran for being a role model and always believing in me. His guidance and encouragement throughout my PhD journey are invaluable to me. I want to thank Prof. Wassgren for being an excellent mentor and teaching me how to teach. I am indebted to Prof. Christov for helping me prepare my lectures for ME308.

I thank Ardekani Lab members: Nikhil, Vaseem, Rajat, Manish, Amir, Ziyang, Adib, Andres, and Monsurul. I especially thank Nikhil and Vaseem for the many intellectually rewarding discussions and making my transition from an undergraduate to a graduate student seamless. I enjoyed working with Andres and Monsurul and wish them all the best for their future endeavors!

I will cherish all the memories I made with Aditya, Sachin, Tanmay, and Vaishnavi while at Purdue. I am grateful to Akriti, Jashan, and Sheel for bearing me at times when I could be unbearable and for always being there. I will miss hanging out with Venky and Praneet. A special thanks to Dr. Abhi Singh for inspiring and supporting me.

Lastly, I express the greatest sense of gratitude to my family for loving me unconditionally and always encouraging me to improve in life. A special thanks to my grandfather, who

ignited the spark of curiosity in me by answering 'what's up there in the sky?' in a way that a four years old kid could understand and get mesmerized by it.

TABLE OF CONTENTS

LIST OF TABLES

LIST OF FIGURES

ABSTRACT

Part I: Micromechanics of dense suspensions

Suspensions of rigid particles in fluid media are ubiquitous in the industry as well as in biological and natural flows. Fresh concrete, uncured solid rocket fuel, and biomass slurries are typical industrial applications of such concentrated suspensions, while silt transport in rivers and blood are examples of naturally occurring suspensions. In these applications, rheological properties and flow behavior are of interest for high-volume fractions of particles. The suspending fluid medium is typically Newtonian in these suspensions; still, these suspensions exhibit a plethora of non-Newtonian properties such as yield stresses, rate-dependent rheology, normal stresses, to name a few. Other than volume fraction, the type of particle material, presence of fluid-particle or particle-particle interactions such as hydrodynamic, Brownian, colloidal, frictional, chemical, and/or electrostatic determine the rheological behavior of suspension. The average inter-particle gaps between the neighboring particles decrease significantly as the suspension volume fraction approaches the maximum dry packing fraction in dense suspensions. As a result, in this regime, the short ranged non-contact interactions of DLVO (Derjaguin and Landau, Verwey and Overbeek) and non-DLVO origins are important. In addition, the particles can come into direct contact due to asperities on their surfaces. The surface asperities are present even in the case of so-called smooth particles, as particles in real suspensions are not perfectly smooth. Hence, contact forces arising from the direct touching of the particles become one of the essential factors to determine the rheology of suspensions.

Part I of this thesis investigates the effects of microscopic inter-particle interactions on the rheological properties of dense suspensions of non-Brownian particles by employing discrete particle simulations. Hydrodynamic interactions are calculated using the Ball-Melrose approximation, and the surface roughness is modeled as a hemispherical asperity on the particle surface. We show that increasing the roughness size results in a rise in the relative viscosity and the normal stress difference in the suspensions. Furthermore, we observe that the jamming volume fraction decreases with the particle roughness underlining the pivotal role in dictating the rheological behavior of dense suspensions of rigid particles. Conse-

quently, for suspensions with volume fractions close to jamming, increasing the asperity size reduces the critical shear rate for shear thickening (ST) transition, resulting in an early onset of discontinuous shear thickening (DST, a sudden jump in the suspension viscosity at the critical shear rate) in terms of volume fraction, and enhances the strength of the ST effect as it leads to an increase in the viscosity of dense suspensions. These findings are in excellent agreement with the recent experimental measurements and provide a deeper understanding of the experimental findings. Finally, we propose a constitutive model to quantify the effect of the roughness size on the rheology of dense ST suspensions to span the entire phase-plane. These equations can predict exact volume fractions and shear stress values for transitions between three regimes on the shear stress-shear rate flow state diagram for different roughness values. Thus, the constitutive model and the experimentally validated numerical framework proposed can guide experiments, where the particle surface roughness is tuned for manipulating the dense suspension rheology according to different applications.

A typical dense non-Brownian particulate suspension exhibits shear thinning (decreasing viscosity) at a low shear rate/stress followed by a Newtonian plateau (constant viscosity) at an intermediate shear rate/stress values which transitions to shear thickening (increasing viscosity) beyond a critical shear rate/stress value and finally, undergoes a second shear-thinning transition at an extremely high shear rate/stress values. In this part, we unify and quantitatively reproduce all the disparate rate-dependent regimes and the corresponding transitions for a dense non-Brownian suspension with increasing shear rate/stress. We find that competition between inter-particle interactions of hydrodynamic and non-hydrodynamic origins and the switching in the dominant stress scale with increasing the shear rate/stress lead to each of the above transitions. The inclusion of traditional hydrodynamic interactions, attractive/repulsive DLVO (Derjaguin and Landau, Verwey and Overbeek), inter-particle contact interactions, and constant friction (or other constraint mechanisms) reproduce the initial thinning as well as the shear thickening transition. However, to quantitatively capture the intermediate Newtonian plateau and the second shear thinning, an additional non-hydrodynamic interaction of non-DLVO origin and a decreasing coefficient of friction, respectively, are essential; thus, providing the first explanation for the presence of the intermediate Newtonian plateau along with reproducing the second shear thinning in a single framework.

Expressions utilized for various interactions and friction are determined from experimental measurements, resulting in an excellent quantitative agreement between the simulations and previous experiments.

Part II: Motion in a stratified fluid

Density and/or viscosity variations due to temperature or salinity variations greatly influence the flow around and the sedimentation of objects such as rigid/porous particles, drops/bubbles, and micro/small organisms in the atmosphere, oceans, and lakes. Density stratification hampers the vertical flow and substantially affects the sedimentation of an isolated object, the hydrodynamic interactions between a pair, and the collective behavior of suspensions in various ways depending on the relative magnitude of stratification, inertia (advection), and viscous (diffusion) effects. This thesis discusses these effects and elicits the hydrodynamic mechanisms behind some commonly observed fluid-particle transport phenomena in oceans and the atmosphere, like aggregation in horizontal layers. The physical understanding can help us better model these phenomena and, hence, predict their geophysical, engineering, ecological, and environmental implications. To this end, in this part of the thesis, using fully resolved simulations, we probe the locomotion of individual organisms and the pair interactions between them, and the sedimentation of spheroidal shaped particles in a stratified fluid.

We investigate the self-propulsion of an inertial swimmer in a linear density stratified fluid using the archetypal squirmer model, which self-propels by generating tangential surface waves. We quantify swimming speeds for pushers (propelled from the rear) and pullers (propelled from the front) by direct numerical solution of the Navier-Stokes equations using the finite volume method for solving the fluid flow and the distributed Lagrange multiplier (DLM) method for modeling the swimmer. We find that increasing stratification reduces the swimming speeds of swimmers relative to their speeds in a homogeneous fluid while reducing their swimming efficiency. The increase in the buoyancy force experienced by these squirmers due to the trapping of lighter fluid in their respective recirculatory regions as they move in the heavier fluid is one of the reasons for this reduction. Stratification also stabilizes the flow around a puller, keeping it axisymmetric even at high inertia, thus leading to otherwise absent stability in a homogeneous fluid. On the contrary, a strong stratification leads to instability in the motion of pushers by making the flow around them unsteady 3D, which is otherwise steady axisymmetric in a homogeneous fluid. Data for the mixing efficiency generated by individual squirmers explain the trends observed in the mixing produced by a swarm of squirmers.

In addition to the motion of individual organisms, their interactions also play a significant role in their collective motion and their ecological and environmental impacts. However, ubiquitous vertical density stratification in these aquatic environments significantly alters the swimmer interactions compared to in a homogeneous fluid. To this end, we numerically investigate the interactions between a pair of model swimming organisms in two configurations: 1) approaching each other, & 2) moving side-by-side with finite inertia in a linear density stratified fluid. Depending on the squirmer inertia and stratification, we observe that the squirmer interactions can be categorized as i) pullers getting trapped in circular loops, ii) pullers escaping each other with separating angle decreasing with increasing stratification, iii) pushers sticking to each other after the collision and deflecting away from the collision plane, iv) pushers escaping with an angle of separation increasing with stratification. Stratification also increases the contact time for squirmer pairs. The results presented can help understand the mechanisms behind the accumulation of planktonic organisms in horizontal layers in a stratified environment like oceans and lakes.

Much work has been done to understand the settling dynamics of spherical particles in a homogeneous and stratified fluid. However, the effects of shape anisotropy on the settling dynamics of a particle in a stratified fluid are not completely understood. To this end, we perform numerical simulations for settling oblate and prolate spheroids in a stratified fluid. We find that both the oblate and prolate spheroids reorient to the edge-wise and partially edge-wise orientations, respectively, as they settle in a stratified fluid completely different from the steady-state broad-side on orientation observed in a homogeneous fluid. We observe that reorientation instabilities emerge when the velocity magnitude of the spheroids fall below a particular threshold. We also report the enhancement of the drag on the particle from stratification. The torque due to buoyancy effects tries to orient the spheroid in an edge-wise orientation while the hydrodynamic torque tries to orient it to a broad-side on orientation. Below the velocity threshold, the buoyancy torque dominates; resulting in the onset of reorientation instability. Finally, the asymmetry in the distribution of the baroclinic vorticity generation term around the spheroids explains the onset of the reorientation instability. We also show that the insights obtained here are also true in a fluid with higher Prandtl number $Pr = 7.0$.

PART I

MICROMECHANICS OF DENSE SUSPENSIONS: MICROSCOPIC INTERACTIONS TO MACROSCOPIC RHEOLOGY

1. INTRODUCTION

1.1 Motivations

Particulate suspensions—the heterogeneous mixture formed by submerging several particles in a fluid medium—is the focus of this thesis. The particles can be rigid/deformable, isotropic/anisotropic in shape, mono/bi/poly-dispersed, active/passive and have a variety of other properties. Similarly, the suspending fluid can be Newtonian, Non-Newtonian, or viscoelastic. This wide variety of possible particle and fluid properties results in some of the most interesting and complex flow behaviors for suspensions. Colloids are suspensions of very small particles (orders of nanometres). At this scale, Brownian motion is dominant making the particles continuously and randomly bounce around in the fluid. Typically, suspensions with particle sizes $> 100\ nm$ are considered as a different class than colloids and solutions. This thesis concerns itself with suspensions of such larger particles, i.e., non-colloidal suspensions.

Like other fluids, suspensions are ubiquitous in nature and industrial applications. Mud or muddy water where soil, clay, or silt particles are suspended in water, sandy water where sand is suspended in water, and blood are some of the examples of naturally occurring suspensions. Ceramics, paper pulp, adhesives, paints, highly conducting metal pastes, biomass slurries, uncured rocket fuels, fresh concrete, chocolate, and pharmaceutical suspensions are well-known examples of suspensions in industrial applications. Oobleck—which is a concentrated mixture of corn starch and water—is a popular example of suspension which is used to demonstrate non-Newtonian behavior of fluids to school kids and non-scientific audience at large. In these examples, the particle sizes widely vary. They can vary from a few $100\ nm$ (e.g., in blood or mud) to centimeters (e.g., concrete or rocket fuel). Thus, the flow states exhibited by suspensions vary from very low-viscosity gas-like behavior to highly viscoelastic ordered structures. Fig. 1.1 shows a simple visualization of suspensions in terms of particle size to pure solutions and colloids.

Predicting and understanding the macroscopic behavior of these suspensions by considering their microscopic properties is a key question of great relevance in both theory and practice. The macroscopic behaviors include static (equilibrium) as well as dynamic (non-

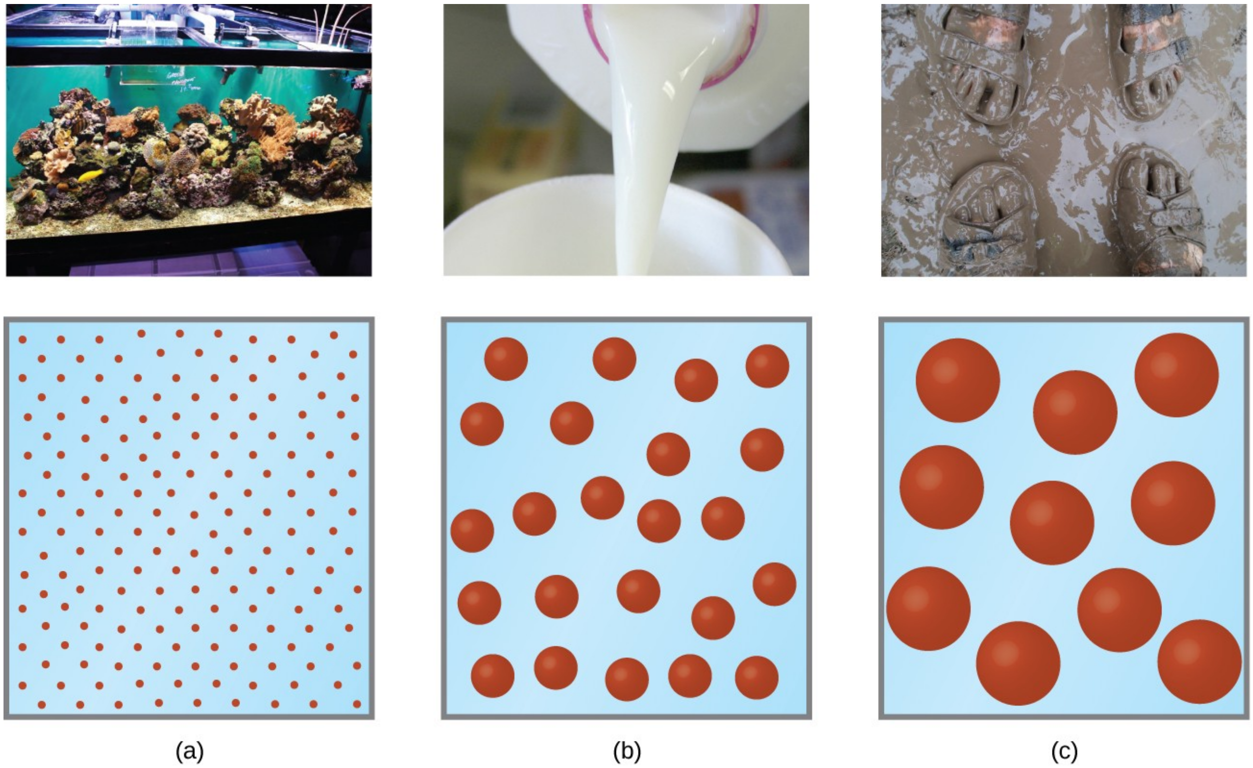

Figure 1.1. A schematic showing a) pure solution, particle size $< 10^{-7} cm$, e.g., seawater, b) colloid, particle size from 10^{-7}-10^{-5} cm, e.g., milk, and c) a suspension, particle size $> 10^{-5}$ cm, e.g., mud. Source.

equilibrium) situations. The non-equilibrium problems such as flowing sand, mixing cement and concrete; and equilibrium problems like diffusion of proteins, and drug delivery are all studied. For instance, the clusters and chains formation by stones in the concrete aggregate can cause blockages in pipes. So, understanding the impact of an imposed shear rate on particle aggregation could help in predicting these blockages a priori so that we could prevent them. Similarly, ability to predict the effective viscosity of this mixture would assist onsite engineers to optimize the pumping operations, e.g., choosing the most efficient pump and pumping pressure. Being able to predict and manipulate the suspension micro-structure would allow us to tune the thermal conductivity of suspension materials like Thermal Interface Materials (TIMs) routinely used in cooling electronics [1]. In addition, finding ways to increasing the amount of solid material that can be accommodated in these suspensions is important in many applications, e.g., in biofuel plants, as it increases the rate of materials processed, leading to higher biofuel production.

As a result of this rich and complex behavior exhibited by suspensions, it has been an active topic of research from as early as the 20^{th} century. The investigation of the flow behavior of suspensions fits organically in the field of rheology: the branch of fluid mechanics that deals with the deformation and flow of fluids, especially the non-Newtonian flow of liquids and the plastic flow of solids. Understanding the fluid behavior when it is subjected to an imposed stress—for example, being pumped through a pipe or streaming down a surface—is crucial to determining its flow. To this end, a wide range of rheological experiments and tools have been developed to describe the reactions of a fluid to various stresses. To analyse these reactions, however, requires coupling these measurements to theory. The internal structure of the fluid governs the reaction of the fluid to imposed stress. Thus, rheologists utilize the theory of the structure to predict the behaviour of classes of fluid. Particles by their presence, aggregation and dispersion provide a great deal of structure to a suspension material making it a natural problem for rheologists to investigate.

1.2 Suspension as a single effective fluid

The interactions between particles and their resulting microstructural arrangement govern the particle dynamics and suspending fluid flow at the microscopic scale. But at the macroscopic scale, the mixture of the suspending fluid and particles can be seen as a continuous effective fluid. How these microscopic inter-particle interactions govern the macroscopic bulk rheology of suspensions is precisely the focus of this thesis as depicted by the schematic in Fig. 1.2.

The first rheological question asked of suspensions was how the addition of particles affects the viscosity of a fluid. The viscosity of a fluid, η_0, is a measure of its resistance to deformation or flow. The traditional method to measure fluid viscosity is by measuring the force it exerts on parallel plates when it is sheared in between them. This gives a measure of the internal forces in the fluid which is often represented as the stress. In the simplest case, we may find that there is a linear relationship between the stress, σ, and the strain rate it is experiencing, $\dot{\gamma}$, representing the movement of the fluid,

$$\sigma = \eta_0 \dot{\gamma} \tag{1.1}$$

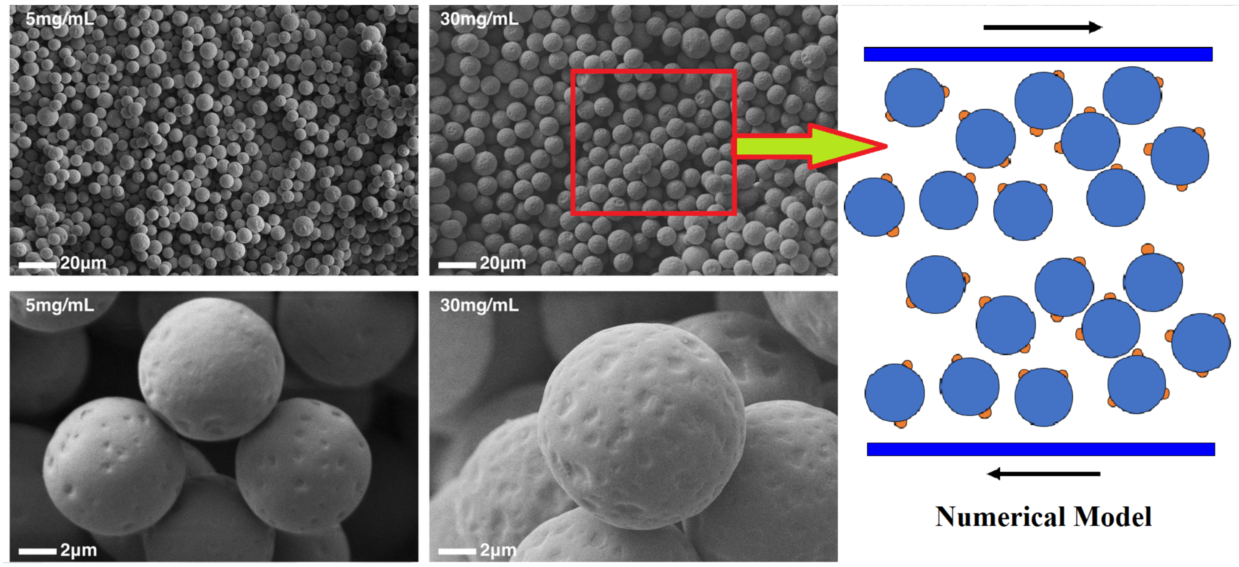

Figure 1.2. Spray dried Trehalose particles used for the preparation of pharmaceutical suspensions. Scanning electron microscope images are reproduced from [2]. The particle surface morphology clearly shows the non-uniformities on the particle surfaces. The numerical investigations in this thesis [3]–[6] which explain the results from recent experiments [2], [7]–[9] show that these non-uniformities affect the suspension flow properties in interesting and non-intuitive ways. Thus, suspension properties can be manipulated by carefully designing the particle surface morphology. However, to be able to do that, we first need to understand the various microscopic inter-particle interactions that are governed by particle material, shape and surface tribology which is the focus of this thesis.

The viscosity term, η_0 is a constant in this linear relationship, and if this relationship holds, we say that the fluid is Newtonian. This class of fluids includes simple fluids like water and air.

Many fluids including suspensions, however, do not behave in this way, and have stresses which depend on not just the shear rate but the instantaneous shear strain, time, temperature, and/or historical values of these quantities. The addition of particles makes the fluid inhomogeneous and so unsurprisingly the Newtonian stress–shear rate relation might no longer be valid. Therefore, we define the effective viscosity of the suspension, η, to be the viscosity of the Newtonian fluid which gives the same stress at the same shear rate.

The first major theoretical contribution to understanding the rheological behavior of suspensions came from none other than Albert Einstein in 1906 [10] with a correction in 1911

[11]. Einstein related the viscosity of a dilute suspension composed of spherical particles of equal sizes in a Newtonian medium with a constant viscosity, η_0, to the volume fraction, ϕ, which is the fraction of particles' volume to the total volume in the Stokes flow limit:

$$\eta_r = 1 + \frac{5}{2}\phi. \tag{1.2}$$

This the well-known expression proposed by Einstein for the suspension relative viscosity, η_r (η/η_0, ratio of the suspension viscosity to the viscosity of the suspending medium) for $\phi < 10\%$ [11]. The inter-particle interactions can be ignored in the dilute regime and thus, Einstein calculated this viscosity by considering the effect of immersing a single solid spherical particle in a linear shear flow.

The physical origin of this increase in viscosity can be understood by looking at the flow around a freely suspended single particle (no net force or torque acts on it) in a shearing flow. The ambient shearing flow is composed of a rotational flow component and a straining flow component (see Fig. 1.3). The solid-body rotation of the sphere due to the rotating component of the shearing flow creates no disturbance. The rigid particle, however, resists the straining component of the shearing flow producing a disturbance flow. This disturbance flow consequently leads to an increase in the rate of viscous dissipation and hence, an added contribution to the bulk stress of the material owing to the presence of the particles called particle stress. This particle stress can be quantified by using the stresslet induced by an isolated particle in a simple shear flow [12]. In simple words, the resistance of the rigid particle to the straining component of the shearing force causes the rise in the suspension viscosity.

Many researchers have extended Einstein's analysis using a variety of methods to include particle interaction effects and calculate the particle stress contribution to the total bulk stress to predict the suspension viscosity in a semi-dilute regime ($\phi < 0.15$) [13]. The final results is an improvement to Einstein's formula (eq. 1.2) usually done by adding more polynomial terms in the expression of η_r, such that [14], [15],

$$\eta_r = 1 + 5/2\phi + K\phi^2 + O(\phi^3), \tag{1.3}$$

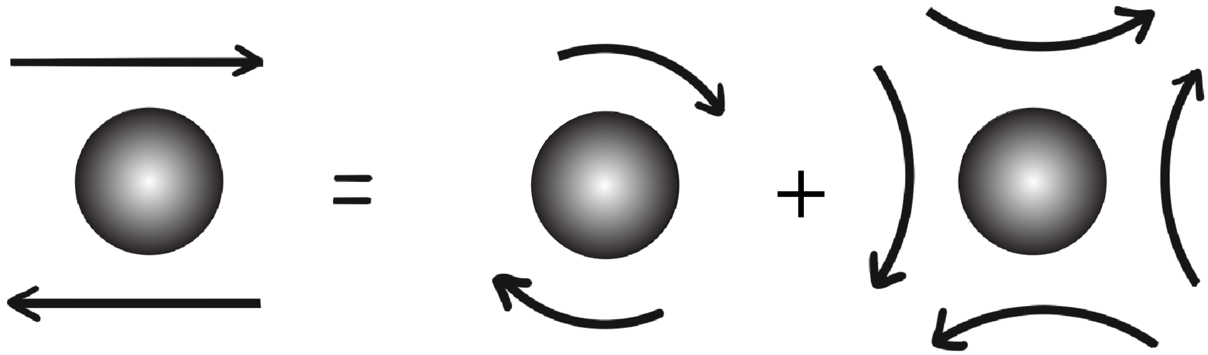

Figure 1.3. Decomposition of a sphere in a simple shear flow by combining a sphere in rotational flow and a sphere in a straining flow.

where K is a constant. In the semi-dilute and concentrated suspensions, the interactions between particles cannot be neglected. For example, at 10 % volume fraction, the average inter-particle distance is $d/2\phi^{1/3} \approx d$, where d is the particle diameter. Thus, pair hydrodynamic interactions become significant yielding a viscosity contribution of $O(\phi^2)$. However, these hydrodynamic interactions are long-ranged and hence, their calculation difficult [12]. The disturbance flow created by a point force decays as $O(1/r)$, while by a freely suspended sphere in a shearing flow decays as $O(1/r^2)$ with the radial distance from the center, r. This leads to an added stress on a nearby sphere which scales as $O(1/r^3)$. To calculate this added stress a special method known as hydrodynamic renormalisation must be employed [15], [16] because a simple integration over the entire domain assuming a uniform pair distribution function diverges. For a pure straining flow this gives $K = 6.95$. However, for a simple shear flow, defining the pair probability is complicated because of the existence of closed trajectories due to the rotational flow component. Assuming a random microstructure leads to $K \approx 5$ which agrees reasonably with the experimental data in the semi-dilute regime (up to $\phi \approx 0.10 - 0.15$) but fails to capture rapid rise in viscosity in the concentrated regime ($\phi > 0.2$). Thus, the mechanics of suspensions in a dilute and semi-dilute regime, where theoretical studies are possible, is fairly well understood and well quantified.

Complications arise once we look beyond the dilute regime and consider moderately and highly concentrated suspensions even for mono-disperse suspensions. This complexity is a direct result of the non-linear effects coming from the inter-particle interactions such as long-

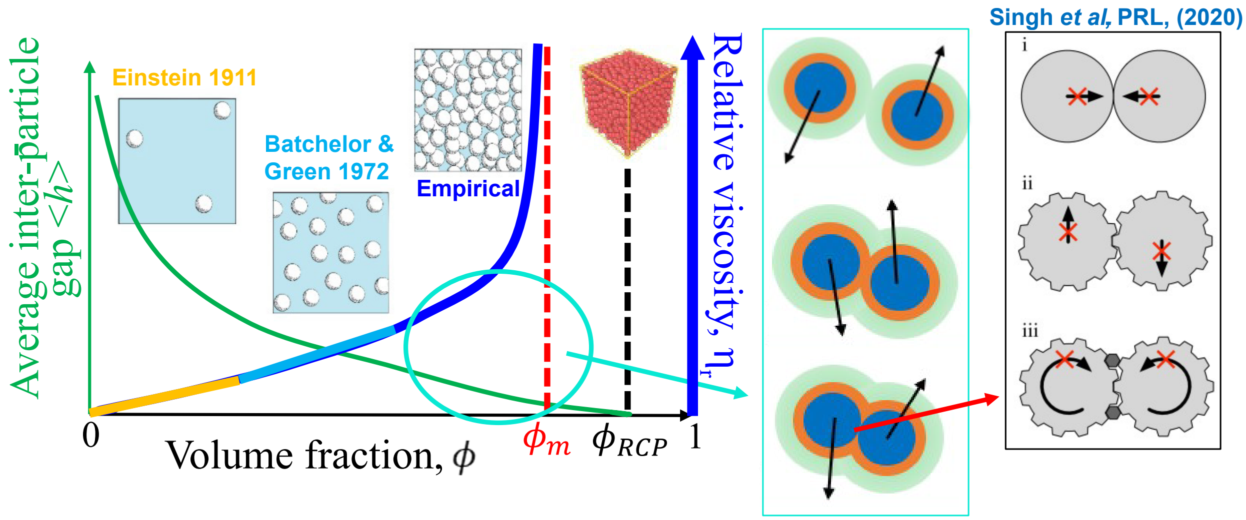

Figure 1.4. A schematic summary of rheology of suspensions.

ranged hydrodynamic interactions, short-ranged pair-wise lubrication interactions, and inter-particle interactions of other origins. The effects of these interactions manifest themselves in the bulk rheological properties and the microstructure of the suspensions as summarized in Fig. 1.4. The simple expression for η_r derived in the dilute/semi-dilute limit is no more applicable for the concentrated or dense suspensions. The best way to understand the rheological behavior of concentrated suspensions is by performing experiments and coming up with constitutive equations that can help to predict the suspension viscosity. This was the main focus in the field in most of the last century. The efforts were made mainly to relate the relative viscosity of the suspension to its volume fraction.

Intuitively, one can imagine that the viscosity would approach to a very high value as the suspension volume fraction gets closer to the maximum volume fraction, ϕ_m, beyond which the suspension stops flowing or jams. The jamming fraction is usually smaller than the random close packing fraction, ϕ_{RCP}, for dry granular suspensions. This is because of the governing role of short range non-contact and contact interactions in dense suspensions as the average inter-particle gap becomes very small as depicted in Fig. 1.4. Due to this commonality among all the suspensions irrespective of particle properties, it has been observed that, η_r vs ϕ/ϕ_m plots collapse on a single curve for an appropriate value of ϕ_m [28]–[31] (see fig. 1.5). These experiments were performed in either low-shear or high-shear limits in which

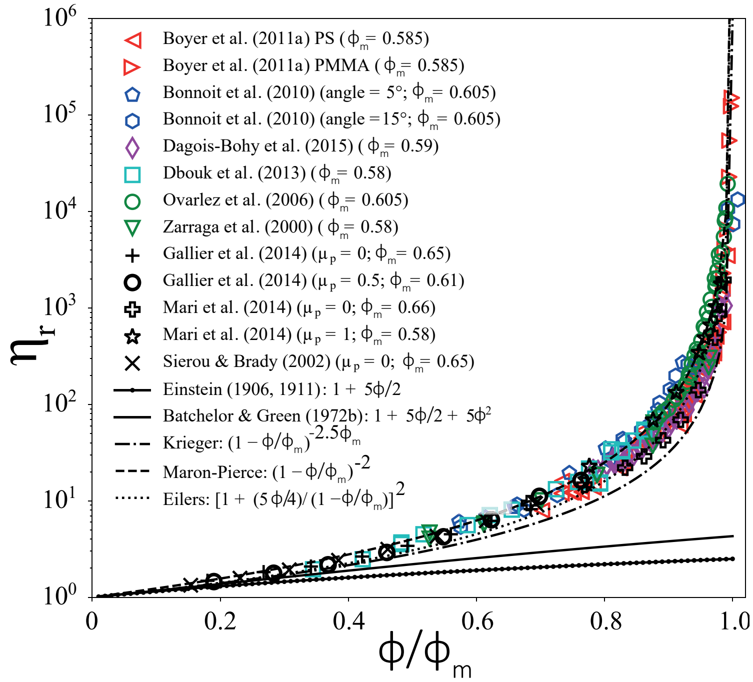

Figure 1.5. Relative viscosity, η_r vs reduced volume fraction, ϕ/ϕ_m. Experiments: Boyer *et al.* (2011a) [17]; Bonnoit *et al.* (2010) [18]; Dagois-Bohy *et al.* (2015) [19]; Dbouk, Lobry & Lemaire (2013) [20]; Ovarlez, Bertrand & Rodts (2006) [21]; and Zarraga, Hill & Leighton (2000) [22]. Numerical simulations: Sierou & Brady (2002) [23] and Gallier *et al.* (2014) [24] with (μ =0.5) and without (μ = 0) friction; of Mari **et al.** (2014) [25] with (μ = 1) and without (μ =0) friction, where μ is the friction coefficient between the spheres. Viscosity laws: of Einstein (1906) [10] of Batchelor & Green (1972) [15], of Krieger and Maron–Pierce, and of Eilers (Stickel & Powell 2005 [26]). Adapted from [27] with permission from Cambridge University Press.

the suspension viscosity is independent of the shear rate value. As a result, many satisfactory models for η_r vs ϕ/ϕ_m exist, among which Krieger-Dougherty ($\eta_r = (1 - \phi/\phi_m)^{-[\eta]\phi_m}$, where $[\eta]$ is a fitting constant) [32] and Maron-Pierce ($\eta_r = (1 - \phi/\phi_m)^{-2}$) [33] are widely used. However, this is not the entire picture as suspensions exhibit a gamut of other non-Newtonian behaviors.

Non-Newtonian and shear rate dependent behaviors are commonplace for dense suspensions with $\phi > 40\%$. The literature hints that suspensions are generally shear thinning (i.e., their viscosity decreases with shear rate) with a Newtonian limiting behavior in the low and high shear rate limits. But this is not at all always true. Many researchers have

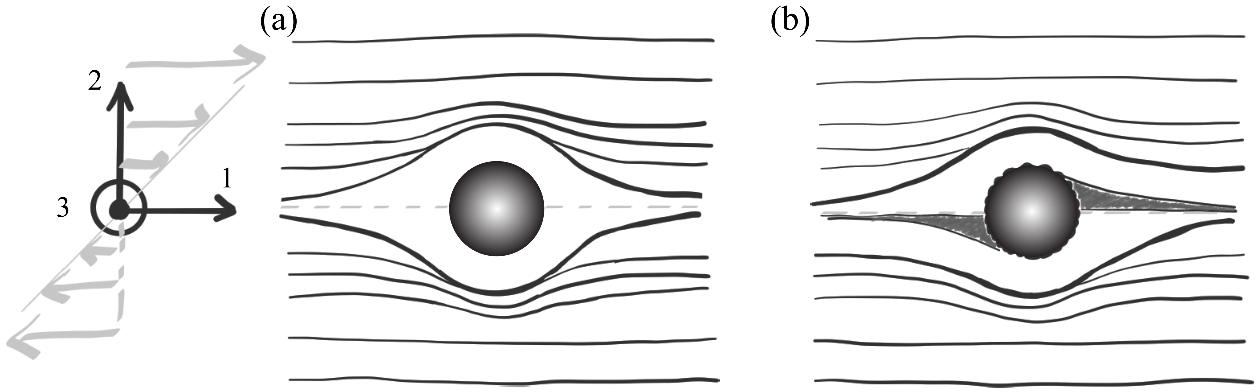

Figure 1.6. Sketch of the pair interactions between spheres under simple shear. (a) For perfectly smooth spheres, the trajectories exhibit a fore–aft symmetry. (b) For rough spheres, the trajectories are irreversible and asymmetric. Adapted from [27].

observed that a high shear rate limit is a Newtonian plateau before the onset of shear thickening (ST) with increasing shear rate [34], [35]. Shear thickening signifies an increase in the suspension viscosity with increasing shear rate. The experimental data suggest that any kind of suspension can show shear thickening given the right circumstances [35]. The divergence of suspensions from Newtonian behavior is not limited just to shear-thinning or thickening. Yield stress [36], non-zero normal stress differences [37], particle migration [38] and anisotropic microstructure [39] are some of the well-known non-Newtonian behaviors reported in the rheology of suspensions.

The loss of isotropy of the suspension microstructure has a direct link with the Non-Newtonian behavior in suspensions. Some basic physical understanding of the emergence of, e.g., normal-stress differences can be obtained by looking at the pair interactions between two spheres in a simple shear flow in Stokes flow limit as depicted in Fig. 1.6. Two colliding perfectly smooth spheres exhibit reversible and symmetric trajectories which follows the basic reversibility of the Stokes flow (see Fig. 1.6a). This pair interaction creates additional shear stress, however, it does not lead to normal-stress differences owing to the equal but opposite effects of the compressive and extensive portions of the flow. But in reality, many imperfections exist leading to the breaking of reversibility, e.g., contacts between the particles due to asperities on their surfaces. These contacts make the trajectories irreversible and asymmetric, resulting in non-isotropic normal stresses (see Fig. 1.6b) as the effects of the compressive and extensive portion of the flow no more cancel each other. However, measuring and quantifying these effects can be challenging and is elaborated in the following section.

1.3 Rheometry and the need of computer simulations

Measuring the rheological properties of suspensions (even viscosity) may prove to be challenging as it requires a specific procedure and analysis depending on the suspension. Unintended effects such as the wall-slip effect, sedimentation (if particles have higher density then the fluid) or creaming (if the particles have a lower density then the fluid), shear-induced particle migration, and sample ejection at high shear rates can thwart the measurements. Traditionally, rotational rheometers such as cone-and-plate, parallel plate and Couette rheometers have been commonly used for bulk viscosity measurements and are presented in Fig. 1.7. The less popular inclined-plane rheometer is also used to measure rheological properties of suspensions as it permits the exploration of a larger ϕ range. Non-intrusive techniques such as magnetic resonance imaging (MRI) or ultrasound can be used in conjunction with classical rheometers to overcome aforementioned unintended effects to perform local measurements.

Compared to macroscopic viscosity measurements, normal-stress differences are more difficult to measure. Standard rheological tools shown in Fig. 1.7 have been used but also adapted, e.g., with pressure transducers at the wall [20], [40] as shown in Fig. 1.7e. Alternative approaches utilizing the surface diflections caused by the anisotropic stress in sheared suspensions have also been undertaken to infer the normal-stress difference, e.g., in a Weissenberg or rotating-rod cell and in a tilted trough (see Fig. 1.7f-g). Weissenberg geometry method is well known in polymers as the rod-climbing effect. However, for suspensions of spheres, a rod-dipping effect is obsrved as the normal stress differences are negative and as will be discussed in the following chapters of the thesis. The second tilted-trough method (Fig. 1.7g) has some significant advantages over conventional rheometers, e.g., reduced confinement effects and improved sensitivity [41]–[43]. Coupling the non-conventional rheological tools (rotating rod and tilted trough) with conventional rheometers yields a complete measurement of the viscosity and the two normal stress differences, N_1 and N_2 [22], [43]. In addition, particle pressure is another important rheological property in suspensions. It is an

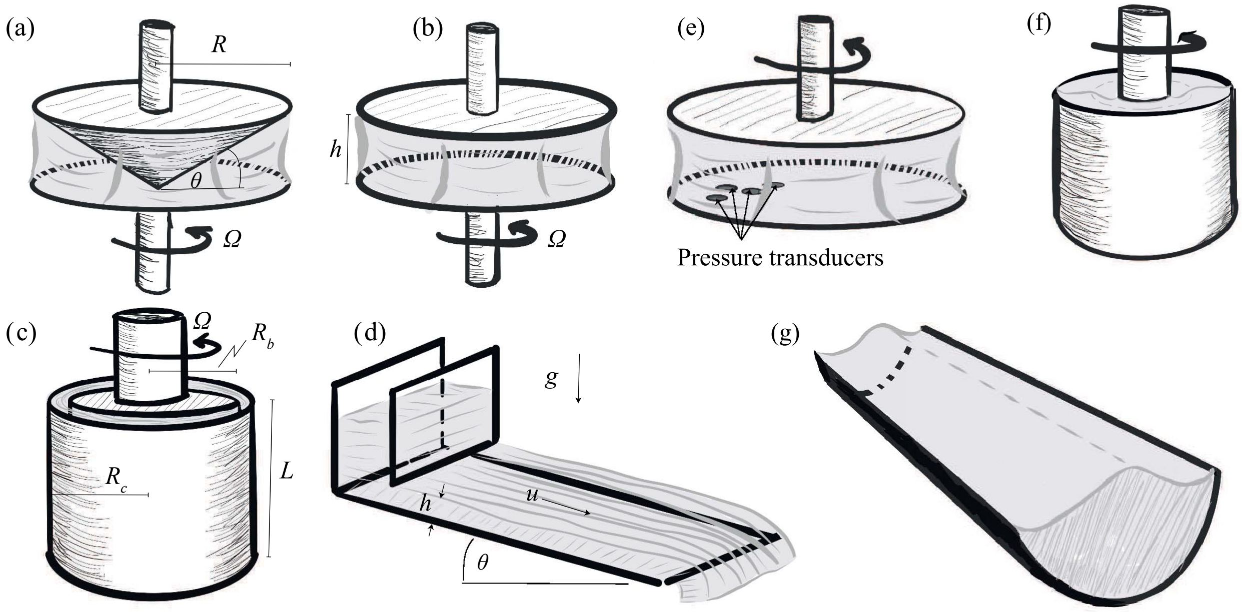

Figure 1.7. Rheometry used for measuring the viscosity of suspensions. (a) Cone-and-plate rotational rheometer. The fluid sample is sheared between the cone and plate and the viscosity is given by $\eta = 3\theta T/(2\pi R^3\Omega)$, where T is the measured torque. Normal force acting on the upper plate yields the first normal-stress difference, N_1. (b) Parallel-plate rotational rheometer. Viscosity is given by $\eta = 2Th/(\pi R^4\Omega)$. The normal force acting on the upper plate gives the difference between the first and second normal-stress differences, $N_1 - N_2$. (c) Couette rotational rheometer. The fluid sample sheared in the annular gap and the viscosity is given by $\eta = T(R_c - R_b)/[\pi L\Omega(R_c + R_b)R_b^2]$. (d) Inclined plane rheometer. The fluid flows down an inclined plane, and the viscosity is given by $\eta = \rho g h^2 \sin\theta/(2u)$, where ρ is the fluid density. (e) Parallel-plate rheometer with differential pressure transducers for measuring the radial profile of the normal stress along the velocity gradient direction yielding $N_2 + N_1/2$ and $N_1 + N_2$. (f) Weissenberg, or rotating rod, flow. The anisotropic stress induce free surface deflection (rod dipping in the case of suspensions) and yield $N_2 + N_1/2$. (g) Tilted-trough flow. N_2 induces the free-surface deflection (a bulge in the middle) which gives a direct measurement of N_2. Valid for small angles and small gaps. Adapted from [27].

analogue to the osmotic pressure exerted by colloidal particles and arises due to the shear rate induced agitation and collisions between the particles [27].

Computer simulations have been significantly helpful in overcoming the limitations of rheology measurements and understanding the fundamental mechanisms behind the different non-Newtonian behaviors observed for dense suspensions. Before 2000, *Stokesian dynamics* [44] was the predominantly used method for simulations of particulate suspensions. In this method, linear Stokes flow equations are solved for all the particles simultaneously at discrete time steps to solve for the hydrodynamic interactions. The result of these calculations is a system of linear equations for all the particles which can be represented in a matrix form linearly relating particle velocities and the forces acting on them. If we calculate velocities from the forces acting on the particles, it is called the resistance formulation and the inverse problem is called the mobility formulation, and the corresponding matrices in these formulations are called the resistance matrix and the mobility matrix, respectively. Using the multi-pole expansion form of the solution to the Stokes equations, one can construct the resistance matrix as described in [45] and solve for the particle velocities and stresses. Other simulations techniques are the dissipative particle dynamics [46], the lattice Boltzmann method [47], the force coupling method [48] and the fictitious domain method [24]. The method of choice for the simulation of dense suspensions near their jamming volume fraction limit is the one proposed by Ball & Melrose [49], which is an approximation of the Stokesian dynamics for the dense suspensions.

The current understanding in the field is that there is no fundamental time scale that determines the flow behavior of suspensions. But there exists a force/stress scale which determines the various rate-dependent behaviors shown by dense suspensions [50], [51]. So, in recent years, researchers have devoted significant efforts in understanding the mechanisms which can introduce a force scale in the problem involving the flow of suspensions. These forces can arise due to multiple reasons such as the chemical interactions between the particle and the fluid, the electrostatic interactions between neighboring particles, DLVO (named after Derjaguin and Landau, Verwey and Overbeek) interactions, Brownian motion, and friction to name a few. This thesis is concerned with exploring the role of one such inter-

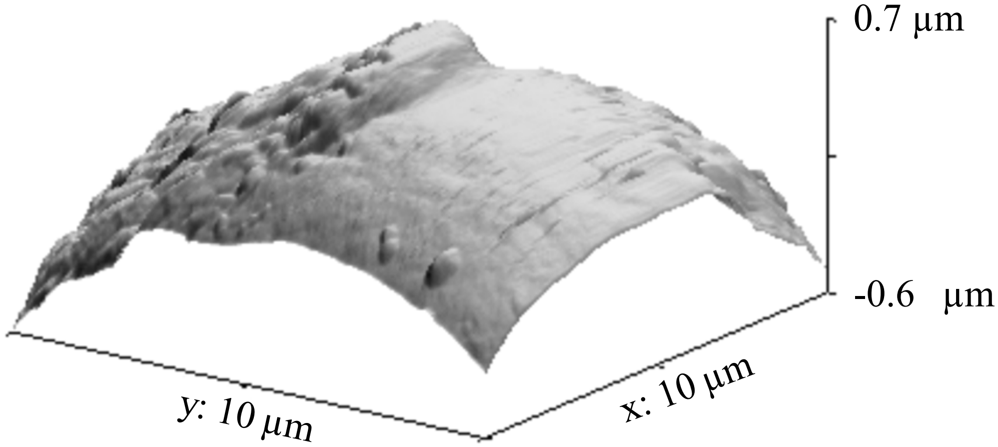

Figure 1.8. Atomic force microscope (AFM) image of polystyrene particle surface. Reproduced from Lobry *et al.* (2019) [52].

particle force interaction known as the contact forces, which arise due to the contact between the particles due to the presence of irregularities on their surfaces.

Among all the properties of the particles which can give rise to a force, the particle surface roughness is a peculiar one. This is because, even in the ideal case of smooth spheres, the spheres are not perfectly smooth and have surface asperities of $\approx O(10^{-3} - 10^{-2})$ times their radii [53]. Fig. 1.8 shows the AFM image of a polystyrene particle which clearly shows the presence of irregular asperities on the particle surface. So, in the dense suspension limit, the lubrication film (which theoretically can prevent the contact between the particles) can break and the particles can directly touch each other owing to the presence of surface roughness. This leads to contact forces which can be split into two components: 1) the normal forces acting along the line joining the centers of the particles, and 2) the tangential forces acting in the tangent plane to the contacting particles. Tangential forces also result in a torque on the particle and most importantly friction between the particles.

To this end, we numerically investigate the effects of particle roughness in determining the rheological behavior of dense suspensions. To do that, first, we model the fluid-particle and particle-particle interactions to be able to accurately perform the simulations. This involves calculating the hydrodynamic interactions between the particles, modeling the surface asperities, incorporating the contact and other external forces between the particles, solving for particle velocity, and integrate particle velocities forward in time to calculate the suspension micro-structure. We also calculate the bulk stress in the system which is consequently utilized to extract relevant rheological data from the simulations such as, the shear stress, σ, the relative viscosity of the suspension, η_r, the first N_1, and second, N_2, normal stress differences. We elaborate more on the governing equations and the methodology in the following sections.

1.4 Governing Equations

This section presents the numerical model for simulating the flow of dense suspensions. Dynamic simulations of suspensions involve modeling the hydrodynamic interactions, contact forces, other inter-particle interaction forces (if present) and the evolution of microstructure. Lubrication interactions scale with the inverse of the gap between the neighboring particles and are theoretically large enough to prevent the inter-particle contacts. But in reality, the presence of asperities on the surface of the particles promotes an early contact between the particles. As a result, asperities dictate the surface-to-surface separation which affects the lubrication stresses and in addition give rise to contact stresses. Hence, accurate modeling of the contact dynamics is essential in such simulations. The next few sub-sections explain the approaches utilized to model all these effects properly.

1.4.1 Particle Dynamics

The fluid motion is governed by the Navier-Stokes equations and the particle motions are governed by the force balance for individual particle according to the Newton's second law given as follow:

$$\mathbf{M}\frac{d}{dt}\begin{pmatrix}\mathbf{U}\\ \mathbf{\Omega}\end{pmatrix} = \sum_{\alpha}\begin{pmatrix}\mathbf{F}_{\alpha}(\mathbf{U},\mathbf{\Omega},\mathbf{r})\\ \mathbf{T}_{\alpha}(\mathbf{U},\mathbf{\Omega},\mathbf{r})\end{pmatrix}, \tag{1.4}$$

where $\mathbf{M}$ is the $(6N \times 6N)$ mass/moment of inertia matrix for N particles, $\mathbf{U}$ and $\mathbf{\Omega}$ are velocity and angular velocity vectors of size $3N$, respectively. $\mathbf{F}_{\alpha}$ and $\mathbf{T}_{\alpha}$ are various force and torque vectors of size $3N$ acting on the particles and $\mathbf{r}$ is the 3-D position vector.

In the case of suspension of non-Brownian rough particles, the forces acting on the particles are hydrodynamic interaction and the inter-particle contact forces between the pair of particles in contact due to presence of finite roughness. The above force balance can be written as,

$$\mathbf{M}\frac{d}{dt}\begin{pmatrix}\mathbf{U}\\ \boldsymbol{\Omega}\end{pmatrix} = \begin{pmatrix}\mathbf{F}_H\\ \mathbf{T}_H\end{pmatrix} + \begin{pmatrix}\mathbf{F}_C\\ \mathbf{T}_C\end{pmatrix}, \tag{1.5}$$

where subscripts H and C denote hydrodynamic and contact forces respectively.

The particle sizes in such suspensions typically range from 10 μm to 100 μm [7], [20], [22], [54], [55]. As a result, the Reynolds number, $Re = \rho_0 a^2\dot{\gamma}/\eta \approx O(10^{-5} - 10^{-7})$, where ρ_0 is the mass density of the particles, a is the particle radius, $\dot{\gamma}$ is the shear rate and η is the viscosity of the carrier fluid, is negligible and the particle inertia can be neglected for neutrally buoyant particles. Also, the Péclet number, $Pe = 6\pi\eta a^3\dot{\gamma}/kT > O(10^6)$ [7], [26], [54], where kT is the Boltzmann constant times the absolute temperature, means the flow is in non-Brownian regime. This means the motion of the particles is governed by the balance between the hydrodynamic and the contact forces alone. Since the focus of this paper is to study the effect of particle surface roughness on the rheology of suspensions, other inter-particle interaction forces (e.g., electrostatic repulsive forces due to presence of charge, Van der Waals forces, etc) are neglected, but they can be included in a straightforward manner whand is done in chapter 5. So we can equate the LHS in the above equations to $\mathbf{0}$ and get,

$$\mathbf{0} = \begin{pmatrix}\mathbf{F}_H\\ \mathbf{T}_H\end{pmatrix} + \begin{pmatrix}\mathbf{F}_C\\ \mathbf{T}_C\end{pmatrix}. \tag{1.6}$$

In this work, we study the behavior of suspension in a Newtonian fluid medium with a constant viscosity η under an imposed shear flow given as:

$$\mathbf{U}^{\infty}(\mathbf{r}) = \boldsymbol{\Omega}^{\infty} \times \mathbf{r} + \mathbf{E}^{\infty}\cdot\mathbf{r}, \tag{1.7}$$

where $\mathbf{U}^{\infty}(\mathbf{r})$ is the imposed velocity field expressed using the angular velocity vector $\boldsymbol{\Omega}^{\infty}$ and the rate-of-strain tensor $\mathbf{E}^{\infty}$. For a shear rate $\dot{\gamma}$, a simple shear flow can be expressed with the following non-zero elements, $\Omega_3^{\infty} = -\dot{\gamma}/2$ and $E_{12}^{\infty} = E_{21}^{\infty} = \dot{\gamma}/2$.

In the Stokes flow regime, velocities of the particles have linear dependence on the hydrodynamic forces acting on the particles. This linear relation is often represented in the form of the resistance relations [12], [44]. So, Eq. 1.6 becomes,

$$\mathbf{0} = -\mathbf{R} \cdot \begin{pmatrix} \mathbf{U} - \mathbf{U}^{\infty} \\ \mathbf{\Omega} - \mathbf{\Omega}^{\infty} \\ -\mathbf{E}^{\infty} \end{pmatrix} + \begin{pmatrix} \mathbf{F}_C \\ \mathbf{T}_C \end{pmatrix}. \tag{1.8}$$

Here $\mathbf{R}$ is the grand resistance matrix for all the particles [44] relating particle velocities to the forces and torques. The above equation can be solved to calculate the particle velocities at any time step. The positions of the particles at the next time step $t + dt$ can then be obtained by time integration of these velocities.

1.4.2 Hydrodynamic interactions

Instead of solving the Stokes equations, which is computationally expensive, we make use of the Ball-Melrose [49] approximation to approximate the hydrodynamic interactions in terms of near field lubrication interactions which are pair-wise additive unlike the many-body nature of long range hydrodynamic interactions [44]. The lubrication interactions diverge as the narrow inter-particle gaps between the nearby solid particles reduces. As a result, the grand resistance matrix $\mathbf{R}$ can be represented as a sum of contribution from Stokes drag and a contribution from the lubrication interactions [25], [49], [56]:

$$\begin{pmatrix} \mathbf{F}_H \\ \mathbf{T}_H \\ \mathbf{S}_H \end{pmatrix} = -(\mathbf{R}^{stokes} + \mathbf{R}^{lub}) \cdot \begin{pmatrix} \mathbf{U} - \mathbf{U}^{\infty} \\ \mathbf{\Omega} - \mathbf{\Omega}^{\infty} \\ -\mathbf{E}^{\infty} \end{pmatrix}, \tag{1.9}$$

where $\mathbf{S}_H$ is the hydrodynamic stresslet acting on the particles [12], [13] and is required for calculation of the stress tensor. $\mathbf{R}^{stokes}$ is the diagonal matrix giving Stokes drag forces and torques. $\mathbf{R}^{lub}$ is the sparse matrix giving near-field lubrication interactions and can be calculated as:

$$\mathbf{R}^{lub} = \begin{bmatrix} \mathbf{R}_{FU} & \mathbf{R}_{F\Omega} & \mathbf{R}_{FE} \\ \mathbf{R}_{TU} & \mathbf{R}_{T\Omega} & \mathbf{R}_{TE} \\ \mathbf{R}_{SU} & \mathbf{R}_{S\Omega} & \mathbf{R}_{SE} \end{bmatrix} = \eta \begin{bmatrix} \mathbf{A} & \widetilde{\mathbf{B}} & \widetilde{\mathbf{G}} \\ \mathbf{B} & \mathbf{C} & \widetilde{\mathbf{H}} \\ \mathbf{G} & \mathbf{H} & \mathbf{M} \end{bmatrix}. \tag{1.10}$$

Here $\mathbf{A}$, $\mathbf{B}$, $\mathbf{C}$ are second order tensors while $\mathbf{G}$, $\mathbf{H}$ are third order tensors and $\mathbf{M}$ is a fourth order tensor which depend on the dimensionless inter-particle gap between i^{th} and j^{th} particles with radii a_{i} and a_{j}, $s^{(\mathrm{i,j})} = 2(d^{(\mathrm{i,j})} - a_{\mathrm{i}} - a_{\mathrm{j}} - h_r)/(a_{\mathrm{i}} + a_{\mathrm{j}})$, the center-to-center normal vector $\mathbf{n}^{(\mathrm{i,j})} = \mathbf{d}^{(\mathrm{i,j})}/d^{(\mathrm{i,j})}$ with $\mathbf{d}^{(\mathrm{i,j})} = (\mathbf{r}^{(\mathrm{j})} - \mathbf{r}^{(\mathrm{i})})$ being the particle center to center vector and $d^{(\mathrm{i,j})} = |\mathbf{d}^{(\mathrm{i,j})}|$ and the particle radius ratio $\lambda = a_{\mathrm{j}}/a_{\mathrm{i}}$. h_r is the height of the asperity on the particle surface (Fig. 1.9) and the tilde $\tilde{}$ on the top are used to denote transpose.

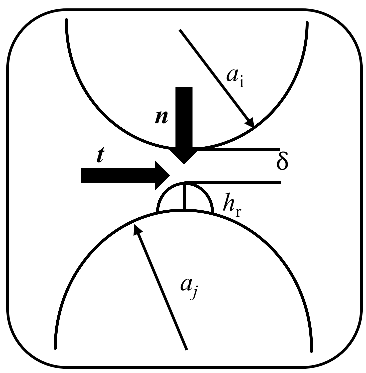

Figure 1.9. Sketch of roughness model. δ is the hydrodynamic separation distance and h_r is the roughness height.

We follow the approach of Mari *et al.* [25] and consider only the squeeze, shear and pump modes of Ball and Melrose and neglect the twist mode. This is physically consistent as the modes considered contain $1/s^{(\mathrm{i,j})}$ and $\log(1/s^{(\mathrm{i,j})})$ as the leading terms which are dominant in the near-field interactions [12], [57]. The twist mode is not associated with any of the diverging terms during the particle-particle contact and hence can be neglected. Further details for calculating the elements of the lubrication resistance matrix can be found in Mari *et al.* [25].

Thus, the leading terms are divergent as the particles approach very close to each other and theoretically should prevent the inter-particle contact. But as mentioned before, this is not observed in reality and the particles come into contact owing to the presence of finite roughness on their surfaces [58]. These contacts give rise to contact forces which have significant impact on the rheology of such suspensions [7], [54]. Hence, accurate modeling of the contact forces is important to obtain the observed behavior for suspensions of rigid rough particles. the following subsection gives a brief review of the contact model implemented. We implement different models for the friction between the particles to recover experimentally observed shear thinning and shear thickening behavior in the intermediate and the dense volume fraction limits. Hence, the contact model is discussed again in detail in each of the remaining chapters.

1.4.3 Roughness model and contact forces

In the recent years, researchers have studied the effects of inter-particle contacts on the rheology of suspensions [24], [25], [59]. The emphasis is on the accurate modeling of contact forces which is often times done based on the Discrete Element Modeling approach widely used in granular mechanics. Recently, Lobry *et al.* [52] have utilized the normal load dependent friction model given by Brizmer *et al.* [60] to simulate shear thinning that is routinely observed in experiments involving shear flow of suspensions. For this study, we utilize the same elastic-plastic mono-asperity contact model as it is valid for the materials commonly used in experiments. This contact model has been previously used by Lobry *et al.* [52]. Actual asperities are not hemispherical [7]; so the modelling is only one possibility. Aside from the known reduction in friction coefficient by load in elastomers [61] the presence of fluid will also alter the coefficient of friction between the particles. But we neglect these effects in the present study for simplicity. We do not include the viscous damping in order to be consistent with previous studies [24], [52], [62]. A brief explanation for the contact model is provided below.

Let us consider two spherical particles with radii a_{i} and a_{j} with surface roughness $h_r = \epsilon_r a_1$ (a_1 = characteristic particle size) coming into contact as shown in Fig. 1.9. ϵ_r is the dimensionless roughness. The contact between the particles takes place via the hemispherical

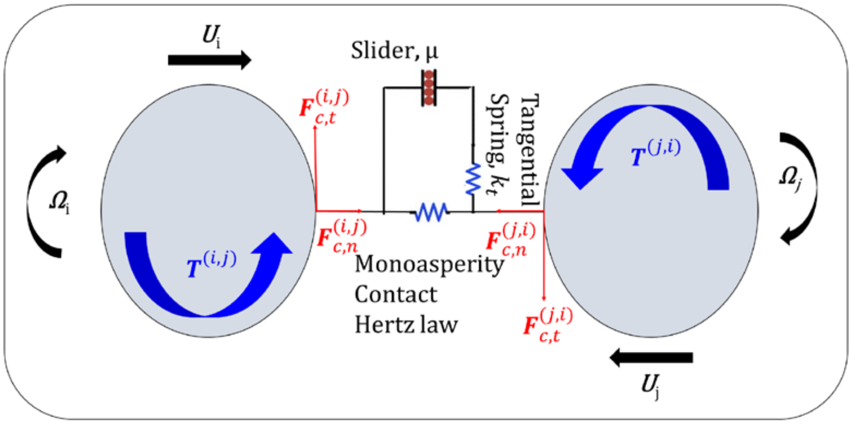

Figure 1.10. Schematic showing contact dynamics between contacting particles and corresponding force models used for force and torque calculations

asperity. The contact causes the asperity to deform which in turn gives rise to contact forces between the touching particles. The asperity deformation can be defined as $\delta = (d^{(\mathrm{i,j})} - a_\mathrm{i} - a_\mathrm{j} - h_r)$, we say the contact occurs when $\delta \leq 0$. Furthermore, we split the contact force ($\mathbf{F}_C^{(\mathrm{i,j})}$) into two components [24], [25], [52], i) $\mathbf{F}_{C,n}^{(\mathrm{i,j})}$ which is the normal contact force acting along the line of centers of the two particles, and ii) $\mathbf{F}_{C,t}^{(\mathrm{i,j})}$ which is the tangential contact force acting along the tangent plane at the particle contact.

$$\mathbf{F}_C^{(\mathrm{i,j})} = \mathbf{F}_{C,n}^{(\mathrm{i,j})} + \mathbf{F}_{C,t}^{(\mathrm{i,j})}. \tag{1.11}$$

A schematic of contact forces is presented in fig. 1.10. Contact forces also induce an additional contact stresslet for the particle given by the vector product of particle center to center vector and the contact force as [25]:

$$\mathbf{S}_C^{(\mathrm{i,j})} = \mathbf{d}^{(\mathrm{i,j})} \otimes \mathbf{F}_C^{(\mathrm{i,j})}. \tag{1.12}$$

1.4.4 Stress and bulk rheology calculations

To calculate the rheological properties we need the bulk stress in the suspension. The bulk stress in a suspension of rigid particles in a flow with strain rate $\mathbf{E}^{\infty}$ is (subtracting isotropic part of the fluid pressure):

$$\boldsymbol{\Sigma} = 2\mu\mathbf{E}^{\infty} + \boldsymbol{\Sigma}^{p}, \tag{1.13}$$

where $\boldsymbol{\Sigma}^{p}$ is the particle contribution to the bulk stress, and is given by the sum of hydrodynamic stress $\boldsymbol{\Sigma}^{H}$ and the contact stress $\boldsymbol{\Sigma}^{C}$ as:

$$\boldsymbol{\Sigma}^{p} = \boldsymbol{\Sigma}^{H} + \boldsymbol{\Sigma}^{C}, \tag{1.14}$$

where $\boldsymbol{\Sigma}^{H}$ and $\boldsymbol{\Sigma}^{C}$ can be calculated by taking ensemble average of the hydrodynamic $\mathbf{S}_{H}$ and contact $\mathbf{S}_{C}$ stresslets at each time step. We get,

$$\boldsymbol{\Sigma}^{H} = \frac{1}{V}\left(\sum_{\mathrm{i}} \mathbf{S}_{H}^{(\mathrm{i})}\right), \tag{1.15}$$

$$\boldsymbol{\Sigma}^{C} = \frac{1}{V}\left(\sum_{\mathrm{i}>\mathrm{j}} \mathbf{S}_{C}^{(\mathrm{i,j})}\right). \tag{1.16}$$

Therefore,

$$\boldsymbol{\Sigma} = 2\mu\mathbf{E}^{\infty} + \frac{1}{V}\left(\sum_{\mathrm{i}} \mathbf{S}_{H}^{(\mathrm{i})} + \sum_{\mathrm{i}>\mathrm{j}} \mathbf{S}_{C}^{(\mathrm{i,j})}\right), \tag{1.17}$$

where V is the volume of the domain, L^3. Shear stress σ, normal stress differences N_1 and N_2, relative viscosity η_r, and normal stress difference (N) can then be defined as $\sigma = \Sigma_{12}$, $N_1 = \Sigma_{11} - \Sigma_{22}$, $N_2 = \Sigma_{22} - \Sigma_{33}$, $\eta_r = \sigma/(\eta\dot{\gamma})$ and $N = N_1 - N_2$. The systematic splitting of the particle stress in contributions from hydrodynamic and contact stresses allows us to understand the relative contributions from lubrication and contact interactions to the rheological properties. E.g., the contribution from the hydrodynamic stress to the relative viscosity is $\eta_r^H = 1 + \Sigma_{12}^H/(\eta\dot{\gamma})$ and the corresponding contribution from the contact stresses is $\eta_r^C = \Sigma_{12}^C/(\eta\dot{\gamma})$ and so on.

1.5 Part I outline

With the fundamental concepts and numerical framework discussed, this section outlines the structure of part I of the thesis. Here we only provide a big picture view of each of the following chapters, with motivations behind choosing those problems and detailed analysis in the respective chapters. The remaining part I is organized as follow:

Chapter 2 is motivated by the experimental results from Tanner & Dai [7], who, for the first time, showed that increasing the particle roughness leads to an increase in the suspension viscosity. This result is significant as earlier theoretical and numerical studies had predicted that increasing the particle roughness will lead to a decrease in the suspension viscosity, contrary to the recent experiments. With the numerical framework developed we show that the suspension relative viscosity and the normal stress difference increase with the roughness of the particles. These findings show a satisfactory agreement with recent experiments from Tanner & Dai [7]. We propose a modified Maron-Pierce law to predict the relative viscosity with varying volume fractions and roughness. The jamming volume fraction decreases with the particle roughness owing to the increase in effective particle radii and the average coefficient of friction with roughness. The jamming fraction is also dependent on the stress and increases with stress. This directly leads to the increase in the relative viscosity with roughness in suspensions of rough non-Brownian particles. These findings suggest that accurate modeling of the contact dynamics and friction is crucial to accurately simulate the rheological behavior of dense suspensions subjected to shear flow.

Chapter 3 builds on the findings of chapter 2 and investigates the role of particle roughness in governing the shear thickening (ST) behavior typically observed for dense suspensions. A rise in the suspension viscosity and the reduction in the jamming fraction with roughness signifies that dense suspensions of rough particles would undergo ST at an earlier shear rate and a lower volume fraction compared to their smooth counterparts. This has recently been shown by experiments as well [8], [9]. To this end, we numerically investigate the effects of systematically increasing the particle surface roughness on ST suspensions. We show that increasing roughness leads to the early onset of shear-thickening, especially discontinuous shear thickening, in terms of both the critical shear rate and the critical volume fraction. In addition, roughness enhances the strength of the ST effect as it leads to an increase in the viscosity of dense suspensions. We explain these results by investigating the role of roughness in the evolution of contact networks and the jamming fraction. Increasing roughness leads to denser contact networks with high contact stresses and reduction in the jamming fraction. Finally, we visualize the effect of roughness on the phase diagram for viscosity in the shear rate - volume fraction plane. The results presented in this chapter are consistent with the mentioned experimental studies which indicate that the computational framework developed can be utilized to predict and tune suspension behavior for specific applications.

Chapter 4 brings the findings from previous chapters together in the form of a constitutive model to quantify the effects of increasing the particle roughness on the ST suspensions. The constitutive model proposed can be utilized to predict the rheological properties such as the relative viscosity and the normal stress differences for any roughness value, volume fraction, and applied shear stress. The results from this chapter can be used to tune the particle surface roughness for manipulating the dense suspension rheology according to different applications [63].

Chapter 5 probes beyond just contact interactions induced by the asperities on the particle surfaces by incorporating other non-contact interactions between the particles such as DLVO (Derjaguin and Landau, Verwey and Overbeek) and non-DLVO. Doing so, we unify and quantitatively reproduce all the disparate rate dependent regimes and the corresponding transitions observed for a dense non-Brownian suspension with increasing shear rate/stress. Inclusion of traditional hydrodynamic interactions, attractive/repulsive DLVO interactions, the inter-particle contact interactions and a constant friction (or other constraint mechanism) reproduce the initial thinning as well as the shear thickening transition. However, to quantitatively capture the intermediate Newtonian plateau and the second shear thinning, an additional non-hydrodynamic interaction of non-DLVO origin and a decreasing coefficient of friction, respectively, are essential; thus, providing the first explanation for the presence of the intermediate Newtonian plateau along with reproducing the second shear thinning in a single framework. Expressions utilized for various interactions and friction are determined from experimental measurements and hence, result in an excellent quantitative agreement between the simulations and previous experiments.

Chapter 6 summarize all the above studies in the context of our original goal. Also, this chapter proposes further investigation ideas that can help to improve our fundamental understanding of the rheology of dense non-Brownian suspensions.

1.6 Publications and division of work between authors

The main advisor for the project is Prof. Arezoo M. Ardekani (AMA). AMA was responsible for conceptualization, project administration and funding accusation.

1. Chapter 2: Related publication - More, R. V. and Ardekani, A. M., Effect of roughness on the rheology of concentrated non-Brownian suspensions: A numerical study. *Journal of Rheology*, 64(1), pp.67-80, 2020.. Author contributions - Rishabh V. More (RVM) developed the code, and performed simulations. RVM and AMA developed methodology, analyzed the results and wrote the paper.

2. Chapter 3: Related publication - More, R. V. and Ardekani, A. M., Roughness induced shear thickening in frictional non-Brownian suspensions: A numerical study. *Journal of Rheology*, 64(2), pp.283-297, 2020. Author contributions - RVM developed the code, and performed simulations. RVM and AMA developed methodology, analyzed the results and wrote the paper.

3. Chapter 4: Related publication - More, R. V. and Ardekani, A. M., A constitutive model for sheared dense suspensions of rough particles. *Journal of Rheology*, 64(5), pp.1108-1120, 2020. Author contributions - RVM developed the code, and performed simulations. RVM and AMA developed methodology, analyzed the results and wrote the paper.

4. Chapter 5: Related publication - More, R. V. and Ardekani, A. M., Unifying disparate rate-dependent rheological regimes in non-Brownian suspensions. *Physical Review E*, 103(6), p.062610, 2021. Author contributions - RVM developed the code, and performed simulations. RVM and AMA developed methodology, analyzed the results and wrote the paper.

2. EFFECT OF ROUGHNESS ON THE RHEOLOGY OF CONCENTRATED NON-BROWNIAN SUSPENSIONS

2.1 Introduction

Suspensions of rigid particles in fluid media are ubiquitous in industry as well as in biological and natural flows. Fresh concrete and uncured solid rocket fuel are two typical industrial applications of such concentrated suspensions for which rheological properties and flow behavior are of interest for high volume fractions (ϕ) of particles. The suspending fluid medium is typically Newtonian in these suspensions. Other typical examples are metal pastes which consists of a functional powder (organic/inorganic) in a fluid which is often composed of polymeric binder, surfactant and solvent to provide suitable rheological properties [64]–[70] and dispersion state [65], [71]–[74] for processing and quality-control purposes. These metal pastes have found widespread applications in ceramics [75], [76], solid oxide fuel cell [77], [78], and inorganic solar cell [79], [80] industries. Many studies have been performed to date to understand the intricate physics governing suspensions of rigid particles in Newtonian/non-Newtonian suspending fluids but the understanding is far from complete. This complexity mainly comes from the wide variety of fluid-particle or particle-particle interactions such as hydrodynamic, Brownian, colloidal, frictional, collisional, electrostatic [81]. As a result, even the most idealized case of smooth perfectly rigid monodisperse spheres is likely to exhibit strong non-Newtonian effects such as yielding [82], shear-thinning [83], shear-thickening [25], [56], [84]–[86], particle migration [38] or anisotropic microstructures [26], [39], [87].

The rheological characteristics of such dense suspensions, like viscosity, normal stress differences and normal forces depend on solid concentration, friction between the particles [24], [25], [82], roughness of particles [7], [24], [54], [88], particle size distribution [89], particle shape [90]–[92], chemical composition of the carrier fluid [19], particle-fluid interactions [82], [93], and many other factors. Researchers have attempted to understand the effects of these factors on the rheology of suspensions in the last few decades [26], [27], [85], [94]. However, compared to other factors affecting the suspension behavior, the effects of particle roughness on the rheological properties of dense suspensions have not been much explored.

Recent computational studies have revealed the crucial role played by the inter-particle friction in governing the suspension behavior in shear flows [24], [25], [52], [56], [62]. Friction gives rise to tangential forces in addition to normal forces between the particles. Simulations for non-Brownian suspensions of rough particles at a fixed volume fraction show an increase in the relative viscosity with an increase in the coefficient of friction which results due to increase in contact stresses with friction [24]. Friction also plays a significant role in giving rise to continuous and discontinuous shear thickening [25], [56], [95], [96]. A coefficient of friction that increases with shear stress in the suspensions leads to shear thickening in dense suspensions ($\phi > 50\%$) [97]. On the other hand, a normal load dependent coefficient of friction which decreases with normal force between the particles [60] can reproduce shear-thinning behavior which is often observed in sheared suspensions [7], [54]. These studies show that friction and hence all the parameters influencing friction such as roughness, shear rate, shear stress, volume fraction play a role in determining the behavior of sheared suspensions. As a result, much of the focus in recent years in the field has been on understanding these effects. Among all the parameters mentioned above, roughness is one of the most important ones. This is because particles are never perfectly smooth. Even the smoothest particles have a roughness of $O(10^{-3} - 10^{-2})$ times their radii [7], [52], [53]. These non-uniformities on the particle surface lead to early contacts between particles which would otherwise be prevented due to lubrication interaction in the case of smooth particles.

These intermittent contacts due to the presence of particle surface roughness lead to dynamic irreversibilities and chaos in oscillating shear flows [98], [99] as well as the elimination of the closed orbit trajectories of the particles found in smooth dilute suspensions [100], [101] (See Fig. 5 in reference [27]). Roughness and friction between the particles lead to the breaking of symmetric trajectories present for smooth particles in a shear flow and change the stresslets of the particles as well [24], [102]. Surface roughness can therefore significantly affect the rheology and microstructure of the suspensions as shown by various numerical studies [23], [102]–[105].

Theoretical studies regarding the effects of roughness on the rheology of suspensions in dilute regime concluded that large roughness leads to decrease in relative viscosity and increase in the magnitude of normal stress differences [37], [88], [95], [106]. A direct numerical simulation study using a simple mono-asperity assumption and Hertz contact law for modeling contact dynamics also shows a similar trend of decrease in viscosity with particle roughness [24]. The friction model used in this study was intentionally kept simple to isolate the effect of friction on the rheology of suspensions. Other computational studies which don't explicitly model the roughness but have a repulsive force analogous to the normal forces induced by roughness also predict a weak decrease in relative viscosity of suspensions with increasing the range of the repulsive force [23], [48], [107].

To the best of our knowledge, prior to these theoretical and computational studies, no experiments were performed to quantify the effects of roughness on the rheology of suspensions. Recently, Moon *et al.* [54] and Tanner & Dai [7] introduced roughness on the particles by a special grinding process and performed experiments to quantify the effects of roughness on the rheological properties of suspensions. They found that relative viscosity as well as the normal force increase with an increase in the particle roughness in suspensions of non-Brownian rough particles. These findings are strikingly opposite of what had been computed and predicted by prior analyses [37], [88], [95], [106] and computations [23], [24], [48], [107]. Thus, the role of roughness on the rheology of suspensions is far from being understood completely.

The aim of this chapter is to study the effect of roughness on the rheological properties of rough non-Brownian suspensions via numerical simulations. Given the disagreement in experiments and previous computational and theoretical studies, it is imperative to implement a contact model which captures the fundamental mechanisms involved in contacts and inter-particle friction and is applicable to the materials used in the experiments. We use the normal load dependent coefficient of friction model given by Brizmer *et al.* [60] for contact between a sphere and a flat and modified by Lobry *et al.* [52] for simulation of dense suspensions. For modelling the hydrodynamic interactions we use the Ball-Melrose approximation [49]. The governing equations and the hydrodynamic force calculations remain the same as explained in chapter 1–Sec. 1.4. Hence, we do not discuss these here. We focus on elaborating the contact model utilized in detail in the following subsections.

2.1.1 Contact model

In the recent years, researchers have studied the effects of inter-particle contacts on the rheology of suspensions [24], [25], [59]. The emphasis is on the accurate modeling of contact forces which is often times done based on the Discrete Element Modeling approach widely used in granular mechanics. Recently, Lobry *et al.* [52] have utilized the normal load dependent friction model given by Brizmer *et al.* [60] to simulate shear thinning that is routinely observed in experiments involving shear flow of suspensions. For this study, we utilize the same elastic-plastic mono-asperity contact model as it is valid for the materials commonly used in experiments. This contact model has been previously used by Lobry *et al.* [52]. Actual asperities are not hemispherical [7]; so the modelling is only one possibility. Aside from the known reduction in friction coefficient by load in elastomers [61] the presence of fluid will also alter the coefficient of friction between the particles. But we neglect these effects in the present study for simplicity. We do not include the viscous damping in order to be consistent with previous studies [24], [52], [62]. A brief explanation for the contact model is provided below. For a detailed discussion, please refer to Lobry *et al.* [52].

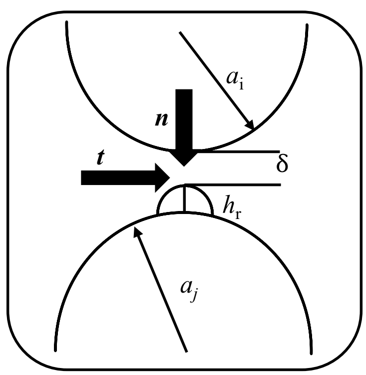

Figure 2.1. Sketch of roughness model. δ is the hydrodynamic separation distance and h_r is the roughness height.

Let us consider two spherical particles with radii a_i and a_j with surface roughness $h_r = \epsilon_r a_1$ (a_1 = characteristic particle size) coming into contact as shown in Fig. 2.1. ϵ_r is the dimensionless roughness. The contact between the particles takes place via the hemispherical asperity. The contact causes the asperity to deform which in turn gives rise to contact forces between the touching particles. The asperity deformation can be defined as $\delta =$

$(d^{(\mathrm{i,j})} - a_\mathrm{i} - a_\mathrm{j} - h_r)$, we say the contact occurs when $\delta \leq 0$. Furthermore, we split the contact force ($\mathbf{F}_C^{(\mathrm{i,j})}$) into two components [24], [25], [52], i) $\mathbf{F}_{C,n}^{(\mathrm{i,j})}$ which is the normal contact force acting along the line of centers of the two particles, and ii) $\mathbf{F}_{C,t}^{(\mathrm{i,j})}$ which is the tangential contact force acting along the tangent plane at the particle contact Fig. 2.2.

$$\mathbf{F}_C^{(\mathrm{i,j})} = \mathbf{F}_{C,n}^{(\mathrm{i,j})} + \mathbf{F}_{C,t}^{(\mathrm{i,j})}. \tag{2.1}$$

Contact forces also induce an additional contact stresslet for the particle given by the vector product of particle center to center vector and the contact force as[25]:

$$\mathbf{S}_C^{(\mathrm{i,j})} = \mathbf{d}^{(\mathrm{i,j})} \otimes \mathbf{F}_C^{(\mathrm{i,j})}. \tag{2.2}$$

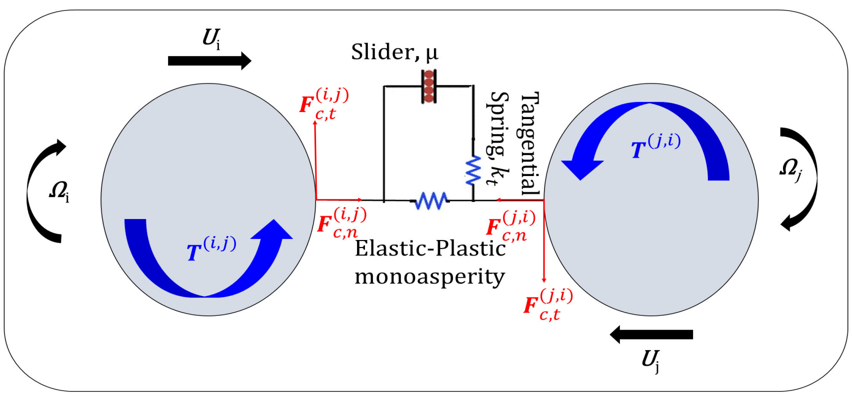

Figure 2.2. Schematic showing contact forces and torques acting on the particles and corresponding models used for their calculations

2.1.1.1 Normal Contact Force

The contact is elastic or plastic depending on the relative magnitude of the overlap with respect to some critical overlap δ_c. If $|\delta| \leq \delta_c$ (elastic region) we have,

$$\mathbf{F}_{C,n}^{(\mathrm{i,j})} = -L_c \left(\frac{|\delta|}{\delta_c}\right)^{3/2} \mathbf{n}^{(\mathrm{i,j})}, \tag{2.3}$$

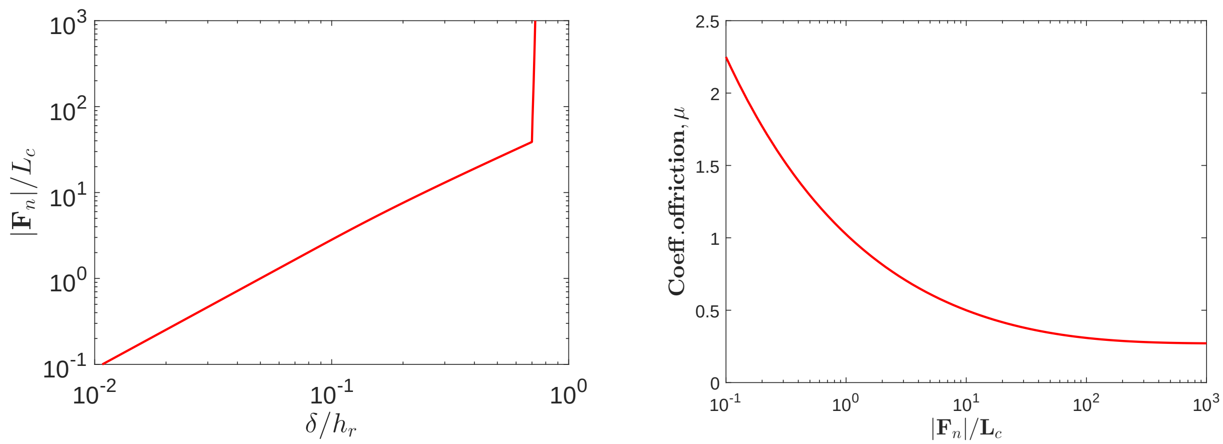

(a) **(b)**

Figure 2.3. Contact model: a) Dimensionless normal contact force as a function of dimensionless overlap for $\epsilon_r = 5 \times 10^{-3}$. Eq. 2.3 and 2.6 for $|\delta| < \delta_c$ and $\delta_c \leq |\delta| \leq 0.7h_r$, respectively. $\mathbf{F}_n$ goes to ∞ as $|\delta| \to 0.8h_r$. b) Friction coefficient as a function of dimensionless contact normal force (Eq. 2.10).

where L_c and δ_c depend on the particle properties such as poisson's ratio (ν), Youngs modulus (E) and yield strength (Y_0) of the material. Their expressions are given in Brizmer *et al.* [60] as follow:

$$L_c = \bar{L_c}\boldsymbol{\pi}^3 \frac{Y_0}{6} C_\nu^3 \left(h_r \frac{2(1-\nu^2)Y_0}{E} \right)^2, \tag{2.4}$$

$$\delta_c = \bar{\delta_c} h_r \left(\boldsymbol{\pi} C_\nu \frac{(1-\nu^2)Y_0}{E} \right), \tag{2.5}$$

where $C_\nu = 1.234 + 1.256\nu$, $\bar{L_c} = 8.88\nu - 10.13(\nu^2 + 0.089)$ and $\bar{\delta_c} = 6.82 - 7.83(\nu^2 + 0.0586)$.

If we have $|\delta| \geq \delta_c$ (plastic region), the normal force is softer and calculated using the following expression:

$$\mathbf{F}_{C,n}^{(\mathrm{i,j})} = -L_c \left(\frac{|\delta|}{\delta_c} \right)^{3/2} \left[1 - exp \left(\frac{1}{1 - \left(\frac{|\delta|}{\delta_c} \right)^\beta} \right) \right] \mathbf{n}^{(\mathrm{i,j})}, \tag{2.6}$$

where $\beta = 0.174 + 0.08\nu$. $\mathbf{F}_{C,n}^{(\mathrm{j,i})}$ is just $-\mathbf{F}_{C,n}^{(\mathrm{i,j})}$.

In addition, owing to the finite time steps and large magnitude of contact forces at higher shear rates and/or at higher volume fractions, it is possible that particles may overlap. To prevent overlaps we need to use very small time steps which is computationally expensive.

Hence, to avoid this issue, the normal force is multiplied by a function which goes to infinity as the inter-particle distance falls below a specified threshold. This threshold value can be chosen arbitrarily and has been shown to have negligible influence on the lubrication and contact stresses [52]. To be consistent with the previous studies [52] we choose the threshold to be $\delta = 0.8h_r$. The multiplying function is multiplied if $\delta \geq 0.7h_r$ (See Fig. 2.3a). The multiplying function used was $f(\delta) = 3^{(\delta-0.7h_r)/(0.8h_r-\delta)}$.

2.1.1.2 Tangential Contact Force

We model the tangential contact force as a linear spring with Amontons-Coulomb friction law [24], [108], [109]. The tangential contact force and the resulting contact torque acting on the particle is then given as:

$$\mathbf{F}_{C,t}^{(\mathrm{i,j})} = k_t \xi^{(\mathrm{i,j})} \mathbf{t}^{(\mathrm{i,j})}, \tag{2.7}$$

$$\mathbf{T}_{C}^{(\mathrm{i,j})} = a_{\mathrm{i}} \mathbf{n}^{(\mathrm{i,j})} \times \mathbf{F}_{C,t}^{(\mathrm{i,j})}, \tag{2.8}$$

and satisfy friction law as $|\mathbf{F}_{C,t}^{(\mathrm{i,j})}| \leq \mu |\mathbf{F}_{C,n}^{(\mathrm{i,j})}|$. In the above expression for tangential contact force, k_t is the tangential spring stiffness coefficient and can be calculated as [52], [62], [110]:

$$k_t = \frac{2}{7} \frac{|\mathbf{F}_{C,n}^{(\mathrm{i,j})}|}{|\delta|}. \tag{2.9}$$

The tangential spring stretch, $\xi^{(\mathrm{i,j})}$ can be calculated from the normal ($\mathbf{U}_n^{(\mathrm{i,j})} = \mathbf{n}^{(\mathrm{i,j})}\mathbf{n}^{(\mathrm{i,j})} \cdot (\mathbf{U}^{(\mathrm{j})} - \mathbf{U}^{(\mathrm{i})})$) and tangential ($\mathbf{U}_t^{(\mathrm{i,j})} = (\mathbf{I} - \mathbf{n^{(i,j)}n^{(i,j)}}) \cdot [\mathbf{U^{(j)}} - \mathbf{U^{(i)}} - (\mathbf{a_i\Omega^i} + \mathbf{a_j\Omega^j}) \times \mathbf{n^{(i,j)}}]$) relative velocities between the particles i and j by applying the algorithm described in Luding [109] and Mari *et al.* [25]. $\mathbf{t}^{(\mathrm{i,j})}$ is a vector normal to $\mathbf{n}^{(\mathrm{i,j})}$ in the tangential direction to the particles and given as: $\mathbf{F}_{C,t}^{(\mathrm{i,j})}/|\mathbf{F}_{C,t}^{(\mathrm{i,j})}|$.

2.1.1.3 Load dependent coefficient of friction

It has been shown recently by Lobry *et al.* [52] that a load dependent coefficient of friction which decreases with increase in normal load between the particles can successfully reproduce the shear thinning behavior observed in many practical suspensions. Taking inspiration from this study, we use the friction coefficient calculated by Brizmer *et al.* [60].

$$\mu = 0.27\text{coth}\left[0.27\left(\frac{|\mathbf{F}_n^{(\mathrm{i,j})}|}{L_c}\right)^{0.35}\right]. \tag{2.10}$$

The above models for the normal contact force and the coefficient of friction is valid for a range of materials with ν in the range (0.3-0.5). The tangential force model is slightly different from that of Brizmer *et al.* [60]. This is because for convenience of computations a simple linear spring model is used widely in the literature [24], [25], [52], [62] (Please refer to Lobry *et al.* [52] for a detailed discussion on validity of this model). Furthermore, the aim of this study is to understand the effect of roughness on the rheology of suspension whose effect is captured in the modeling of the normal contact force and by extension the coefficient of friction. Hence, to develop an understanding of this effect, it is important to start with a relatively simple model for the tangential force.

2.1.2 Stress and bulk rheology calculations

To calculate the rheological properties we need the bulk stress in the suspension. The bulk stress in a suspension of rigid particles in a flow with strain rate $\mathbf{E}^\infty$ is (subtracting isotropic part of the fluid pressure):

$$\mathbf{\Sigma} = 2\mu\mathbf{E}^\infty + \mathbf{\Sigma}^p, \tag{2.11}$$

where $\mathbf{\Sigma}^p$ is the particle contribution to the bulk stress, and is given by the sum of hydrodynamic stress $\mathbf{\Sigma}^H$ and the contact stress $\mathbf{\Sigma}^C$ as:

$$\mathbf{\Sigma}^p = \mathbf{\Sigma}^H + \mathbf{\Sigma}^C, \tag{2.12}$$

where $\mathbf{\Sigma}^H$ and $\mathbf{\Sigma}^C$ can be calculated by taking ensemble average of the hydrodynamic $\mathbf{S}_H$ and contact $\mathbf{S}_C$ stresslets at each time step. We get,

$$\mathbf{\Sigma}^H = \frac{1}{V}\left(\sum_{\mathrm{i}} \mathbf{S}_H^{(\mathrm{i})}\right), \tag{2.13}$$

$$\mathbf{\Sigma}^C = \frac{1}{V}\left(\sum_{\mathrm{i>j}} \mathbf{S}_C^{(\mathrm{i,j})}\right). \tag{2.14}$$

Therefore,

$$\mathbf{\Sigma} = 2\mu\mathbf{E}^\infty + \frac{1}{V}\left(\sum_{\mathrm{i}} \mathbf{S}_H^{(\mathrm{i})} + \sum_{\mathrm{i>j}} \mathbf{S}_C^{(\mathrm{i,j})}\right), \tag{2.15}$$

where V is the volume of the domain, L^3. Shear stress σ, normal stress differences N_1 and N_2, relative viscosity η_r, and normal stress difference (N) can then be defined as $\sigma = \Sigma_{12}$, $N_1 = \Sigma_{11} - \Sigma_{22}$, $N_2 = \Sigma_{22} - \Sigma_{33}$, $\eta_r = \sigma/(\eta\dot{\gamma})$ and $N = N_1 - N_2$. The systematic splitting of the particle stress in contributions from hydrodynamic and contact stresses allows us to understand the relative contributions from lubrication and contact interactions to the rheological properties. E.g., the contribution from the hydrodynamic stress to the relative viscosity is $\eta_r^H = 1 + \Sigma_{12}^H/(\eta\dot{\gamma})$ and the corresponding contribution from the contact stresses is $\eta_r^C = \Sigma_{12}^C/(\eta\dot{\gamma})$ and so on.

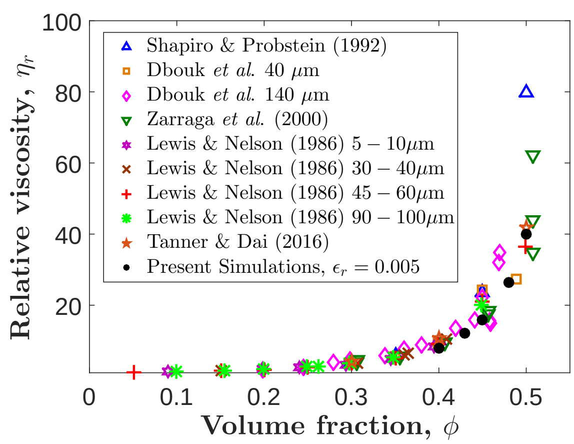

Figure 2.4. Relative viscosity for various volume fractions at $\sigma = 10$ (Pa) from simulations against previous experimental results. The relative viscosity values are consistent with experiments [7], [20], [22], [111], [112].

2.1.3 Simulation conditions

1. *Bidisperse suspension* We simulate suspensions of sheared bidisperse spheres where $a_2/a_1 = 1.4$. Smaller and larger spheres have the same volume fractions ($\phi_1 = \phi_2$). The particles are neutrally buoyant. These assumptions are often made in simulation studies of suspensions of rough particles [25], [52]. This choice of particle size distribution is inspired by the fact that there is significant cluster formation/crystallization in the simulations of monodisperse spheres which can be avoided by the introduction of slight bidispersity [25], [52], [56], [113]. Also, this choice of the radius ratio and volume fractions for the smaller and larger spheres was found to produce results very close to their monodisperse counterparts [55], [89] and Fig. 2.4.

2. *Boundary conditions and domain size*: We calculate the bulk properties of the sheared suspensions such as relative viscosity and normal stress differences. We use the Lees-Edwards periodic boundary conditions [114], which are widely used in the literature for simulation of sheared flows and have been observed to produce accurate results for bulk properties. This choice of boundary condition enables us to simulate the sheared suspension for a fixed domain volume without loss of generality. For this study, we simulate shear flow of suspension in a cubic box with sides $15a_1$, where a_1 is the radius of the smaller particles [52]. We repeated our simulations for a larger domain with larger sides viz., $20a_1$ which has almost twice the number of particles as compared to the smaller domain. Increasing the domain size reduces the error but the mean values are still the same (See Table 2.2 in Sec. 2.1.4.1). Hence, we perform all the simulations for a cubic box with sides $15a_1$. A detailed validation of the model is presented in Sec. 2.1.4.

3. *Range of parameters investigated*: Typically, polystyrene beads are used for studying the effects of roughness on suspension rheology [7], [52], [54]. The required material properties and simulation parameters are listed in table 2.1. The presence of multiple length scales $[a_\mathrm{i}, a_\mathrm{j}, h_r, \delta_c]$ introduces multiple time scales and as a result the simulation time step required for accurate simulations turns out to be very small. Hence, to keep the time step in a reasonable range ($\geq 1 \times 10^{-5}/\dot{\gamma}$), we fix $\delta_c = 0.05h_r$ following

Lobry *et al.* [52]. We use a time step of $2.5 \times 10^{-5}/\dot{\gamma}$ for most of the cases except for $\phi = 48\%$ and 50% at $\dot{\gamma} = 0.1$ and $0.3s^{-1}$ where $\Delta t = 1 \times 10^{-5}/\dot{\gamma}$. This timestep was sufficiently small to observe smooth attachment-detachment of the contacts and a continuous variation in the contact forces. The aim of this study is to understand the effects of varying particle surface roughness on the rheology of suspension. Hence, we simulate the shear flow of rough particles for 6 different dimensionless roughness values $\epsilon_r = h_r/a_1$ viz., (0.005, 0.01, 0.017, 0.025, 0.04, 0.05). The simulations were carried out for shear rate values $\dot{\gamma}$ in the range [0.1 - 10] for volume fractions (0.40, 0.43, 0.45, 0.48, 0.50).

Table 2.1. Simulation parameters

E (Pa)	Y_0 (Pa)	ν	ϕ	$\dot{\gamma}(s^{-1})$	$\epsilon_r(\%)$
3×10^9	30×10^6	0.4	0.40 - 0.50	0.1 - 10	0.5 - 5.0

2.1.4 Validation

2.1.4.1 Domain size independence test

Table 2.2 shows the results for η_r for two different cubic domains with size $15a_1$ and $20a_1$. The values for η_r are in reasonable agreement for both the domain sizes. Hence, we run all the simulations for the smaller domain, i.e., for a cubic box with sides $15a_1$.

2.1.4.2 Comparison with Lobry *et al.* [52]

Fig. 2.5 shows the comparison of η_r for this study and that of Lobry *et al.* [52], which uses the same contact model. Lobry *et al.* [52] present all their results in terms of the dimensionless reduced shear rate ($\dot{\Gamma} = 6\pi\eta a_1^2\dot{\gamma}/L_c$) defined by their eq. (2.12). The focus of their study was the shear thinning effect which could be reproduced by a normal load dependent coefficient of friction decreasing with increase in the normal load (which in turn depends on the shear stress). Our focus is to investigate a possible mechanism to explain the experimental study by Tanner & Dai [7], thus, we present our results in terms of dimensional shear rate and stress. In order to compare these studies, we present our results in terms of

Table 2.2. Domain independence. η_r for two domain sizes, $(15 \times 15 \times 15)\, a_1$ (D_1) & $(20 \times 20 \times 20)\, a_1$ (D_2) for $\epsilon_r = 0.005$

Reduced shear rate, $\dot{\Gamma}$	ϕ (%)	η_r, D_1	η_r, D_2
0.1	40	9.29	9.65
1.0	40	8.32	8.63
10.0	40	7.64	7.77
0.1	45	18.42	18.9
1.0	45	15.51	15.28
10.0	45	13.23	12.87
0.1	50	43.55	42.72
1.0	50	30.32	29.62
10.0	50	25.73	25.42

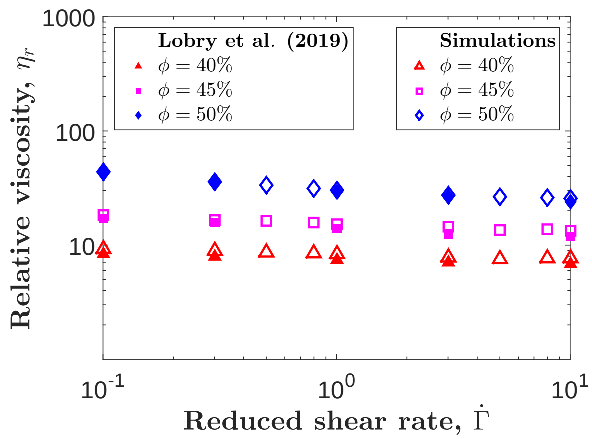

Figure 2.5. Comparison of η_r with Lobry *et al.* [52]. The comparison is satisfactory. The slight difference in the viscosities is due the different model used for calculating hydrodynamic interactions. Open symbols: simulation results, closed symbols: results from Lobry *et al.* [52].

Table 2.3. Comparison of N_1/σ and N_2/σ for $\epsilon_r = 0.005$ at $\phi = 40\%$ and $\phi = 50\%$ with the results from Lobry *et al.* [52]. PS = Present simulations.

$\phi(\%)$	N_1/σ, Lobry *et al.* [52]	N_1/σ, PS	N_2/σ, Lobry *et al.* [52]	N_2/σ, PS
40	-0.055	-0.043	-0.28	-0.27
50	-0.083	-0.099	-0.37	-0.33

reduced shear rate in this section. Fig. 2.5 compares the relative viscosity of the suspensions at volume fractions 40 %, 45 % and 50 % with a roughness ratio $\epsilon_r = 0.005$ with calculations of Lobry *et al.* [52] with the same simulation parameters. In addition, table 2.3 compares the values of dimensionless normal stress differences in the present study with Lobry *et al.* [52]. These results show that data from the present simulations is consistent with that of Lobry *et al.* [52].

2.2 Results and Discussion

This section is devoted to the important results of the simulations. The main focus of this study is to understand the effects of varying the particle surface roughness on the rheology of suspensions. The simulations for different parameters were carried out for a total of 30-50 strain units, i.e., $t_{final} = (30 - 50)/\dot{\gamma}$. The first 10 strain units were discarded owing to the transient behavior of simulations in the initial time. All the rheological properties presented below are calculated by averaging after 20 % strain units and only the average values are presented. The standard deviation was less than 10 % in most of the cases except a few in which maximum standard deviation was around 15 %. It is now quite established that in non-Brownian suspensions there is no time scale but rather a stress-scale that can explain either the shear thickening or the shear thinning behavior [27]. Since stress is the governing parameter, we present the results in terms of shear stress ($\sigma = \eta_r \eta \dot{\gamma}$) for better understanding of the governing mechanism. To calculate relative viscosity at a constant stress for suspensions with different volume fractions interpolation has been performed whenever needed.

2.2.1 Effects of roughness on the relative viscosity

Fig. 2.6a shows the effect of increasing roughness from 0.5 % to 5.0 % at different shear stress values for $\phi = 50\%$. From the figure, it is clear that a contact model wherein the coefficient of friction decreases with normal load can produce the experimentally observed shear thinning behavior [7], [52], [54] in the suspensions. The agreement between trends and behavior of η_r obtained in experiments and the simulations is clear from the figure. For comparison purposes, we assume the simulation case with the roughness ratio, $\epsilon_r = 1\%$ to be representative of the suspension of smooth spheres, i.e., no grinding case in Tanner & Dai

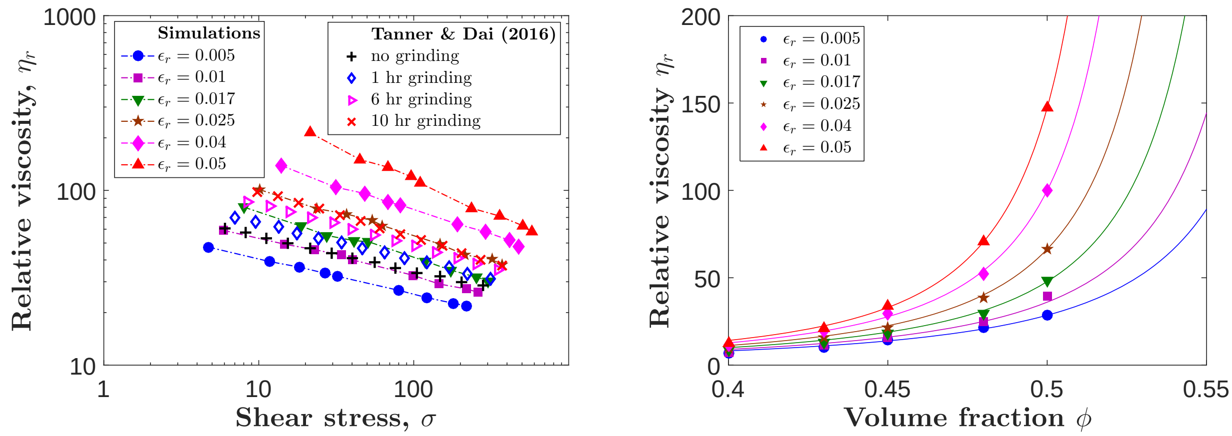

(a) (b)

Figure 2.6. Variation of relative viscosity, η_r with a) shear stress (σ) for different particle roughness for $\phi = 50\%$ (scatter plot shows the data from Tanner & Dai [7]) and b) volume fraction at a constant $\sigma = 50$ (Pa). Increase in relative viscosity with roughness for various volume fractions at $\sigma = 50$ (Pa). The solid lines show the Maron-Pierce law (see section III-C) fitting to the data. The increase in relative viscosity with roughness becomes more prominent at higher volume fractions owing to the fact that the number of particles in contact at a particular time increases with volume fraction. The contact model implemented in this study can reproduce the experimentally observed shear thinning behavior in suspensions as well as predicts that the relative viscosity will increase with increase in surface roughness of the particles.

[7]. This is a valid assumption since even the smoothest spheres in reality have roughness of O($10^{-3} - 10^{-2}$) [7], [53].

There is a clear increase in the relative viscosity of the suspension for all the volume fractions considered as we increase particle roughness (Fig. 2.6b). At $\dot{\gamma} = 1s^{-1}$, we observe about 28 %, 38 % and 55 % increase for suspensions with 40 %, 45 % and 50 % volume fractions, respectively, for a roughness ratio of 2.5 %. The corresponding increase for a roughness ratio of 5 % is 50 %, 95 % and 175 % increase for suspensions with 40 %, 45 % and 50 % volume fractions, respectively. An increase of similar magnitudes in the relative viscosity with increasing roughness is observed for all the volume fractions and shear rates simulated in this study. Tanner & Dai [7] observe 21 % and 78 % increase in the viscosity for 40 % and 50 % volume fraction suspensions at $\dot{\gamma} = 1s^{-1}$ which is in agreement with what we observe for a roughness ratio of 2.5 % in our simulations.

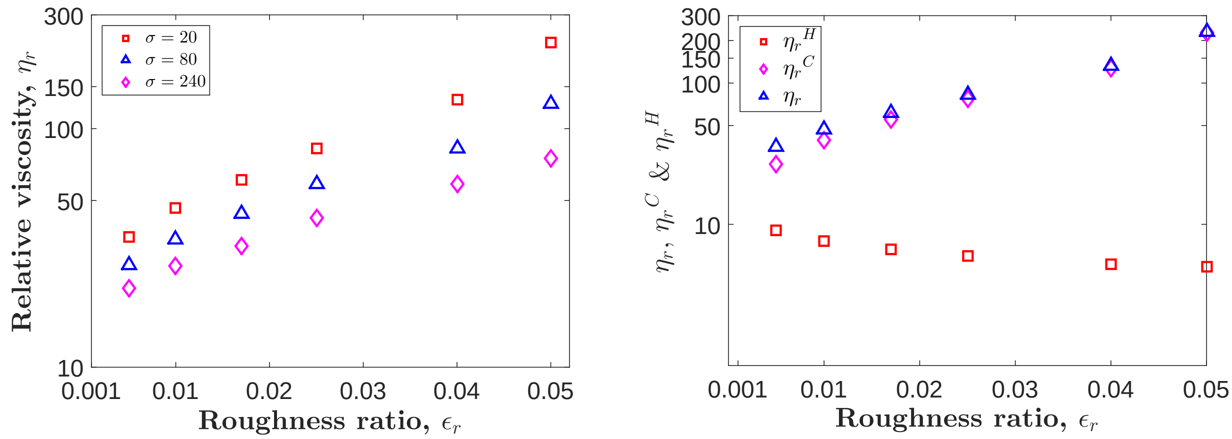

(a) **(b)**

Figure 2.7. a) Variation of η_r for $\phi = 50$ % with roughness for three different shear stresses, σ = 20, 80 and 240 Pa. b) Variation in contributions from hydrodynamic ($\eta_r{}^H$) and contact ($\eta_r{}^C$) interactions to the relative viscosity (η_r) with roughness for $\phi = 50\%$ at $\sigma = 20$ Pa. The relative contribution from the contact interactions to the total viscosity increases with increasing roughness which results in the increase in η_r with roughness.

The differences in relative viscosity between our simulations and the experiments from Tanner & Dai [7] can be attributed to some fundamental assumptions used while modelling the suspensions and contact forces. The main reason for this seems to be the geometry of the roughness in the experiments and that in the simulations. Tanner & Dai [7] used grinding for introducing roughness which may or may not preserve the spherical shape of the particles. We model the roughness as hemispherical asperities on perfectly spherical surfaces. As a result, we cannot compare our data quantitatively with the experiments, but the models that we used accurately capture the trends and behaviors of concentrated rough sheared suspensions observed in experiments.

Fig. 2.7a shows the increase in relative viscosity for a suspension with 50 % volume fraction for 3 different shear stresses. It can be concluded from this figure that the relative increase in the viscosity of suspensions with higher roughness compared to the smoothest case decreases as we increase the shear stress. This can be understood if we look at the microscopic balance between the lubrication and contact forces and coefficient of friction with stress. With increase in shear rate, the shear stress, which is directly proportional to

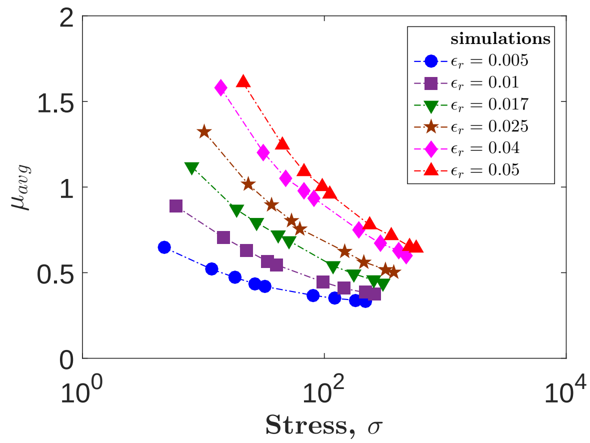

Figure 2.8. Variation in the average coefficient of friction for the suspensions with the dimensionless roughness for $\phi = 50\%$ with stress for different roughness values. μ_{avg} increases with ϵ_r and the relative increase in μ_{avg} reduces with increasing σ. This indicated that the variation in μ_{avg} becomes less important at high stress values.

the shear rate, also increases. Increase in shear stress directly increases the magnitude of normal forces between the particles [52]. But this increase in the normal contact force means reduction in the coefficient of friction as per Eq. 2.10 (See Fig. 2.8). We expect a reduction in the average coefficient of friction (Fig. 2.8) with shear stress with all other parameters held constant which eventually results in a decrease in the relative viscosity with increasing shear stress.

This point becomes clear if we look at the variation of average coefficient of friction with roughness at constant stresses (See Fig. 2.8). For higher values of stresses the relative increase in the average coefficient of friction reduces, i.e., the variation in average coefficient of friction is less and less important as stress increases and as a result the variation in viscosity becomes less and less for high shear rates or high shear stresses.

It is also interesting to look at the contributions from hydrodynamic and the contact stresses to the relative viscosity. Fig. 2.7b shows that hydrodynamic contribution decreases with increase in ϵ_r. This is to be expected as the average inter-particle gap increases with increase in roughness. The hydrodynamic stresslet depends on the inverse of the inter-particle gap. Higher inter-particle gap leads to a reduction in hydrodynamic stresslet. But this reduction in the hydrodynamic stress is overcompensated by the increase in the contact stress which increases by around 200 % from the smoothest to roughest case. The reason behind such a huge increase is again related to the relative magnitude of the normal contact forces and the dependence of coefficient of friction on the normal forces. Higher inter-particle gaps mean reduction in the lubrication forces. As a result, small deformations of the asperities are enough to balance the lubrication forces as the roughness increases. Lower deformations mean a lower contact force and according to Eq. 2.10, a higher coefficient of friction. Given the steep behavior of coefficient of friction in the lower range of normal force, we get such a huge increase in the contact contribution to the particle stresses.

To elaborate further on the above point, we need to look at the force scale associated with the elastic to plastic transition. Here, L_c gives us the force scale for the transition from the elastic region (where μ is high) to the plastic region (where µ decreases and levels off in the plastic regime). From eq. 2.4 we can conclude that the force scale for this transition increases with roughness as $L_c \propto {h_r}^2$. So, for a constant stress, as we increase the roughness, the contacts move towards the elastic region, where we have a relatively large coefficient of friction (see Fig. 2.3b). Thus, with increase in roughness, larger and larger stress is needed for the asperities to yield which results in the increase in viscosity with roughness.

The direct numerical simulation (DNS) study by Gallier *et al.* [24] observed a decrease in the contributions from both hydrodynamic and contact stresses to η_r with increasing roughness while their relative magnitudes remaining constant ($\eta_r^H \approx 0.68\eta_r$ and $\eta_r^C \approx 0.32\eta_r$). In our simulations, we observe that the relative contribution from the contact interactions to the stress increases with increase in roughness which is mainly responsible for the increase in η_r with increasing ϵ_r. This difference can be attributed to the fact that Gallier *et al.* [24] used Hertz contact model for the normal contact forces in which the normal stiffness coefficient (k_n) was calculated by balancing the hydrodynamic and contact forces instead of getting it from the particle material properties like ν, E, and Y_0. Since they did not consider any relationship between μ and ϵ_r these differences are expected. No such assumptions have been used in our simulations. k_n (which can be considered analogous to $L_c/(\delta_c)^{3/2}$) in our simulations remain constant for all $\dot{\gamma}$ for a given ϵ_r. As a result, we have a competition between the lubrication and contact interactions and a force scale for which the cntact transitions from elastic to plastic regime. Owing to the dominant increase in the contact stresses we observe the increasing trends in η_r with increasing roughness.

2.2.2 Effects of roughness on normal stress differences

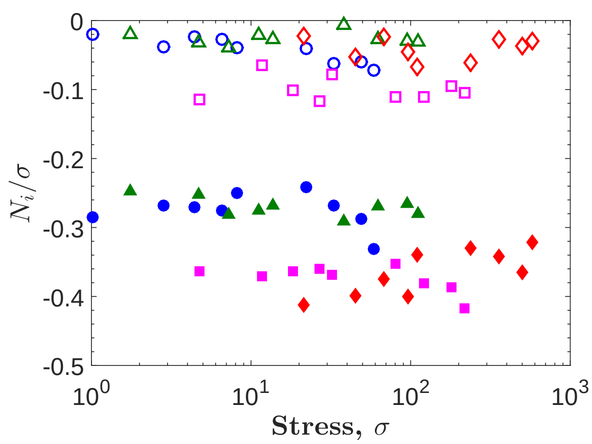

Figure 2.9. Variation of dimensionless N_1 and N_2 with stress for $\phi = 40\%$ (O for $\epsilon_r = 0.005$ and $\triangle$ for $\epsilon_r = 0.05$) and $\phi = 50\%$ ($\square$ for $\epsilon_r = 0.005$ and $\Diamond$ for $\epsilon_r = 0.05$). Hollow symbols are for N_1/σ and filled symbols are for N_2/σ. This plot shows that roughness reduces the magnitude of N_1/σ while the magnitude of N_2/σ remains almost constant with roughness.

Apart from the relative viscosity, first and second normal stress differences are also important rheological properties of suspensions and have been a focus of many recent studies [23]–[25], [37], [42], [89], [107]. In this section we present results for dimensionless N_1, N_2 and $N = N_1 - N_2$.

N_2 varies linearly with shear stress in the sense that its magnitude increases with the shear rate. We obtain negative values of N_2 for all the roughness and shear rates (and much larger than N_1, Fig. 2.10a. The values of dimensionless $-N_2$, i.e., $-N_2/\sigma$ lie in the range 0.2 - 0.5 (see Fig. 2.9 and 2.10a). These magnitudes are consistent with most of the experimental and computational data available [20], [22], [24], [25], [42], [43], [55], [107]. The increase in N_2 with roughness is expected since N_2 has origins in the contact interactions [24]. As previously explained increase in roughness leads to an increase in the contact stress in the suspension.

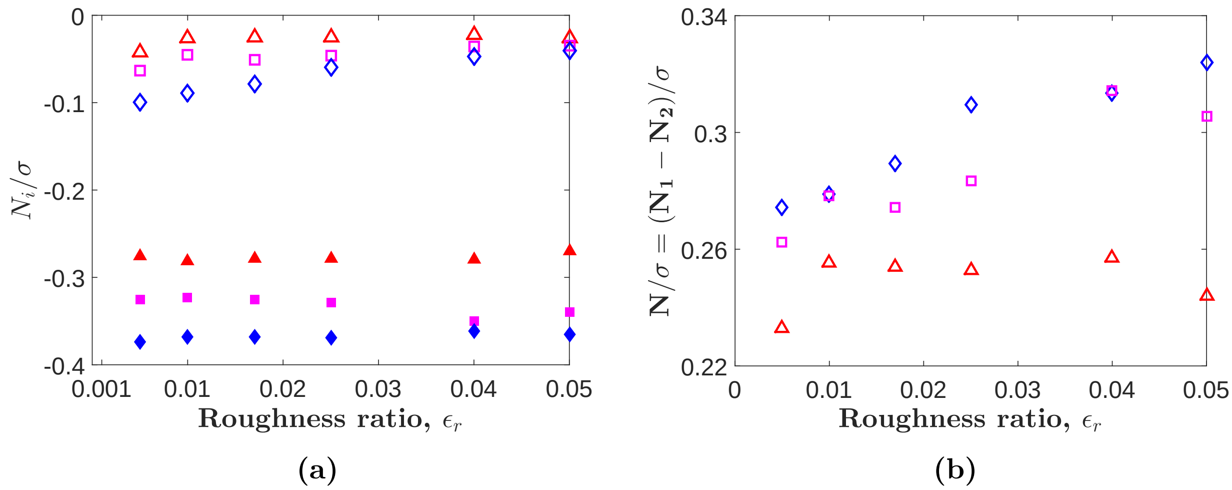

Figure 2.10. a) Variation of average dimensionless N_1 and N_2 with ϵ_r for different volume fraction values. $\phi = 40\%(\triangle), 45\%(\square)$ & $50\%(\Diamond)$. Hollow symbols are for N_1/σ and filled symbols are for N_2/σ. b) Variation of dimensionless normal stress difference $N/\sigma = (N_1 - N_2)/\sigma$ with ϵ_r for $\phi = 40\%(\triangle), 45\%(\square)$ & $50\%(\Diamond)$. N is directly related to the normal force acting in a parallel plate rheometer. Thus, increasing roughness increases the normal force on the plate in a parallel plate rheometer.

Fig. 2.9 gives the variation of magnitude of dimensionless N_1 and N_2 with stress for 40 % and 50 % suspensions for smoothest ($\epsilon_r = 0.005$) and the roughest case ($\epsilon_r = 0.05$). We don't observe a monotonous behavior in N_1 with roughness or stress as we do for N_2, but the magnitude of dimensionless N_1 decreases with roughness. This becomes clear if we take an average over for all the shear rates for a particular roughness. Fig. 2.10a shows the variation of N_1/σ and N_2/σ averaged over for all the stresses for a fixed roughness. We observe that the magnitude of N_2/σ remains almost constant for different roughness values since it increases linearly with σ in our simulations, while the magnitude of N_1/σ decreases with roughness. The observed behavior can be understood by looking at the average coefficient of friction for different roughness values. It is clear from Fig. 2.8 that the average coefficient of friction increases with roughness. Increasing coefficient of friction reduces the magnitude of N_1/σ [24], which is depicted in Fig. 2.10a

Gallier *et al.* [24] is the only computational study which computed the variation of normal stress differences with roughness that we could find. They obtained almost no variation in N_1/σ and N_2/σ with varying roughness from 0.01 % to 1 %. The range of roughness in our case is very high as compared to that of Gallier *et al.* [24]. Please note here that the contact dynamics model used by Gallier *et al.* [24] is very simple, where the coefficient of friction has been assumed to have a constant value independent of the roughness and the competition between the hydrodynamic and contact forces has been eliminated by setting shear stress dependent values of k_n, so these differences are expected.

Finally, we plot the dimensionless normal stress difference which is given by $N/\sigma = (N_1 - N_2)/\sigma$ in Fig. 2.10b. We obtain an increasing trend for N with increase in roughness. This is in agreement with the experimental results from Tanner & Dai [7] and Dai *et al.* [43]. $N_1 - N_2$ is directly related to the normal force acting on the plate in the parallel plate rheometer [7], which means the normal force on the plate increases with an increase in the particle roughness.

2.2.3 Effect of roughness on jamming fraction

Fig. 2.6b shows the behavior of relative viscosity with the volume fraction. It is well known in the literature of non-Brownian suspensions that the relative viscosity diverges as the volume fraction approaches to a maximum value beyond which no flow is possible [113]. This maximum is known as the jamming fraction which is different from the random close packing fraction (RCP). The jamming fraction ϕ_m depends on many factors like stress, coefficient of friction, roughness, bidispersity ratio, etc [25], [52], [83], [89], [115]. The relative viscosities for high volume fractions can be described by Maron-Pierce formula given by Metzner [116]:

$$\eta_r = [1 - \phi/\phi_m]^{-2}. \tag{2.16}$$

This formula however cannot capture the shear thinning behavior observed in sheared suspensions if we assume a fixed value for ϕ_m. In the experimental study by Tanner & Dai [7] the formula does a good job only for smooth spheres at $\dot{\gamma} = 1s^{-1}$ with the assumption that $\phi_m = 0.59$. But along with the volume fraction the relative viscosity depends on other factors mentioned before. We, thus, need to account for them in order to describe the relative viscosity. One of the important factors governing the relative viscosity is the coefficient of friction, μ. Wyart and Cates [97] suggested the following model for frictional suspensions:

$$\eta_r = f(\phi, \mu), \tag{2.17}$$

where the friction coefficient μ is a function of the shear stress. In this study, the coefficient of friction is governed by the stress and the roughness. Hence, we cannot disassociate friction from roughness or stress. Since the original Maron-Pierce formula is a reasonable approximation to the relative viscosity at high volume fractions, we assume,

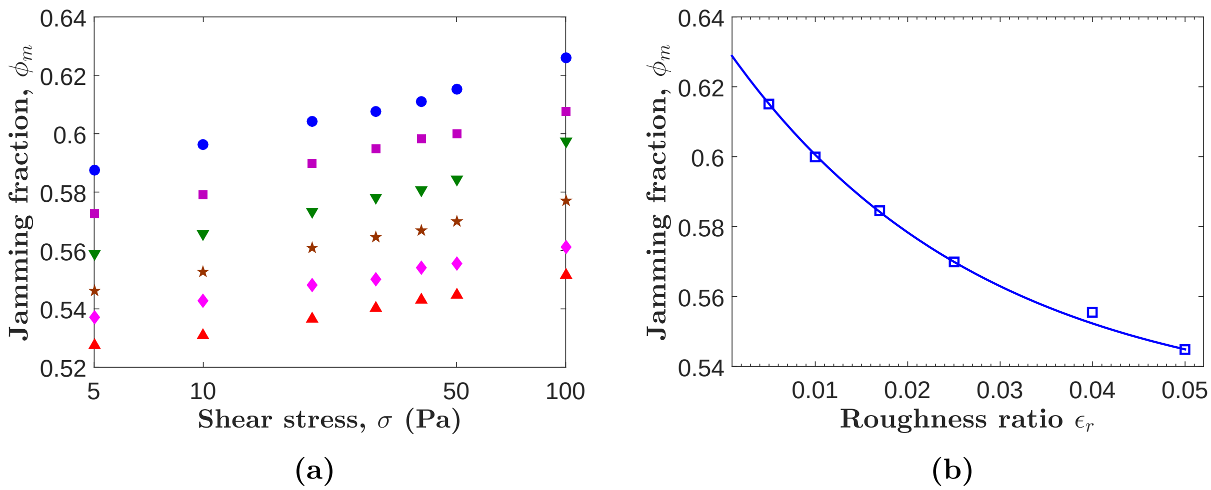

Figure 2.11. Variation of ϕ_m: a) Variation in the jamming volume fraction with shear stress. The maximum packing fraction above which suspension ceases to flow decreases with increasing roughness and increases with increase in the shear stress because of the increase in μ_{avg} with roughness and decrease in μ_{avg} with stress, respectively. (Legends are the same as Fig. 2.6b). b) Variation in the jamming fraction with ϵ_r at $\sigma = 50$ (Pa). Solid line is the fitting curve using equation 2.19. The jamming fraction reduces with roughness for a given stress owing to the increase in μ_{avg} and in effective radius of the spheres with roughness.

$$\eta_r = [1 - \phi/\phi_m(\sigma, \epsilon_r)]^{-2}. \tag{2.18}$$

We would also like to obtain the effect of varying stress and roughness on the the jamming fraction. Hence, instead of assuming a constant value for ϕ_m, we calculate it by fitting the data with the above equations. Solid lines in Fig. 2.6b represent the fitting curves given in Eq. 2.18 for the simulation data. In addition, the following equations [52], [82], [117] have been used for fitting the ϕ_m vs ϵ_r. The fitting parameters obtained are presented in Table 2.4.

$$\phi_m(\sigma, \epsilon_r) = \phi_m^\infty(\sigma) + [\phi_m^0(\sigma) - \phi_m^\infty(\sigma)]\frac{\exp(-X_\phi^p \mathrm{atan}(\epsilon_r)) - \exp(-\pi X_\phi^p/2)}{1 - \exp(-\pi X_\phi^p/2)}. \tag{2.19}$$

Fig. 2.11a and 2.11b show that the jamming fraction decreases with increasing the roughness. This is due to the fact that rough spheres behave like spheres with larger radii. Hence, the effective volume fraction increases by a factor of $(1+\epsilon_r)^3$. For $\phi = 50\%$, the effective ϕ is 57.88 % for $\epsilon_r = 0.05$, while the effective $\phi = 50.75\%$ for $\epsilon_r = 0.005$. Thus, the effective ϕ for higher roughness values is closer to the maximum packing fraction for smooth spheres (jamming fraction for smooth spheres ≈ 0.625, see Fig. 2.11b). Hence, the maximum packing fraction reduces with roughness and as a result, we see an increase in viscosity at a particular volume fraction due to the apparent increase in the volume fraction due to roughness.

Table 2.4. Fitting parameters for Eq. 2.19

σ (Pa)	ϕ_m^0	ϕ_m^∞	X_ϕ^p
5	0.519	0.605	46.163
10	0.521	0.615	43.747
20	0.522	0.622	38.326
30	0.523	0.624	35.554
40	0.527	0.628	37.299
50	0.528	0.633	36.648
100	0.536	0.646	39.349

The reduction in ϕ_m with increasing stress has also been observed in experiments [83], [115]. For a real suspension made of particles that have a given roughness, they observed that, indeed, the jamming fraction depends on the stress. They showed that at low shear stress values, the suspension does not flow but is able to flow at higher stress values meaning that ϕ_m depends on the shear stress and all the factors determining the shear stress.

The reduction in ϕ_m is also consistent the variation of the average coefficient of friction (calculated by averaging the coefficient of friction (μ_{avg}) between all the contacting particles). If we look at μ_{avg} for a particular shear rate (stress) and volume fraction, we observe that it increases very rapidly with roughness. It has been shown in previous studies [25], [52] that the jamming fraction reduces with increase in coefficient of friction. Hence, we expect a reduction in ϕ_m with increase in roughness, as the average coefficient of friction tends to increase with roughness. This idea is indeed reflected in our simulation results as shown in Fig. 2.8. Mari *et al.* [25] find that for smooth friction-less bimodal suspensions, the jamming fraction is 0.66 which decreases as we increase the coefficient of friction. A value of around 0.7 for jamming fraction was observed by Lobry *et al.* [52] for $\mu = 0$. In the present study, even in the case of smooth spheres, the coefficient of friction is not zero and has an average value around 0.3 for the smoothest case (see Fig. 2.8). So, we expect a maximum packing fraction value to be smaller than 0.66. The value we calculate for the smoothest case is $\approx$ 0.62 which is expected since the simulations in this study are not friction-less. This is in agreement with Lobry *et al.* [52] who obtain $\phi_m \approx 0.62$ for $\mu = 0.27$.

The contacts between the particles are intermittent but they depend on the shear stress and the volume fraction. We expect (and observed) more contacts at higher shear stress and volume fractions. Thus, for a particular roughness value and volume fractions we expect more number of particles in contact with increase in shear stress. We also observe that the asperity deformation (δ) reduces with increasing roughness for a fixed stress. For lower roughness a small stress is required for yielding (i.e., to transition from elastic to plastic regime) as compared to larger roughness where a larger stress is needed for the asperities to yield. This means as we increase the roughness particle-particle contacts move more towards the elastic region for a fixed stress. And since in the elastic region, the coefficient of friction has a high value we get an increase in the η_r and the reduction in ϕ_m with increasing the roughness. Also, Fig. 2.7a and 2.8 reveal a strong correlation between the coefficient of friction and the variation of relative viscosity, further corroborating the hypothesis that friction has a very important role in governing the suspension rheology.

3. ROUGHNESS INDUCED SHEAR THICKENING IN NON-BROWNIAN SUSPENSIONS

3.1 Introduction

Suspensions of rigid particles in a variety of fluid media exhibit a rich variety of non-Newtonian behaviors such as yielding [82], shear-thinning [7], [52], [54], [83], [118], shear-thickening [25], [50], [56], [84]–[86], [94], particle migration [38], [41] and anisotropic microstructures [26], [39], [87]. The viscosity of suspensions at moderately high volume fractions usually decreases with increasing the applied shear rate [7], [52], [54], i.e., they shear thin. But dense suspensions show the opposite behavior: their viscosity increases with increasing the shear rate (or shear stress) above a critical value [8], [35], [41], [119]–[123], this phenomenon is known as shear thickening (ST). Example of a ST suspension is cornstarch in water, although not all cornstarch solutions exhibit a shear thickening behavior [124]. Depending on the applied shear rate and the solid loading, ST can occur in two ways: 1) when the viscosity increases gradually with increasing shear rate (or stress) it is called *Continuous Shear Thickening* (CST), or 2) when the viscosity increases abruptly at the critical shear rate it is termed as *Discontinuous Shear Thickening* (DST).

Shear thickening, especially DST, has a long and rich history of scientific investigation with some earlier works dating back to early 20^{th} century [125]–[128]. Some earlier explanations for the phenomenon include sudden onset of turbulent flow between the particles forcing particles to gather in hollow enclosures [129], order disorder transitions [34], [130]–[132], flow induced particle clustering [45], [133]–[136]. But these explanations fail to predict the viscosity jump of required magnitude [9], [25], [119], [137].

The current consensus is that friction between the particles gives rise to DST as it triggers anisotropic force chain networks and granular-type behavior [122], [138]–[140] which has been corroborated by theory [141], simulations [25], [56], [84] and experiments [9], [58], [122], [142], [143]. Friction plays a crucial role in governing the behavior of rigid particle suspensions [24], [51], [52], [117]. This is because in dense suspensions, the lubrication film keeping particles apart breaks and owing to the irregularities on the particle surface, the particles come into contact. Such contacts give rise to tangential forces in addition to the normal repulsive forces. This is true even in the most idealized case of smooth sphere suspensions as even the smooth particles have a roughness of $O(10^{-2} - 10^{-3})$ times the particle radius [39], [52], [53]. As a result, much of the efforts have been involved in understanding the effect of friction between the particles on the ST behavior and the understanding of this mechanism has advanced many folds in the past few years [25], [59], [86], [94], [117], [144], [145]. The most notable effects of increasing friction between the particles is the reduction in the jamming fraction (ϕ_m) [8], [25], [52], [141] and increase in the strength of the ST effect [9], [25], [86], [117]. However, the effect of particle asperities on ST which are the fundamental reason for particle contacts and friction has not been explored much and it is only recently that researchers have started to investigate it.

Early theoretical and computational studies suggested that suspension viscosity should decrease with roughness owing to the reduction in hydrodynamic stresses. Larger asperities increase the lubrication gap between the particles and the hydrodynamic stresses are inversely proportional to the inter-particle gap [24], [37], [88], [95], [106]. But contrary to these predictions, it has been observed in experiments [7], [9], [54] and simulations [118] that the suspension viscosity increases with increase in roughness size. These studies suggest that increasing roughness lowers the critical shear rate (for CST and DST both) and the critical volume fraction (for DST). Recently, Hsu *et al.* [8] demonstrated that rough particles exhibit DST over a wider range of shear rates and solid loadings which are significantly lower than that of smooth particle colloids. The reason behind this is the interlocking of asperities. They introduced roughness artificially by electrostatic adsorption of silica nano-particles onto larger silica particles. In addition, a computational study based on Stokesian Dynamics [44] simulations showed that friction increases the magnitude of ST for suspensions of particles with roughness equal to 1 % of the particle radius [59]. However, this study focused on only 2-D domains with fixed particle roughness (= 1 % of the particle radius) which corresponds to smooth suspensions [39], [52], [53]. As a result they observed only a mild ST and didn't reproduce DST.

The aim of this chapter is to quantify the effect of systematically increasing particle roughness size on the rheology of ST rigid particle suspensions. This paper proposes a simple computational framework which successfully reproduces CST as well as DST and predicts the anticipation and the rise in the magnitude of ST effect with increasing roughness. To this extent, we first elaborate the methods and models used to simulate suspensions of rough particles in a simple shear flow and elements of contact dynamics crucial to reproduce the experimentally observed ST. Then we present the effects of varying particle roughness on the rheology of ST suspensions by studying its effects on the friction-less and frictional jamming fractions, relative viscosity and normal stress differences. We also discuss the possible mechanisms determining the rheology and finally present a phase diagram in shear rate - volume fraction plane to visualize the various transitions and states encountered as we explore a wide range of parameters.

3.2 Methodology

This section describes the models and algorithms used to simulate sheared flow of rough non-Brownian suspensions. We use the same governing equations and hydrodynamic foce calculations as explained in chapter 1–Sec. 1.4. We elaborate on the contact and friction models used below.

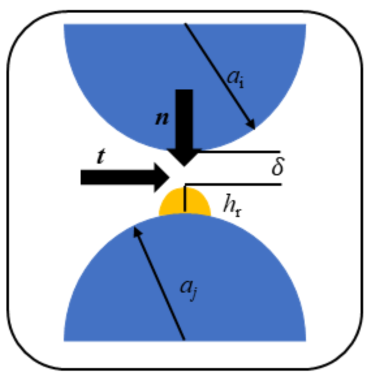

Figure 3.1. Schematic of the asperity geometry: Asperity is modelled as a hemisphere on the particle surface (denoted by yellow). δ is the hydrodynamic separation distance, h_r is the asperity size.

We model the contact forces between the particles as it is done in Discrete Element Method (DEM), a popular method in granular physics [146], [147]. For two spherical particles with radii a_i and a_j with surface roughness $h_r = \epsilon_r(a_\mathrm{i} + a_\mathrm{j})/2$ (ϵ_r is the dimensionless roughness) coming into contact as shown in Fig. 3.1, the contact between the particles takes

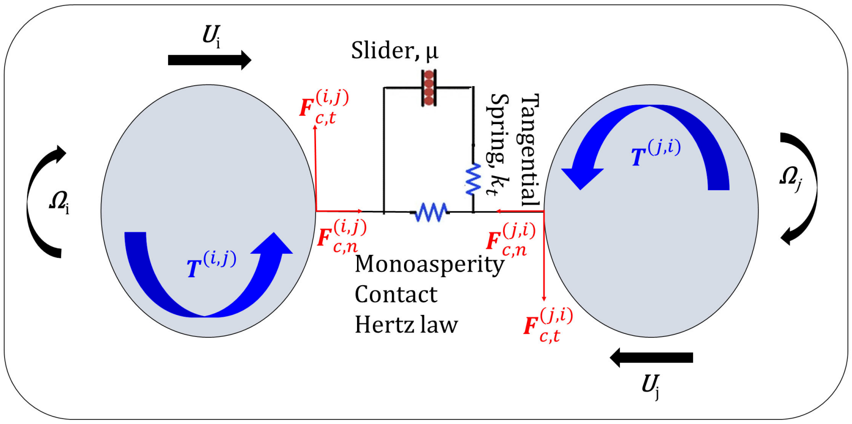

Figure 3.2. Schematic showing contact dynamics between contacting particles and corresponding force models used for force and torque calculations

place via the hemispherical asperity. The contact causes the asperity to deform which in turn gives rise to contact forces between the touching particles. The asperity deformation can be defined as $\delta = (d^{(\mathrm{i,j})} - a_\mathrm{i} - a_\mathrm{j} - h_r)$, the contact occurs when $\delta \leq 0$. Please note that we do not include viscous damping in order to be consistent with previous studies [24], [52], [62].

Furthermore, we split the contact force ($\mathbf{F}_C^{(\mathrm{i,j})}$) into two components [24], [25], i) $\mathbf{F}_{C,n}^{(\mathrm{i,j})}$ which is the normal contact force acting along the line of centers of the two particles, and ii) $\mathbf{F}_{C,t}^{(\mathrm{i,j})}$ which is the tangential contact force acting along the tangent plane at the particle contact Fig. 3.2.

$$\mathbf{F}_C^{(\mathrm{i,j})} = \mathbf{F}_{C,n}^{(\mathrm{i,j})} + \mathbf{F}_{C,t}^{(\mathrm{i,j})}. \tag{3.1}$$

The normal contact force is modelled using Hertz law,

$$\mathbf{F}_{C,n}^{(\mathrm{i,j})} = -k_n \left(|\delta|\right)^{3/2} \mathbf{n}^{(\mathrm{i,j})}, \tag{3.2}$$

here the compression of the asperity has been readily accounted for through the asperity deformation δ. The hydrodynamic force is still calculated for the base particles with the actual inter-particle gap which is equal to $h_r - \delta$ [24], [52], [62]. The dissipative nature of lubrication forces in such conditions will change the rotational dynamics as well, as it overdamps the motion of particles. Since contact interactions are dominant as compared to the lubrication interactions for contacting particles, we expect these effects to not be significant.

The normal stiffness k_n can be evaluated in terms of particle mechanical properties like Young's modulus, Poisson's ratio and Elastic modulus. But, for real materials this value comes out to be very large which forces the time-step to be very small in order to have numerical stability. Hence, for numerical tractability, the normal stiffness k_n is chosen sufficiently high so as to mimic rigid particles and changing k_n does not have a significant impact on the bulk rheology [24], [25], [62], [144]. Here, we take the dimensionless normal stiffness $k_n/(\eta\dot{\gamma}a^2{h_r}^{-3/2}) = 2 \times 10^4$.

The tangential contact force and the resulting contact torque ($\mathbf{T}_C^{(\mathrm{i,j})}$) acting on the particle is then given as:

$$\mathbf{F}_{C,t}^{(\mathrm{i,j})} = k_t \xi^{(\mathrm{i,j})} \mathbf{t}^{(\mathrm{i,j})}, \tag{3.3}$$

$$\mathbf{T}_C^{(\mathrm{i,j})} = a_\mathrm{i} \mathbf{n}^{(\mathrm{i,j})} \times \mathbf{F}_{C,t}^{(\mathrm{i,j})}. \tag{3.4}$$

In the above expression for tangential contact force, k_t is the tangential spring stiffness coefficient and can be calculated as [24], [52], [110]:

$$k_t = \frac{2}{7} \frac{|\mathbf{F}_{C,n}^{(\mathrm{i,j})}|}{|\delta|}. \tag{3.5}$$

The tangential spring stretch, $\xi^{(\mathrm{i,j})}$ can be calculated from the normal ($\mathbf{U}_n^{(\mathrm{i,j})} = \mathbf{n}^{(\mathrm{i,j})}\mathbf{n}^{(\mathrm{i,j})} \cdot (\mathbf{U}^{(\mathrm{j})} - \mathbf{U}^{(\mathrm{i})})$) and tangential ($\mathbf{U}_t^{(\mathrm{i,j})} = (\mathbf{I} - \mathbf{n}^{(\mathrm{i,j})}\mathbf{n}^{(\mathrm{i,j})}) \cdot [\mathbf{U}^{(\mathrm{j})} - \mathbf{U}^{(\mathrm{i})} - (a_\mathrm{i}\boldsymbol{\Omega}^\mathrm{i} + a_\mathrm{j}\boldsymbol{\Omega}^\mathrm{j}) \times \mathbf{n}^{(\mathrm{i,j})}]$) relative velocities between the particles i and j by applying the algorithm described in Luding [148] and Mari *et al.* [25]. $\mathbf{t}^{(\mathrm{i,j})}$ is a vector normal to $\mathbf{n}^{(\mathrm{i,j})}$ in the tangential direction to the particles and given as: $\mathbf{F}_{C,t}^{(\mathrm{i,j})}/|\mathbf{F}_{C,t}^{(\mathrm{i,j})}|$. Contact forces also induce an additional contact stresslet for the particle given by the vector product of particle center to center vector and the contact force as [24]:

$$\mathbf{S}_C^{(\mathrm{i,j})} = \frac{1}{2}\left(\frac{\mathbf{d}^{(\mathrm{i,j})}}{2} \otimes \mathbf{F}_C^{(\mathrm{i,j})} + \mathbf{F}_C^{(\mathrm{i,j})} \otimes \frac{\mathbf{d}^{(\mathrm{i,j})}}{2}\right). \tag{3.6}$$

Since we have a balance between the hydrodynamic and contact forces owing to the choice of k_n as described above, there is no competition between the governing forces which is the fundamental mechanism for observing shear rate dependent rheological behavior [25], [54], [94]. Hence, in addition to above contact forces, we introduce an extra force scale in the friction law itself. This is called *Critical Load Model* (CLM) [25]. This force is a threshold normal force (F_{CL}) below which the particles interact as friction-less hard spheres and above which friction between the particles is activated. This is a simple model which can successfully reproduce the continuous and discontinuous shear thickening behavior observed in suspensions and has been extensively used in the literature [25], [56], [59]. This type of frictional behavior has also been observed experimentally [58],

$$|\mathbf{F}_{C,t}^{(\mathrm{i,j})}| \leq \begin{cases} \mu\left(|\mathbf{F}_{C,n}| - F_{CL}\right), & \text{if } |\mathbf{F}_{C,n}| \geq F_{CL} \\ 0, & \text{otherwise.} \end{cases} \tag{3.7}$$

Finally, to calculate the rheological properties, we need the bulk stress in the suspension. The bulk stress in a suspension of rigid particles in a flow with strain rate $\mathbf{E}^{\infty}$ is (after subtracting isotropic part of the fluid pressure):

$$\mathbf{\Sigma} = 2\mu\mathbf{E}^{\infty} + \mathbf{\Sigma}^{p}, \tag{3.8}$$

where $\mathbf{\Sigma}^{p}$ is the particle contribution to the bulk stress, and is given by the sum of hydrodynamic stress $\mathbf{\Sigma}^{H}$ and the contact stress $\mathbf{\Sigma}^{C}$ as:

$$\mathbf{\Sigma}^{p} = \mathbf{\Sigma}^{H} + \mathbf{\Sigma}^{C}, \tag{3.9}$$

where $\mathbf{\Sigma}^{H}$ and $\mathbf{\Sigma}^{C}$ can be calculated by taking ensemble average of the hydrodynamic ($\mathbf{S}_{H}$) and contact ($\mathbf{S}_{C}$) stresslets at each time step. We get,

$$\mathbf{\Sigma}^{H} = \frac{1}{V}\left(\sum_{\mathrm{i}} \mathbf{S}_{H}^{(\mathrm{i})}\right), \tag{3.10}$$

$$\mathbf{\Sigma}^{C} = \frac{1}{V}\left(\sum_{\mathrm{i}>\mathrm{j}} \mathbf{S}_{C}^{(\mathrm{i,j})}\right). \tag{3.11}$$

Therefore,

$$\mathbf{\Sigma} = 2\mu\mathbf{E}^{\infty} + \frac{1}{V}\left(\sum_{\mathrm{i}} \mathbf{S}_H^{(\mathrm{i})} + \sum_{\mathrm{i>j}} \mathbf{S}_C^{(\mathrm{i,j})}\right), \tag{3.12}$$

where V is the volume of the domain which is given by L^3 for a cubic domain with sides equal to L. Shear stress σ, normal stress differences N_1 and N_2, and relative viscosity η_r can then be defined as $\sigma = \Sigma_{12}$, $N_1 = \Sigma_{11} - \Sigma_{22}$, $N_2 = \Sigma_{22} - \Sigma_{33}$, and $\eta_r = \sigma/(\eta\dot{\gamma})$. The systematic splitting of the particle stress in contributions from hydrodynamic and contact stresses allows us to understand the relative contributions from lubrication and contact interactions to the rheological properties. The contribution from the hydrodynamic stress to the relative viscosity is $\eta_r^H = 1 + \Sigma_{12}^H/(\eta\dot{\gamma})$, the corresponding contribution from the contact stresses is $\eta_r^C = \Sigma_{12}^C/(\eta\dot{\gamma})$ and so on.

3.2.1 Simulation conditions

1. *Bidisperse suspension*: Cluster formation and/or crystallization present in the simulations of monodisperse suspensions can be avoided by introducing slight bidispersity in the particle sizes [25], [52], [56]. So, we consider bidisperse spheres with $a_2/a_1 = 1.4$ and the same volume fractions for smaller and larger spheres. The particles are neutrally buoyant. In addition, this choice of the radius ratio and volume fractions for the smaller and larger spheres was found to produce results very close to their monodisperse counterparts [52], [55], [149].

2. *Boundary conditions and domain size*: Lees-Edwards periodic boundary conditions [114] have been applied to all the sides. These boundary conditions enable us to simulate the sheared suspension for a fixed domain volume without loss of generality and produce accurate results for bulk rheological properties like viscosity and normal stress differences. For this study, we simulate shear flow of suspension in a cubic box with sides $15a_1$, where a_1 is the radius of the smaller particles [52]. We repeated the simulations for a bigger domain with sides $20a_1$. There is no significant change in the rheological properties, so we decided to run all the simulations for a domain with sides $15a_1$.

3. *Shear rate dependence*: We have another force scale besides the hydrodynamic one which is required to yield shear-rate dependence. In CLM the threshold value gives the force scale F_{CL}. Therefore, the shear rate dependence is given by the ratio, $\dot{\gamma}/\dot{\gamma}_0$, with $\dot{\gamma}_0 = F_{CL}/6\pi\eta a^2$.

4. *Range of parameters investigated*: The simulation parameters are listed in table 3.1. The aim of this study is to understand the effects of varying particle surface roughness on the rheology of suspension. Hence, we simulate the shear flow of rough particles for 7 different dimensionless roughnesses $\epsilon_r = 2h_r/(a_\mathrm{i} + a_\mathrm{j})$ viz., (0.005, 0.01, 0.03, 0.05, 0.075, 0.1, 0.125). The simulations were carried out for dimensionless shear rate values $\dot{\gamma}/\dot{\gamma}_0$ in the range [0.001 - 1.0] for a range of volume fractions in (0.45-0.56).

Table 3.1. Simulation parameters

ϕ	$\dot{\gamma}/\dot{\gamma}_0(s^{-1})$	μ	$\epsilon_r(\%)$
0.45 - 0.56	0.001 - 1.0	1	0.5 - 12.5

3.3 Results and discussion

This section presents the results of simulations for the range of parameters investigated. Since the focus of this study is to investigate the effects of varying particle roughness on the behavior of shear thickening suspensions, we kept μ a constant with value 1 for all the simulations except for the zero shear limit cases for which $\mu = 0$. Since zero shear limit and frictionless particles have the same rheology, we use both interchangeably throughout the text. The simulations for different parameters were carried out for a total of 50 strain units, i.e., $t_{final} = 50/\dot{\gamma}$. Time step was decided by using a hard-sphere algorithm [49] with upper bound of $1 \times 10^{-4}/\dot{\gamma}$. The first 10 strain units were discarded owing to the transient behavior of simulations in the initial time. All the rheological properties presented below are calculated by averaging after 10 strain units and only the average values are presented.

Rheological data are plotted versus shear rates and shear stresses which have been non-dimensionalized by the characteristic shear rate $\dot{\gamma}_0 = F_{CL}/6\pi\eta a^2$ and characteristic stress, $\sigma_0 = \eta\dot{\gamma}_0$, respectively, where η is the viscosity of the suspending fluid.

3.3.1 Rheology of smooth and rough suspensions

Fig. 3.3a and 3.3b, show the variation of relative viscosity with volume fraction for different roughness values. We present the results in the zero shear and infinite shear limits in order to demonstrate the effects of varying roughness in low and high shear rate (stress) limits. In the low shear rate limit ($\dot{\gamma} \to 0$) the interparticle contacts are mostly frictionless (i.e., $|\mathbf{F}_{C,n}| < F_{CL}$, Lubricated region [144]). So, the zero shear limit is the same as setting the interparticle friction equal to 0 (hence frictionless). On the other hand, the high shear rate limit ($\dot{\gamma} \to \infty$) shows the rheological behavior typical to a system close to jamming transition (i.e., $|\mathbf{F}_{C,n}| \geq F_{CL}$, frictional region [144]).

We find that for all the cases, relative viscosity diverges as the volume fraction (ϕ) approaches a particular value for each roughness. This value of volume fraction is termed as the jamming volume fraction (ϕ_m) above which the suspension is jammed and no flow is possible. We fit our data to a modified Maron-Pierce law [7], [141] $\eta_r = C(1 - \phi/\phi_m)^{-2}$, with parameters (C, ϕ_m) [25].

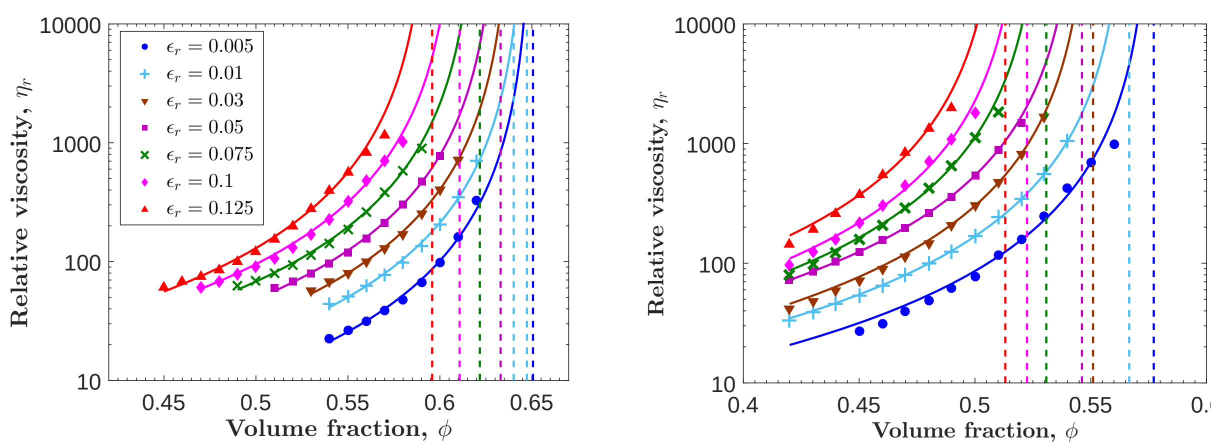

(a) (b)

Figure 3.3. Relative viscosity variation with roughness in a) zero shear limit which is equivalent to setting $\mu = 0$ or $\dot{\gamma} \to 0$, b) High shear limit ($\mu = 1$ and $\dot{\gamma} \to \infty$). Solid lines represent the modified Maron-Pierce law fit to the data. Dotted lines show the jamming fraction for each roughness. Jamming fraction reduces with roughness due to increase in viscosity and the effective radii of the particles with roughness. ϕ_m in the high shear limit is significantly lower than the one in the zero shear limit.

The effect of varying roughness is clear from both the figures. Increasing roughness increases the viscosity of suspension at a particular volume fraction owing to denser contact networks (See section 3.3.4). For the smoothest case, i.e., $\epsilon_r = 0.005$, we find $\phi_m \approx 0.66$. This is in agreement with the previous studies [25], [117] which find a similar value for the jamming fraction in the zero shear limit. For the frictional case, $\mu = 1$ (i.e., high shear limit), we find that the jamming fraction reduces significantly from that of the friction-less case. For the smoothest frictional suspensions, we find $\phi_m \approx 0.571$ which is close to the value obtained by Mari *et al.* [25] for $\mu = 1$. Again, increasing roughness reduces the jamming fraction and the reduction is even more for the frictional suspensions as compared to their friction-less counterparts. For the roughest case ϕ_m is as low as ≈ 52 %. The reduction in ϕ_m is expected and can be explained by the increase in the effective radii of the particles with roughness and the increased frequency of particle-particle contacts. As the roughness increases, the effective radii of the particles, given by, $a_\mathrm{e} = a(1+\epsilon_r)$, increase as well. So the effective volume fraction, given by, $\phi_\mathrm{e} = \phi(1+\epsilon_r)^3$, also increases with roughness, resulting in denser contact networks with higher contact stresses (See section 3.3.4). This eventually leads to the increase in the viscosity and the reduction in the jamming fraction.

These observation are consistent with the experimental study by Hsu *et al.* [8] and Hsiao *et al.* [9] and a numerical study by More & Ardekani [118]. These studies observed a decrease in jamming fraction with increasing roughness (See fig. 2-C in Hsu *et al.* [8], fig. 3 in Hsiao *et al.* [9] and fig. 10-b in More & Ardekani [118]). We observe a similar trend of decrease in ϕ_m with roughness.

3.3.2 Roughness enhances shear thickening

The suspension of frictional particles experiences two limiting rheology states depending on the shear rates. At small shear rates, the suspension is in a lubricated state where most of the contacts are frictionless and hence it has a lower viscosity. Large shear rates trigger the formation of frictional contacts and the suspension is in a high viscosity (stress) state. At the intermediate shear rates the suspension viscosity is in between these two extremes and as a result we observe shear thickening [25], [141]. For each ϕ, there is a critical $\dot{\gamma}$ above which the transition from the lubricated to frictional regime starts, this is often termed as the critical shear rate, $\dot{\gamma}_c$. This transition can be smooth and over a range of shear rates, in which case, it is called *continuous shear thickening* (CST) or it can be sudden like a step function at a particular shear rate, in which case it is called *discontinuous shear thickening* (DST). DST occurs only above a critical volume fraction ϕ_c [25], [94], [117], [144]. So, we can predict that there will be shear thickening as we increase the shear rate. In the subsequent subsections, we describe conditions under which CST and DST occur, present the values of $\dot{\gamma}_c$ and ϕ_c and discuss the role roughness plays in determining the suspension behavior.

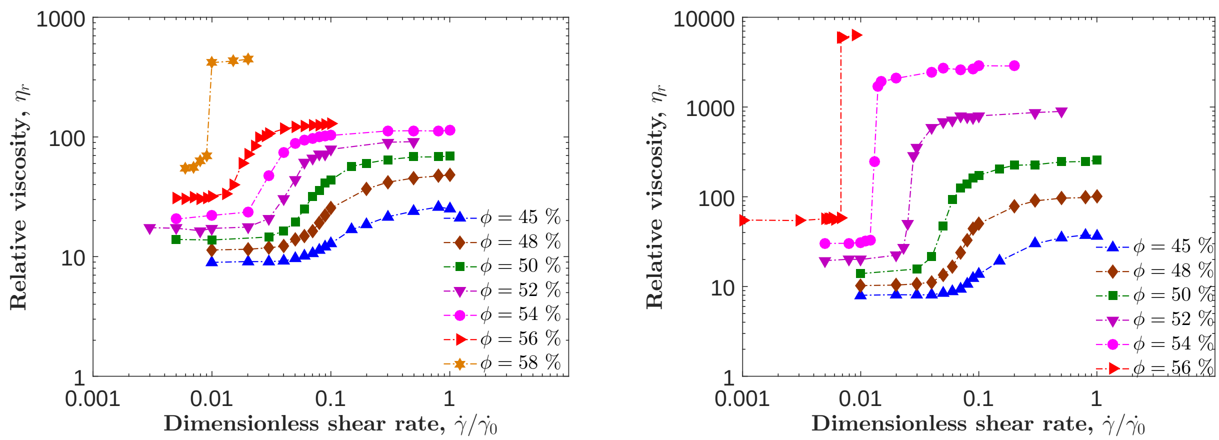

(a) **(b)**

Figure 3.4. Relative viscosity dependence on shear rate for a) smooth suspensions ($\epsilon_r = 0.01$) and b) rough suspensions ($\epsilon_r = 0.05$). Increasing roughness increases the strength of shear thickening (given by the slope of η_r vs $\dot{\gamma}/\dot{\gamma}_0$ curve in the transition region). Roughness also reduces $\dot{\gamma}_c$ and ϕ_c.

Fig. 3.4a and 3.4b show the variation of relative viscosity with dimensionless shear rate for two different roughness values 1 % and 5 % of the particle radii. For the lower roughness, we observe only CST for the investigated ϕ range with the magnitude of CST increasing with ϕ. As we increase the roughness of the particles to 5 %, we observe DST for $\phi > 52\%$. Thus, increasing the roughness reduces $\dot{\gamma}_c$ and ϕ_c. This has been also observed in experiments [8], [9]. For a very high roughness value, i.e., 12.5 %, we see DST for a volume fraction as low as 49 % (The corresponding plots can be found in Sec. 3.3.6). Thus, roughness enhances ST by increasing the relative viscosity and reducing the jamming fraction.

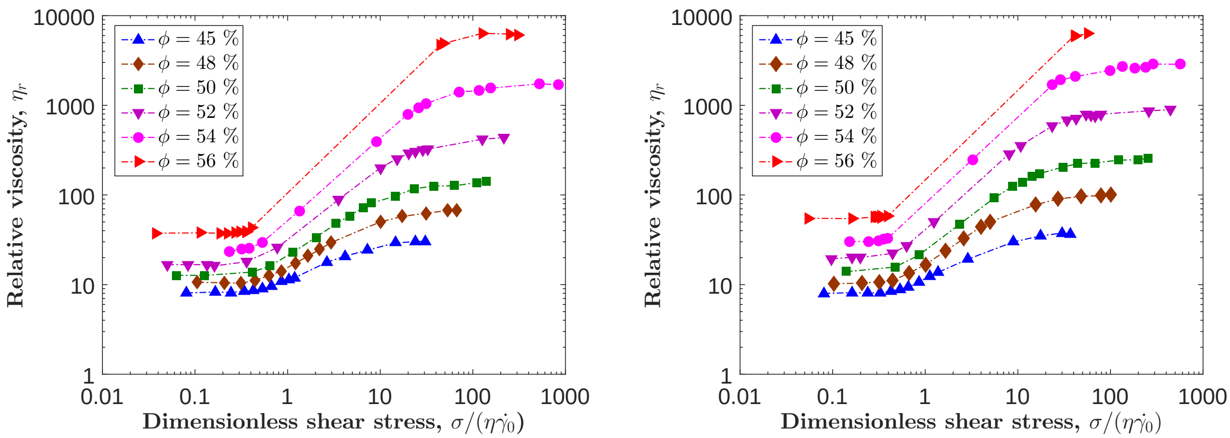

(a) (b)

Figure 3.5. Relative viscosity dependence on dimensionless shear stress for a) smooth suspensions ($\epsilon_r = 0.01$) and b) rough suspensions ($\epsilon_r = 0.05$). The transition stress, σ_{ST} is a constant and is independent of roughness and volume fraction. Stress follows the same behavior in the shear thickened regime.

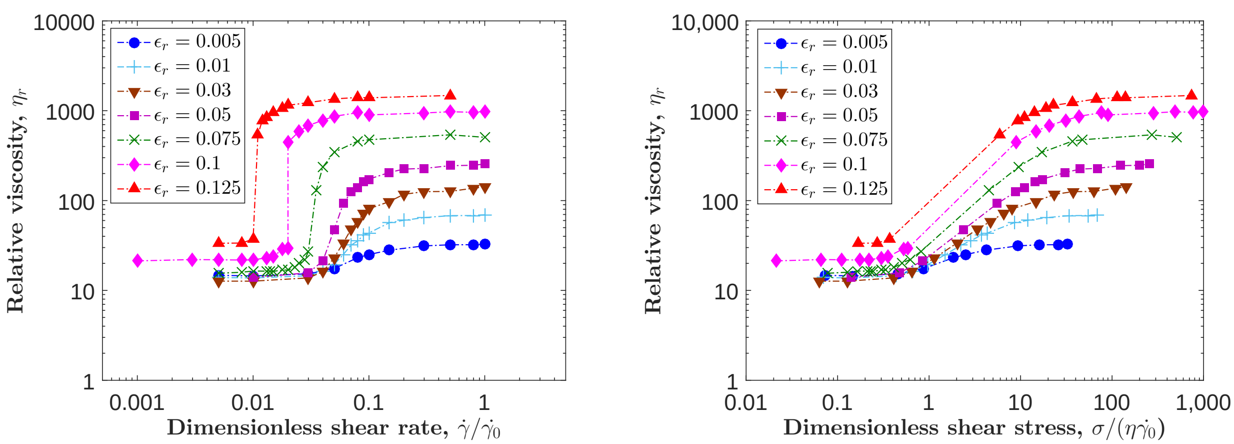

(a) (b)

Figure 3.6. Relative viscosity variation with roughness for $\phi = 50\%$ for a) different $\dot{\gamma}$ and b) different σ. The transition stress, σ_{ST} is a constant and is independent of roughness and volume fraction. Stress follows the same behavior in the shear thickened regime.

Fig. 3.5a and 3.5b show the variation of viscosity with dimensionless stress for $\epsilon_r = 0.01$ and $\epsilon_r = 0.05$, respectively. These figures show that the transition to shear thickening from the lubricated state occurs at a constant dimensionless stress, $\sigma^L_{ST}/(\eta\dot{\gamma_0}) \approx 0.3$ which is independent of volume fraction and roughness. Same is true for the transition to the other extreme, where viscosity attains a shear rate independent high value plateau, $\sigma^H_{ST}/(\eta\dot{\gamma}_0) \approx 20$. These findings are in agreement with previous study by Mari *et al.* [25] and has also been observed in experiments for smooth spheres [119], [120], [137], [150]–[155]. If we balance the applied stress with the stress scale for ST transition, we get, $\sigma \approx F_{CL}/A$, where A is the area over which a unit critical load for ST is applied. At the high viscosity transition, almost all the particles are in frictional contacts, that means, $\sigma = \sigma^H_{ST}$ and $A = A^H_{ST} \approx a^2$, leading to $\sigma^H_{ST} \approx 6\pi$. On the other hand, at the low viscosity regime (onset of ST), the contact chains (with frictional contacts) are sparsely observed, meaning $A = A^L_{ST}$ must be higher than A^H_{ST}. Balancing σ^L_{ST} with F_{CL}/A^L_{ST} we find $A^L_{ST} \approx (7a)^2$ [25].

Fig. 3.6a and 3.6b show the variation of relative viscosity for $\phi = 50\%$ for different roughness values. From these plots we can see the effect of increasing roughness on η_r and ST. ST is continuous at low roughness values, which correspond to smooth particles. This effect can be quantified by defining the ST index, β, which can be obtained by fitting a power law to η_r vs σ in the transition region where the rheology is transitioning from low viscosity values to high viscosity values, i.e., $\eta_r \propto (\sigma)^{(\beta)}$. Higher the value of β stronger is the ST effect. For $\phi = 50\%$, β increases from 0.27 to 0.98 for $\epsilon_r = 0.005$ and $\epsilon_r = 0.075$, which indicates that increasing roughness enhances ST. For a very high roughness values, i.e., $\epsilon_r \geq 10\%$, the suspension undergoes DST, suggesting that ϕ_c for such high roughness values is $< 50\%$. Fig. 3.6b again confirms that the onset of ST and the transition to shear thickened high viscosity regime is roughness independent and is determined by the stress in the system, but the magnitude of viscosity increases with roughness. Another interesting insight can be obtained if we compare Fig. 3.4b and 3.5b with Fig. 3.6a and 3.6b, respectively. The comparison shows that increasing roughness has a similar effect as increasing the volume fraction on ST behavior. This can be understood if we look at the effective radius ($a_\mathrm{e}(a, \epsilon_r) = a(1 + \epsilon_r)$) and the effective volume fraction ($\phi_\mathrm{e}(\phi, \epsilon_r) = \phi(1 + \epsilon_r)^3$) for a given roughness. Thus, $\phi_\mathrm{e}(45, 0.05) \approx \phi_\mathrm{e}(50, 0.01) \approx 52\%$ and $\phi_\mathrm{e}(56, 0.05) \approx \phi_\mathrm{e}(50, 0.1) \approx 65\%$ have similar rheological behavior, CST and DST respectively for the two cases. We also observe that we can predict onset of DST for a given roughness from its effective volume fraction. For any roughness and volume fraction, if $\phi_\mathrm{e}(\phi, \epsilon_r) > 63\%$ then we expect the suspension to undergo DST. In addition, if $59\% \leq \phi_\mathrm{e} \leq 63\%$, we get strong CST and for $\phi_\mathrm{e} < 59\%$ we get CST. These values might change if we use a different coefficient of friction. Effective volume fraction can help us to predict the qualitative rheological behavior of the rough dense suspensions, but it should be borne in mind that it cannot predict the early onset and the strength of the ST effect which are solely governed by the asperity size and the volume fraction. E.g., i) the critical shear rate for the onset of ST, $\dot{\gamma}_c/\dot{\gamma}_0$, for a 50 % suspension with roughness 10 % is ≈ 0.02, while for 56 % suspension with 5 % roughness its value is ≈ 0.008 even though they have the same ϕ_e, ii) These two suspensions also have a different viscosities and viscosity jump as they transition from the lubricated to the shear thickened regime is also roughness size and volume fraction dependent. Even for N_1 (3.3.3), the effective volume fraction can only predict the sign transition of N_1, but the relative change in the magnitude of N_1 depends on the roughness size. These results show that increase in the effective is just one of the effects of increasing roughness and not the only effects as roughness modifies the interparticle contacts as well as we show in Section 3.3.4

3.3.3 Normal stress differences

Fig. 3.7 and Fig. 3.8 show the variation of the first normal stress difference, N_1 and the second normal stress difference, N_2 for 50 % volume fraction suspensions for different roughness values. We obtain negative values of N_2 for all the cases with magnitude much larger than that of N_1. These findings are consistent with previous studies [20], [24], [25], [51], [52], [156].

Fig. 3.7a shows the variation of normalized N_1 with dimensionless shear rate. We would like to mention that there have been contradictory reports on the magnitude and sign of N_1 in the literature [157]–[159] with accurate measurements becoming possible with advanced normal stress transducers and controlled stress rheometry only recently [156]. Prior to the onset of ST, N_1 is close to 0 with a negative sign. During the ST transition, N_1 behaves in two different ways depending on the roughness value. For lower roughness, N_1 decreases across ST (i.e., becomes more negative), while at higher roughness N_1 increases across ST. In both the cases (smooth and rough), we observe that the magnitude of N_1 increases across ST with relative increase becoming larger for higher roughness. This result is consistent with the study by Mari *et al* [25]. who observed two different behaviors for N_1 at low and

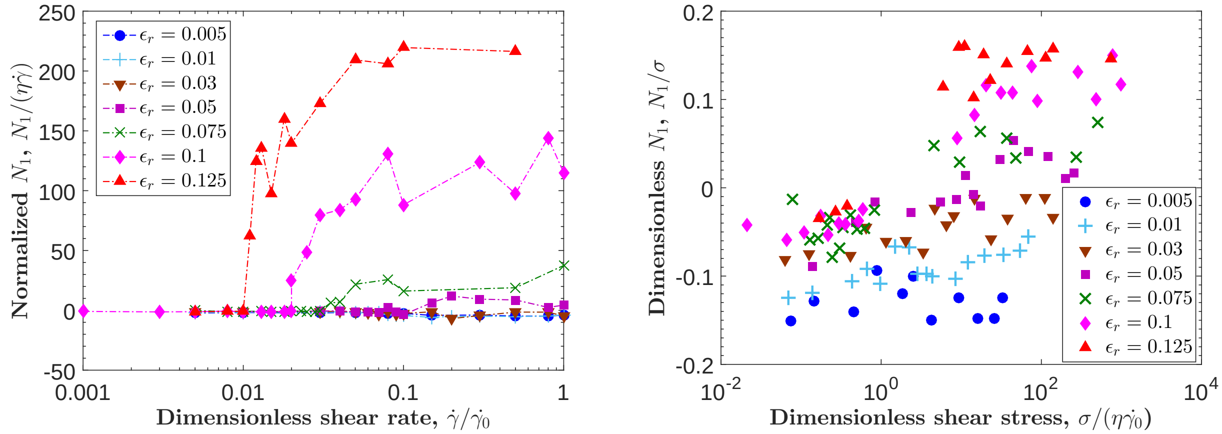

(a) **(b)**

Figure 3.7. First normal stress for 50 % suspension for different roughness values a) variation of normalized N_1 with dimensionless shear rate and b) variation of dimensionless N_1 with dimensionless stress. N_1 increases with roughness and becomes positive for higher roughness values.

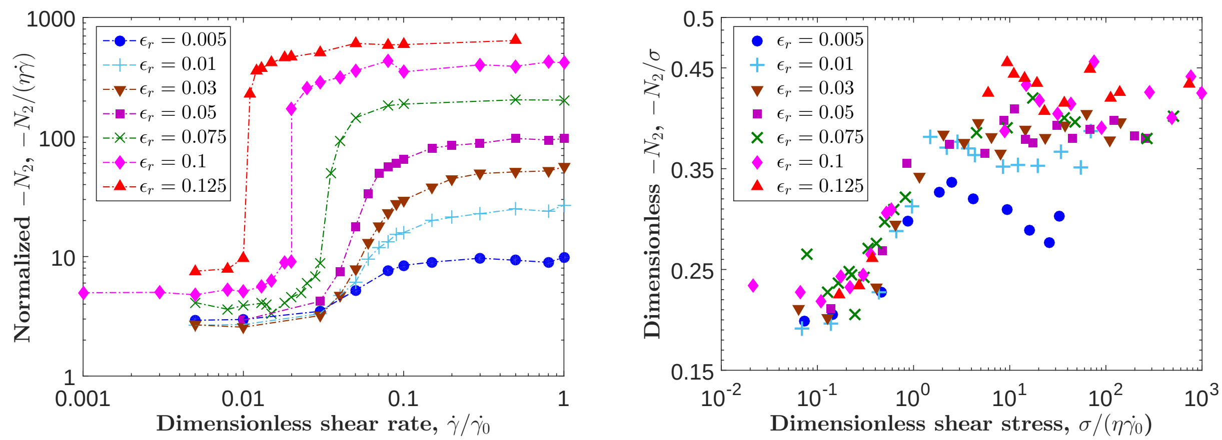

(a) **(b)**

Figure 3.8. Second normal stress for 50 % suspension for different roughness values a) variation of normalized N_2 with dimensionless shear rate and b) variation of dimensionless N_2 with dimensionless stress. Behavior of N_2 is reminiscent of stress in the system.

high volume fractions. The behavior at low volume fraction is similar to the behavior we obtain for low roughness values and the behavior for high volume fractions is same as what we obtain for high roughness values. This is expected and can be explained by the increase in the effective volume fraction with increase in the roughness.

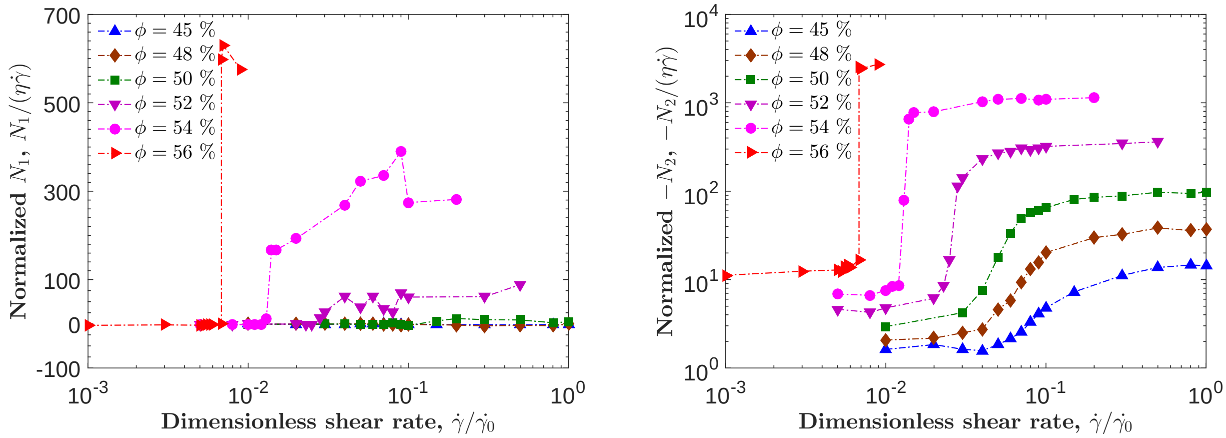

(a) **(b)**

Figure 3.9. Normal stress differences for suspensions with $\epsilon_r = 0.05$ for different volume fractions a) variation of normalized N_1 with dimensionless shear rate and b) variation of normalized $-N_2$ with dimensionless shear rate. Behavior of N_2 is reminiscent of stress in the system.

Fig. 3.7b shows that dimensionless N_1 increases with increase in roughness. We obtain negative values for N_1 before the onset of ST for all the cases, which is consistent with the behavior obtained for N_1 in many previous studies [8], [9], [25], [42], [119], [154]. However, for high roughness values we find that N_1 becomes positive after ST has taken place with the magnitude of N_1/σ not exceeding 0.2. Similarly, for a constant roughness we obtain negative N_1 at low volume fractions and a positive N_1 at very high volume fractions (see Fig. 3.9). These results are in agreement with experiments [8], [9], [22], [94], [107], [119], [154], [160] and computations [9], [25], [56], [117].

For N_2, we obtain behavior and trends consistent with most experimental data available, i.e., N_2 has a negative value and a magnitude much larger than N_1. N_2 varies linearly with stress which is clear if we compare Fig. 3.8a and 3.6a. Another interesting behavior of N_2 is that, the dimensionless N_2, i.e., N_2/σ falls on a single curve for all the volume fractions at a given roughness, again corroborating the fact that the behavior of N_2 is reminiscent of that of stress [25]. Fig. 3.8b shows that ST leads to almost doubling the value of dimensionless N_2.

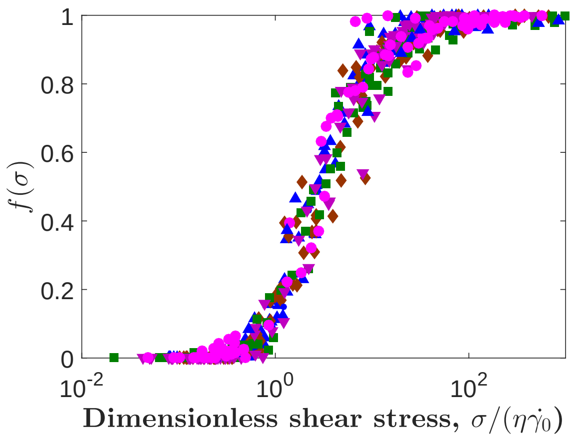

Figure 3.10. Average fraction of particle pairs in frictional vs stress for different volume fractions for all roughness values. $\triangle$ = 45%, $\Diamond$ = 48%, $\Box$ = 50%, $\bigtriangledown$ = 52%, O= 54%.

3.3.4 Contact networks and the role of asperity deformation

It has been shown by Mari *et al.* [25] that the ST transition with shear rate (stress) is mainly due to increasing number of frictional particle-particle contacts with shear rate (stress). Since we have a stress scale (F_{CL}/a^2) in the simulations above which friction activates, frictional contacts appear more frequently as we increase the imposed stress. The consequence of this is that, at low shear rates (stress), frictional contacts are seldom and most of the contacts are lubricated which results in a low viscosity of the suspension. As we increase shear rate (stress), the contacts yield and more contacts enter in the frictional regime increasing the viscosity and resulting in ST. The natural question to ask is, how does roughness affects these contacts? The answer to this question becomes clear if we think particles with roughness as a bigger particle with the radius equal to the effective radius, a_{e}. So, as we increase roughness of the particles, the probability of two particles coming into contact increases at a fixed stress. Hence, the number of particle pairs in frictional contact naturally increases with increasing roughness which increases the viscosity. As a result, ST effect improves.

This becomes clear if we plot the fraction of particle-particle pairs in frictional contact with varying stress. Let $f(\sigma)$ be the average ratio of number of particle pairs in frictional

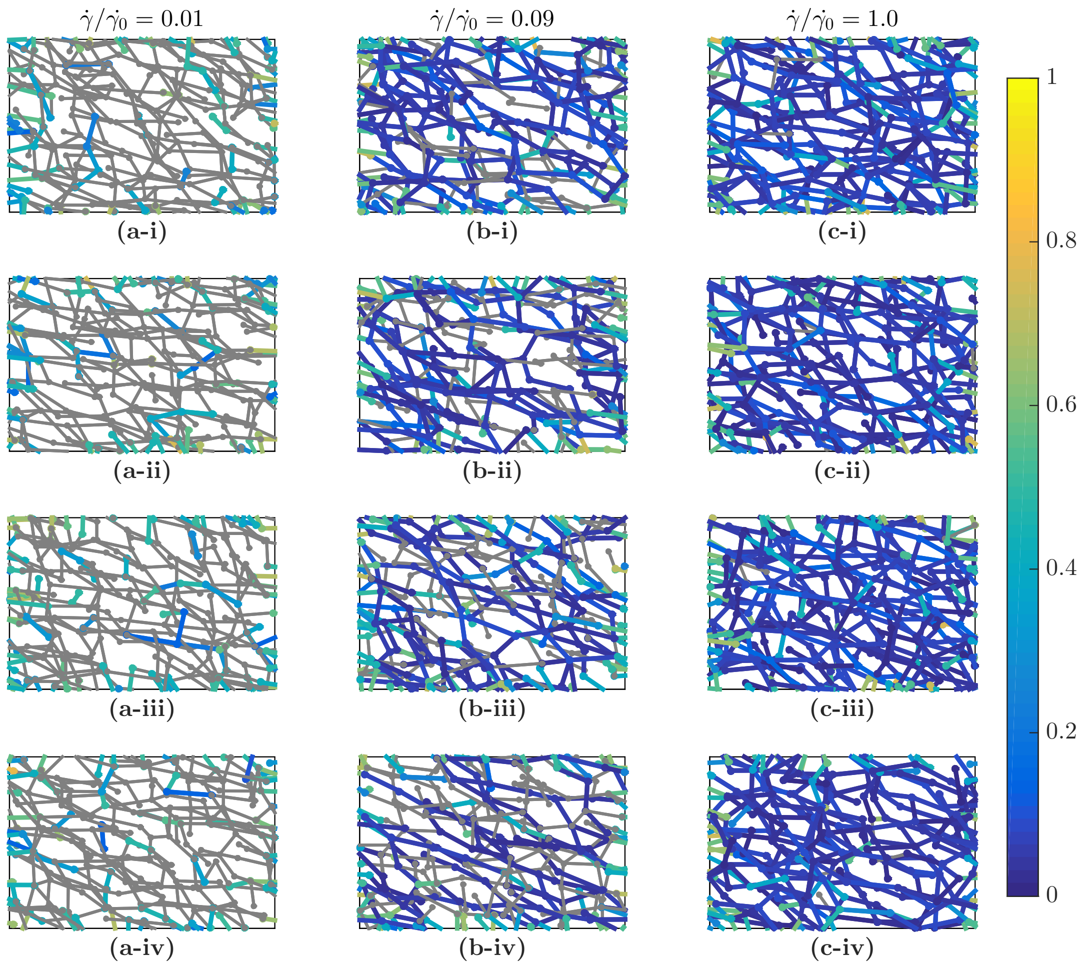

Figure 3.11. Snapshots of contact networks at 4 different times during the simulations of a 50 % volume fraction suspension with particle roughness 1 %. We observe CST for these simulation parameters. a) $\dot{\gamma}/\dot{\gamma}_0 = 0.01$ (before ST), b) $\dot{\gamma}/\dot{\gamma}_0 = 0.09$ (during CST), c) $\dot{\gamma}/\dot{\gamma}_0 = 1.0$ (After ST). i, ii, iii, iv correspond to different times, $20/\dot{\gamma}$, $30/\dot{\gamma}$, $40/\dot{\gamma}$, $50/\dot{\gamma}$, respectively. Colorbar shows the magnitude of dimensionless normal force between the contacting particle pairs. Force has been scaled by the maximum normal force corresponding to flattening of the asperities, $\mathbf{F}_{C,n}^{max} = k_n h_r^{3/2}$. Grey color denotes friction-less contacts.

contacts to the number of particle pairs in contact. Fig. 3.10 shows the fraction of frictional contacts for different volume fractions and roughness values for varying stress. The data falls on a single curve for all the roughness and volume fractions [25], [94], [144]. Thus the fraction of particle contacts is governed by the stress in the system. But since increasing roughness

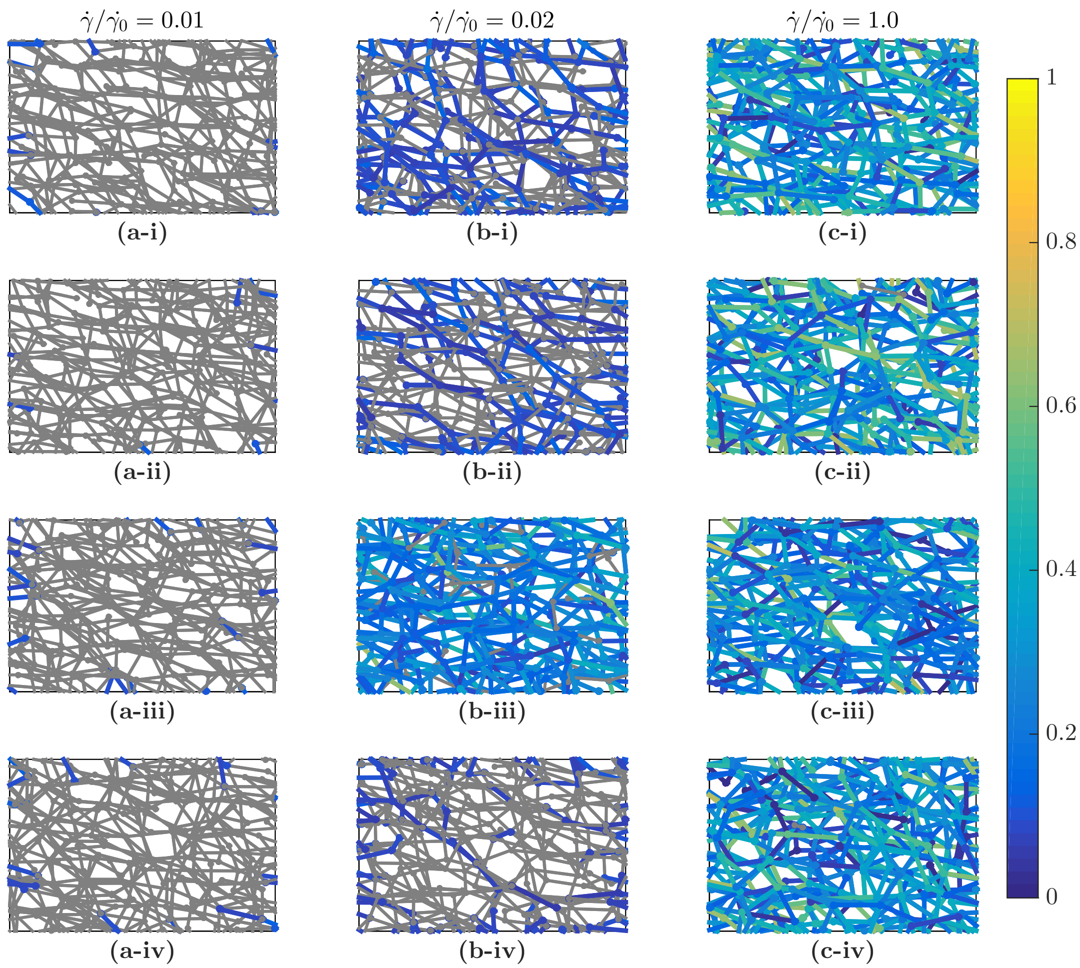

Figure 3.12. Snapshots of contact networks at 4 different times during the simulations of a 50 % volume fraction suspension with particle roughness 10 %. We observe DST for these simulation parameters. a) $\dot{\gamma}/\dot{\gamma}_0 = 0.01$ (before ST), b) $\dot{\gamma}/\dot{\gamma}_0 = 0.02$ (during DST), c) $\dot{\gamma}/\dot{\gamma}_0 = 1.0$ (After ST). i, ii, iii, iv correspond to different times, $20/\dot{\gamma}$, $30/\dot{\gamma}$, $40/\dot{\gamma}$, $50/\dot{\gamma}$, respectively. Colorbar shows the magnitude of dimensionless normal force between the contacting particle pairs. Force has been scaled by the maximum normal force corresponding to flattening of the asperities, $\mathbf{F}_{C,n}^{max} = k_n h_r^{3/2}$. Grey color denotes friction-less contacts.

increases the number of particle contacts, number of frictional contacts and contact forces at a fixed stress thus are higher for rougher suspensions. A look at the evolution of contact networks makes this point clear.

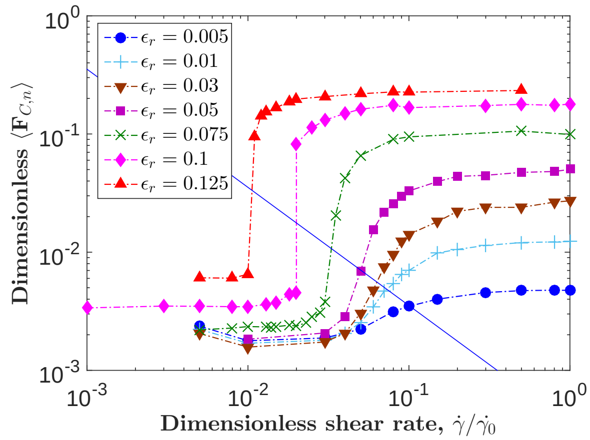

Figure 3.13. Average dimensionless normal force magnitude for $\phi = 50\%$ for different roughness values. The solid line indicates dimensionless F_{CL}, the force scale corresponding to the transition from friction-less to frictional contact. Asperity deformation increases with increasing roughness resulting in higher contact stresses for rough suspensions. Forces have been scaled by the maximum normal force corresponding to flattening of the asperities, $\mathbf{F}_{C,n}^{max} = k_n h_r^{3/2}$.

Fig. 3.11 and 3.12 elucidate the governing role played by frictional contact networks in the suspension behavior. For a low roughness value (Fig. 3.11), the contacts are friction-less and mostly in the lubricated regime at a shear rate before the onset of ST. At this low viscosity end, force chains appear intermittently in the direction of compression axis. On the other hand, at the high shear rate, frictional contacts is a norm with almost all the contacts being in the frictional regime. Between these two extremes, the contact network transitions from low viscosity to high viscosity state with the fraction of frictional contacts gradually increasing. However, for a high viscosity value (Fig. 3.12), most of the contacts are friction-less at a shear rate below $\dot{\gamma}_c$ and the contact network transitions abruptly to a state where all of the contacts are frictional. But, for $\dot{\gamma}$ around $\dot{\gamma}_c$ where we get DST, the suspension switches between a low stress and a high stress state erratically during the time evolution (depicted by the contact networks show in Fig. 3.12 (b-ii and b-iii) which is termed as hysteresis [25] and looks like activated events [119], [120], [161]–[165].

For smooth suspensions, as discussed before, the probability of two particles coming into contact is lower than the case of rough suspensions owing to the lower effective radius. This fact also gets reflected in Fig. 3.11 and 3.12 if we look at the density of the particle-particle contacts. For lower roughness, the contacts are sparse (area covered by the white space is more) and the lubrication film is intact for many particles which are close to each other but not contacting. For a larger roughness, the lubrication film breaks for most of the particles which are close to each other leading to a dense network (area covered by the white space has decreased) of contacts. Thus, roughness simply increases the number of particle pairs coming into contact which eventually results in the rise in the viscosity.

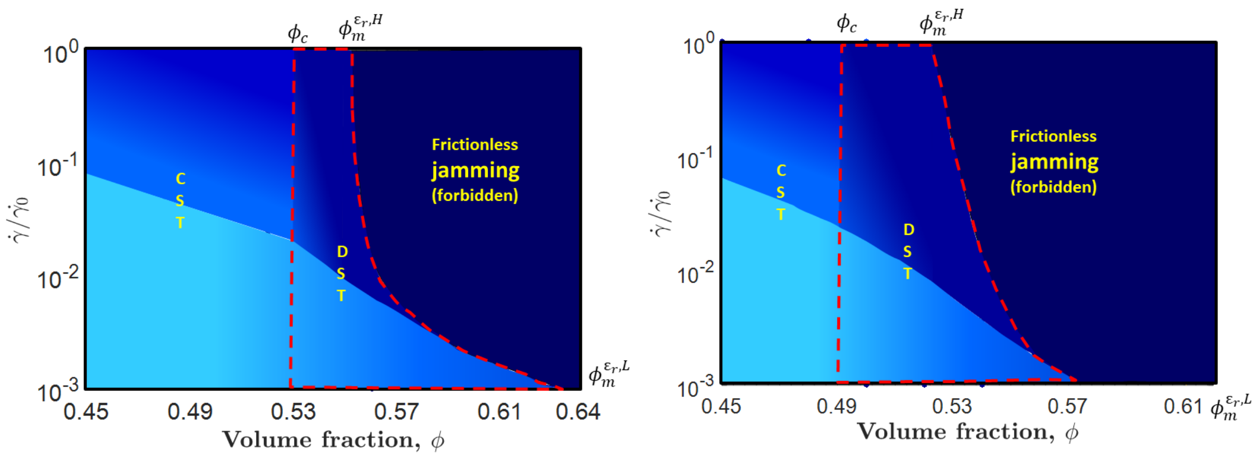

(a) (b)

Figure 3.14. Phase diagram for viscosity in the shear rate vs volume fraction plane for a) low roughness suspensions ($\epsilon_r = 0.05$) and b) high roughness suspensions ($\epsilon_r = 0.1$). $\phi_m^{\epsilon_r,L}$ = jamming fraction for friction-less case and $\phi_m^{\epsilon_r,H}$ = jamming fraction for frictional case as $\dot{\gamma} \to \infty$. The viscosity is color coded: darker the shade higher is the viscosity value. Sharp transitions in colors indicate critical parameter values. Please note that in the DST region, the suspension might switch between the low and high viscosity state during the time evolution of the simulations for a small range of $\dot{\gamma}$ around $\dot{\gamma}_c$ [25], and this region is not shown in the phase diagram.

The colorbar on Fig. 3.11 and 3.12 shows the magnitude of the dimensionless normal contact force for two different roughness values corresponding to smooth and rough case, respectively. By comparing both the figures we can conclude that the magnitude of contact forces increases with increase in roughness which results in larger contact stresses. In addition, we can calculate the value for critical overlap, δ_c corresponding to the transition from frictionless to frictional contact. This can be done by balancing the force scale F_{CL} with the normal contact force for $\delta = \delta_c$. We get, $\delta_c = 0.005(1/\dot{\gamma})^{2/3}$, which depends on the shear rate. So, if $\delta > \delta_c$, then friction is activated (This is equivalent to saying $|\mathbf{F}_{C,n}| > F_{CL}$). But once the deformation larger than δ_c, increase in the deformation directly leads to increase in the contact stress which increases the suspension viscosity. We observe that, for the contact model implemented, asperities with bigger sizes tend to deform more, leading to rise in the suspension stress and hence, result in the increase in viscosity (see Fig. 3.13).

3.3.5 Phase diagram

The results of this study show that as we change the volume fractions and the shear rates, the materials undergo a range of rheological states depending on the roughness value. This can be demonstrated with the help of a phase diagram which clearly demarcates the various states and transitions the suspensions undergo. ST is closely related to the jamming transition as it is clear from the variation of ϕ_m with roughness, which directly influences the ST behavior for rough suspensions.

Fig. 3.14a and 3.14b show $\dot{\gamma} - \phi$ phase diagram for viscosity. At low shear rates and low volume fractions, the suspension is in low viscosity state with contacts mostly in the lubricated state. This rheology diverges at the friction-less jamming fraction, $\phi_m^{\epsilon_r,L}$. The friction-less jamming point reduces as we increase roughness, thus, increasing the viscosity for the same volume fraction as compared to the smooth case and reducing the values of critical parameters.

The rheology in the upper part of the phase diagram is frictional and is in a high viscosity state. This is due to the fact that with increase in the shear rate, the stress in the system increases and activates the frictional contacts. This introduces a limit on the volume fraction beyond which the suspensions jams and no flow is possible. This volume fraction is the frictional jamming point, $\phi_m^{\epsilon_r,H}$. $\phi_m^{\epsilon_r,H}$ also decreases with roughness which results in the increases viscosity in the ST state with increasing roughness.

Friction-less and frictional regimes co-exist in the phase diagram with intermediate rheological properties in between the two diverging states. As a results we observe CST if $\phi < \phi_c$ and DST if $\phi_c < \phi < \phi_m$. Again, we observe that ϕ_c decreases with roughness. This is a

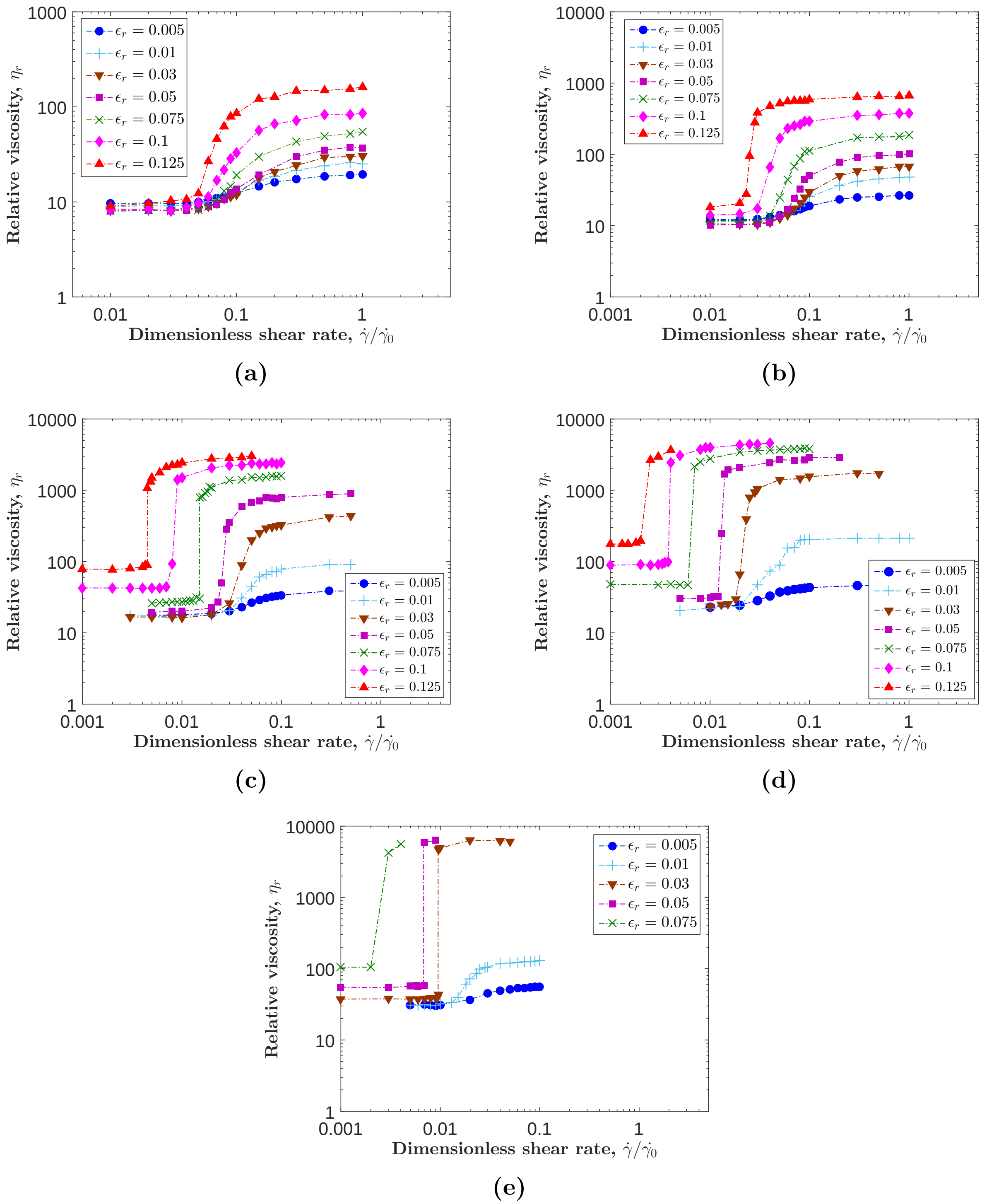

Figure 3.15. Relative viscosity vs dimensionless shear rate for different asperity sizes for a) $\phi = 45\%$, b) $\phi = 48\%$, c) $\phi = 52\%$, d) $\phi = 54\%$, e) $\phi = 56\%$.

direct consequence of the fact that both friction-less and frictional diverging volume fractions reduce with roughness. We observe that for a volume fraction $\phi_m^{\epsilon_r,H} < \phi < \phi_m^{\epsilon_r,L}$, the flowable regions shrinks rapidly as we increase the volume fraction and the suspension jams even without undergoing DST as ϕ gets closer to $\phi_m^{\epsilon_r,L}$.

3.3.6 Simulation data for different ϕ and ϵ_r

This section presents the relative viscosity vs shear rate plots (Fig. 3.15) for different volume fraction values and all the roughness sizes considered in the paper. These plots clearly show that, 1) strength of the ST effect increases as we increase roughness size for a given volume fraction, and 2) increasing roughness size leads to early onset of ST both in terms of the critical shear rate ($\dot{\gamma}_c$) and the critical volume fraction for DST (ϕ_c).

4. A CONSTITUTIVE MODEL FOR SHEARED DENSE SUSPENSIONS OF ROUGH PARTICLES

4.1 Introduction

Shear thickening (ST) in non-Brownian suspensions has been known for a long time [35], [121], [125]–[128], [162]. Owing to the advent of simulation techniques, ST in particulate suspensions has been a focus of investigation of many scientific efforts in the last few decades. As a result, a range of explanations can be found in the literature for the ST phenomenon in dense suspensions. These include formation of hollow enclosures of particles due to sudden onset of turbulent flow between them [129], order disorder transitions [34], [130]–[132], particle clustering induced by fluid flow [45], [133]–[136]. These explanations provide us with insights in the physics of ST in suspension, but they come with their own shortcomings, e.g., under-prediction of the viscosity jump magnitude [9], [25], [119], [137].

Many studies have shown that in dense suspensions, the inter-particle contacts between the neighbouring particles have a governing role in determining the stress in the sheared suspensions [25], [51], [62], [84], [85], [94]. This is because contacts not only give rise to normal forces between the particles, which are essentially a type of repulsive force, but they also lead to friction and resistance to rolling motion. As a result, friction between the particles triggers anisotropic force chain networks [161] and granular-type behavior [122], [138]–[140] consequently giving rise to ST. This hypothesis has been corroborated by theory [141], simulations [25], [56], [84] and experiments [9], [58], [122], [142], [143], [160]. It is well known that, ST can occur in two ways. When the viscosity increases gradually with increasing shear rate (or stress) it is called *Continuous Shear Thickening* (CST). On the other hand, when the viscosity increases abruptly at the critical shear rate it is termed as *Discontinuous Shear Thickening* (DST). Even though, the understanding of ST due to friction has advanced many folds in the past few years [25], [59], [86], [94], [117], [144], [145], the effect of particle asperities on ST has not been explored much and it is only recently that researchers have started to investigate it [4], [166], [167]. Roughness plays a crucial role in suspension of dense particles as even the smooth particles have nominal surface roughness $\approx O(10^{-3} - 10^{-2})$ times their sizes [53].

In dense suspensions, increasing the particle roughness size leads to an increase in the suspension viscosity and an reduction in the jamming fraction (ϕ_m), the volume fraction beyond which the suspension stops flowing [3], [7]. This results in an enhanced ST behavior for dense suspensions of rough particles compared to smooth particles [4], [8]. The effect of roughness is to increase the apparent radii of particles and an increase in the density of the frictional contact networks leading to reduction in the critical shear rate ($\dot{\gamma}_c$) for ST and the critical volume fraction (ϕ_c) for the DST transition [4]. Using the *Critical Load Model* (CLM) and a hemispherical mono-asperity model, it has been shown that we get stress/rate value independent but roughness size dependent rheology in the low and high shear stress/rate limits, respectively [4]. The transition from the lubrication dominated (low stress) to friction dominated (high stress) contact networks as we increase the shear stress induces ST behavior in dense suspensions [25], [144]. The rheological properties in between these two extremes can be interpolated by using a unique microscopic parameter which gives the fraction of frictional contacts at a given shear stress in the suspension [50], [117], [168] (henceforth mentioned as WC model as it was proposed by Wyart-Cates [50]). An extension of this model was recently used to come up with a constitutive model which captures the effect of friction on the rheology of dense ST suspensions [117].

Depending on the volume fraction (ϕ) and the viscosity jump magnitude, we can observe three forms of stress curves as a function of shear rate in WC model [50], [117]. For conditions under which suspensions undergo CST ($\phi < \phi_c$), the shear stress in the suspension increases monotonically with the applied shear rate. For the conditions under which DST is observed ($\phi_c < \phi < \phi_m$) and suspensions have a large enough but finite viscosity contrast, shear stress vs shear rate curve has a non-monotonic behavior which has an S-shape. Finally, at very large volume fractions which are higher than the jamming fraction ($\phi > \phi_m$), we get a backward bending curve in the shear stress vs shear rate plot which means the suspension can only flow at a small shear stress. Non-monotonic flow curves can only be observed in shear stress controlled experiments [143], [169]–[171] and simulations [117]. Increasing roughness size essentially lowers the values of ϕ_c and ϕ_m which result in the transitions between various flow state curves to take place at lower volume fractions than their smooth suspension counterparts.

The aim of this work is to quantify the effect of systematically increasing particle roughness size on the rheology and the flow curves of ST rigid particle suspensions by providing a constitutive equation capturing these effects. We extend the ideas of WC model and propose a constitutive model which expresses the suspension rheology in terms of the applied shear stress and the roughness size. To this end, we briefly discuss the governing equations, the simulation algorithm and the simulation conditions in Sec. 4.2. Then we elaborate on the constitutive model equations in Sec. 4.3. Finally, in Sec. 4.4 we present results obtained by applying this model to our simulation data which demonstrates the model's efficacy in predicting the suspension rheology given data only in the low and high shear limits and the function quantifying the fraction of frictional contacts at a given shear stress.

4.2 Methodology

This section describes the models and algorithms used to simulate shear flow of rough non-Brownian suspensions. We have used the same governing equations and numerical framework to simulate the hydrodynamic interactions as explained in chapter 1–Sec. 1.4. The only difference being we perform stress controlled simulations in this paper as opposed to the shear rate controlled simulations in the previous chapters. We, therefore, elaborate only on the contact and friction models used below.

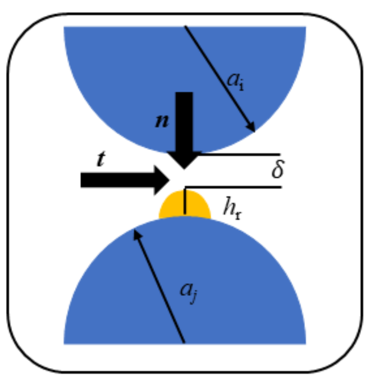

Figure 4.1. Schematic of the asperity geometry: Asperity is modelled as a hemisphere on the particle surface (denoted by yellow). δ is the hydrodynamic separation distance, h_r is the asperity size. The arrows show the contact forces and torques acting on ith particle due to contact between ith and jth particles.

4.2.1 Contact forces

We model the contact forces between the particles as it is done in the Discrete Element Method (DEM), a popular method in granular physics [146], [147]. We assume that the contact between the particles takes place via the hemispherical asperity. The asperity deformation after the contact can be defined as $\delta = (d^{(\mathrm{i,j})} - a_{\mathrm{i}} - a_{\mathrm{j}} - h_r)$, and we say the contact occurs when $\delta \leq 0$. Here the touching spherical particles have radii a_{i} and a_{j} with surface roughness $h_r = \epsilon_r(a_{\mathrm{i}} + a_{\mathrm{j}})/2$ (ϵ_r is the dimensionless roughness) coming into contact as shown in Fig. 4.1. We do not include viscous damping in order to be consistent with previous studies [3], [4], [24], [52], [62].

We split the contact force ($\mathbf{F}_C^{(\mathrm{i,j})}$) into two components [24], [25], i) $\mathbf{F}_{C,n}^{(\mathrm{i,j})}$, the normal contact force, and ii) $\mathbf{F}_{C,t}^{(\mathrm{i,j})}$ which is the tangential contact force (Fig. 4.1).

$$\mathbf{F}_C^{(\mathrm{i,j})} = \mathbf{F}_{C,n}^{(\mathrm{i,j})} + \mathbf{F}_{C,t}^{(\mathrm{i,j})}. \tag{4.1}$$

The normal contact force is modelled using Hertz law,

$$\mathbf{F}_{C,n}^{(\mathrm{i,j})} = -k_n \left(|\delta|\right)^{3/2} \mathbf{n}^{(\mathrm{i,j})}, \tag{4.2}$$

here the compression of the asperity has been readily accounted for through the asperity deformation δ.

The normal stiffness k_n can be evaluated in terms of particle mechanical properties like Young's modulus, Poisson's ratio and Elastic modulus. But, for real materials this value comes out to be very large which forces the time-step to be very small in order to have numerical stability. Hence, for numerical tractability, the normal stiffness k_n is chosen sufficiently high so as to mimic rigid particles and changing k_n does not have a significant impact on the bulk rheology [4], [24], [25], [62], [144]. Here, we take the dimensionless normal stiffness $k_n/(\sigma a^2 {h_r}^{-3/2}) = 2 \times 10^4$ where σ is the imposed shear stress [4]. The dependence of the contact stiffness values on the hydrodynamic stress and roughness size is an important feature and assumption of many contact force models for non-Brownian suspensions [4], [24], [25], [56], [62]. As there is no inherent time-scale in non-Brownian suspensions, it is the competition between the various forces/stresses that determines the bulk stress in the suspensions [27]. The mentioned feature of the contact model allows us to systematically vary the relative magnitudes of the competitive forces in the suspension to recover the rate dependent rheological behavior [4].

The tangential contact force and the resulting contact torque ($\mathbf{T}_C^{(\mathrm{i,j})}$) acting on the particle is then given as:

$$\mathbf{F}_{C,t}^{(\mathrm{i,j})} = k_t \xi^{(\mathrm{i,j})} \mathbf{t}^{(\mathrm{i,j})}, \tag{4.3}$$

$$\mathbf{T}_C^{(\mathrm{i,j})} = a_\mathrm{i} \mathbf{n}^{(\mathrm{i,j})} \times \mathbf{F}_{C,t}^{(\mathrm{i,j})}. \tag{4.4}$$

In the above expression for tangential contact force, k_t is the tangential spring stiffness coefficient and can be calculated as [24], [52], [110]:

$$k_t = \frac{2}{7} \frac{|\mathbf{F}_{C,n}^{(\mathrm{i,j})}|}{|\delta|}. \tag{4.5}$$

The tangential spring stretch, $\xi^{(\mathrm{i,j})}$ can be calculated from the normal ($\mathbf{U}_n^{(\mathrm{i,j})} = \mathbf{n}^{(\mathrm{i,j})}\mathbf{n}^{(\mathrm{i,j})} \cdot (\mathbf{U}^{(\mathrm{j})} - \mathbf{U}^{(\mathrm{i})})$) and tangential ($\mathbf{U}_t^{(\mathrm{i,j})} = (\mathbf{I} - \mathbf{n}^{(\mathrm{i,j})}\mathbf{n}^{(\mathrm{i,j})}) \cdot [\mathbf{U}^{(\mathrm{j})} - \mathbf{U}^{(\mathrm{i})} - (a_\mathrm{i}\mathbf{\Omega}^\mathrm{i} + a_\mathrm{j}\mathbf{\Omega}^\mathrm{j}) \times \mathbf{n}^{(\mathrm{i,j})}]$) relative velocities between the particles i and j by applying the algorithm described in Luding [148] and Mari *et al.* [25]. $\mathbf{t}^{(\mathrm{i,j})}$ is a vector normal to $\mathbf{n}^{(\mathrm{i,j})}$ in the tangential direction to the particles and given as: $\mathbf{F}_{C,t}^{(\mathrm{i,j})}/|\mathbf{F}_{C,t}^{(\mathrm{i,j})}|$. Contact forces also induce an additional contact stresslet for the particle given by the vector product of particle center to center vector and the contact force as [24]:

$$\mathbf{S}_C^{(\mathrm{i,j})} = \frac{1}{2}\left(\frac{\mathbf{d}^{(\mathrm{i,j})}}{2} \otimes \mathbf{F}_C^{(\mathrm{i,j})} + \mathbf{F}_C^{(\mathrm{i,j})} \otimes \frac{\mathbf{d}^{(\mathrm{i,j})}}{2}\right). \tag{4.6}$$

The focus of this study is to quantify the effect of roughness size on the ST behavior of dense suspensions. Hence, we only vary the roughness size which is h_r. This is like increasing the sizes of the bumps on the particles surfaces while keeping their mean radii the same with a uniform distribution of the asperities on the particle surface [3], [4], [24], [52], [62], [172]. It has been shown recently that it is not only the frictional contacts, but resolving for the particle roughness will entirely change the hydrodynamic interactions between rough particles as well [167]. As also shown in ref. [166], these hydrodynamic interactions by themselves can recover DST behavior without any frictional contact. Here for the sake of simplicity we do not include the consequences of having rough particles on tangentially-translated hydrodynamic interactions due to presence of rough asperities. However, the resistance to sliding and the rolling motion [173] is included via tangential spring and consequently, via the contact torques acting on the particles, respectively. The focus of this study is to propose a constitutive model to account for the effect of roughness size on the behavior of ST suspensions based on the philosophy of Wyart-Cates [50]. Hence, we keep the hydrodynamic interaction calculations simple but focus more on the roughness size and contact dynamics modelling.

4.2.2 Friction: Critical Load Model

Since we have a balance between the hydrodynamic and contact forces owing to the choice of k_n as described above, there is no competition between the governing forces which is the fundamental mechanism for observing shear rate dependent rheological behavior [25], [54], [94]. Hence, in addition to above contact forces, we introduce an extra force scale in the friction law itself. This is called *Critical Load Model* (CLM) [25]. This force is a threshold normal force (F_{CL}) below which the particles interact as friction-less hard spheres and above which friction between the particles is activated. This is a simple model which can successfully reproduce the continuous and discontinuous shear thickening behavior observed in suspensions and has been extensively used in the literature [4], [25], [56], [59]. This type of frictional behavior has also been observed experimentally [58],

$$|\mathbf{F}_{C,t}^{(\mathrm{i,j})}| \leq \begin{cases} \mu\left(|\mathbf{F}_{C,n}| - F_{CL}\right), & \text{if } |\mathbf{F}_{C,n}| \geq F_{CL} \\ 0, & \text{otherwise.} \end{cases} \tag{4.7}$$

4.2.3 Bulk rheology and shear rate calculation

We perform stress controlled simulations for this study. Thus, for a given imposed shear stress, σ, we calculate the shear rate, $\dot{\gamma}$, which is an unknown a priori. The bulk stress in a suspension of rigid particles in a flow with strain rate $\mathbf{E}^{\infty}$ is (after subtracting isotropic part of the fluid pressure):

$$\mathbf{\Sigma} = 2\eta\left(1+\frac{5}{2}\phi\right)\mathbf{E}^{\infty} + \mathbf{\Sigma}^{p}, \tag{4.8}$$

where $\mathbf{\Sigma}^{p}$ is the particle contribution to the bulk stress, and is given by the sum of hydrodynamic stress $\mathbf{\Sigma}^{H}$ and the contact stress $\mathbf{\Sigma}^{C}$ as:

$$\mathbf{\Sigma}^{p} = \mathbf{\Sigma}^{H} + \mathbf{\Sigma}^{C}, \tag{4.9}$$

where $\mathbf{\Sigma}^{H}$ and $\mathbf{\Sigma}^{C}$ can be calculated by taking ensemble average of the hydrodynamic ($\mathbf{S}_{H}$) and contact ($\mathbf{S}_{C}$) stresslets at each time step. We get,

$$\mathbf{\Sigma}^{H} = \frac{1}{V}\left(\sum_{\mathrm{i}}\mathbf{S}_{H}^{(\mathrm{i})}\right), \tag{4.10}$$

$$\mathbf{\Sigma}^{C} = \frac{1}{V}\left(\sum_{\mathrm{i}}\mathbf{S}_{C}^{(\mathrm{i,j})}\right). \tag{4.11}$$

Therefore,

$$\mathbf{\Sigma} = 2\eta\left(1+\frac{5}{2}\phi\right)\mathbf{E}^{\infty} + \frac{1}{V}\left(\sum_{\mathrm{i}}\mathbf{S}_{H}^{(\mathrm{i})} + \sum_{\mathrm{i}}\sum_{\mathrm{j}}\mathbf{S}_{C}^{(\mathrm{i,j})}\right), \tag{4.12}$$

where V is the volume of the domain which is given by L^{3} for a cubic domain with sides equal to L. Shear stress σ, normal stress differences N_1 and N_2, and relative viscosity η_r can then be defined as $\sigma = \Sigma_{12}$, $N_1 = \Sigma_{11} - \Sigma_{22}$, $N_2 = \Sigma_{22} - \Sigma_{33}$, and $\eta_r = \sigma/(\eta\dot{\gamma})$. The shear stress, σ, is given by,

$$\sigma = \Sigma_{12} = \eta\left(1+\frac{5}{2}\phi\right)\dot{\gamma} + \dot{\gamma}[\left(\mathbf{R}_{SE} - \mathbf{R}_{SU}\cdot\mathbf{R}_{FU}^{-1}\cdot\mathbf{R}_{FE}\right) : \hat{\mathbf{E}}^{\infty}]_{12} + \Sigma_{12}^{C}, \tag{4.13}$$

where $\hat{\mathbf{E}}^{\infty}$ is the shear rate normalized rate-of-strain tensor. The shear rate can then be calculated as [117],

$$\dot{\gamma} = \frac{\sigma - \Sigma_{12}^{C}}{\eta(1+\frac{5}{2}\phi) + [\left(\mathbf{R}_{SE} - \mathbf{R}_{SU}\cdot\mathbf{R}_{FU}^{-1}\cdot\mathbf{R}_{FE}\right) : \hat{\mathbf{E}}^{\infty}]_{12}}, \tag{4.14}$$

4.2.4 Simulation conditions

1. *Bidisperse suspension*: We consider bidisperse spheres with $a_2/a_1 = 1.4$ with equal volume fractions for smaller and larger spheres. This is done to avoid any cluster formation and/or crystallization which is otherwise observed for monodisperse suspensions [25], [52], [56]. In addition, this choice of bidispersity parameters results in a rheology very close to their monodisperse counterparts [3], [52], [55], [149]. In experiments, one will need to critically measure and calculate the actual volume fraction of the particles, using a variety of techniques [9]. In the present study, we calculate the volume fraction based on the base particle radii a_1 and a_2.

2. *Boundary conditions and domain size*: Lees-Edwards periodic boundary conditions [114] have been applied to all the sides. These boundary conditions enable us to simulate the sheared suspension for a fixed domain volume without loss of generality and produce accurate results for bulk rheological properties like viscosity and normal stress differences. For this study, we simulate shear flow of suspension in a cubic box with sides $15a_1$, where a_1 is the radius of the smaller particles [3], [4]. We repeated the simulations for a bigger domain with sides $20a_1$. There is no significant change in the rheological properties, so we decided to run all the simulations for a domain with sides $15a_1$.

3. *Shear stress/rate dependence*: We have an additional force scale besides the hydrodynamic one which is required to yield shear-rate dependence. In CLM the threshold value gives the force scale F_{CL}. Therefore, the shear rate dependence is given by the ratio, $\dot{\gamma}/\dot{\gamma}_0$, with $\dot{\gamma}_0 = F_{CL}/6\pi\eta a^2$ and the shear stress dependence is given by the dimensionless shear stress, $\tilde{\sigma} = \sigma/\sigma_0$ with $\sigma_0 = \eta\dot{\gamma}_0$

4. *Range of parameters investigated*: The simulation parameters are listed in table 4.1. The aim of this study is to understand the effects of varying particle surface roughness on the rheology of suspension. Hence, we simulate the shear flow of rough particles for 5 different dimensionless roughness values, $\epsilon_r = 2h_r/(a_\mathrm{i} + a_\mathrm{j})$ viz., (0.01, 0.03, 0.05,

Table 4.1. Simulation parameters

ϕ	σ/σ_0	μ	$\epsilon_r(\%)$
0.45 - 0.56	0.1 - 100.0	1	1.0 - 10.0

0.075, 0.1). The simulations were carried out for dimensionless shear stress values $\tilde{\sigma}$ in the range [0.1 - 100.0] for a range of volume fractions in (0.45-0.56).

4.2.5 Validation of the numerical tool

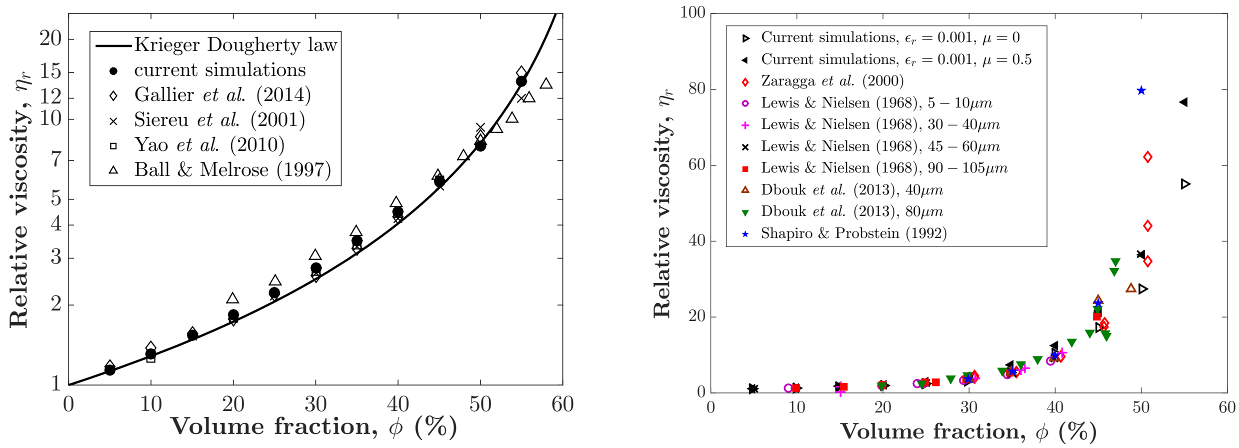

(a) **(b)**

Figure 4.2. a) Comparison of high-frequency shear viscosity with previously published results [24], [48], [49], [174]. b) Comparison of relative viscosity with a constant coefficient of friction, $\mu = 0$ and 0.5 with experiments [20], [22], [112], [175]

This section presents the high frequency shear viscosity calculations from the numerical tool utilized in this study with previously published results. High frequency shear viscosity means the particles are frozen at their respective positions. So, we calculate the high frequency relative viscosity for 10 different random particle configurations and their average values are presented in Fig. 4.2a. The slight difference difference with Ball & Melrose (1997) [49] is due to neglecting the twist mode in the present work [3], [25].

Fig. 4.2b compares the relative viscosity at different volume fractions calculated for smooth suspensions with $\epsilon_r = 0.001$ for two different constant coefficient of friction $\mu = 0$

and $\mu = 0.5$ with previously published experimental data [20], [22], [112], [175]. We turn off the *CLM* model (eq. 4.7) and carry out the simulations for constant μ. The agreement is satisfactory.

4.3 Constitutive model

We observe stress independent but roughness size dependent rheological behavior in the low/zero (denoted by superscript $\{\}^0$) and the high/infinite (denoted by superscript $\{\}^\infty$) shear stress/rate limits. As there are multiple variables that vary in the two extreme stress limits, we use $\{\}$ as a generic symbol to indicate the variables. The rheological properties in the two extreme stress conditions can be expressed in terms of volume fraction (ϕ), jamming volume fraction ($\phi_m^{0,\infty}$), fitting constants ($\alpha^{0,\infty}, \beta^{0,\infty}, \chi^{0,\infty}$) in the two extreme stress limits, respectively, as:

$$\eta_r^0\left(\phi, \epsilon_r\right) = \alpha^0\left(\epsilon_r\right)\left(\phi_m^0\left(\epsilon_r\right) - \phi\right)^{-2}, \tag{4.15}$$

$$\eta_r^\infty\left(\phi, \epsilon_r\right) = \alpha^\infty\left(\epsilon_r\right)\left(\phi_m^\infty\left(\epsilon_r\right) - \phi\right)^{-2}, \tag{4.16}$$

$$-\frac{N_2^0}{\eta\dot{\gamma}}\left(\phi, \epsilon_r\right) = \beta^0\left(\epsilon_r\right)\phi^2\left(\phi_m^0\left(\epsilon_r\right) - \phi\right)^{-2}, \tag{4.17}$$

$$-\frac{N_2^\infty}{\eta\dot{\gamma}}\left(\phi, \epsilon_r\right) = \beta^\infty\left(\epsilon_r\right)\phi^2\left(\phi_m^\infty\left(\epsilon_r\right) - \phi\right)^{-2}. \tag{4.18}$$

$$\frac{N_1^0}{\eta\dot{\gamma}}\left(\phi, \epsilon_r\right) = \chi^0\left(\epsilon_r\right)\phi^2\left(\phi_m^0\left(\epsilon_r\right) - \phi\right)^{-2}, \tag{4.19}$$

$$\frac{N_1^\infty}{\eta\dot{\gamma}}\left(\phi, \epsilon_r\right) = \chi^\infty\left(\epsilon_r\right)\phi^2\left(\phi_m^\infty\left(\epsilon_r\right) - \phi\right)^{-2}. \tag{4.20}$$

The expressions for volume fraction dependence of viscosity and the normal stress differences, i.e., $\left(\phi_m\left(\epsilon_r\right) - \phi\right)^{-2}$ and $\phi^2\left(\phi_m\left(\epsilon_r\right) - \phi\right)^{-2}$, respectively, are consistent with correlations proposed for constant volume [176], [177] and constant pressure conditions [17] and have also been used in the constitutive modelling of ST suspension based on coefficient of friction [117]. Here we retain the dependence of ϕ_m on the roughness ratio, ϵ_r, as the jamming fraction depends on the roughness ratio along with the imposed stress values. We assume a constant coefficient of friction for this study with value equal to 1. Hence friction dependence is not shown in the constitutive equations, but it can be included in a straightforward manner [117].

We observe that the fitting constants are roughness size dependent in the zero shear limit even though the suspension is effectively friction-less in this regime since $|\mathbf{F}_N| << F_{CL}$. So, α^0, β^0 and χ^0 are μ independent but vary with ϵ_r. This is to be expected since roughness leads to an increase in viscosity and a reduction in the jamming fraction of dense non-Brownian suspensions [3], [4], [7]. We need to be more careful with handling N_1 as it has been harder to measure experimentally [119], [159], [178] and compute numerically [24], [25], [52]. In addition, N_1 has been known to switch signs from negative to positive as the suspension shear thickens. This effect is more notable at high volume fractions than at lower volume fractions [4], [25], [117].

The rheological properties at a finite stress value $0 < \tilde{\sigma} < \infty$ can similarly be expressed in terms of the volume fraction (ϕ), jamming volume fraction ($\phi_m\left(\tilde{\sigma}, \epsilon_r\right)$), fitting constants $\left(\alpha\left(\tilde{\sigma}, \epsilon_r\right), \beta\left(\tilde{\sigma}, \epsilon_r\right), \chi\left(\tilde{\sigma}, \epsilon_r\right)\right)$ as:

$$\eta_r\left(\phi, \tilde{\sigma}, \epsilon_r\right) = \alpha\left(\tilde{\sigma}, \epsilon_r\right)\left[\phi_m\left(\tilde{\sigma}, \epsilon_r\right) - \phi\right]^{-2}, \tag{4.21}$$

$$-\frac{N_2}{\eta\dot{\gamma}}\left(\phi, \tilde{\sigma}, \epsilon_r\right) = \beta\left(\tilde{\sigma}, \epsilon_r\right)\phi^2\left[\phi_m\left(\tilde{\sigma}, \epsilon_r\right) - \phi\right]^{-2}. \tag{4.22}$$

$$\frac{N_1}{\eta\dot{\gamma}}\left(\phi, \tilde{\sigma}, \epsilon_r\right) = \chi\left(\tilde{\sigma}, \epsilon_r\right)\phi^2\left[\phi_m\left(\tilde{\sigma}, \epsilon_r\right) - \phi\right]^{-2}. \tag{4.23}$$

The jamming fraction and the fitting constants at an intermediate finite $\tilde{\sigma}$ can be calculated by interpolating their corresponding values in the low and high stress limits [50] as follow:

$$\phi_m\left(\tilde{\sigma}, \epsilon_r\right) = \phi_m^0\left(\epsilon_r\right)\left[1 - f\left(\tilde{\sigma}\right)\right] + \phi_m^\infty\left(\epsilon_r\right)\left[f\left(\tilde{\sigma}\right)\right], \tag{4.24}$$

$$\alpha\left(\tilde{\sigma},\epsilon_r\right)=\alpha^0\left(\epsilon_r\right)\left[f\left(\tilde{\sigma}\right)\right]+\alpha^\infty\left(\epsilon_r\right)\left[1-f\left(\tilde{\sigma}\right)\right], \tag{4.25}$$

$$\beta\left(\tilde{\sigma},\epsilon_r\right)=\beta^0\left(\epsilon_r\right)\left[f\left(\tilde{\sigma}\right)\right]+\beta^\infty\left(\epsilon_r\right)\left[1-f\left(\tilde{\sigma}\right)\right], \tag{4.26}$$

$$\chi\left(\tilde{\sigma},\epsilon_r\right)=\chi^0\left(\epsilon_r\right)\left[f\left(\tilde{\sigma}\right)\right]+\chi^\infty\left(\epsilon_r\right)\left[1-f\left(\tilde{\sigma}\right)\right], \tag{4.27}$$

here $f(\tilde{\sigma})=\exp(-\tilde{\sigma}^*/\tilde{\sigma})$ is the average fraction of frictional contacts in the suspension for a particular $\tilde{\sigma}$ and which is based on previously published experiments and simulations [3], [25], [122], [160], [171], [179]. We use $\tilde{\sigma}^*=4$. This particular value of $\tilde{\sigma}^*$ was obtained by fitting $f(\tilde{\sigma})=\exp(-\tilde{\sigma}^*/\tilde{\sigma})$ to the average fraction of frictional contacts vs $\tilde{\sigma}$ data from the simulations. In addition, fitting constants, α, β and χ as well as the jamming fraction, ϕ_m in the low and high shear stress limits can be expressed in terms of the dimensionless roughness, ϵ_r and fitting constants $\{\phi_m,\alpha,\beta,\chi\}^0_S$, $\{\phi_m,\alpha,\beta,\chi\}^\infty_R$, and $X^{0,\infty}_{\phi_m,\alpha,\beta,\chi}$. We use subscripts $_S$ and $_R$ to denote the values of these fitting constants for the smoothest and the roughest cases. respectively. We use:

$$\{\phi_m\}^{0,\infty}(\epsilon_r)=\{\phi_m\}^{0,\infty}_R+[\{\phi_m\}^{0,\infty}_S-\{\phi_m\}^{0,\infty}_R]\exp\left(-\{X\}^{0,\infty}_{\phi_m}/\epsilon_r\right), \tag{4.28}$$

$$\{\alpha\}^{0,\infty}(\epsilon_r)=\{\alpha\}^{0,\infty}_R+[\{\alpha\}^{0,\infty}_S-\{\alpha\}^{0,\infty}_R]\exp\left(-\{X\}^{0,\infty}_{\alpha}/\epsilon_r\right), \tag{4.29}$$

$$\{\beta\}^{0,\infty}(\epsilon_r)=\{\beta\}^{0,\infty}_R+[\{\beta\}^{0,\infty}_S-\{\beta\}^{0,\infty}_R]\exp\left(-\{X\}^{0,\infty}_{\beta}/\epsilon_r\right), \tag{4.30}$$

$$\{\chi\}^{0,\infty}(\epsilon_r)=\{\chi\}^{0,\infty}_R+[\{\chi\}^{0,\infty}_S-\{\chi\}^{0,\infty}_R]\exp\left(-\{X\}^{0,\infty}_{\chi}/\epsilon_r\right). \tag{4.31}$$

Here $\{\}^{0,\infty}$ gives the values of the fitting constants in the zero ($\{\}^0$) and infinite ($\{\}^\infty$) shear stress limits, respectively, depending on whether we choose ^{0} or $^\infty$ as the superscript. The same superscript must be chosen on the right hand side. This exponential description for the fitting constants on the dimensionless roughness size, i.e., $\exp(-\{\}/\epsilon_r)$ is inspired from the expression used for $f(\tilde{\sigma})$. This completes the description of the constitutive equations.

4.4 Results and discussion

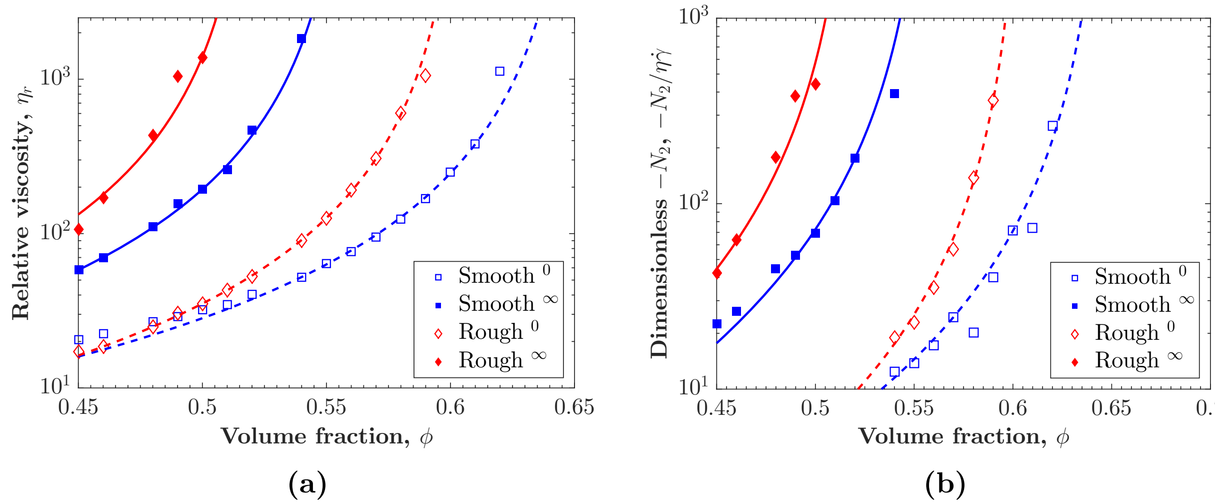

Figure 4.3. Rheological properties of the smoothest ($\epsilon_r = 1\%$, "Smooth") and roughest ($\epsilon_r = 10\%$, "Rough") suspensions for different volume fraction values. Symbols are simulation results. Dashed and solid lines represent fitting equations in the low (^{0}, equations 4.15 & 4.17) and high ($^\infty$, equations 4.16 & 4.18) shear rate limits. a) Relative viscosity, b) Second normal stress difference. Roughness leads to increase in η_r and $-N_2$ in both the low and high shear rate limits. We postpone results for N_1 till Sec. 4.4.3 due to its peculiar behavior. This roughness dependent rheology will be observed irrespective of *CLM* (eq. 4.7). We will get either ^{0} or $^\infty$ rheological measurements depending on whether we choose $\mu = 0$ or 1, respectively.

This section presents the results of stress controlled shear flow simulations of dense rough particle ST suspensions for the range of parameters investigated. Since the focus of this study is to investigate the effects of varying particle roughness on the behavior of ST suspensions, we kept μ a constant with value 1 for all the case. The simulations for different parameters were carried out for a total of 100 - 200 strain units, i.e., $t_{final} = (100 - 200)/\dot{\gamma}$. Time step was decided by using a hard-sphere algorithm [49] with upper bound of $1 \times 10^{-4}/\dot{\gamma}$. The first 30 % strain units were discarded owing to the transient behavior of rheological properties in the initial time. All the rheological properties presented in the subsequent subsections are calculated by averaging after 30 % strain units and only the average values are presented.

4.4.1 Roughness dependent rheology

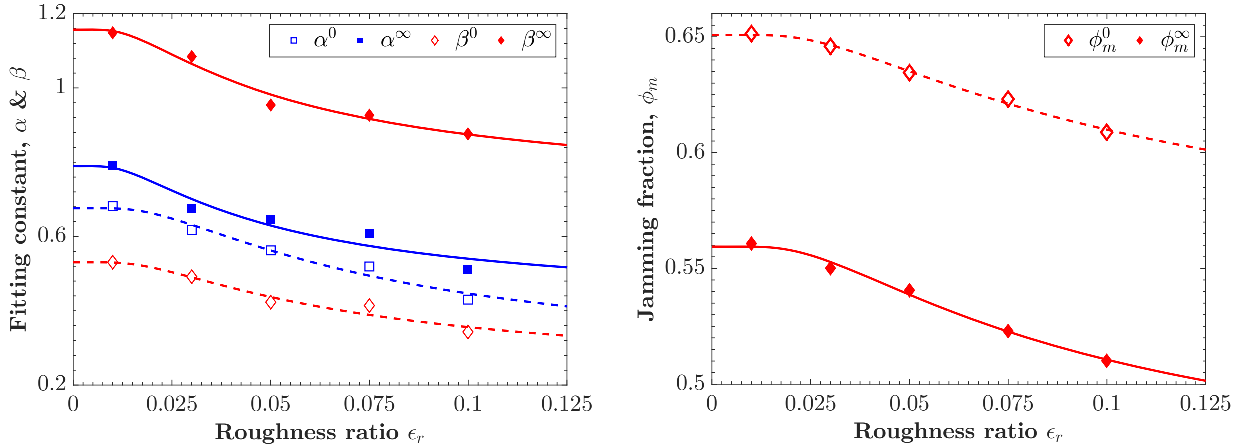

(a) **(b)**

Figure 4.4. Fitting constants for different roughness values. Symbols are fitting constants obtained from simulations. Dashed and solid lines represent fitting equations (equations 4.28, 4.29 & 4.30) in the low (^{0}) and high ($^\infty$) shear rate limits. a) α & β, b) jamming fraction, ϕ_m. Roughness leads to decrease in α and β in both the low and high shear rate limits. Increasing roughness leads to a reduction in the jamming volume fraction due to the increase in viscosity and the increase in the effective particle radii [4]. We postpone results for χ till Sec. 4.4.3 due to peculiar behavior of N_1.

It has been observed in experiments [7], [8], [54] and computations [3], [4] that roughness leads to increase in viscosity of suspension of rough particles due to reduction in the jamming fraction. In our simulations, the rheology in the low shear limit is friction-less because all the contacts are non-frictional ($|\mathbf{F}_N| < F_{CL}$). But still we observe an increase in η_r and $-N_2/\eta\dot{\gamma}$ in this limit with roughness. This is to be expected for dense suspensions as roughness basically leads to early contact and rise in the contact stresses. Fig. 4.3a and 4.3b show the relative viscosity and the second normal stress difference against volume fraction of the suspensions for the smoothest ($\epsilon_r = 1\%$) and the roughest ($\epsilon_r = 10\%$) particles in the low and high shear rate limits along with the modified Maron-Pierce fitting curves (Eq. 4.15, 4.16, 4.17, 4.18). In addition, the reduction in the jamming fraction, ϕ_m, with increasing stress and increasing particle roughness is consistent with experiments [9], [93].

Please note that due to the anomalous behavior of N_1, we defer the discussion on N_1 to Sec. 4.4.3.

Table 4.2. Roughness dependent model constants for η_r, $-N_2/\eta\dot{\gamma}$ and ϕ_m. Brackets ({}) in the column headers stand for the fitting constants α, β and ϕ_m for the respective rows.

	$\{\}_S^0$	$\{\}_R^0$	$X_{\{\}}^0$	$\{\}_S^\infty$	$\{\}_R^\infty$	$X_{\{\}}^\infty$
α	0.2123	0.6761	0.0703	0.4006	0.7894	0.0445
β	0.2040	0.5305	0.0626	0.7009	1.157	0.0480
ϕ_m	0.5442	0.6508	0.0958	0.4445	0.5594	0.0856

We observe that the fitting constants and the jamming fraction depends only on the particle roughness in the low and high shear rate limits. As a result they can be expressed in terms of ϵ_r as shown in equations 4.28, 4.29, 4.30. Fig. 4.4a and 4.4b show that equations 4.28, 4.29 and 4.30 are a good fit and accurately capture the effect of increasing the particle roughness on the rheology of dense suspensions with rough particles in the low and high shear limits. Table 4.2 summarizes the values obtained for the roughness dependent model constants obtained after a least square fit procedure.

Before presenting the stress dependent rheology, we would like to mention that the roughness size dependence and the stress dependence are not interrelated. We utilize *CLM* (eq. 4.7) to recover the stress dependent rheological behavior while roughness dependence comes from varying the roughness size h_r. In the absence of eq. 4.7, we only get the roughness size dependence which is presented in Fig. 4.3 and modeled in eq. 4.28 - 4.31. We will get either 0 stress limit or ∞ stress limit rheology depending on whether $\mu = 0$ or 1, respectively. But we will still get the increase in the viscosity with roughness size which is consistent with previous simulations [4] and experiments [7].

4.4.2 Stress dependent viscosity

In this section we present the data from the stress controlled simulations for suspensions with varying particle surface roughness values along with the constitutive equation fitting curves. Once the rheological properties and the jamming fraction in the low and high shear stress limits are known, it has been shown that the rheological properties in the intermediate

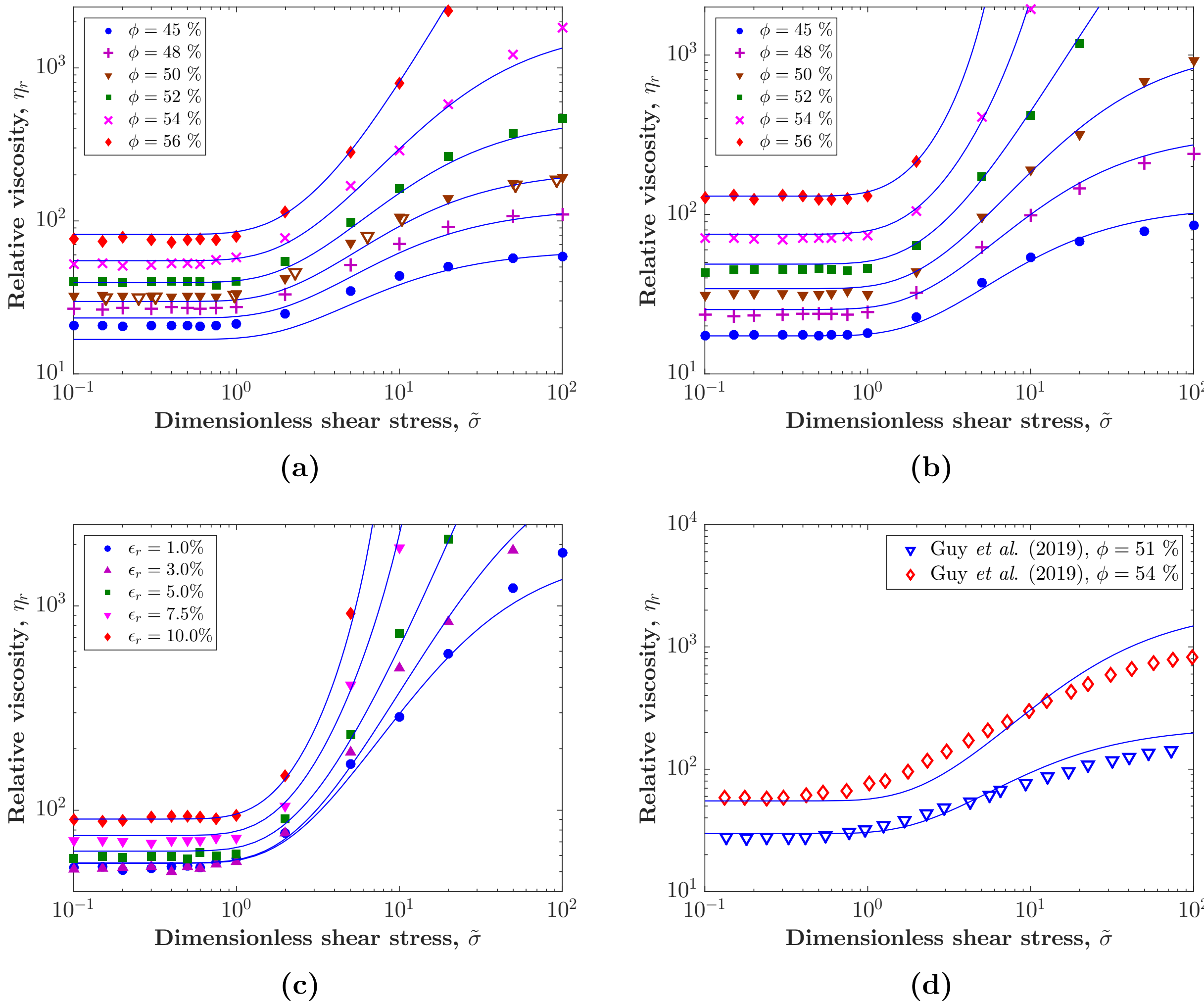

Figure 4.5. Relative viscosity as a function of dimensionless shear stress, $\tilde{\sigma}$: a) for smooth particle suspension, $\epsilon_r = 0.01$. Filled symbols are the simulation results for stress controlled simulations. Open symbols for $\phi = 50\%$ are the simulations results for shear rate controlled simulations with $\epsilon_r = 0.01$, b) for rough particle suspension, $\epsilon_r = 0.075$, c) $\phi = 54\%$, for different roughness values. ST transition takes place at a constant $\tilde{\sigma} = 1$ [4]. d) Comparison of the constitutive model with the experimental data from Guy et al. (2015, 2019) [93], [122]. We assume the particles to have a roughness size, $\epsilon_r = 0.5$ % and $\sigma_0 = 4$ (Pa) for the experimental data. The solid lines represent equation 4.21 with the values of fitting parameters obtained using the simulation data.

stress values can be interpolated [50]. This is the basis of proposing the roughness and stress dependent constitutive equations in Sec. 4.3.

Fig. 4.5 shows the relative viscosity dependence on dimensionless shear stress for the smooth ($\epsilon_r = 1$ %) and rough ($\epsilon_r = 7.5$ %) particle suspensions for volume fractions investigated in this study. As we present simulations data only for $\epsilon = 1$ % and $\epsilon_r = 7.5$ % in the main text, we refer to these cases as "smooth" and "rough" henceforth in the article. Simulation data and the corresponding constitutive equation fits for the remaining roughness values, viz., $\epsilon_r = 3$, 5, and 10 % are provided in the Sec. 4.4.4. We have shown in our previous study [4] that the qualitative behavior of the suspension rheology, i.e., whether they will undergo CST or DST can be predicted with the help of effective volume fraction of the suspension given as, $\phi_\mathrm{e} = \phi(1 + \epsilon_r)^3$. Effective volume fraction can help us to predict the qualitative rheological behavior of the rough dense suspensions, but it should be borne in mind that it cannot predict the early onset and the strength of the ST effect which are solely governed by the asperity size and the base volume fraction. In addition, the critical shear rates for the ST transitions are also different even is two suspensions have the same ϕ_e. Increasing the roughness size in the current contact model also leads to distinct changes in the contact networks as shown in our previous study [4]. We elaborate more on this in Sec. 4.4.4.

The proposed model does an excellent job in predicting η_r in the intermediate $\tilde{\sigma}$ regime for both roughness cases. We also present the results for the relative viscosity from shear-rate controlled simulations for a suspension with 50% volume fraction and $\epsilon_r = 0.01$ in Fig. 4.5a which are denoted with open symbols. This shows that both the shear rate-controlled and shear-stress controlled simulations are in agreement. As the plots show, roughness leads to increase in the strength of CST at low volume fractions and leads to a bigger viscosity jump for the cases when DST is observed. Fig. 4.5c shows η_r for a fixed volume fraction of 54 % for various particle roughness values showing the effect of roughness on η and the accuracy of the constitutive model.

We can use the values of fitting parameters obtained from the simulation data to predict the relative viscosity of smooth particle suspensions. This has been done in Fig. 4.5d where we compare the predictions of the model developed with the experimental data from Guy *et al.*, (2015, 2019) [93], [122]. The model does a satisfactory job of estimating the relative viscosity for experimental systems. For this comparison we assume the particles in the experiments to have a nominal roughness size, $\epsilon_r = 0.5$ %. We also assume $\sigma_0 = 4$ Pa in order to non-dimensionalize the experimental stress values. Guy *et al.*, (2015, 2019) [93], [122] find $\phi_m^0 \approx 0.63$ and $\phi_m^\infty \approx 0.56$ for sterically stabilized PMMA suspensions. We predict $\phi_m^0 \approx 0.64$ and $\phi_m^\infty \approx 0.56$ for $\epsilon_r = 0.5\%$. Thus the results from the simulations show a satisfactory agreement with the experimental data.

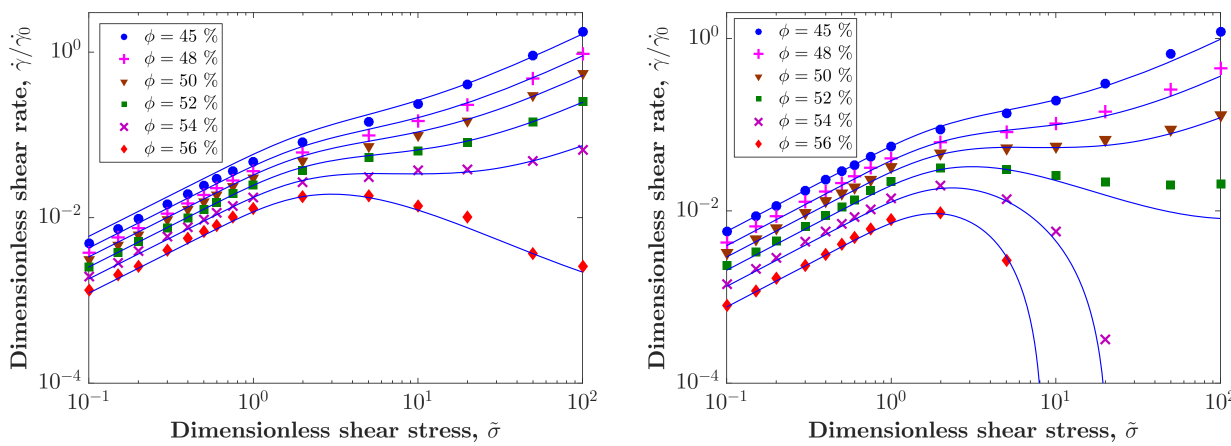

(a) **(b)**

Figure 4.6. Dimensionless shear rate vs dimensionless shear stress, $\tilde{\sigma}$: a) for smooth particle suspension, $\epsilon_r = 0.01$, $\phi_c \approx 54\%$, b) for rough particle suspension, $\epsilon_r = 0.075$, $\phi_c \approx 50\%$. Symbols are simulation results. The solid lines represent the fitting equation, $\tilde{\sigma}/\eta_r(\phi, \tilde{\sigma}, \epsilon_r)$ with $\eta_r(\phi, \tilde{\sigma}, \epsilon_r)$ from eq. 4.21

In addition to the jamming fraction, the critical volume fraction, ϕ_c, for the CST to DST transition, and the critical shear rate, $\dot{\gamma}_c$, for the onset of ST are two important parameters which determine the flow state of a suspension. They can be calculated from the relationship between σ and $\dot{\gamma}$. At $\dot{\gamma}_c$, the viscosity value starts to transition from the lubricated low magnitude regime to a frictional high magnitude regime. This transition is gradual for $\phi < \phi_c$ as the suspension undergoes CST. But for $\phi \geq \phi_c$ the viscosity abruptly jumps from the lubricated low value to a frictional high value signifying onset of DST. ϕ_c is the lowest volume fraction at which $d\dot{\gamma}/d\sigma$ becomes zero for some $\tilde{\sigma} = \bar{\sigma}_c$. This happens for $\phi_c \approx 54\%$ for a smooth particle suspension and for $\phi_c \approx 50\%$ for a rough particle suspension as can be seen in Fig. 4.6a and 4.6b, respectively and Fig. 4.8. From the constitutive equations presented in Sec. 4.3, we can quantify ϕ_c and $\bar{\sigma}_c$ by calculating the ϕ and σ/σ_0 for each roughness value where $d\dot{\gamma}/d\sigma$ becomes 0 first (See Fig. 4.6 and 4.8). In addition, the critical shear rate for ST transition decreases with roughness and can be found by $\dot{\gamma}_c/\dot{\gamma}_0 = 1/\eta_r(\phi, \epsilon_r, 1)$ as the ST starts at a constant $\tilde{\sigma} = 1$ [4], [25]. We observe a reduction in both $\dot{\gamma}_c$ and ϕ_c with increasing the roughness size which is well captured by the constitutive equations.

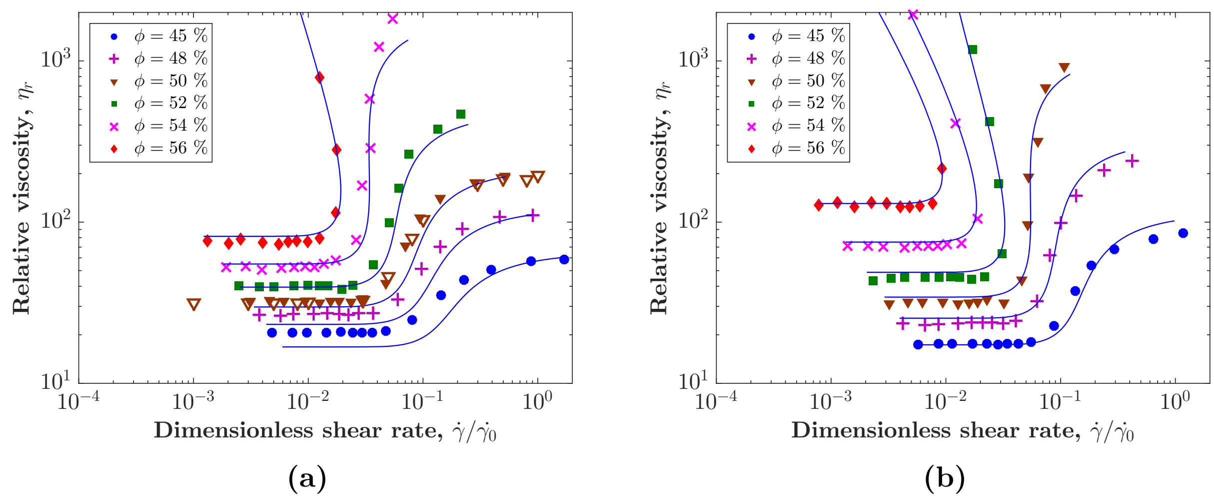

Figure 4.7. Relative viscosity vs dimensionless shear rate: a) for a smooth suspension, $\epsilon_r = 0.01$. Open symbols for $\phi = 50\%$ are the simulations results for shear rate controlled simulations with $\epsilon_r = 0.01$, b) for a rough suspension, $\epsilon_r = 0.075$ %, at different volume fraction values. Filled symbols are the stress controlled simulation results. Solid lines are the fitting equation (eq. 4.21). Increasing roughness leads to an increase in the CST strength at low volume fractions which can be clearly seen from the increase in the slope of the fitting curves in the ST transition regimes. At higher volume fractions, increasing roughness leads to higher viscosity jump across DST. At $\phi > \phi_c$ the suspension can only flow at small stress values.

Fig. 4.6 also shows the three flow state curves as discussed in Sec. 4.1. For smooth suspensions (Fig. 4.6a, $\epsilon_r = 1$ %), we observe a monotonic curve for $\sigma(\dot{\gamma})$ for $\phi < 53$ % which becomes non-monotonic S-shaped for $\phi > 53$ %. Eventually at higher volume fractions, i.e., $\phi > 56$ % we get the backward bending branch. With an increase in the roughness size (Fig. 4.6b, $\epsilon_r = 7.5$ %), the volume fractions dividing these three regimes are lowered with values $\phi_c = 50$ % for the monotonic to non-monotonic transition, and the S-shaped to backward bending transition takes place for $\phi \approx 53$ %. Fig. 4.8 demarcates the various transitions and regions in the flow state diagram ($\sigma(\dot{\gamma})$) of dense ST suspensions for the smooth and the rough case. It clearly shows the effect of increasing roughness is to lower the transition volume fractions for the monotonic to non-monotonic flow state curves.

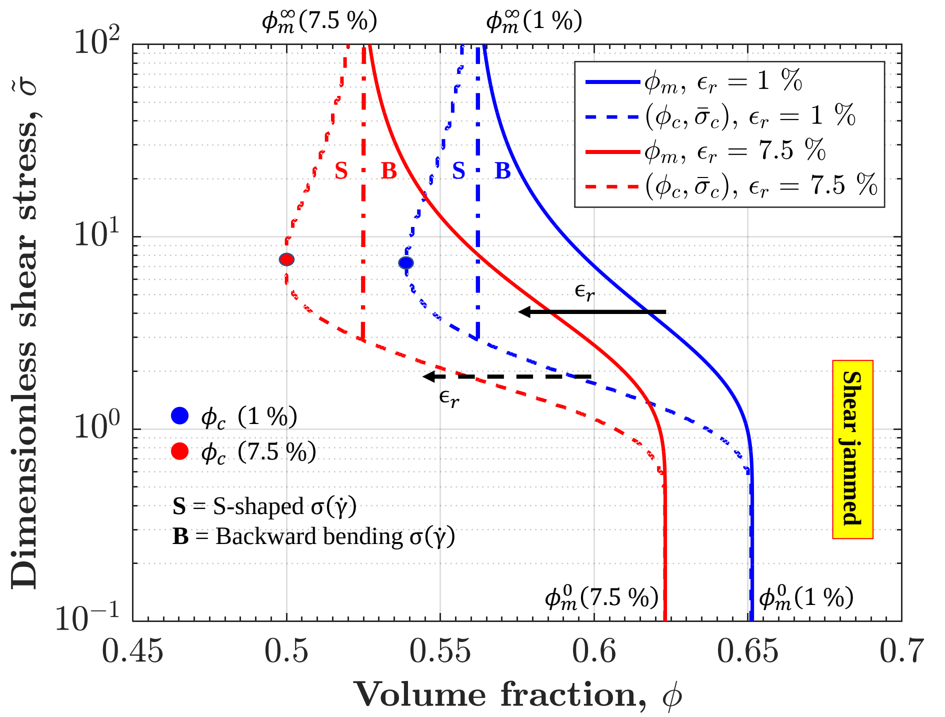

Figure 4.8. $\tilde{\sigma} - \phi$ phase space diagram for smooth ($\epsilon_r = 1\ \%$) and rough ($\epsilon_r = 7.5\ \%$) suspensions showing $\phi_m(\tilde{\sigma}, \epsilon_r)$ and $(\phi_c, \bar{\sigma}_c)(\epsilon_r)$ curves. Dotted curve shows the values of $\tilde{\sigma}$ and ϕ for which $d\dot{\gamma}/d\sigma = 0$. The big dots on the $(\phi_c, \bar{\sigma}_c)$ curve give the critical volume fraction for DST. Increasing roughness leads to decrease in the critical volume fraction for the DST onset. For the regions on the left to dotted lines suspensions undergo CST while they undergo DST for the regions between the dotted and solid curves. The dash-dotted lines in the DST region separate the parameter space for which we get S-shaped curve and backward bending curve in the $\sigma(\dot{\gamma})$ phase space. The suspension is shear jammed for the region on the right of the solid curves.

4.4.3 Stress dependent normal stress differences

We present the simulation data for N_2 for smooth and rough suspensions in Fig. 4.9. N_2 is always negative and its magnitude increases with increasing roughness. This is in agreement with previous studies [8], [9], [25], [37], [42], [119], [154]. This is to be expected as N_2 mimics the shear stress in the system [4], [25]. The constitutive equations proposed provide a good

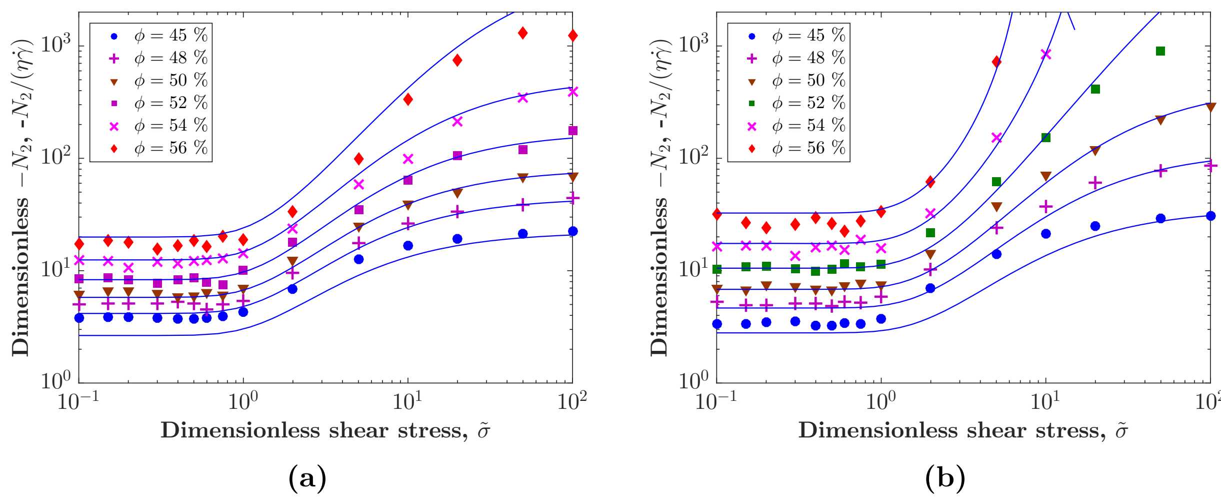

Figure 4.9. Dimensionless $-N_2$ vs stress: a) for a smooth suspension, $\epsilon_r = 1$ %, b) for a rough suspension, $\epsilon_r = 7.5$ %, at different volume fraction values. Symbols are simulation results. Solid lines are the fitting curves as given in equation 4.22.

fit to the simulation data and hence can be utilized to predict the behavior of N_2 as we change the particle surface roughness size. The normal stress difference, $N = N_1 - N_2$ is directly related to the normal force acting in a parallel plate rheometer. Since the magnitude of N_1 is low compared to N_2, we can say that the normal force is directly proportional to N_2. Thus, increasing roughness increases the normal force on the plate in a parallel plate rheometer.

Fig. 4.10a shows the effect of roughness on N_1 for a fixed volume fraction $\phi = 50$ %. The behavior of N_1 is not as straight-forward as other rheological properties of rough suspensions [42], [107], [157]–[159]. N_1 has a negative value at low volume fractions and its magnitude increases as the suspension undergoes shear thickening. But, at high stress values the value of $N_1/\eta\dot{\gamma}$ becomes less negative. On the other hand, for higher ϕ, N_1 is negative at low stress values and switches sign and becomes positive if the suspension undergoes DST. As a result, care must be taken while choosing the sign of fitting constant χ. This switching of the sign by N_1 with roughness has also been observed experimentally for rough colloidal suspensions [9]. The results obtained in the present simulations are consistent with these experimental observations.

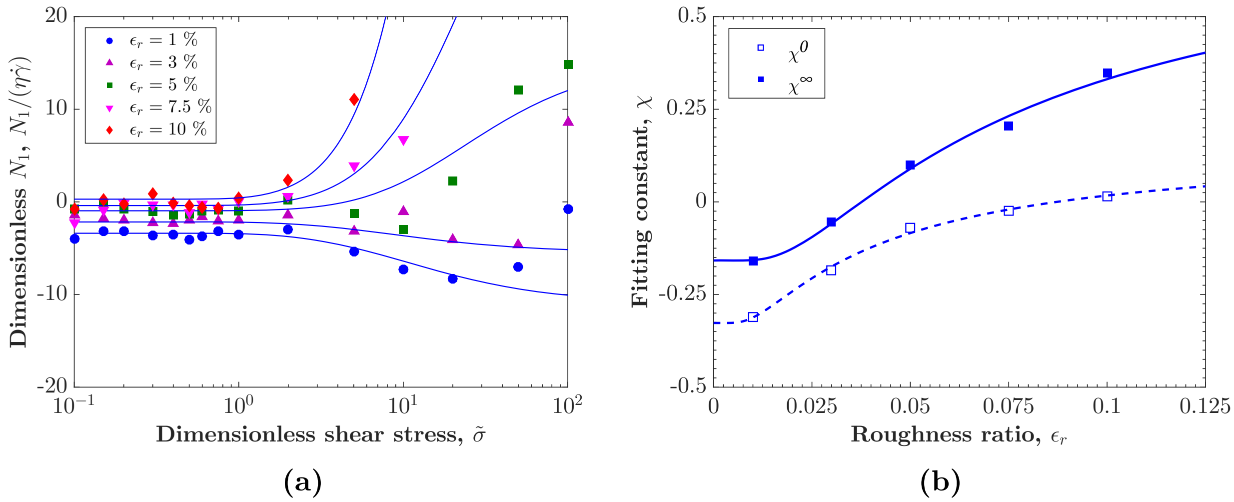

Figure 4.10. a) Dimensionless N_1 vs stress for $\phi = 50$ % at various roughness values. Solid lines are the fitting curves as given in equation 4.23. b) fitting constant, χ at different roughness values. Dashed and solid lines represent fitting equations (eq. 4.27) in the low (^{0}) and high ($^\infty$) shear rate limits. Symbols are simulations results.

We find that, in the low stress limit, N_1 is negative for all the roughness values except for a very high roughness value, i.e., $\epsilon_r = 10$ % for the explored volume fraction range. This is to be expected as the effective radii of the particles at such a high roughness is large and the suspension behaves the same way as a highly concentrated suspension of smooth particles would. $N_1/\eta\dot{\gamma}$ attains a high positive value at higher roughness values and in the high stress limit. These observations are in agreement with experiments [8]. These observations are shown in Fig. 4.10a along with the fitting curves using equation 4.23.

Table 4.3. Roughness dependent model constants for $N_1/\eta\dot{\gamma}$.

χ_S^0	χ_R^0	X_χ^0	χ_S^∞	χ_R^∞	X_χ^∞
-0.1609	-0.3268	0.0349	0.8102	-0.1581	0.0683

Fig. 4.10b shows the variation of the fitting constant χ in the constitutive equations for $N_1/\eta\dot{\gamma}$ with roughness size. The fitting constants in the roughness dependent model for χ in the low and high shear stress/rate limit, i.e., equation 4.31, are summarized in table 4.3. χ^0 is mostly negative for all roughness values except for very high roughness sizes > 10 %. Similarly, χ^∞ is also negative for smaller roughness values $\epsilon_r < 3$ %, but switches sign once

the roughness is high $\epsilon_r > 3$ %. Note that, the value of χ in the low and high shear stress limits increases with roughness as opposed to α and β which decrease with roughness in these stress limits. This again indicates the peculiar behavior of as compared to η_r and N_2. Thus, the constitutive model presented captures the anomalous behavior $N_1/\eta\dot{\gamma}$ satisfactory if we choose the sign of fitting constants carefully.

4.4.4 Further analysis of the results and the complete simulation data

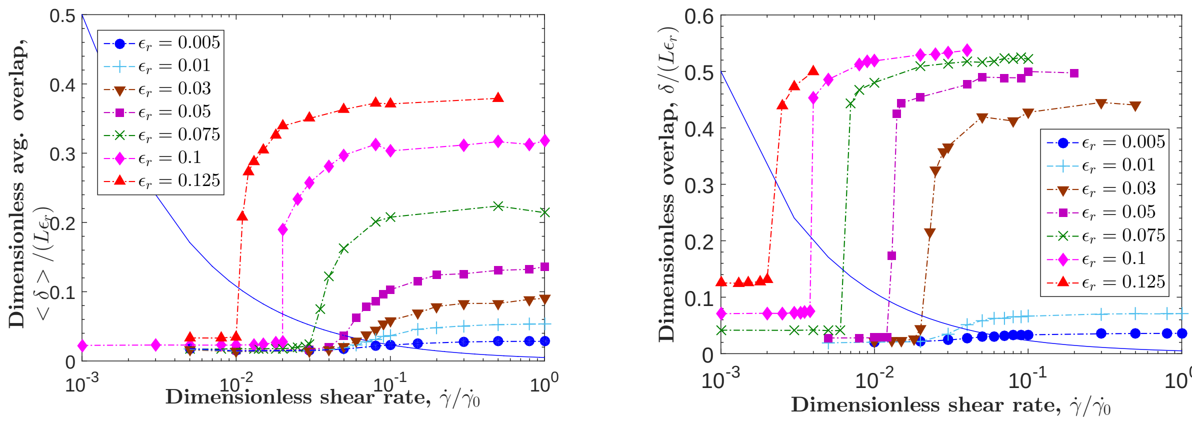

(a) (b)

Figure 4.11. Dimensionless average asperity deformation for a) 50 % and b) 52 % at various roughness values.

Here we present a detailed analysis of the results to show that increasing the roughness is not the same as increasing the volume fraction. The way we have modelled the particle surface roughness geometry, one can say that the rough particles act as bigger spheres with radii $a(1+\epsilon_r)$. We call this radius the effective radius of the particles, a_e. We can calculate the effective volume fraction of the suspensions bases on a_e as $\phi_\mathrm{e} = \phi(1+\epsilon_r)^3$. As we increase the roughness size, the effective radii of the particles increase which leads to early contacts between the particles. But we assume this to not alter the hydrodynamics interactions which are calculated for the base particles with radii a.

If increasing the surface roughness has the same effect as that of increasing the volume fraction of the suspensions, two suspensions with the same effective radii would have the exact same rheology. But this is not the case. The observed trends are not solely due

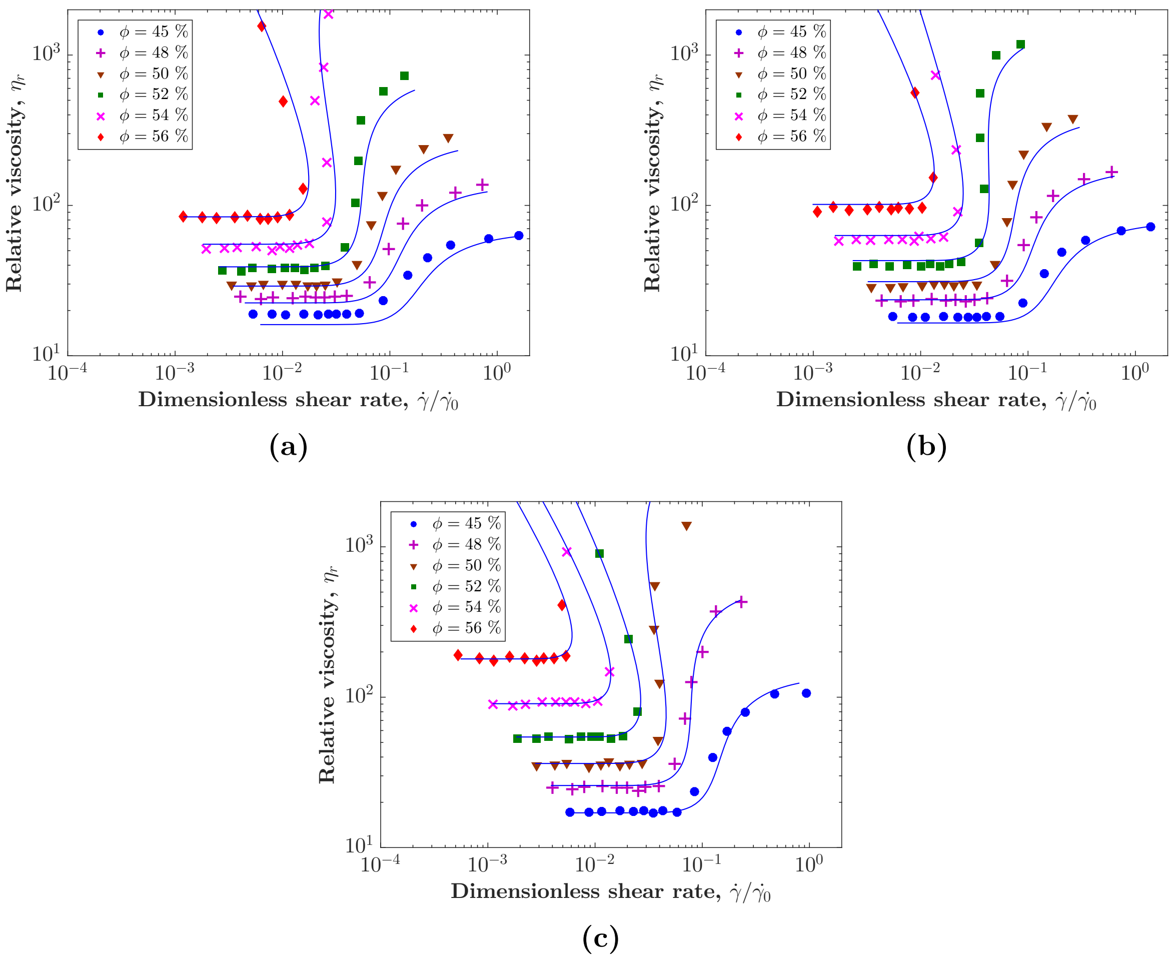

Figure 4.12. Relative viscosity vs dimensionless shear rate for different roughness values: a) $\epsilon_r = 0.03$, b) $\epsilon_r = 0.05$, c) $\epsilon_r = 0.1$. Filled symbols are the stress controlled simulation results. Solid lines are the fitting equation (eq. 4.21).

to the increase in the effective volume fractions, but also have explicit dependence on the roughness size. We explain why increase in the effective volume fraction is not the only factor governing the rheology and the model is doing more than that with the following features of the numerical modelling:

1. *Rolling motion*:

   The contact model implemented makes sure that the rolling motion of the particles is resolved which eventually influences the rheology i.e., the onset and the strength of the shear thickening (ST) effect observed. This is achieved by the tangential linear spring force implementation in the contact dynamics. To calculate the tangential force, we

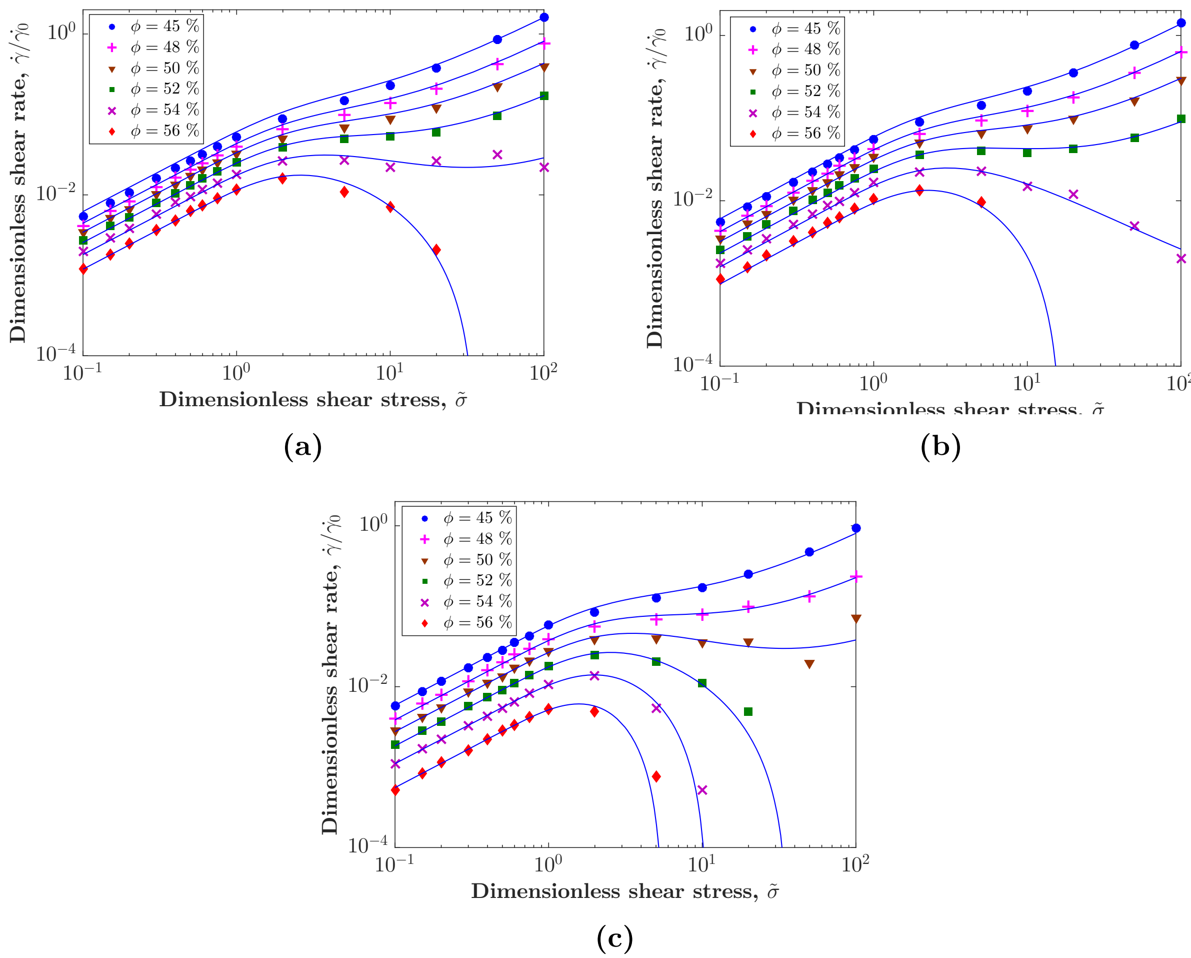

Figure 4.13. Flow state diagrams $\dot{\gamma}/\dot{\gamma}_0(\tilde{\sigma})$ for different roughness values: a) $\epsilon_r = 0.03$, b) $\epsilon_r = 0.05$, c) $\epsilon_r = 0.1$. Symbols are simulation results. The solid lines represent the fitting equation, $\tilde{\sigma}/\eta_r(\phi, \tilde{\sigma}, \epsilon_r)$ with $\eta_r(\phi, \tilde{\sigma}, \epsilon_r)$ from eq. 4.21.

calculate the tangential spring deformation by integrating the relative rolling velocities of two particles in contact. Calculating the relative rolling velocities (which we call relative sliding velocity in the text and its equation is provided in the paragraph right after equation 10) require us to calculate the angular velocities of the particles at each time step. Because of this tangential force the particles also experience a torque (equation 10 in the text) in addition to the contact forces. In addition, Critical Load Model (CLM) ensures that the contact torque is zero as long as the contact is frictionless (i.e., $|\mathbf{F_n}| < F_{CL}$, see equation 9 and 12 in the main text) and it increases with the

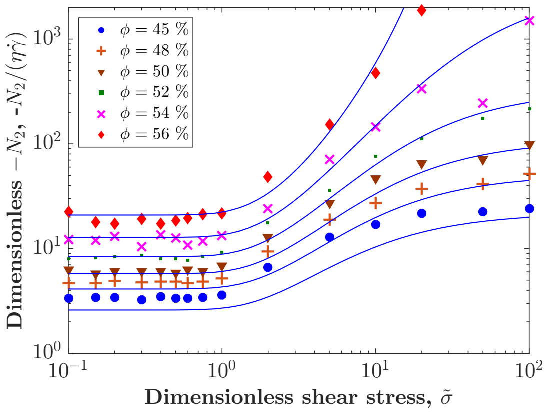

(a)

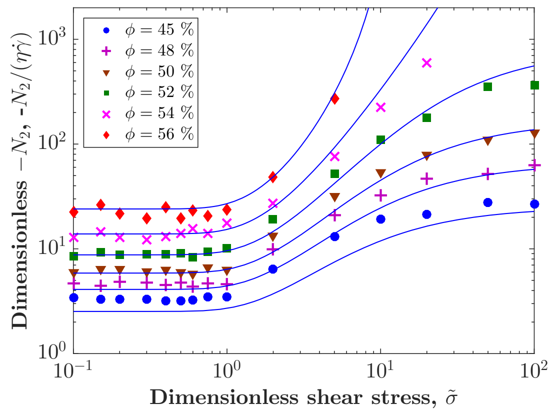

(b)

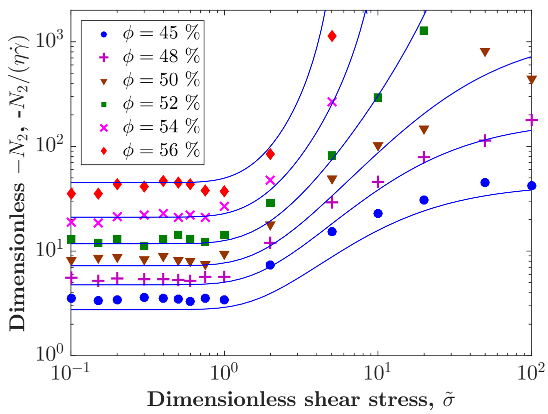

(c)

Figure 4.14. Dimensionless $-N_2$ vs dimensionless shear stress for different roughness values: a) $\epsilon_r = 0.03$, b) $\epsilon_r = 0.05$, c) $\epsilon_r = 0.1$. Symbols are simulation results. Solid lines are the fitting curves as given in equation 4.22.

tangential force as the contact becomes frictional. So, we calculate the rolling motion (translational as well as angular velocities of the particles and the resistance to rolling motion) of the particles and its effect is captured in the contact model implemented.

2. *Non-linear normal force*:

While Mari et al. (2014) use a linear spring for their contact normal force calculation, we use a more general and experimentally supported Hertz contact law which is not linear. So, with increasing asperity size, the normal force is not increasing linearly even though the contact interaction range is increasing linearly. If we had used a linear spring for the normal contact force, then we would expect, increasing the asperity size

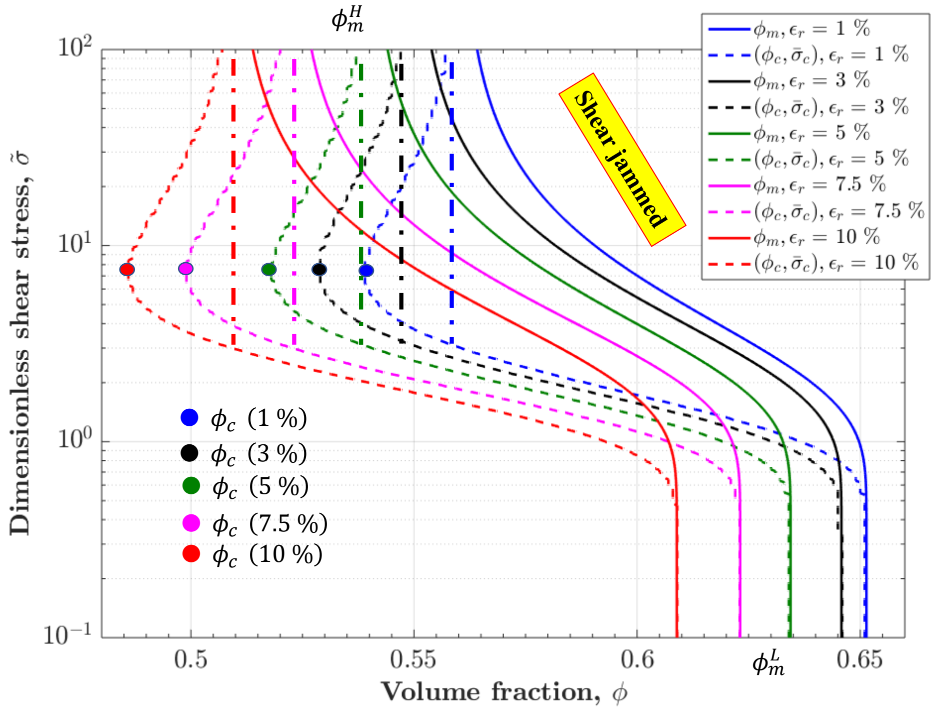

Figure 4.15. $\tilde{\sigma} - \phi$ phase space diagram for different ϵ_r suspensions showing $\phi_m(\tilde{\sigma}, \epsilon_r)$ and $(\phi_c, \bar{\sigma}_c)(\epsilon_r)$ curves. Dotted curve shows the values of $\tilde{\sigma}$ and ϕ for which $d\dot{\gamma}/d\sigma = 0$. The big dots on the $(\phi_c, \bar{\sigma}_c)$ curve give the critical volume fraction for DST. Increasing roughness leads to decrease in the critical volume fraction for the DST onset. For the regions on the left to dotted lines suspensions undergo CST while they undergo DST for the regions between the dotted and solid curves. The dash-dotted lines in the DST region separate the parameter space for which we get S-shaped curve (left region) and backward bending curve (right region) in the $\sigma(\dot{\gamma})$ phase space. The suspension is shear jammed for the region on the right of the solid curves.

to be the same as increasing the volume fraction, but the Hertz contact law considers the effect of area of contact which also depends on the asperity size and determines the normal contact force.

3. *Increasing asperity size does more than just extension of the contact distance between the particles*:

   CLM introduces a force scale in the simulations which governs the transition from the lubricated to frictional regime. It is known that the imposed shear stress on the suspension determines the normal force between the particles. So, if we do a rough scaling analysis and balance the critical load (F_{CL}) with the magnitude of the normal force, we can calculate the dimensional critical deformation ($\delta_c = 0.005 h_r(\dot{\gamma}_0/\dot{\gamma})^{(2/3)}$) of the asperities needed for the transition from frictionless to frictional contacts which is roughness size dependent. Choice of the normal contact stiffness ($k_n = 2{*}10^4/\sigma h_r^{(-3/2)}$) also introduces the effect of asperity size in the contact model.

Fig. 4.11 shows the average dimensionless asperity deformation ($F_n \propto \delta^{(3/2)}$) for two suspensions with volume fractions 50 % and 52 % respectively. The solid line gives the critical deformation needed for transition from a frictionless to frictional contact. These plots clearly show that the magnitude of the deformation of the asperities is dependent on the base volume fraction and the roughness and increases with both the base volume fraction and the roughness. If we consider 52 % suspension with dimensionless roughness ($\epsilon_r = 0.03$), the effective volume fraction is 57 % and for a 50 % suspension with $\epsilon_r = 0.05$, the effective volume fraction is 58 %. If the model was just calculating viscosities at higher volume fractions, then we should have same plots for the dimensionless overlaps for the two cases which is not the case. In addition, since effective volume fraction for 52 % with $\epsilon_r = 0.03$ is lower than the effective volume fraction for the 50 % with $\epsilon_r = 0.05$, we would have expected the viscosity for the later to be higher than the former if increasing the roughness was just resulting in increased volume fraction. But this is also not the case. While the relative viscosity for 52 % with $\epsilon_r = 0.03$ after ST is around 800, the relative viscosity for 50 % with $\epsilon_r = 0.05$ after ST is around 400 (see Fig. 4.12a and 4.12b). This clearly shows that the contact model implemented is achieving more than just calculating the rheology at higher volume fractions. We have provided all the data at different volume fractions and roughness values in Sec. 4.4.4 for further comparison.

4. *Lubrication interactions*: The lubrication interactions between two close particles are still calculated based on the interparticle gap between the base spheres. This makes sure that the lubrication interactions are not for the higher effective volume fraction and are still valid for the actual volume fraction. This is an important detail as they govern the motion of the particles (both translational and rotational). Doing so, we

are dissociating the role of roughness and hydrodynamics as the effect of roughness comes only via contact interactions. This is off course a simplification but is done in order to keep the calculations tractable.

These details show that the contact model implemented is nuanced and accurately incorporates the basic physics of contact interactions via surface asperities. The choice of the normal stiffness and friction model gives us the roughness dependent rheology in addition to the increase in the effective radius with surface roughness which alone cannot explain all the results presented in the manuscript.

In addition, the critical shear rates for the ST transitions are also different in both these cases. Increasing the roughness size in the current contact model also leads to distinct changes in the contact networks as shown in chapter 4.

Fig. 4.12, 4.13, 4.14 the simulations data and the constitutive model fits for the remaining roughness values, i.e., $\epsilon_r = 3$ %, 5 % and 10 %. These plots show the effect of increasing the roughness size on the rheology of rough particle suspensions, 1) magnitude of the ST index and the viscosity jump across the ST transition increase as we increase roughness size for a given volume fraction, and 2) increasing roughness size reduces the the critical shear rate ($\dot{\gamma}_c$) and the critical volume fraction for DST (ϕ_c). These plots demonstrate the accuracy of the model over a wide range of parameters. The change in the volume fraction ranges for the transitions between the three regimes in the flow state diagram with increasing roughness size can be seen in Fig. 4.15.

5. UNIFYING DISPARATE RATE DEPENDENT REGIMES IN NON-BROWNIAN SUSPENSIONS: ONE CURVE TO UNIFY THEM ALL

5.1 Introduction

Dense suspensions of particles are abundant in nature and industrial applications with examples ranging from household cornstarch solution to metallic pastes used in solar cells [3]. In spite of the Newtonian behavior of the suspending fluid medium, suspensions exhibit plethora of non-Newtonian behaviors including yield-stress [82], non-zero normal stress differences [37], shear rate dependent rheology [34], [83], and particle migration [38] to name a few [26]. The general consensus amongst researchers is that there is no time scale but a stress scale that gives rise to the non-linear rate dependent behavior in dense particulate suspensions [51].

Historically, it has been reported that a typical dense (volume fraction, $\phi \gtrapprox 0.5$) non-Brownian suspension (particle sizes $> O(1\mu m)$) exhibits four distinct rate dependent regimes in its rheological flow curve. The suspension rheological behavior transitions from one regime to the other with increasing the imposed shear rate/stress. The suspension exhibits shear thinning (decreasing viscosity) at low shear rates followed by a Newtonian plateau (almost constant viscosity) at intermediate shear rates which transitions to shear thickening (ST, increasing viscosity) beyond a critical shear rate. ST can be gradual (*continuous* ST) or sudden (*discontinuous* ST). Finally, if we further increase the shear rate/stress to extremely high values, the suspension again undergoes another shear thinning transition [26], [34], [83], [131], [180]. This is depicted in Fig. 5.1.

Numerical models and theoretical studies to date are able to quantitatively capture the shear thinning at low shear rates [25], [82], [181] and the ST transition at intermediate shear rates [25], [45], [138], [166], [181], [182]. The initial shear thinning at low shear rates arises from the presence of repulsive double layer barrier (steric interactions) and the Van der Waals attractive forces (collectively known as DLVO interactions).

ST in suspensions has been known from the early 20^{th} century and has been an active topic of research since then. As a result, a plethora of explanations for this phenomenon can be found in the literature. Some of these explanations include sudden emergence of turbulence between the particles [129], order disorder transitions [130], [183], hydrodynamics induced particle clustering [45], [133], [134], [136]. But none of these explanations can quantitatively reproduce the viscosity jump observed in ST transitions [25], [119], [137]. For example, purely hydrodynamic interactions based simulations [44], [182], [184], [185] give a weak logarithmic shear thickening (weak CST). Even though this purely hydrodynamics based point of view is able to describe the rheology of moderately concentrated suspensions ($\phi < 45\%$) which exhibit a weak CST, it cannot predict the strong CST and CST to DST transition routinely observed in highly concentrated suspensions ($\phi > 50\%$) [25], [122], [136], [155], [157], [160]. The recently proposed lubricated to frictional transition of the particle contacts [25], [58], [173] and constraint based mechanisms [50], [181] have been proven to be very efficient in capturing the ST onset, CST to DST transition and the shear jamming in dense suspensions.

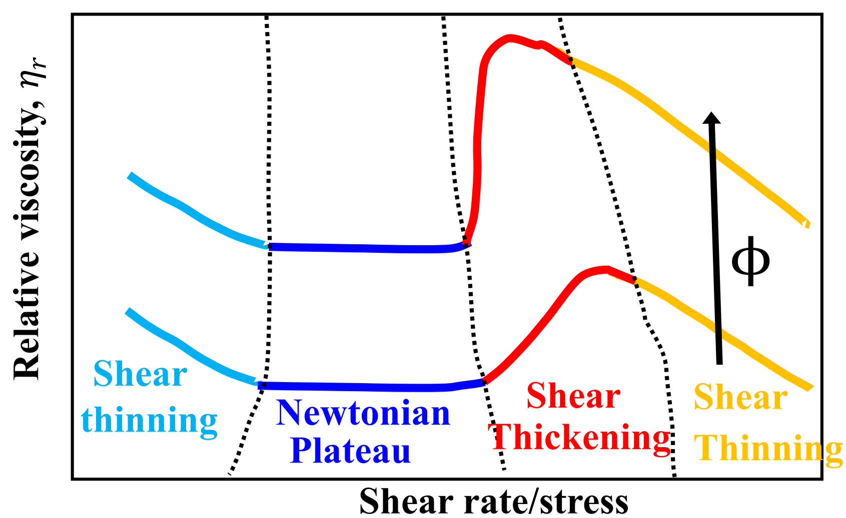

Figure 5.1. Schematic showing the typical rheological flow curve for dense non-Brownian suspensions. This rheological behavior is commonly observed for non-Brownian suspensions [26], [34], [83], [131].

Over the years, many explanations have been given for the second shear thinning at extremely high shear rates. These include an increase in the maximum packing density due to breakdown of spanning clusters [186], elastohydrodynamic effects [187], micro-scale non-Newtonian shear thinning effects of the interstitial solvent [188], inhomogeneous microstructure at high shear rates after the ST transition [153], surface tension effects and eventual sample ejection [155], adhesion-based constraint relaxation due to stress [181]. However, none of these explanations can make quantitative predictions for the second shear thinning regime. In addition, the reason for the intermediate Newtonian plateau still eludes researchers [26], [83]; limiting the existing numerical and theoretical frameworks from being able to quantitatively reproduce the entire unified flow curve. Thus, understanding the origins of the Newtonian plateau is a crucial piece of the puzzle that allows us to unify all the four rate dependent regimes and the corresponding transitions from one regime to the other.

To this end, we propose a unifying mechanism which quantitatively reproduces various regimes and transitions in the rheological flow curve of a dense non-Brownian suspension of smooth hard spheres. Since we are specifically interested in non-Brownian suspensions, we assume the Péclet number (Pe) to be $>> O(10^3)$ which typically corresponds to particle sizes $> O(1\ \mu m)$. Quantitative agreement between the discrete particle dynamics simulations based on the proposed mechanism and the experimental data bolsters the validity of the proposed model. Though bits and pieces of this puzzle have been studied in detail in the contexts of specific suspensions showing specific behaviors, e.g., initial shear thinning due to the presence of attractive forces [82] and ST due to lubricated to frictional contact transition [25], [142], [160], an effort to unify all the four disparate regimes has not been done. Furthermore, as mentioned, there is no explanation for the Newtonian plateau in the literature and the explanations given for the second shear thinning are not quantitative. We show that the inclusion of inter-particle interactions of non-DLVO origin is the key to explain and quantitatively capture the intermediate Newtonian plateau regime. Relaxation of constraint on the particle motion in the form of decreasing friction accurately predicts the second shear thinning; thus, unifying all the four disparate regimes observed in the flow curve of a non-Brownian dense suspension for the first time. Finally, we will also demonstrate the versatility of the proposed model to reproduce various other rheological flow curves containing one or more of the above mentioned four regimes.

5.2 Philosophy behind unification

In a Stokes flow regime, i.e., the particle Reynolds number, Re, is negligible, the particle motion in suspensions is governed by a simple balance between the hydrodynamic ($\mathbf{F}^H$)

and the sum of all other non-hydrodynamic interaction acting on the particle ($\sum_\alpha \mathbf{F}^\alpha$) [44]. Each of these interactions lead to corresponding stress scales in the system which scale as $\approx O(|\mathbf{F}^\alpha|/6\pi a^2)$, where a is the particle characteristic length scale. This scaling implicitly tells us that each interaction is competing with the hydrodynamic interactions which scale as $|\mathbf{F}^H| \approx 6\pi\eta_0 a^2\dot{\gamma}$, where $\dot{\gamma}$ is the imposed shear rate and η_0 is the suspending fluid viscosity. There is a general consensus that the competition between these stress scales gives rise to the rate dependent rheological behavior in dense suspensions [51]. Previous experiments [83] and computations [82] show that the attractive and repulsive forces of DLVO origin gives rise to the first shear thinning at low shear rates suspensions and hence are the choice of interactions for capturing the first shear thinning regime. The exact expressions for DLVO interactions are readily available from theoretical analyses and previous experimental data [83], [189].

We hypothesize that the presence of non-DLVO forces, which are non-contact inter-particle interactions and become dominant when the particles are extremely close but not touching each other, delay the ST transition to higher shear rates after the initial shear thinning. This happens because non-DLVO forces introduce an additional stress scale which needs to be overcome before the activation of the constraint mechanism (explained below) required for ST transition; and hence, gives rise to the intermediate Newtonian plateau. The presence of the non-DLVO forces has been confirmed by experimental measurements [190] and has been analyzed theoretically as well [191]–[193]. The non-DLVO forces can arise due to the presence of charge layers on the particle surface or due to hydration effects [190]. As will be shown from the simulation results, it is the magnitude of the non-DLVO forces which determines the range of shear rate/stress where the Newtonian plateau is observed. Absence of non-DLVO interactions lead to disappearance of the intermediate Newtonian plateau. The quantitative matching with the experimental data can only be obtained by accounting for the non-DLVO forces, thus, corroborating the validity of this hypothesis.

Any microscopic mechanism that introduces constraints on particle motion can result in the shear thickening transition, while relaxation of such a constraint can qualitatively reproduce the shear thinning. Lubrication interactions between individual asperities on particle surfaces can lead to *continuous* (CST) as well as *discontinuous* (DST) shear thickening

[166]. Constraint formation and relaxation by stress e.g., adhesion, can qualitatively reproduce the shear thickening and shear thinning transitions, respectively [181]. However, to obtain a quantitative matching with experiments, we must know the exact expressions from experimental measurements for these constraint interactions. Hard particle-particle contacts resulting in friction is a constraining mechanism which has been investigated thoroughly and hence, exact expressions from experimental measurements are available. So, without the loss of generality, friction is the choice of constraint mechanism for this study to quantitatively reproduce the CST, DST and CST to DST transition with increasing ϕ, and second shear thinning in the flow curve of a dense non-Brownian suspensions.

It has been shown that a sudden activation of friction between the particles as they come into dry contacts owing to the irregularities on particle surfaces result in ST transition (CST and DST depending on the suspensions volume fraction, ϕ) [4], [25]. The same has also been validated by experiments [58], [84]. This is analogous to activating a constraint on the relative motion between the particles. On the other hand, a coefficient of friction μ decreasing with the normal load between the particles is analogous to relaxation of the constraint and hence would result in shear thinning [3], [52]. Constraint mechanisms based on friction have been proven to be very efficacious in reproducing various shear stress-shear rate curves that are observed experimentally for dense suspensions, CST to DST transition beyond a critical volume fraction and most importantly jamming [5], [117]. Furthermore, there are many experimental studies that validate the role of friction [52], [58], [84]. Hence, friction is the constraining mechanism utilized here. We would like to emphasize that, owing to the additive nature of the non-hydrodynamic forces, any other constraining mechanism can be readily used, given expressions for the interactions are known. So, the proposed unifying mechanism utilizes the well known Stribeck curve for inter-particle friction along with hydrodynamic, DLVO (attractive, repulsive forces), non-DLVO and contact forces to unify disparate regimes in the flow curve of non-Brownian dense suspensions.

5.2.1 Stribeck curve for friction

The Stribeck curve for friction has been used widely in the literature to explain the sliding phenomenon occurring in lubricated contacts [194]. In a typical Stribeck curve, the

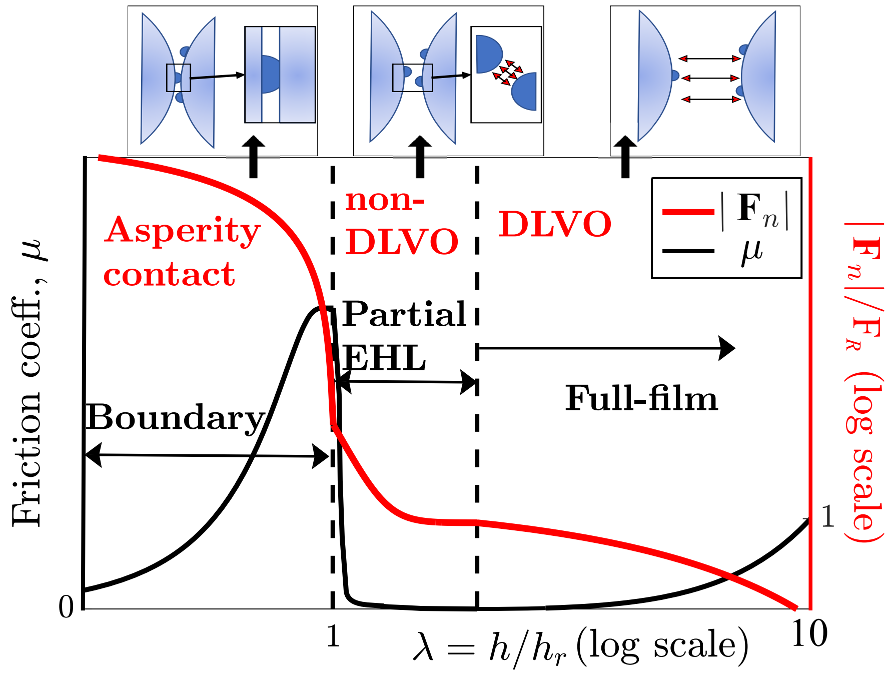

Figure 5.2. Schematic showing the coefficient of friction, μ (thin black line), and the dimensionless normal force magnitude, $|\boldsymbol{F}_n|$ (thick red line), between a close particle pair as a function of dimensionless inter-particle gap, $\lambda = h/h_r$. Boundary, partial elastohydrodynamic (EHL) and full film lubrication regimes in the Stribeck curve are demarcated based on the value of λ. Similarly, dominant inter-particle interactions in each of these regimes are also shown in red font. The insets at the top show the various regimes in terms of separation between two close particles. The arrows in these insets are shown to qualitatively indicate the size of the inter-particle gap and the range of the dominant inter-particle interaction with respect to the roughness and the particle size.

coefficient of friction, μ, is plotted as a function of the Sommerfeld number, $S = \eta V/W$, where η is the lubricant dynamic viscosity, V is the relative sliding velocity between contacting surfaces and W is the normal load [194]. However, for rough surfaces, the surface asperity height dictates the full-film to boundary lubrication contact transition (see [195] and the references therein). Particle surface roughness is one of the important parameters governing the rheology of dense suspensions as even the most idealized smooth particles have surface irregularities of $O(0.001 - 0.01)$ times the particle radii [52]. These surface asperities not only lead to inter-particle contacts, but also dictate the friction in interesting ways. Hence, efforts on investigating the influence of particle roughness on dense suspension rheology have gained much traction in the recent years [4], [5], [7], [166].

In the case of particles coming into contact, the average roughness height results in an additional secondary length scale (along with the primary length scale which is particle size, a) in the system. While the particle size distribution governs the hydrodynamic interactions, the secondary length scale introduces geometrical and inter-particle force constraints [4]. So, we define λ as the dimensionless gap between the particles, i.e., $\lambda = h/h_r$. Here, h is the inter-particle gap, and h_r is the average roughness height (defined below). High λ ($\lambda > 2$) signifies well separated particles without a dry contact and the friction force is mostly due to lubrication interactions (full-film contact) [194]. The effect of increasing the shear rate/stress in the suspension is to reduce the average inter-particle gap thus bringing particles close to each other. As particles come closer to each other, λ decreases, and partial-elastohydrodynamic lubrication (partial-EHL) results in a sudden rise in μ [196], [197]. In this regime ($1 < \lambda < 2$), partial dry contact between the particles is expected to occur. In addition, as the inter-particle gap becomes comparable to mean particle surface roughness size, repulsive forces of non-DLVO origin (arising due to hydration or stagnant charge layer on the particle surface) are expected to be present with magnitudes a few orders higher than the repulsive forces of DLVO origin, viz, arising from the double layer potential [198]–[200].

As λ decreases further ($\lambda < 1$), the contact enters boundary lubrication, i.e., full dry contact between the particles. In this regime, the coefficient of friction has a high value if the contact between the particles is elastic which is true if the asperity deformation is smaller than a threshold value δ_c [60]. If λ decreases even further, the contact enters a plastic regime which results in a significant reduction in the coefficient of friction. This reduction in the friction coefficient with plastic deformation of asperities requires tremendous normal load which happens only at extremely high shear rate/stress values. As a result, we get the second shear thinning regime. These phenomena are depicted in Fig. 5.2.

5.2.2 Summary of relevant Interactions

The transitions in the flow curves are governed by the competition between various stress scales in the system for non-Brownian suspensions. In the present study, we have four such stress scales that determine the various transitions:

1. In the regime of attractive and repulsive forces when the particles are not touching and are separated, i.e., $\lambda > 2$ (full film regime in the Stribeck curve). In this regime, the friction is due to the tangential lubrication forces which is implicit in our hydrodynamic force modeling. Hence, Coulomb's friction law is not applicable.

2. The non-DLVO force is a noncontact force, and hence does not lead to constraints on sliding motion. This force is present only when the particles are not touching but are very close to each other, i.e., $1 < \lambda < 2$ (EHL regime on the Stribeck curve).

3. The inter-particle contact and a high coefficient of friction when the particles just come into contact ($0.95 < \lambda \leq 1$) lead to the shear thickening transition.

4. The decrease in the coefficient of friction as the asperities deform more and enter a plastic region ($\lambda \leq 0.95$) explains the second shear thinning regime. It should be noted that the second shear thinning was also observed for non-attractive & non-adhesive particles [180] which cannot be explained by stress induced relaxation of constraints.

We briefly elaborate on the methods and simulation framework used in this study in the following section before presenting the main results.

5.3 Simulation methodology

We simulate the shear flow of neutrally buoyant inertia-less bi-spherical particles with radius ratio 1.4 and equal volume fractions in a cubical domain of size $L = 15a$. Here a is the radius of the smaller particle. For this particular particle size distribution, the dry close packing fraction (ϕ_d) is 0.66 [5]. We use ϕ_d to normalize the volume fraction (ϕ) values in this study for direct comparison with experiments. Simulation results do not change much for a bigger domain size $L = 20a$. The suspending fluid is Newtonian with viscosity, η_0. The imposed shear rate is $\dot{\gamma}$ with Lees-Edwards periodic boundary conditions on all the sides. Also, the Péclet number, $\mathrm{Pe} > O(10^3)$ [26], [34], [83], so, the flow is in the non-Brownian regime.

We use Ball-Melrose approximation [49] to calculate the hydrodynamic interactions, $\boldsymbol{F}^H$, repulsive force of electrostatic origin, $\boldsymbol{F}^R$, Van der Waals attractive force, $\boldsymbol{F}^A$, repulsive forces

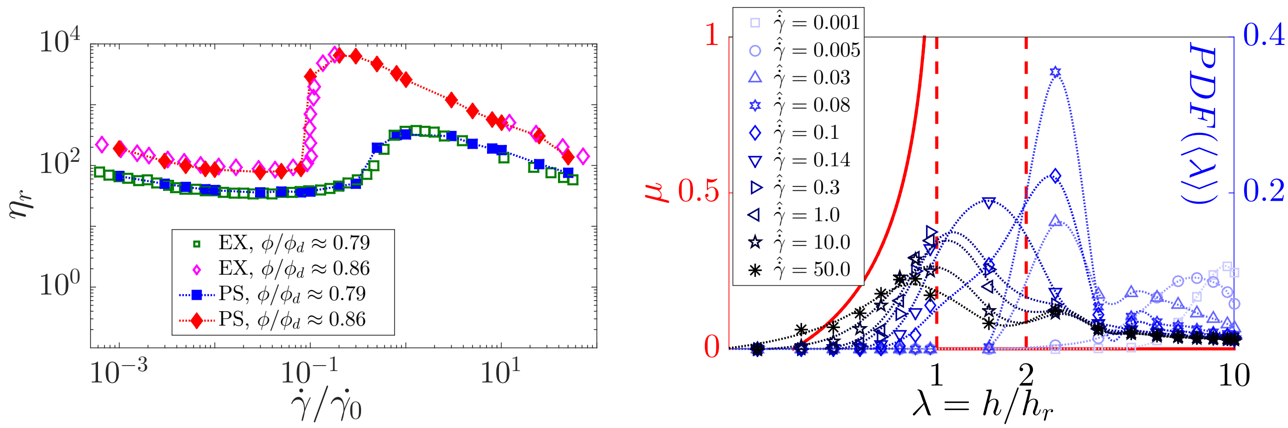

(a) **(b)**

Figure 5.3. a) Relative viscosity as a function of dimensionless shear rate ($\dot{\gamma}/\dot{\gamma}_0$) for two different volume fractions (PS = present simulations) compared against experiments (EX = Experiments, $\dot{\gamma}_0 = 200s^{-1}$ for experimental data) of Chatté *et al.*, (2018) [83]. The volume fractions are scaled with dry close packing fraction ϕ_d for direct comparison. $\phi_d = 0.66$ for the simulations. b) Probability distribution function (PDF, dotted lines) of the average dimensionless inter-particle gap ($\langle\lambda\rangle$) with increasing $\hat{\dot{\gamma}} = \dot{\gamma}/\dot{\gamma}_0$ (legends) along with the friction coefficient (solid lines) for *log decay friction* model. Dotted lines are spline fits to guide the eye. Dashed lines demarcate the transition between interaction ranges as explained in fig.5.2.

of non-DLVO origin, $\boldsymbol{F}^{ND}$, and contact interactions, $\boldsymbol{F}^{C}$. The repulsive forces ($\boldsymbol{F}^{R}$ and $\boldsymbol{F}^{ND}$) act normally towards the particle center. $\boldsymbol{F}^{R}$ decays with inter-particle surface separation h over a Debye length κ^{-1} as $|\boldsymbol{F}^{R}| = F_R\exp(-\kappa(h-2h_r))$ for $h > 2h_r$ and $|\boldsymbol{F}^{R}| = F_R$ for $h \leq 2h_r$. The non-DLVO repulsive forces are dominant when the inter-particle gap is comparable to particle surface roughness size [201], [202]. So, we use a non-DLVO repulsive force for $h_r \leq h \leq 2h_r$ with an exponentially decaying form $|\boldsymbol{F}^{ND}| = F_{ND}\exp(-A(h-h_r)/a)$ for $h \geq h_r$ [190] and $|\boldsymbol{F}^{ND}| = F_{ND}$ for $h < h_r$. We choose $A = 1000$ for this study. Similarly, the attractive force of Van der Waals origin also acts normally but in the opposite direction to the repulsive force and is modelled as $|\boldsymbol{F}^{A}| = F_A/\left((h-h_r)^2 + 0.01\right)$. 0.01 is used to prevent the divergence in $\mathbf{F}^{A}$ when $h \to h_r$ [82]. We use the DLVO repulsive force as the characteristic force scale to non-dimensionalize the governing forces. So, the characteristic stress scale is given by $\sigma_0 = F_R/6\pi a^2$ (and rate scale, $\dot{\gamma}_0 = \sigma_0/\eta_0$), related to the transition

Table 5.1. Simulation parameters

ϕ	$\dot{\gamma}/\dot{\gamma}_0$	κ^{-1}	F_A	h_r	F_{ND}
0.52 & 0.57	$0.001 - 50.0$	$0.04a$	$10^{-3}F_R$	$0.01a$	$10F_R$

from lubricated contacts (hydrodynamic) where particles are separated to direct contact between particles.

We model the surface roughness as a hemispherical bump of size, h_r, on the base sphere as shown in Fig. 5.2. The contact interactions are modeled using the Hertz law for the normal contact force ($|\boldsymbol{F}_n^C| = k_n(\delta/\delta_c)^{3/2}$) and a linear spring for the tangential contact force ($\boldsymbol{F}_t^C = k_t\boldsymbol{\xi}_t$), respectively [3]. Here, $\delta = h_r - h$ is the asperity deformation, δ_c is the threshold for elastic to plastic transition and $\boldsymbol{\xi}_t$ is the tangential spring stretch. The contact activates only when $h \leq h_r$. Contact interactions obey the Coulomb's friction law, $|\boldsymbol{F}_t^C| \leq \mu \boldsymbol{F}_n^C$. The details and validation of the algorithm are presented in chapters 2, 3, and chapter 4. Fig. 5.2 depicts how $|\boldsymbol{F}_n| = |\mathbf{F}^R| + |\mathbf{F}^{ND}| - |\mathbf{F}^A| + |\mathbf{F}_n^C|$ varies with λ. It is well known that μ is not constant and depends on the normal load $|\boldsymbol{F}_n^C|$ [58], [60], [83]. Since $|\boldsymbol{F}_n^C| \propto \delta^{3/2}$ following the Hertz law, μ can also be described as a function of the dimensionless inter-particle gap, $\lambda = h/h_r$, (since $\delta = 1 - \lambda h_r$). We calculate the bulk stress $\boldsymbol{\sigma}$ in the system by volume averaging the stresslets due to all the interactions [3]–[5]. Rheological properties can be quantified from the bulk stress, e.g., the relative viscosity of the suspension, $\eta_r = \sigma_{12}/(\eta_0\dot{\gamma})$, second normal stress difference, $N_2 = \sigma_{22} - \sigma_{33}$.Values of simulation parameters used (unless mentioned otherwise) are summarized in Table 5.1.

Friction coefficient. We use the dimensionless gap size dependent (($\lambda = h/h_r$)) Stribeck curve to model μ [197]. For $\lambda > 1$, the reduction in μ with decreasing λ is captured in lubrication interactions [138] and hence there is no need to use Coulombs friction law explicitly. We approximate μ in the partial-EHL regime by a step function [138] for simplicity. For $\lambda \leq 1$, asperities come into contact resulting in a sudden rise in μ. μ has a high value if the contact is elastic, i.e., $\delta \leq \delta_c$, where δ is the asperity deformation defined as $\delta = |h - h_r|$ [52], [60]. If the asperities deform further such that, $\delta > \delta_c$, the contacts transition into plastic regime resulting in a steep decrease in μ. Experimental measurements [83] have shown that the friction coefficient decreases with the normal load as $\mu = -a * \ln(|\boldsymbol{F}_n^C|) + b$ or in terms of

λ (since $|\mathbf{F}_n^C| \propto \delta^{3/2}$ by Hertz law and $\delta = h_r(1-\lambda)$) we can say, $\mu = -a\ln((1-\lambda)) + b$ for $0 < \lambda < 1$ where a, b, a and b are constants. We choose $a = 1/2$ and $b = -0.2$ in this study. We call this friction model *log decay friction.* Data for additional friction models along with results for varying a and b in the *log decay model* are shown in Sec. 5.5.

Thus, all the expressions used for various forces have a solid experimental backing. One way to distinguish them experimentally is to measure them carefully in terms of the inter-particle gaps as modeled in the paper. We have used the expressions from the experimental measurements [83], to make a quantitative comparison with their results. However, the freedom to choose the values of various input parameters such as the relative magnitudes of the forces, the Debye length, parameters a and b in the friction law and the roughness size based on the system enables the model to capture various regimes in the flow diagram. For the systems which do not show a Newtonian plateau, one only needs to switch off the non-DLVO forces or make their magnitude 0. This allows us to unify various flow regimes observed for non-Brownian suspensions as demonstrated in the following sections.

5.4 Results and discussion

We demonstrate the accuracy of the proposed model by direct comparison of the calculated suspension relative viscosity with experimental values for polyvinyl chloride particles suspended in a Newtonian fluid medium [83] in Fig. 5.3a. Chatté *et al.* (2018) [83] used a system that has previously been characterized to take advantage of the data from the literature. They use a suspension of polyvinyl chloride (PVC) particles suspended in a Newtonian fluid (1,2-cyclohexane dicarboxylic acid diisononyl ester). The classical studies by Hoffman [34], [131] also used PVC particles. In addition, PVC particles are known to transition from a lubricated-to-frictional contact regime [58]. They use two suspension with a lognormal (D1) and a trimodal with lognormal peaks (D2). The sizes of the particles are chosen in such a way that the Brownian effects are negligible. Hence, these suspensions are non-Brownian.

It has been shown that a poly-disperse system with a log-normal distribution of the particle sizes can be quantitatively modeled as a bi-disperse system in a way such that both of these suspension have similar rheological property values [149]. Hence, we are particularly interested in the D1 suspension as we can use a simple bi-disperse system and still reproduce

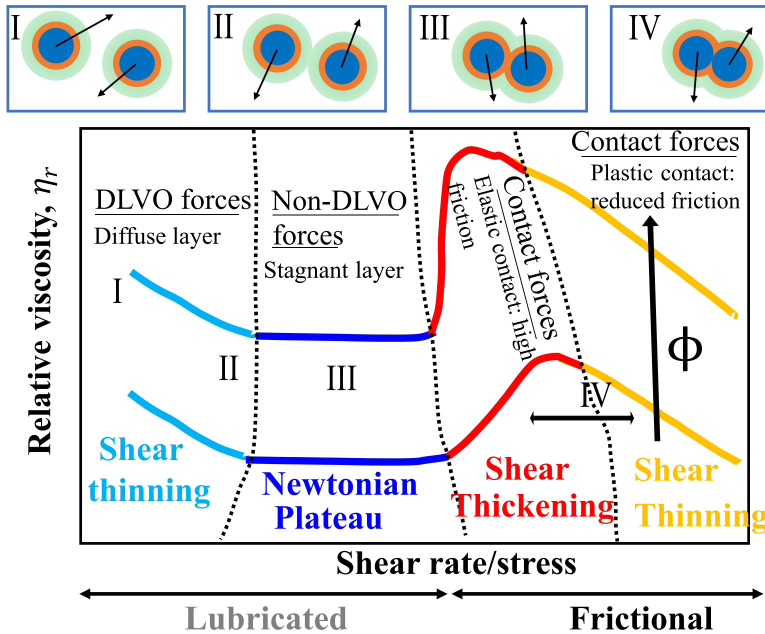

Figure 5.4. Scheme of the physics involved in the shear thinning ($I - II$) - Newtonian plateau (III) - shear thickening - shear thinning (IV) regimes in the rheological behavior of a typical dense non-Brownian suspension. The insets at the top show the approximate inter-particle gaps in regimes $I-IV$. In these insets, the outermost circle represents the range of DLVO forces, the inner orange circle represents the range in which non-DLVO forces are dominant and the innermost circle represents the particles. Thus, with increasing shear rate we observe different regimes depending on which forces are dominant in the suspension on average as depicted by the overlaps of different force zones in the insets.

the same rheology as done in the main text. However, because these two systems have different random packing fractions (ϕ_d), in order to compare the viscosities, we need to normalize the volume fraction values for these systems by ϕ_d [51]. The random packing fraction for D1 suspension is $\approx$ 69% while the random packing fraction for the bi-disperse system used for simulations is $\approx$ 67%. Hence, a close quantitative agreement between the experiments and simulations is expected if we accurately model the underlying physics. Also note that to access such a wide range of shear rate values and the different regimes in the flow curve of these suspensions, they use a combination of rotational and special capillary rheometers as simple rotational rheometers cannot access regions of very high normal stress

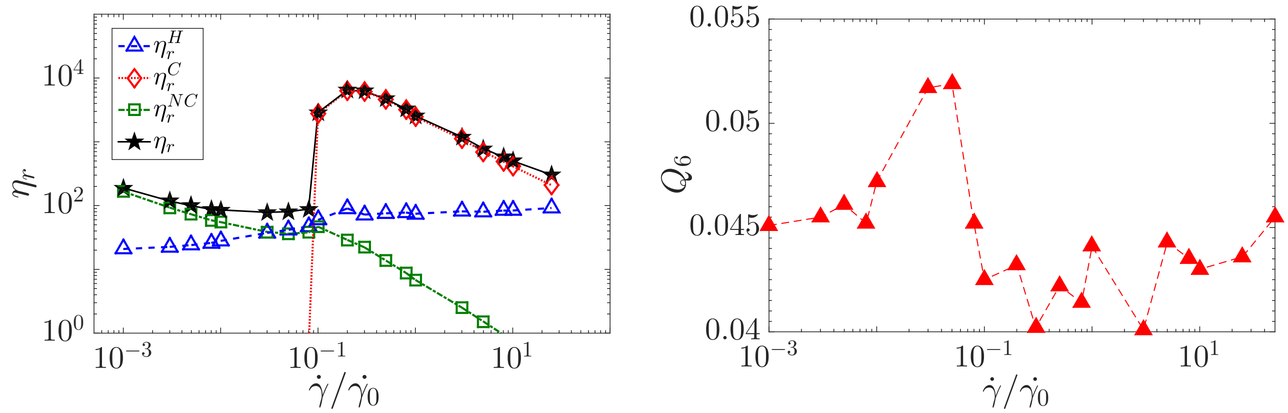

(a) **(b)**

Figure 5.5. a) Contributions from hydrodynamic (η_r^H), non-contact (DLVO and non-DLVO, η_r^{NC}) and contact (η_r^C) interaction to the total relative viscosity of the suspension for $\phi/\phi_d \approx 0.86$. The trends in the respective contribution follow from Fig. 5.4. Lines are for guiding the eye. b) The variation in the order metric Q_6 with dimensionless shear rate.

differences [155], [187]. These regions correspond to high viscosity values after the shear thickening transition and the second shear thinning regime.

Fig. 5.3a shows that the proposed model does an excellent job in quantitatively capturing the rate dependent rheological properties in low, intermediate and high shear rate limits, respectively. This shows that the hypothesis that accounting for non-DLVO interactions recovers the initial transition from shear thinning to the intermediate Newtonian regime. A universal friction law based on the "Stribeck curve" accurately recovers the onset of ST and then the second shear thinning that is typical to dense non-Brownian suspensions is indeed true.

We plot the probability distribution (PDF) of the ensemble average of the dimensionless inter-particle gap $\langle\lambda\rangle$ at different shear rate values corresponding to different regimes in the rheological state diagram (Fig. 5.3b) to explain the observed shear rate dependent rheological behavior. With increasing shear rate values, the peak and mean of the PDF of $\langle\lambda\rangle$ shift to the left on the Stribeck curve. This determines the various transitions in the rheological state diagram. At low shear rates, the particles are prevented from coming into direct contacts due to the combined effect of the repulsive and attractive forces of the DLVO origin. This is analogous to having particles with bigger radii. As we increase the shear rate, the particles are pushed closer resulting in the reduction of this apparent bigger radius. As a result, the effective volume fraction of the suspension decreases with increasing shear rate in this regime which results in the observed shear thinning. In the intermediate shear rate regime, the stress is high enough to overcome the DLVO repulsive barrier between the particles so that the particles are on average separated by a distance $\approx O(h_r)$. But the stress is not high enough to overcome the short range non-DLVO repulsion which is an order of magnitude higher than the DLVO barrier. This leads to the Newtonian plateau in the relative viscosity. This plateau in the η_r at intermediate $\dot{\gamma}$ values is not present if we do not consider short range repulsive forces of non-DLVO origins [82] as shown in Sec. 5.5.2. This indicates the governing role of non-DLVO forces in dense non-Brownian suspensions.

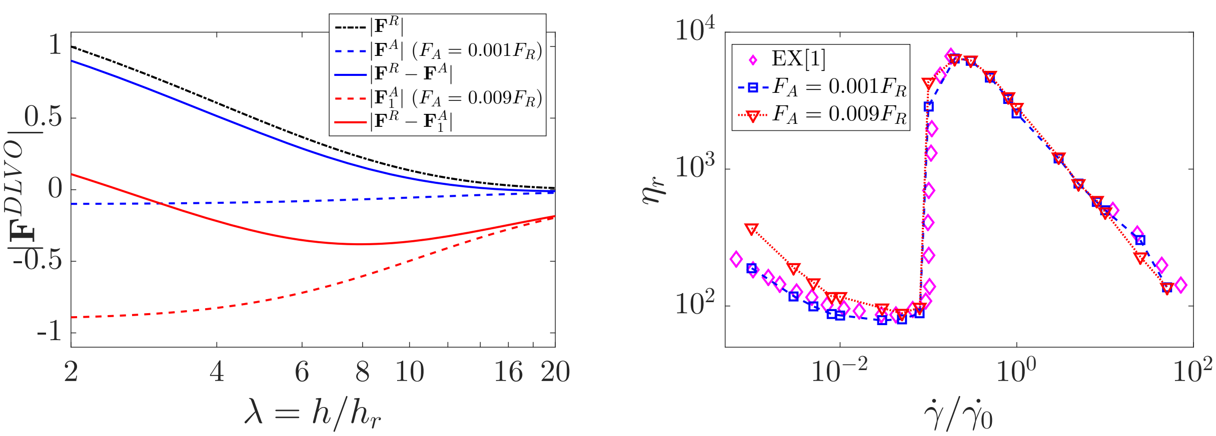

(a) **(b)**

Figure 5.6. a) DLVO force (repulsion & attraction) profiles as a function of dimensionless gap for two different attractive force magnitudes, b) Effect of varying the attractive force magnitude on the first shear thinning regime.

If we increase the shear rate further, the stress in the suspension becomes high enough so that the repulsive barrier due to the DLVO and non-DLVO forces breaks and the particles come into contacts due to the touching of asperities on their surfaces. The contact remains in the elastic region resulting in a high μ between the particles and constraints relative sliding between the particles. This leads to a jump in the suspension viscosity. The shear thickening transition takes place above a critical shear rate value ($\dot{\gamma}_c$, e.g., $\dot{\gamma}_c/\dot{\gamma}_0$ for $\phi/\phi_{RCP} \approx$ 0.86 is 0.1). In the shear thickening transition regime, the viscosity increases gradually (*continuous shear thickening*) at lower volume fractions while it undergoes a sudden increase (*discontinuous shear thickening*) at higher volume fractions. As we increase the shear rate further, the asperities are plastically deformed ($\delta > \delta_c$). As a result the coefficient of friction between the particles decreases significantly which is analogous to relaxation of the constraint on the relative sliding motion between the particles. This gives rise to the second shear thinning transition at high shear rates. The consequences of this shift in the PDF of $\langle\lambda\rangle$ to the left with increasing $\dot{\gamma}$ on the transitions in dominant interaction between the particles and the suspension rheology are depicted pictorially in Fig. 5.4.

The shift in the PDF of $\langle\lambda\rangle$ manifests itself in determining the relative magnitudes of different contributions from hydrodynamic (η_r^H), non-contact (η_r^{NC}, DLVO and non-DLVO) and contact (η_r^C) interaction to the total relative viscosity (η_r) in Fig. 5.5a. As we increase the shear rate, η_r^H increases gradually. At low and intermediate shear rate values, η_r^C is 0 as the repulsive barrier prevents direct contacts. In this regime, η_r^{NC} decreases with increasing the shear rate which explains the first shear thinning behavior. But beyond $\dot{\gamma}_c$ the particles come into direct contacts thus resulting in the sudden jump in η_r due to high η_r^C. This is also known as lubricated-frictional transition which has been well studied [144]. In the high shear rate regime beyond $\dot{\gamma}_c$, the contribution from the contact interactions to the bulk suspension stress is dominant and hence determines the suspension viscosity. Since μ decreases with increasing the shear rate due to lowering of λ, η_r^C and as a consequence η_r decreases with an increase in the shear rate.

The neutron scattering [136] and rheo-confocal [203] measurements for Brownian suspensions (Pe $< O(10^5)$) hint towards the role of ordering in the colloids in the initial shear thinning. Since we use a bidisperse suspension for preventing any clustering and ordering in the suspension, we expect the particles to remain homogeneously distributed. Still, to investigate if there is any ordering in the suspensions, we evaluate the ordering metric Q_6 [204] to quantify the ordering in the suspensions. Q_6 can be calculated as follow:

$$Q_6 = \sqrt{\frac{4\pi}{13} \sum_{m=-6}^{m=6} \langle Y_{6m} \rangle^2}. \tag{5.1}$$

Here $Y_{nm}(\theta, \phi)$ are the spherical harmonics which depend on the polar (θ) and the azimuthal (ϕ) angles which together give us the orientation of the center-to-center vector for the neighbouring particle pairs. $\langle Y_{6m} \rangle$ is the average of $Y_{6m}(\theta, \phi)$ over all the neighbouring particles in the suspension. Q_6 quantifies the ordering in the suspension system. $Q_6 = 0$ indicates a completely homogeneous or disordered system. The maximum value that Q_6 can have is ≈ 0.575. This maximum values is reached for a face-centered cubic structure.

We plot the order metric Q_6 in fig.5.5b. A small value of Q_6 signifies absence of ordering in the suspension, while a large value (> 0.5) indicates a strong ordering. We find that Q_6 values are negligible which tells us the absence of any ordering. However, we observe a gradual rise and a spike in Q_6 for the lower shear rates just before the ST transition (the end of Newtonian plateau). Q_6 drops down significantly once the suspension undergoes ST transition ($\dot{\gamma}/\dot{\gamma}_0 \approx 0.1$). These calculations insinuate that the ordering in the initial thinning regime for monodisperese suspensions might be the consequence of DLVO and non-DLVO forces preventing the particles from coming into hard contacts as the peak in Q_6 coincides with the range of shear rates when DLVO and non-DLVO interactions are dominant.

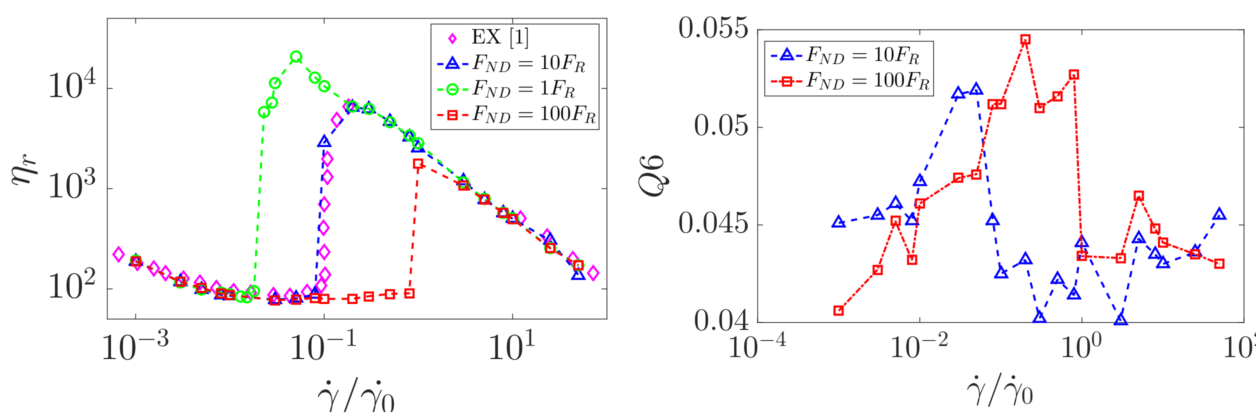

(a) **(b)**

Figure 5.7. a) Effect of changing the magnitude of the non-DLVO force. The Newtonian plateau disappears in the absence of non-DLVO forces. Thus, we can reproduce thinning-thickening-thinning using the proposed model as well. This is useful for suspensions which do not have significant Newtonian plateau e.g., silica particles [136]. b) The order metric Q_6 for two different non-DLVO force magnitude. The gradual increase in Q_6 in the first shear thinning regime and peak in the Newtonian regime hint towards the link between ordering and the initial shear thinning - Newtonian plateau [136].

5.5 Predicting other flow curves

We have used the expressions for DLVO repulsive force and the coefficient of friction from the experimental measurements by Chatté *et al.* (2018) [83] to make a quantitative comparison with their results and validate the model. However, the freedom to choose the values of various input parameters such as the relative magnitudes of the forces, the Debye length, the friction law, and the roughness size based on the system one is trying to model enables the model to capture various regimes and transitions in the flow diagram. Increasing the magnitude of attractive forces or increasing the Debye length with results in a steeper initial thinning [82], [205] (Sec. 5.5.1). Decreasing (increasing) the magnitude of non-DLVO forces will result in a narrower (wider) Newtonian plateau (Sec. 5.5.2). For the systems which do not show the second shear thinning, one only needs to make the coefficient of friction a constant which gives us a constant viscosity in the shear thickened regime [4] (Sec. 5.5.3). Though simulation results show that only constraining the sliding motion between the particles gives a satisfactory agreement with experimental data for smooth particle suspensions [52], our model can also account for roughness effects ((Sec. 5.5.4)) both geometrically (by varying the roughness size [4]) and physically (by constraining the rolling and twisting motion [107]). Other constraints on the particle motion such as rolling and twisting friction become important only for rough particles [173]. Incorporating rolling and twisting friction in the current model is straight-forward but not done as we are dealing with smooth particle suspensions. This makes the proposed model very general and applicable to a wide variety of systems.

In this section, we present the simulation results obtained by varying various controlling parameters in the proposed model. The key parameters in the model are: 1) DLVO repulsive force scale, F_R, 2) DLVO attractive force scale, F_A, 3) non-DLVO short range repulsive force scale, F_{ND} and, 4) the exact dependence of the coefficient of friction on the contact normal load $|\mathbf{F}_c^N|$ or on the asperity deformation δ. Each of these parameters determine the suspension behavior and the critical transition shear rates for the four regimes described.

5.5.1 Magnitude of F_A controls the initial shear thinning

We first plot the DLVO force profiles if we increase the magnitude of the attractive forces, F_A in the DLVO interactions. These are presented in Fig. 5.6a. For these simulations, we keep the other parameters fixed as given in the Table I in the main text. We use the same friction model as in the main text. We only vary the magnitude of the attractive forces, F_A. Fig. 5.6b shows the effect of changing the magnitude of the attractive forces in the DLVO interactions. As expected, with increasing the magnitude of the attractive forces, we observe that the slope of the shear thinning curve at low shear rate values increases [82]. With the increase in F_A, the λ below which the net DLVO force is repulsive, decreases. Note that, the critical shear rate for shear thickening transition does not change with changing F_A. This is because, before the lubricated-to-frictional transition can take place, the particles still need to overcome the non-DLVO repulsive forces. So, in this model, the magnitude of the non-DLVO forces determines the critical shear rate for the onset of shear thickening transition. The Newtonian plateau disappears in the absence of non-DLVO forces. Thus, we can reproduce thinning-thickening-thinning using the proposed model as well. Changing the magnitude of the non-DLVO forces does not change the viscosity jump magnitude and the viscosities in the second shear thinning regime. This is because both of these depend on the friction model used.

5.5.2 F_{ND} controls the presence, absence and the range of the intermediate Newtonian plateau

Fig. 5.7a shows the effect of varying the magnitude of the non-DLVO forces on the flow curve of dense non-Brownian suspensions. For these simulations, we keep the other parameters fixed as given in the Table 5.1 and only change F_{ND}. We use the same friction model as before. We only vary the magnitude of the non-DLVO forces. The range of shear rates over which Newtonian plateau is observed increases with an increase in the magnitude of the non-DLVO forces. This is because non-DLVO forces are essentially non-contact forces. So, as their magnitude increases, the lubricated-to-frictional transition in the particle contacts is pushed to higher critical shear rates. Changing the magnitude of the non-DLVO forces,

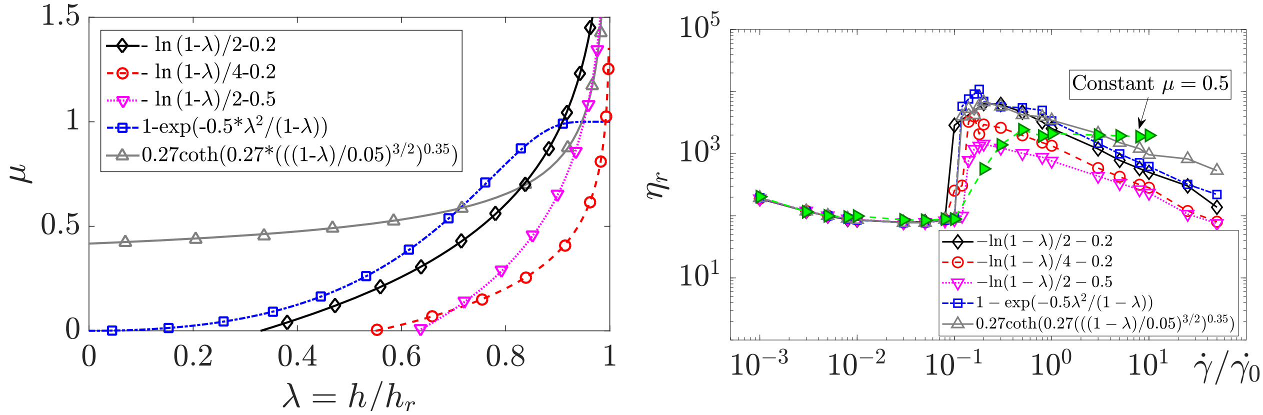

(a) **(b)**

Figure 5.8. a) Different friction laws tested for the sensitivity analysis of the model to μ. $-aln((1-\lambda)+b$ is the *log decay model* derived from the experimental measurements from ref. [83]. The black solid line ($a = 1/2, b = -0.2$), red dashed line ($a = 1/4, b = -0.2$) and the dotted pink line (($a = 1/2, b = -0.5$)) show how μ for *log decay model* changes with dimensionless inter-particle gap $\lambda = h/h_r = 1 + \delta/h_r$. Dash-dotted blue line shows a hypothetical exponentially decaying μ. Finally, the grey solid line shows the Brizmer [60] model for μ which has been previously used in the literature to explain the shear thinning in dense non-Brownian suspensions [52]. b) Variation of viscosity for different friction models. If we use a constant μ instead, we will not observe the second shear thinning regime. The data shows that the friction model determines the viscosity jump during the shear thickening transition and the slope in the second shear thinning regime. The flow curve for suspensions which do not exhibit the second shear thinning can be obtained by choosing a constant coefficient of friction.

however, does not change the slope of the second shear thinning curve at high shear rates as it depends on the friction model. This investigation shows that the presence/absence and the range of the Newtonian plateau is determined by the presence/absence and the magnitude of the non-DLVO interactions, respectively. More experiments measuring the non-DLVO forces between particles made of different materials and their corresponding Newtonian plateau range can shed more light on the role of the non-DLVO interactions.

The effect of changing the magnitude of non-DLVO interactions on the ordering parameter Q_6 is presented in Fig 5.7b. As we use a bi-disperse system, we observe only a weak ordering in the suspensions. Previous studies in the colloidal regime [136], [203], have attributed the shear thinning at low shear rates to the ordering of particles in layers in the colloids. In our simulations for non-Brownian systems, there is no evidence of any significant ordering. Hence, the initial shear thinning regime observed is due to the apparent lowering of the volume fraction as the inter-particle gaps between the particles reduce as we increase the shear rate. The particles are pushed closer as the hydrodynamic force dominates over the non-contact DLVO forces with an increase in the shear rate. We, however, see a gradual rise in Q_6 until it reaches a peak just before the shear thickening transition as shown in Fig. 5.7b. The peak is sustained over the range for which we observe the Newtonian plateau. This hints that the ordering and the flattening of the viscosity just before the shear thickening might be the outcomes of the non-contact interactions between the particles. Experiments can shed more light on this link.

5.5.3 Governing role of friction in the ST transition and rheology at high shear rates

The second shear thinning after the shear thickening transition at high shear rates the result of the decreasing coefficient of friction in the boundary contact regime of the Stribeck curve. Hence, the viscosity jump across the shear thickening transition and the slope of the second shear thickening regime is determined by the friction law used in the model. This is depicted in Fig. 5.8b for friction laws shown in Fig. 5.8a. A higher value of friction leads to a larger viscosity. Hence, the Brizmer model has a larger viscosity in the second shear thinning regime than other friction laws. A friction law with less steep decrease with particle deformation (e.g., Brizmer law) results in a less steep second shear thinning regime. A constant μ will result in the disappearance of the second shear regime [4] (see Fig. 5.8b).

There is an ongoing debate in the community regarding the presence of the second shear thinning regime as it is not observed in all the systems. We would like to point out that the second shear thinning has been observed to be prominent for high volume fractions and has been seen to be present at very high shear rates ($> (10^4 - 10^5)s^{-1}$). Hence, to observe this regime, one would need to be able to shear the suspension at such high shear rates. Most of the experimental studies on ST suspensions do not explore such a high shear rate regime as they stop their investigation right after the suspension undergoes ST [122], [136], [157], [159], [160], [162], [187], [206]. But those which do, have reported the second shear

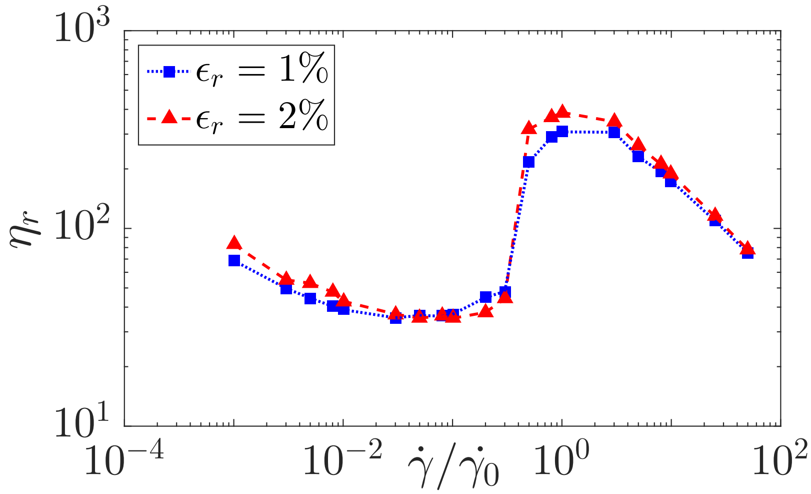

Figure 5.9. Effect of varying particle surface roughness height, ϵ_r on the suspension viscosity. Increasing surface roughness results in a stronger initial shear thinning and increases the viscosity during and beyond the ST transition. Note that the ST transition is governed by the direct contact between the particles which is due to the breaking of the lubrication film due to the particle asperities. Here all the other parameters are the same as given in Table 5.1, except ϵ_r which is varied. $\phi = 52\%$. Increase in the viscosity with roughness in the thinning regimes is consistent with ref. [7] and the increase in the viscosity during the ST jump is consistent with ref. [8]. The viscosities in the Newtonian plateau are comparable for small change in the roughness values.

thinning at high shear rates in suspensions [34], [83], [131], [155]. In addition, we expect the second shear thinning to depend on the particle material as well. Since, the asperities need be deformed plastically to enter the low coefficient of friction region, the stress (and hence shear rate) required for the same would depend on particle properties. E.g., since the Young's and elastic modulus of Silica particles is larger than PVC particles, a significantly higher shear stress/rate would be required to deform Silica asperities plastically. Thus, delaying the onset of second shear thinning to very high $\dot{\gamma}$ values. We expect our simulation results to encourage experimentalists to investigate different suspension systems at very high shear rate values to shed more light on the link between plastic deformation of particle asperities and the second shear thinning regime.

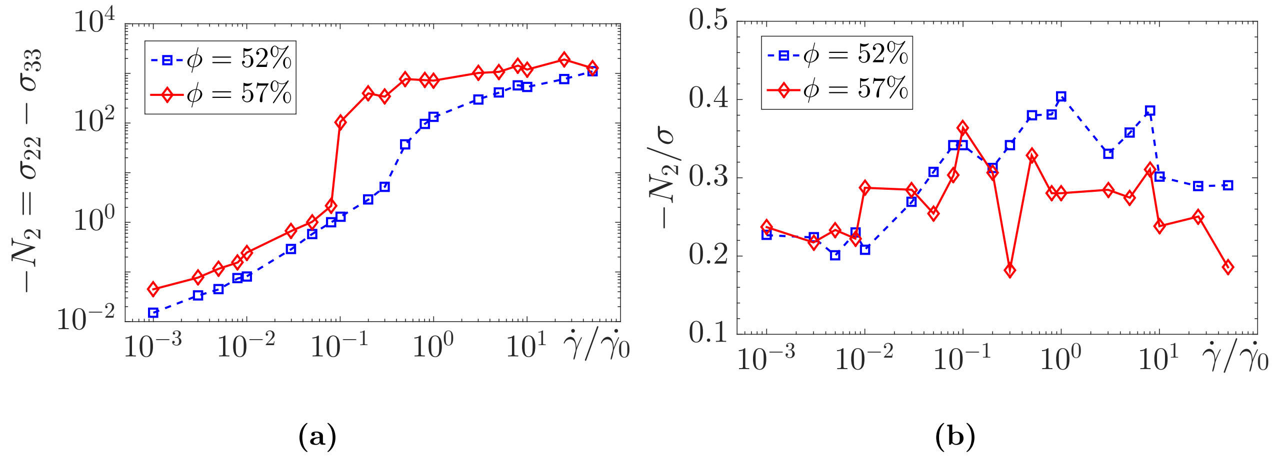

Figure 5.10. a) Evolution of second normal stress difference, N_2 with applied dimensionless shear rate. N_2 is always negative. b) N_2 scaled by the shear stress in the suspension. This plot shows that N_2 mimics the stress in the system.

5.5.4 Effect of particle surface roughness

Earlier theoretical and numerical studies had predicted that increasing the particle surface roughness would lead to a decrease in the suspension viscosity [24]. However, recent experiments show that rough particle suspensions have a higher viscosity compared to smooth particle suspensions [7]. We have resolved this discrepancy and showed that the increase in suspension viscosity with particle surface roughness can be explained by using a normal load/roughness deformation dependent μ [3] similar to the one used in this study.

The proposed model in this study is equipped to quantify the effects of varying particle roughness which is not possible in models which allow particle overlaps. Simulation results accurately predict a rise in the suspension viscosity with with particle asperity size, ϵ_r, as shown in Fig. 5.9. The increase in the suspension viscosity with particle roughness manifests itself in the form of a higher viscosity jump across ST transition, in agreement with previous experiments [8] and simulations [4].

5.6 Normal stress differences

Fig. 5.10a and 5.10b show the dependence of the second normal stress difference $N_2 = \sigma_{22} - \sigma_{33}$ and the dimensionless normal stress difference N_2/σ_{12} in the dimensionless shear rate. We observe N_2 to be negative for all the investigated input parameters. We find that N_2 qualitatively mimics the shear stress σ in the suspension. We also find that the first normal stress difference is small compared to N_2 and is dominated by fluctuations. Hence, it is not presented here.

6. CONCLUSIONS AND FUTURE WORK

Part I of the thesis has established and quantified the effects of increasing the particle surface roughness size on the rheological properties of dense suspensions. We have validated the numerical framework developed against the earlier published data and experiments.

In chapter 2, the effect of varying particle surface roughness on the rheology of concentrated non-Brownian suspensions has been studied numerically. Using an accurate and realistic contact model is crucial for simulating typical suspension properties like shear thinning and obtaining results close to experiments. The hydrodynamic interactions have been modeled using the Ball-Melrose approximation [49]. An elastic-plastic mono-asperity model with varying coefficient of friction [52], [60] has been implemented to model the roughness and contact dynamics.

We observe that the magnitudes of relative viscosity (η_r) and normal force (N) increase with increase in roughness. These findings are in agreement with the experiments carried out by Tanner & Dai [7]. To the best of our knowledge this is the first numerical study to capture the observed trend in experiments. All the previous analyses [22], [88], [95], [106] and computations [23], [24], [48], [107] predicted a trend opposite to experiments. In these studies a simple contact model was used and the reduction in the relative viscosity was attributed to the fact that average inter-particle distance increases with roughness which reduces the hydrodynamic contribution to the total stress. We obtain a similar decrease in the contribution from hydrodynamic stress. However, the increase in contribution from the contact stress is very large which causes the relative viscosity to increase. In addition, for a fixed stress, the particle-particle contacts are more likely to be in the elastic region as we increase the roughness, leading to the increase in viscosity owing to the high value of μ in elastic region.

A coefficient of friction decreasing with the normal load is essential in simulating shear thinning behavior as proposed by Moon *et al.* [54] and shown by Lobry *et al.* [52]. Even though the coefficient of friction between two contacting particles decreases with the normal load, the average coefficient of friction for the suspension as a whole increases with increase in roughness. This results in the increase in the relative viscosity and normal stress difference.

We obtain negative values for N_2 which are much larger than the values of N_1 in magnitude. The magnitudes of non-dimensional normal stress differences are in close agreement with the previous studies. We observe an increase in N_2 and normal force $N = N_1 - N_2$ with an increase in roughness which is in agreement with the experimental results [7]. Magnitude of N_1/σ decreases with increasing roughness due to increase in μ_{avg}. This is consistent with Gallier *et al.* [24] where they observe a decrease in the magnitude of N_1/σ with increasing coefficient of friction.

We also show that Maron-Pierce law can be used to predict the viscosity for different volume fractions and shear stress values. We also find the maximum volume fraction (jamming fraction) decreases with increasing roughness. The reduction in jamming fraction with roughness is due to two reasons: i) The effective radii of rough spheres and consequently the effective volume fraction are larger than their smooth counterparts, and ii) The average coefficient for suspensions increases with increase in roughness which also leads to the reduction in jamming fraction with increase in roughness. The jamming fraction increases with stress which is consistent with experimental observations.

The results presented in chapter 2 established the crucial role of a realistic and accurate contact model to accurately calculate the rheological properties of dense non-Brownian rough suspensions. More studies are needed to develop such models. One of the fundamental mechanisms governing the rheological behavior of sheared suspensions seems to be the increase in average coefficient of friction with increase in roughness. Since modifying coefficient of friction is challenging, we can instead modify other properties of particles influencing friction such as roughness to tune suspension properties according to the need of different applications.

The finding of chapter 2 insinuate that dense suspensions would undergo a shear thickening transition at a lower critical shear rate with an increase in the roughness size of the particles. We tested this hypothesis in chapter 3 with the help of the *Critical Load Model* for friction. We show that increasing the particle roughness results in an earlier onset of shear thickening in terms of the critical shear rate and leads to the continuous shear thickening (CST) to discontinuous shear thickening (DST) transition at a lower critical volume fraction. The denser contact networks with higher roughness explain these findings.

The simulations show that roughness reduces the jamming fraction in the low (or equivalently for friction-less particles) and high shear rate limits due to the increase in the effective radii of particles, which results in denser contact networks as the volume fraction increases. The direct consequence of this is the increase in the viscosity of the suspension with roughness. This result suggests that, roughness should lead to enhancement in the ST effect, i.e., increasing roughness decreases in ϕ_c and $\dot{\gamma_c}$ and increases the ST index β.

Simulations for a range of volume fractions with systematically increasing roughness size indicate that roughness increases the viscosity of suspensions and enhances the magnitude of ST effect. Specifically, roughness leads to decrease in $\dot{\gamma_c}$ and ϕ_c. We also reproduce the experimentally observed DST, where suspension switches abruptly from a low viscosity state to a high viscosity state. Increasing roughness leads to DST at lower volume fractions e.g., for the smooth case ($\epsilon_r = 0.01$), we only observe DST at very high volume fraction $\phi > 57\%$. But, for the roughest case ($\epsilon_r = 0.125$), DST occurs for a volume fraction as low as 49 %. In addition, we can predict the onset of DST for a given roughness from its effective volume fraction, ϕ_{e}. For any roughness and volume fraction, if $\phi_{\mathrm{e}}(\phi, \epsilon_r) > 63\%$ then we expect the suspension to undergo DST, if $59\% \leq \phi_{\mathrm{e}} \leq 63\%$, we get strong CST and for $\phi_{\mathrm{e}} < 59\%$ we get CST. These calculations, however cannot predict the critical shear rate at the onset of ST and the ST index as they depend on the roughness size.

We find that, N_1 increases with increase in roughness and can become positive at higher roughness values or at very high volume fractions. N_1 has a negative value which decreases after ST transition for low roughness values (e.g. for $\phi = 50\%$ and $\epsilon_r < 3\%$), while for higher roughness values, N_1 becomes positive and increases after the ST transition. The dimensionless N_1 has a magnitude lower than 0.2 for all the cases investigated in this study.

We obtain negative values for N_2 with a magnitude much larger than N_1. This result is consistent with most of the previous experimental and computational studies. N_2 mimics the stress in the system and increases with increase in roughness. Plotting dimensionless N_2 for different dimensionless stress values reveals that N_2/σ falls on a single curve independent of roughness. We observe a two-folds increase in N_2/σ during the ST transition.

We visualize the contact network evolution for different roughness values revealing the governing role played by the frictional contacts in the ST behavior of suspensions. The increase in the fraction of frictional particles in the system with stress results directly in ST. With increasing roughness more particles come into contact which results in denser contact networks for higher roughness values. This also results in the increase in the viscosity for a particular volume fraction with roughness which eventually leads to enhancement in the ST effect with roughness. In addition, we calculate the critical deformation related to the force scale for the frictional transition. We find that the average deformation across all the contacting particle pairs increases with asperity size leading to the rise in the contact stresses.

The results presented in chapter 3 are crucial to predict the onset and the strength of ST effect with varying roughness values. Though friction is the basic mechanism for observing ST, tuning friction coefficient in order to manipulate suspension behavior is a tough task. On the contrary, particle surface roughness can be modified easily to enhance or reduce the ST effect according to a specific application [207], [208].

Finally, in chapter 4 we develop a simple constitutive model to quantify the effect of increasing the surface roughness of particles in a ST dense suspension. The model requires knowledge of stress independent rheology in the zero and high shear rate limits for a few roughness values. The rheology between these extremes can then be interpolated using the equations presented in this chapter. The equations developed provide a simple way to calculate the critical volume fraction for the DST onset and the critical shear rate for ST transition.

The proposed constitutive model successfully captures all the rheological properties and flow behaviors observed for ST rough particle suspensions. It spans the entire flow state diagram and shows the transition between monotonic, S-shaped and backward bending curves in the σ vs $\dot{\gamma}$ state diagram. Once the roughness dependence of the rheological properties in the low and high shear state limits is known, we can use the constitutive equations to quantify the exact effect of roughness size on the rheology of rough particle suspensions. E.g., the critical shear rate for the ST transition can be calculated as: $\dot{\gamma}_c/\dot{\gamma}_0 = \tilde{\sigma}_c/\eta_r(\epsilon_r, \tilde{\sigma_c})$ ($\tilde{\sigma}_c = 1$ in this study), the critical volume fraction for DST can be found by calculating the lowest volume fraction for which $d\dot{\gamma}/d\sigma$ becomes 0.

The findings of chapter 4 are useful in quantitatively predicting the behavior of ST suspensions at various particle surface roughness sizes. The insights obtained can potentially be utilized in manipulating the suspension behavior by changing the particle surface roughness size along with mechanisms based on hydrodynamic interaction [166], [167], particle surface coatings/functionalities [209] and friction [117].

Chapter 5 looks beyond the direct contacts and friction by incorporating other pair-wise non-contact interactions such as DLVO and non-DLVO interactions. This chapter proposes a universal model which can quantitatively predict all of the four regimes, viz., shear thinning, Newtonian plateau, shear thickening, and shear thinning and the transition from one regime to the other with increasing shear rate or stress typical to the flow behavior of dense non-Brownian suspensions. Thus, unifying disparate rate-dependent rheological regimes in the flow curve of a dense non-Brownian suspension of smooth particles. The unifying mechanism is based on the competition between the inter-particle hydrodynamic interactions, non-hydrodynamic interactions of DLVO and non-DLVO origins, contact forces and Stribeck curve for the friction coefficient (a constraint mechanism); each interaction resulting in a characteristic stress scale in the system. The switching between dominant stress scales with increasing the shear rate/stress explain the various regimes and transitions observed in a dense non-Brownian suspension (particle sizes $> O(1\mu m)$). Specifically, we show that accounting for the non-DLVO forces and a coefficient of friction decreasing with the increasing normal load (asperity deformation) is crucial to quantitatively reproduce the intermediate Newtonian plateau and the second shear thinning in the same framework. We validate the proposed hypothesis by performing particle scale dynamic simulations and compare the results with previous experiments.

The presence of Newtonian plateau which has eluded researchers [26], [83] is explained by the inclusion of non-DLVO interactions that are non-contact interactions [190] & delay the onset of lubricated to frictional transition (hence ST). Furthermore, we do not find any significant ordering in the initial shear thinning regime as it was observed in some cases for mono-disperse suspensions. This begets an interesting question whether the ordering at low shear rates/stresses for mono-disperse suspensions is an outcome of various non-contact interactions rather than being the reason for the initial shear thinning? Further investigations are needed in this direction.

The results also show that only constraining the sliding motion between the particles is enough for smooth particle suspensions, unlike rough particles, where constraint on rolling motion might be crucial [173]. The ST transition is the result of constraints on the relative particle motions due to friction while the second shear thinning arises due to the reduction in coefficient of friction with asperity deformation (or normal load) at a very high shear rate/stress. Our simulation results show that using experimentally obtained expressions for the non-hydrodynamic interactions and the constraint mechanism (e.g., coefficient of friction) is required to obtain a quantitative agreement with the experimental results.

Although we have used specific force profiles from the direct measurements [83] for DLVO forces and μ, the model can reproduce the flow curve for any generic system given its repulsive, attractive, non-DLVO force profiles and friction law. We demonstrate the versatility of the proposed model to reproduce a gamut of flow behaviors by varying the relative magnitudes and expressions of various interactions. In addition, the model accurately predicts a rise in the suspension viscosity with particle surface roughness, in agreement with recent experiments. These results show that the macroscopic rheological behavior is determined by the microscopic particle pair interactions. It would also be interesting to investigate the effects of other collision models. Thus, to gain further insights into the physics behind the rheological behavior of dense suspensions, accurate measurements of inter-particle interactions (especially non-DLVO interactions) and μ as a function of inter-particle gap while immersed in the fluid medium are needed.

In the future, it will be interesting also to explore the effects of adding polymers in the suspending fluid so that that suspending fluid itself is non-Newtonian. This would have significant and non-intuitive effects on the bulk rheology and can also be used to manipulate suspension rheology. In addition, we only considered the simple shear flow of suspensions. Other flows, such as oscillatory shear flow and shear reversal, are also essential flow conditions under which we want to know the behavior of suspensions. Thus, investigating the influences of these non-contact forces in different flow conditions on the rheological properties of dense suspensions is another excellent direction for future studies.

Since microscopic force magnitudes directly determine the stress scales in suspensions and the critical values for various transitions, our results hint towards the possibility of deducing the magnitudes of microscopic forces (difficult to measure) by measuring the bulk rheology (relatively easier to measure).

PART II

MOTION IN A STRATIFIED FLUID: SWIMMERS AND ANISOTROPIC PARTICLES

7. INTRODUCTION

7.1 Motivations

Fluid heterogeneity is as pervasive as fluids not only below the surface of the Earth in magma [210], on the surface in aquatic bodies [211] and above the surface in the atmosphere [212] but also beyond it in the cosmos [213]. Since gravity is omnipresent and, fluid homogeneity is an exception rather than the rule, the interplay between fluid heterogeneity and gravity results in non-intuitive and striking phenomena of importance in many branches of fluid mechanics. A desire to solve practical problems, for instance, in meteorology, oceanography, and hydraulic engineering, was the impetus behind the progress in the field of stratified flows in the 20^{th} century. Fluid density and/or viscosity stratification are commonly observed fluid heterogeneities. Fluid density stratification is ubiquitous in the Earth's atmosphere, oceans, lakes, magmas, and cosmic gas clusters, while viscosity variations are routinely encountered in nature (e.g., glaciers, magma, blood) and industry (chemical and food industry). Fluid heterogeneities govern the large-scale motions like atmospheric recirculation and ocean currents and significantly influence the localized motion, transport, and interactions of active or passive objects moving in density and/or viscosity stratified fluids. The latter is the focus of this part of the thesis.

Understanding the motion of objects in a stratified environment is crucial in several environmental, geophysical, ecological, and industrial processes. Atmospheric pollutants like particulate matter, soot, dust, aerosols, pollens, volcanic ash, and weather balloons reside in the lower atmosphere [214]. They often come across local temperature gradients, e.g., atmospheric inversions [215], which profoundly affect their vertical settling/rising rates, aggregation, and scattering, which in turn play an important role in cloud formation and air quality [216].

Common marine pollutants like microplastics (MPs) [217] are likely to accumulate in thin layers in the stratified ocean upper layers. The vertical settling of marine snow particles carrying organic matter and alive/dead phytoplankton through thermoclines (temperature variations) and haloclines (salinity variations) in oceans and lakes [211], [218] is responsible for the transfer of nutrients and organic matter, especially carbon within ocean layers

[219]. Large density gradients increase the accumulation of these particles and organisms [220] forming thin nutrient-rich layers with thriving ecosystems. Furthermore, harmful algal blooms are acutely affected by density gradients [220], they are detrimental for ocean ecology [221], hinder measurements from sea platforms [222] and lead to bias in observations of velocity and turbulence by satellites, aircrafts and Lagrangian floats required for weather forecasting [223]. Stratification also hampers Diel Vertical Migration (DMV) of zooplankton [224].

On a global scale, it is still unclear whether the collective motion of marine organisms with inertia can lead to significant mixing in the oceans, even though the collective motion of such organisms has been associated with the local biogenic mixing hot spots [225], [226]. Thus, understanding the influence of stratification on particles and swimmers dynamics is essential to model and predict phenomena such as bio-geochemical fluxes [227] and biogenic mixing [228], retention at pycnoclines, and horizontal layer formation. This would help in better predictions of these biological phenomena in oceans [211], [218]. A summary of the motion at pycnoclines in oceans is shown in Fig. 7.1. Particle motion in density-stratified fluids is also encountered in industrial processes involving mixing different density fluids [229], air conditioning and ventilation systems [230], and chemical plants.

Such practical applications with far-reaching implications motivate theoretical analyses and numerical simulations complementing idealized experimental studies of flows past spheres, drops/bubbles, and microorganisms. However, these particles and organisms come in a variety of shapes like disk-like flat or rod-like elongated [231], pointing towards a need for better understanding the effect of particle shape anisotropy on their dynamics in heterogeneous fluids. The added degree of freedom due to the particle shape anisotropy results in anisotropic drag [232], non-intuitive particle settling paths [233], and orientation instability [231], [234] in a stratified fluids. The consequences of these effects on the hydrodynamic interactions and sedimentation of non-spherical particle suspensions in a stratified fluid are yet to be understood.

Much progress has been made in understanding the effects of fluid heterogeneities on the motion of objects over the past few decades. A thorough discussion on particle scale fluid flow, fluid entrainment, drift volume, and objects crossing immiscible interfaces can be foubd

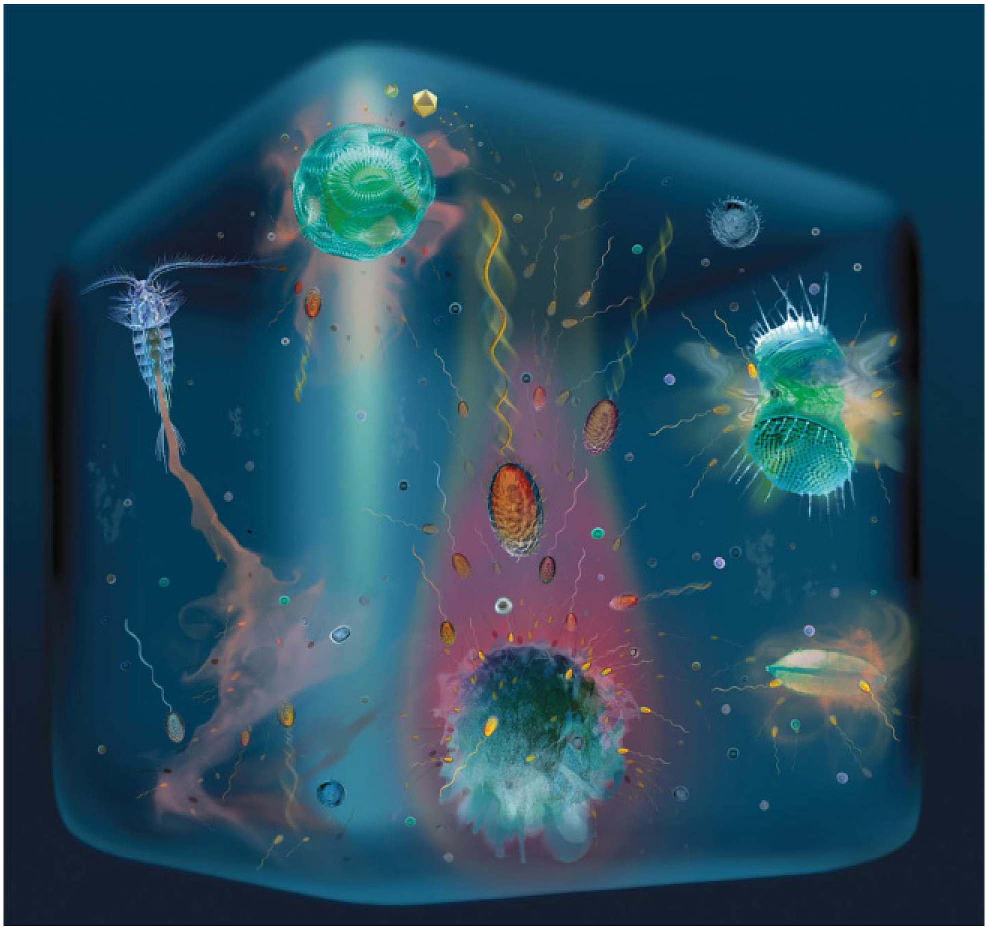

Figure 7.1. Marine microbial environment see a sea of fluid property variations. This schematic shows various processes which contribute to creation of such gradients. Phytoplankton (top), cell lysis events (top right), detritus and marine snow particles (bottom center), and cocepod excretions (left). Adapted from Stocker, *Science*, 2012.

in earlier reviews [235], [236]. The main focus of this part of the thesis is to debunk the effects of stratification on the individual, and pair interaction dynamics of swimmers and probe the influences of particle shape anisotropy on their settling dynamics in a stratified fluid. The physical insights obtained from these investigations explain the hydrodynamic mechanisms behind the accumulation and trapping of these objects in stratified environments, mixing, and the reorientation of anisotropic bodies. The following section presents a brief discussion of governing equations and dimensionless parameters—the subsequent sections delving deeper into understanding the motion in stratified fluids.

7.2 Governing Physics and investigation techniques

Particles, bubbles/drops, or swimmers considered in this review are in the order of $\mu m - mm$. Hence, their Reynolds number Re ranges from $\approx O(0 - 10^3)$ depending on the local conditions and their moving speeds. As a result, we can say that their motion predominantly lies in the "viscous" flow regime, with inertial effects being important in many cases. Hence, various theoretical, semi-analytical, numerical, and experimental techniques have been applied to investigate the motion of these objects in stratified fluids. We provide a summary of these techniques in this section. Before that, it is necessary first to understand the fundamental equations governing the motion in stratified fluids.

7.2.1 Governing equations

The Navier-Stokes equations, along with the Boussinesq approximation for density and the continuity equation, are used to resolve the flow field. In addition, the advection-diffusion equation for density (or equivalently the stratifying agent) is also used to calculate the density field. The fluid is assumed to be Newtonian and incompressible. These equations are written as:

$$\boldsymbol{\nabla} \cdot \mathbf{u} = 0, \tag{7.1}$$

$$\rho_0 \frac{D\mathbf{u}}{Dt} = -\boldsymbol{\nabla} p + \boldsymbol{\nabla} \cdot [\mu(\boldsymbol{\nabla}\mathbf{u} + \boldsymbol{\nabla}\mathbf{u}^T)] + \rho \mathbf{g}, \tag{7.2}$$

$$\frac{D\rho}{Dt} = \boldsymbol{\nabla} \cdot (\kappa \boldsymbol{\nabla} \rho). \tag{7.3}$$

Here $\mathbf{u} = (u, v, w)$ is the velocity field, ρ is the fluid density, p is the pressure, μ is the fluid dynamic viscosity and $\mathbf{g}$ is the acceleration due to gravity which usually points in the downward direction, i.e., $\mathbf{g} = -g\hat{\mathbf{k}}$. In a stratified fluid, the fluid density varies with fluid depth, z, so, $\rho = \rho(z)$. A stable stratification implies that the density increases with depth, i.e., $\rho(z)$ is an increasing function of $-z$. Linear ($\rho(z) = \rho_0 + \rho_z z$) and hyperbolic tangent are some of the routinely used expressions for $\rho(z)$ as they are observed for pycnoclines. Here,

$\rho_z = d\rho/dz$, the background density gradient. It should be noted that the density field is determined by the stratifying agent like temperature, salinity or nutrients and solving eq. 7.3 is the same as solving the advection-diffusion of the stratifying agent. Taking curl of the Navier-Stokes equations 7.2 results in the vorticity $\boldsymbol{\omega} = \boldsymbol{\nabla} \times \mathbf{u}$ advection-diffusion equation given by,

$$\frac{D\boldsymbol{\omega}}{Dt} = (\boldsymbol{\omega} \cdot \boldsymbol{\nabla})\mathbf{u} - \boldsymbol{\nabla} \times \left(\frac{\mu}{\rho_0} \times \boldsymbol{\nabla}\boldsymbol{\omega}\right) + \boldsymbol{\nabla} p \times \boldsymbol{\nabla}\left(\frac{1}{\rho}\right) + 2\boldsymbol{\nabla} \times \left[\frac{\boldsymbol{\nabla}\mu}{\rho_0} \cdot (\boldsymbol{\nabla}\mathbf{u} + \boldsymbol{\nabla}\mathbf{u}^T)\right]. \quad (7.4)$$

The first two terms on the right-hand side give the change of vorticity of a fluid element brought about by the stretching of vortex lines and the diffusion of vorticity from boundaries, respectively, similar to a fluid with a constant density. The third term distinguishes a stratified fluid from a homogeneous one. In a stratified fluid, vorticity is generated whenever pycnoclines are displaced such that $\boldsymbol{\nabla}\rho$ and $\boldsymbol{\nabla}p$ are not parallel. In the simplest case, i.e., hydrostatics, when p depends on gravity alone, this means that the displacements of isopycnals (equal density surfaces) away from the horizontal produces vorticity.

7.2.2 Important dimensionless parameters and length scales

Given the Boussinesq approximation holds, an inviscid fluid element displaced from its equilibrium position in a stratified fluid oscillates in simple harmonic motion with frequency, $N = \sqrt{-\rho_z g/\rho_0}$ ($\rho_z = \partial\rho(z)/\partial z < 0$ is the background density gradient) called the Brunt-Väisälä frequency. This also sets a characteristic time scale in the system $\tau = 2\pi/N$. The dynamics of objects with a characteristic length scale D and density ρ_p moving with a characteristic velocity U in a fluid with kinematic viscosity ν in a stratified fluid is governed by a few important dimensionless parameters. The Reynolds number, $Re = UD/\nu$, measures the relative importance of inertial to viscous forces. The Richardson number, $Ri = N^2D^3/(\nu U)$, which is the ratio of buoyancy to viscous forces, and the Froude number, $Fr = UD/N$, gives the ratio of inertial to buoyancy forces are both used to quantify the strength of stratification. Finally, the density ratio, $\rho_r = \rho_p/\rho_0$ and the Archimedes number, $Ar = \rho_0 g D^3 \left(\rho_p - \rho_0\right)/\mu^2$ tell us about the relative importance of gravitational forces compared to the viscous forces.

In addition, the ratio of momentum diffusivity to the stratifying agent diffusivity is given by the Prandtl number or the mass transfer analog Schmidt number, Pr or $Sc = \nu/\kappa$. The product of Re and Pr gives the Péclet number, $Pe = RePr = UD/\kappa$ which is commonly used in the low Re studies to quantify the importance of advective transport over diffusive transport, e.g., if $Pe \ll 1$ then diffusion dominates and if $Pe \gg 1$ then advection dominates the transport of the stratifying agent.

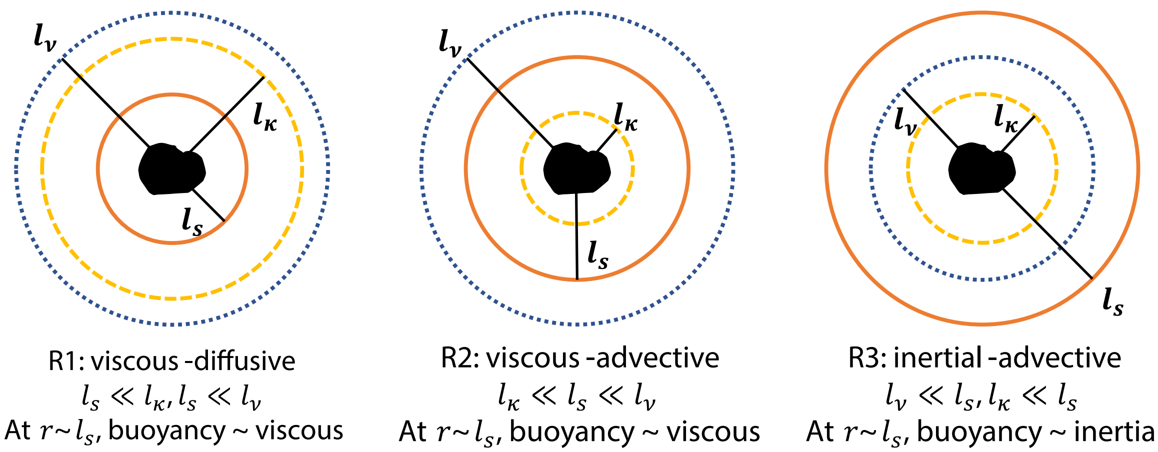

Figure 7.2. Possible stratification regimes depending on the relative magnitudes of the viscous (l_ν, dotted line), advective (l_κ, dashed line) and stratification (l_s, solid line) length scales for a particle with unit characteristic length at low Re ($l_\nu \sim 1/Re$). The high Re ($l_\nu \sim 1/Re^{1/2}$) case is similar except $l_\nu \ll D$ where D is the characteristic particle length.

Depending on the relative magnitude of the length scales associated with stratification l_s, viscosity (l_ν) and stratifying agent diffusivity (l_κ), several distinct regimes have been identified by linearizing the governing equations in terms of disturbance properties and then using a leading order scaling analysis [237]. Regimes R1 and R2 are viscous regimes meaning the fluid inertia is unimportant; however, in regime R3, the inertial fluid effects are important. In addition, the density transport is predominantly diffusive in regime R1, but the density advection dominates in regimes R2 and R3. Thus, the stratification length scale, l_s, can be interpreted as the distance from the particle such that the viscous and buoyancy forces balance in regimes R1 and R2 or the inertial and buoyancy forces balance in regime R3. These are summarized in table 7.1 and plotted in Fig. 7.2. Each regime has its stratification length scale l_s, which determines the extent of the effects of density variations due to stratification on the flow physics.

Table 7.1. Summary table of length scales and stratification regimes

Regime	$l_s\,(Re \ll 1)$	$l_s\,(Re \gg 1)$
R1, viscous-diffusive $l_s \ll l_\nu$, $l_s \ll l_\kappa$	$\sim (Fr/Re)^{1/2}Pr^{-1/4}$ $\equiv (\nu\kappa/N^2)^{1/4}$	$\approx (Fr/Re)^{1/2}Pr^{-1/4}$ $\equiv (\nu\kappa/N^2)^{1/4}$
R2, viscous-advective $l_\kappa \ll l_s \ll l_\nu$	$\sim (Fr^2/Re)^{1/3}$ $\equiv (\nu U/N^2)^{1/3}$	$\sim Re^{-1/2}Fr^{2/(2+\beta)}$, β in $(0-1)$
R3, inertial-advective $l_s \gg l_\nu$, $l_s \gg l_\kappa$	$\sim Fr$ $\equiv U/N$	$\sim Re^{-1/2}Fr$ $\equiv (\nu U/N^2)^{1/2}$

7.2.3 Investigation techniques

For theoretical analysis of the problem of motion in a stratified fluid, the governing equations are usually written in the frame of reference attached to the moving object and for the disturbance variables. The coupling between fluid flow and density transport equations limit theoretical calculations to weak stratification [238]. Fundamental singularities in $Re = 0$ limit, e.g., the point-force (respectively, force-dipole) is a good representation of a settling particle (respectively, neutrally buoyant organism), can be used to calculate the fundamental far-field velocity solutions for low Re flows in a stratified fluid, aptly called "Stratlets" [238]. However, the perturbations of the disturbance variables in terms of a small stratification parameter needed to solve the near-field flow are singular, similar to the perturbation in Re for the homogeneous flow past an infinite circular cylinder [239]. Hence, 'singular perturbation' theory [240] and a matched-asymptotic expansion [241] are used to solve the disturbance flow by matching the inner and outer solutions in the matching zone (when the distance from the particle $r \approx l_s$). The density disturbance effects can also be evaluated by the use of Green's function, making it a suitable method for obtaining the force modifications on rigid particle [242], drops [243] and porous particles [244] in the form of a volume integral over the entire domain. The Lorentz reciprocal theorem can also be used by intelligently choosing the complementary problem, e.g., torque-free spheroid settling in a stratified fluid and the Stokesian rotation of a spheroid in a quiescent ambient [245]. Though theoretical methods can provide crucial information such as stratification drag enhancement, they are limited to isolated objects, negligible Re, and weak stratification situations.

The limitations of the theoretical methods can be overcome by doing numerical simulations. These include Discrete Lagrange multiplier [246], body-fitted grid [247], immerse boundary method [231], volume of fluid [248] and front-tracking [249] all of which either use finite volume or finite element discretization of the governing equations. These methods have been useful in studying the combined effects of inertia and stratification on the flow around the objects, stratification drag enhancement, and the unsteady motion of settling objects in a stratified fluid.

Finally, in laboratory experiments, the two tank method [250], [251] is commonly used for creating a stable linear stratification, while a two-layer stratification can be formed by slowly feeding the heavier fluid under the lighter fluid [252]. Then the particles/drops are carefully released/injected carefully to investigate various phenomena such as their settling and accumulation in horizontal layers [236]. The objects are towed by connecting them to motor-driven carriage plates via wires [253] to study the flow structures of stratified horizontal and vertical flows over them. The flow can be visualized by Schlieren imaging, shadowgraph techniques, PIV measurements, or using fluorescent dye [234], [250], [254]–[256].

7.3 Part II outline

With the fundamental concepts and governing equations discussed, this section outlines the structure of part II of the thesis. Here we only provide a big picture view of each of the following chapters, with motivations behind choosing those problems and detailed analysis in the respective chapters. The remaining part II is organized as follow:

Chapter 8 probes the combined effects of fluid stratification and inertia on the straight line motion of swimmers parallel to the direction of gravity. We use the popular squirmer model to mathematically model the swimmers. We elaborate on the reasons behind the reduction in the swimming speeds of swimmers in stratified fluids compared to their swimming speeds in homogeneous fluids at the same Reynolds numbers. Furthermore, we also explain the reasons behind the decrease in the swimming efficiencies of swimmers due to stratification and what causes the swimmers to have higher mixing efficiencies at higher stratification. Most importantly, we find that the straight line motion of an inertial pullers becomes stable (which is otherwise unstable in a homogeneous fluid), while fluid stratification stabilizes the motion of an inertial pushers (which is otherwise stable in a homogeneous fluid). This chapter dives deeper in unravelling the physical mechanisms behind these non-intuitive observations by examining the effects of fluid stratification on the flow field generated by these swimmers for their locomotion. **Chapter** 9 goes a step further than chapter 8 and investigated the hydrodynamic interactions between a pair of squirmers in a stratified fluid. The results for interactions between a pair of colliding squirmers and squirmers moving side-by-side reveal several trajectory patterns. We explain the physical mechanisms behind these trajectories by examining the flow field around interacting squirmers.

Chapter 10 changes the focus from swimmers to rigid particles and investigates the effects of particle shape anisotropy on their settling dynamics in stratified fluids under the influence of gravity. Fully resolved simulations using the immersed boundary method show that fluid stratification suppresses the oscillatory behavior of spheroid observed when they settle in a homogeneous fluid and also eliminates the oscillatory trajectories. Most importantly, we find that the spheroids settle in a configuration such that their long edge is vertical or parallel to the direction of gravity which contradicts the long edge horizontal settling in a homogeneous fluid. We again examine the flow field and isopycnal deformation around the spheroids to gain insights into the mechanisms behind this reorientation instability. We also discuss the conditions for the reorientation onset and quantify the drag acting on the particles as they settle in a stratified fluid.

Chapter 11 summarizes all the above studies in the context of our original goal. Also, this chapter proposes further investigation ideas that can help to improve our fundamental understanding of the motion in a stratified fluid.

7.4 Publications and division of work between authors

The main advisor for the project is Prof. Arezoo M. Ardekani (AMA). AMA was responsible for conceptualization, developing methodology, project administration and funding accusation.

1. Chapter 8: Related publication - More, R. V. and Ardekani, A. M., Motion of an inertial squirmer in a density stratified fluid. *Journal of Fluid Mechanics*, 905, A9, 2020. Author contributions - Rishabh V. More (RVM) modified the in-house code previously developed by Arezoo M. Ardekani (AMA) such that it can simulate the motion of squirmers in a stratified fluid. RVM performed simulations. RVM and AMA analyzed the results and wrote the paper.

2. Chapter 9: Related publication - More, R. V. and Ardekani, A. M., Hydrodynamic Interactions between swimming micro-organisms in a linearly density stratified fluid. *Physical Review E*, 103(1), p.013109, 2021. Author contributions - RVM modified the in-house code previously developed by AMA such that it can simulate the motion of squirmers in a stratified fluid. RVM performed simulations. RVM and AMA analyzed the results and wrote the paper.

3. Chapter 10: Related publication - More, R. V., Ardekani, M., Brandt, L., Ardekani, A. M., Orientation instability of settling spheroids in a linearly density stratified fluid. *Journal of Fluid Mechanics*, 929, A7, 2021. Author contributions - Mehdi N. Ardekani (MNA) while working with Luca Brandt (LB) developed the code. RVM performed simulations. RVM, MNA, LB and AMA analyzed the results and wrote the paper.

8. MOTION OF AN INERTIAL SQUIRMER IN A DENSITY STRATIFIED FLUID

8.1 Introduction

Movement driven by pervasive impulses acting across multiple spatial and temporal scales, is a fundamental characteristic of all the Earth dwelling organisms since they first learned to move some 565 million years ago [257]. Depending on their surrounding environment, locomotive organisms have developed various techniques to roam around like running, flying, jumping, swimming, rolling, gliding to name a few. This movement plays a crucial role in driving many of the evolutionary and ecological processes [258]–[261]. Especially in aquatic bodies, swimming organisms span across sizes ranging from a few microns to a several meters and exhibit a rich variety of locomotive organs [262], [263].

The magnitude of the Reynolds number $Re = U_0 a/\nu$, which is a dimensionless number quantifying the relative strength of the inertial and viscous effects provides us an insight into the underlying flow physics of swimming organisms. Here, U_0 is the velocity scale, a is the length scale and ν is the kinematic viscosity of the fluid. For swimming microorganisms, the Re ranges from 10^{-4} for bacteria [264], 10^{-3} for *Chlamydomonas*, $0.01-0.1$ for *Volvox* [265], $0.1-1$ for freely swimming zooplankton *Daphnia magna* [266], $0.2-2$ for *Paramecia* depending on swimming or escaping mode [267], $O(10)$ for *Pleurobrachia*, and $20-150$ for copepods [268]. So, organisms employ a wide range of swimming mechanisms. At low Re, they utilize the thrust generated by the locomotive organs like cilia and flagella to oppose the viscous drag forces [269]. At high Re, they utilize the lift-forces generated by the flapping of fins and tails [262].

In many of these swimming microorganisms, the propulsion is produced by a cyclic distortion of the body shape [270], e.g., oscillating cilia or flagella [262], [264]. The spherical squirmer model, first introduced by Lighthill [271] and later modified by Blake [272] mimics the self-propulsion produced by the coordinated motion of dense array of cilia on its surface. These ciliary deformations are axisymmetric resulting in radial (u_r^s) and tangential (u_θ^s)

velocity components on its surface in a frame of reference translating with the squirmer with radius a:

$$u_r^s|_{r=a} = \sum_{n=0}^{\infty} A_n(t)P_n(\cos\theta), \tag{8.1}$$

$$u_\theta^s|_{r=a} = \sum_{n=0}^{\infty} \frac{-2}{n(n+1)} B_n(t)P_n^1(\cos\theta), \tag{8.2}$$

respectively. Here r is the distance from the center of the squirmer, θ is the angle measured from the direction of the locomotion, A_n and B_n are the time dependent amplitudes of ciliary deformations and P_n, P_n^1 are the associated Legendre polynomials of degree n. The swimming speed of a neutrally buoyant squirmer at $Re = 0$, i.e., in a Stokes flow depends only on the first mode of each surface velocity component and is given by, $U_0 = (2B_1 - A_1)/3$. This swimming speed is independent of fluid viscosity and other swimming modes [271].

Magar *et al.* [273] were the first to utilize the squirmer model in a computational study to investigate the nutrient uptake by self-propelled organisms. After that, researchers have investigated the hydrodynamic interactions between two squirmers [267], rheology of suspensions of squirmers [274], mixing by swimmers [275] as well as swimming in non-Newtonian fluids [276] using the squirmer model. However, all these studies were in the limit of Stokes flow, i.e., $Re = 0$.

In the last decade, the focus has shifted on exploring the swimming dynamics of the squirmer at a finite Re [277], [278]. Numerical investigations at a high Re (1-1000) show that inertia results in significant divergences in the motion of a pusher and a puller. Specifically, pushers are stable and the flow around them is steady axisymmetric for Re as high as 1000 [279], [280]. On the contrary, pullers become unstable and the flow around them becomes 3D at a critical Re which depends on the relative magnitudes of the swimming modes [279]. The reasons behind these differences are: i) distinct hydrodynamic interactions between the swimmer bodies and the flow fields created by them, i.e., a pusher will be attracted towards its original trajectory due to its interaction with the flow field when it is perturbed sideways from its original straight-line path while the exact opposite of this effect will be experienced by a puller [280], and ii) the ineffective advection of the vorticity generated by the puller as opposed to a strong and efficient advection of the vorticity downstream by the pusher ([279]). Fig. 8.1a and 8.1b demonstrate these effects for a pusher and a puller moving in a homogeneous fluid, respectively. Furthermore, inertia also affects the hydrodynamic interactions of squirmers resulting in a variety of dissimilar trajectories for puller and pusher pairs depending on Re and β. Inertia of the squirmers alters the time of contact and scattering dynamics of two colliding pushers, and results in hydrodynamic attraction between a pair of puller swimmers [280].

Oceans and lakes are abundant with microorganisms and their motion in these aquatic bodies leads to intense biological activity [218], [281], [282]. This makes studying the motion of swimmers in oceanic environment an interesting problem. However, the problem becomes more complex as the upper layer of the ocean, where these swimmers typically roam, observes a vertical variation in the water density which is ubiquitous in other marine environments as well [211], [283]. This density stratification (pycnoclines) can be due to temperature (thermoclines) or salinity (haloclines) or both. Even though the stratification length scale is $O(km)$, the appropriate length scale to dictate the influence of stratification on the swimmers' motion is $O(100\mu m)$ [284]. Marine microplankton *Ciliates* with sizes ranging from $20-200\mu m$ [285] are abundant in such a stratified environments along with other meso-, macro- and mega-planktonic organisms which have Re ranging from $O(0.01-100)$ [268], [286].

Density stratification leads to accumulation of microorganisms [287]–[289] or marine snow particles and formation of phytoplankton blooms [281]. The accumulation is significant for larger size phytoplankton than the smaller ones [288] implying the role of swimmer inertia is important for the accumulation. Experimental investigations of the flow fields around inertial zooplanktonic organisms in a stratified fluid show that the fluid and mass transport due to the swimming of zooplankton organisms can be comparable to turbulence induced transports typical to stratified marine environments [290]. The collective vertical migration of swimmers in a stratified fluid generates aggregation-scale eddies resulting from the coalescence of the individual organisms' wakes. These eddies produce an apparent turbulent diffusivity up to thousand times larger than the diffusivity of the stratifying agent demonstrating their capability to alter the physical and bio-geo-chemical anatomy of the aquatic environment [226], [291], [292].

Looking at the locomotion of individual organisms can provide insights into the collective hydrodynamic and biological impact of migrating swimmer schools in stratified environments.

At low Re, stratification affects the vertical migration of small organisms by resulting in a smaller flow footprint and nutrient consumption as well as higher energy spending [293]. Stratification lowers the swimming speed and requires swimmers to expend more energy for swimming in Stokes regime [294]. Still, we know little about the effect of stratification on the motion of an individual squirmer at finite Re.

The motion of self-propelling organisms in a stratified fluid is inherently different than that of a rigid object settling as there is a tangential velocity and an active vorticity generation on the surface of the swimmers. To this end, we numerically investigate the effect of density stratification on the motion of an inertial squirmer. First, we elaborate on the governing equations and the computational methodology used to solve these equations. Then we present the results on the steady state swimming speed of the squirmers and the effect of stratification on these speeds for various β and Re. We present the flow field and the evolution of pycnoclines around the squirmer to explain the results on the swimming motion. Finally, we present the effect of stratification on the mixing efficiency and energy expenditure of individual swimmers.

8.2 Methodology

This section explains the governing equations and the computational methods implemented to simulate the motion a squirmer through a linearly stratified fluid at finite Re. We consider a squirmer moving through an incompressible Newtonian viscous fluid. The fluid is linearly stratified and the density increases in the downward z direction as shown in Fig. 8.1c.

8.2.1 Governing equations

The fluid flow is governed by the Navier-Stokes equations for an incompressible Newtonian fluid and these equations are solved in the entire domain, Ω. We utilise the Boussinesq

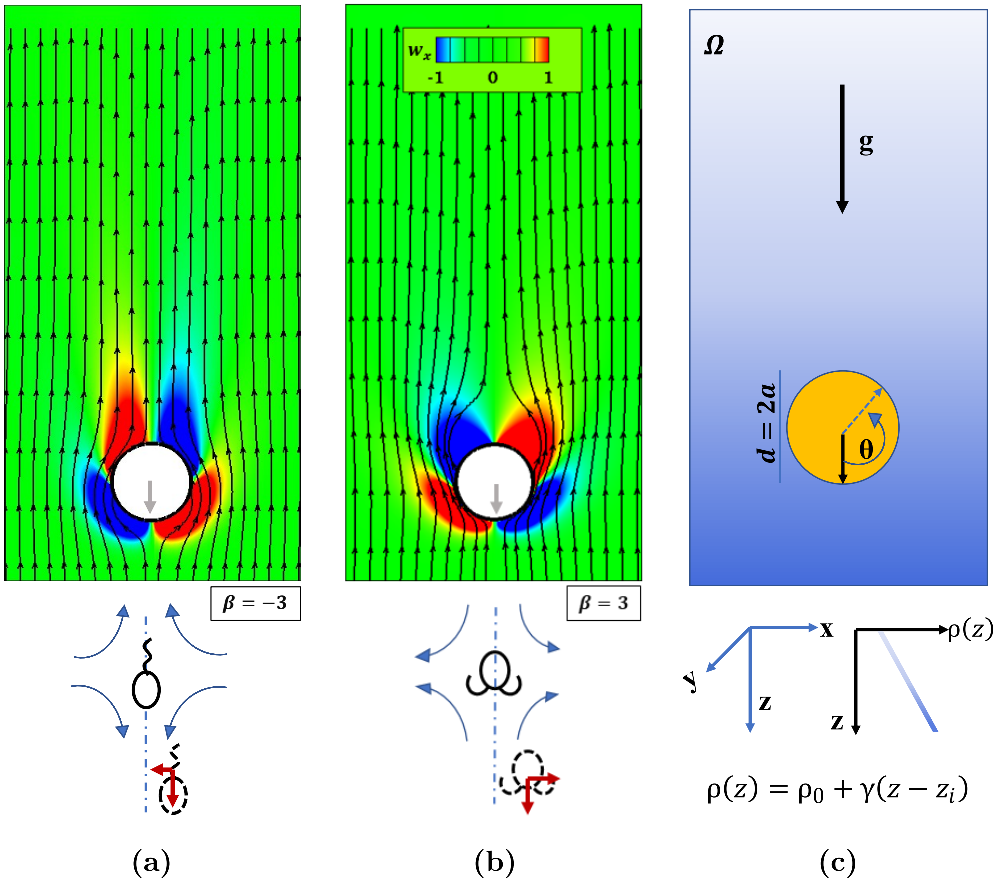

Figure 8.1. a) Vorticity contours and streamlines for a $\beta = -3$ pusher at $Re = 5$ in a homogeneous fluid, b) vorticity contours and streamlines for a $\beta = 3$ puller at $Re = 5$ in a homogeneous fluid. The cartoons below (a) and (b) represent flow around the squirmers. The flow around a $\beta < 0$ squirmer looks like the fluid is being "pushed" by the squirmer, hence the name pusher. On the other hand, the flow around a $\beta > 0$ squirmer looks like the fluid is being "pulled" away from the squirmer, hence it is called puller. The red arrows show the hydrodynamic interactions of the laterally perturbed squirmers with the flow field induced by them. These interactions attract a pusher towards its original straight trajectory making it stable as opposed to puller which is knocked away from the original straight trajectory. The vorticity scale is same for both (a) and (b). The far-field flow decays as $\approx r^{-3}$ for inertial squirmers (see Fig. 8.7). Hence the streamlines away from the squirmers are identical. However, the streamlines are distinct for a puller and a pusher very close to their bodies. There is a recirculatory bubble in front of the pusher and behind the puller. c) Problem setup for an inertial squirmer in a linearly stratified fluid. z_i is the vertical position where we initialize the squirmer. The coordinate system is the same in the subsequent figures wherever relevant.

approximation for simplifying the Navier-Stokes equations for a fluid flow of a density stratified fluid. So, the governing equations are,

$$\rho_0 \frac{\mathrm{D}\mathbf{u}}{\mathrm{D}t} = -\nabla P + \mu \nabla^2 \mathbf{u} + (\rho - \bar{\rho})\mathbf{g} + \mathbf{f}, \text{ in } \boldsymbol{\Omega}, \tag{8.3}$$

$$\nabla \cdot \mathbf{u} = \mathbf{0}, \text{ in } \boldsymbol{\Omega}, \tag{8.4}$$

where t is the time, $\mathbf{u}$ is the velocity vector, P is the hydrodynamic pressure, $\mathbf{g}$ is the acceleration due to gravity, μ is the dynamic viscosity of the fluid, ρ_0 is the reference fluid density and $\bar{\rho}$ is the volumetric average of the density over the entire domain. $D()/Dt$ is the material derivative. We use the phase indicator function ϕ to distinguish the inside and outside of the squirmer. ϕ is 1 inside the squirmer and 0 outside. So, the density, ρ, can be written as, $\rho = \rho_f(1-\phi) + \phi\rho_s$, where the subscript f stands for fluid and s for squirmer. $\mathbf{f}$ in equation 8.3 is the body force which is required for imposing the rigidity constraint inside the squirmer and accounts for fluid-solid interactions in the Distributed Lagrange Multiplier (DLM) method [295]. DLM has been extensively used to investigate the motion of rigid particles and model swimmers in both homogeneous and stratified fluids [280], [292], [296]–[299].

The temporal and spatial evolution of the density is governed by,

$$\frac{\mathrm{D}\rho}{\mathrm{D}t} = \kappa \nabla^2 \rho, \text{ in } \Omega, \tag{8.5}$$

here κ is the diffusivity of the stratifying agent and ρ is the density field. Prandtl number $Pr = \nu/\kappa$, describes the ratio of the momentum diffusivity to the diffusivity of the stratifying agent. We discretized equations 8.3-8.5 on a non-uniform staggered Cartesian fixed grid using a finite volume method [300]. We used first order Euler method for temporal evolution while convection and diffusion terms in momentum and density transport equations have been solved using QUICK (quadratic upstream interpolation for convective kinetics) and central-difference scheme [301], respectively. We initialize the squirmer at a vertical location z_{i} on the center-line of the domain directed in the positive z direction in a domain $9d \times 9d \times 80d$. The initial density of the fluid varies linearly with depth z as $\rho_f = \rho_0 + \gamma(z)$, where γ is the vertical density gradient. We use periodic boundary conditions for velocity and density in x and y directions while the boundary conditions for density and velocity on top and bottom boundaries are $\frac{\partial \rho}{\partial z} = \gamma$ and $\frac{\partial \mathbf{u}}{\partial z} = \mathbf{0}$, respectively. The stratification strength can be quantified by the Brunt–Väisälä frequency, $N = (\gamma g/\rho_0)^{1/2}$, the characteristic oscillation frequency of a fluid parcel displaced vertically from its neutrally buoyant position in a density stratified fluid.

8.2.2 Swimmer model: reduced squirmer

To model the swimmer, we use the squirmer model [271], [272] which has been widely used as a model for swimmers like *Volvox* in the literature [302]. Recently, researchers have studied the effect of finite inertia on the motion of swimmers by extending the squirmer model to low and intermediate Re number regimes [277], [279], [280], [292], [303], [304]. The squirmer self-propels by wavelike motion of its surface.

For this study we consider a reduced order squirmer which has no radial velocity and only the first two modes of the surface tangential velocity. A reduced order squirmer has been used extensively in literature to study the mechanisms of locomotion in a variety of flow conditions [302]. The reduced order squirmer can be thought of as a squirmer with only steady tangential motion on its surface ($A_n = 0$ and $B_n =$ constant). Further simplification is obtained by considering only the first two modes in the tangential motion giving,

$$u_r^s|_{r=a} = 0, \tag{8.6}$$

$$u_\theta^s(\theta) = B_1 \mathrm{sin}\theta + B_2 \mathrm{sin}\theta \mathrm{cos}\theta, \tag{8.7}$$

in the frame of reference moving with the squirmer. Here θ is the angle with respect to the swimming direction, and B_1 and B_2 are the first two squirming modes. In Stokes flow limit, the velocity of a squirmer in an infinite domain is $U_0 = 2B_1/3$, we use this as the velocity scale in this study. Furthermore, a reduced order squirmer can be categorised based on the sign of $\beta = B_2/B_1$ [274], [280]. A squirmer with $\beta < 0$ is called a pusher and a squirmer with $\beta > 0$ is called a puller. See Fig. 8.1a and 8.1b for details.

To impose the above given tangential velocity (eq. 8.7) on the squirmer surface, we set the following divergence free velocity field inside the squirmer [303],

$$\mathbf{u}_{\text{in}} = \left[\left(\frac{r}{a}\right)^m - \left(\frac{r}{a}\right)^{m+1}\right]\left(u_\theta^s \cot\theta + \frac{du_\theta^s}{d\theta}\right)\mathbf{e}_r + \left[(m+3)\left(\frac{r}{a}\right)^{m+1} - (m+2)\left(\frac{r}{a}\right)^m\right]u_\theta^s \mathbf{e}_\theta, \tag{8.8}$$

here a is the radius of the squirmer, r is the distance from the squirmer's center, $\mathbf{e}_r$ and $\mathbf{e}_\theta$ are the unit vectors in the radial and polar directions, and m is any integer. The simulation results do not depend on the choice of m. This is because the expression for $\mathbf{u}_{\text{in}}$ is divergence free and recovers eq. 8.6 and 8.7 at the squirmer surface locations irrespective the value of m. The squirmer velocity is calculated by solving the following equations:

$$\mathbf{U} = \frac{1}{M_p}\int_{V_p} \rho_s(\mathbf{u} - \mathbf{u}_{\text{in}})dV, \tag{8.9}$$

$$\mathbf{I_s}\boldsymbol{\omega} = \int_{V_p} \mathbf{r} \times \rho_s(\mathbf{u} - \mathbf{u}_{\text{in}})dV, \tag{8.10}$$

where V_p, M_p, and $\mathbf{I_s}$ are volume, mass and the moment of inertia of the squirmer. $\mathbf{U}$ and $\boldsymbol{\omega}$ is the translational and the rotational velocity of the squirmer. Finally, the force $\mathbf{f}$ is calculated by the following iterative formula:

$$\mathbf{f} = \mathbf{f}^* + \alpha\frac{\rho\phi}{\Delta t}(\mathbf{U} + \boldsymbol{\omega} \times \mathbf{r} + \mathbf{u}_{\text{in}} - \mathbf{u}), \tag{8.11}$$

where $\mathbf{f}^*$ is the force calculated in the previous iteration and α is a dimensionless factor chosen in such a way that iterations for calculating $\mathbf{f}$ converge quickly [280], [299]. The iterations are performed until the maximum of Euclidean norm of $(\mathbf{f} - \mathbf{f}^*)/\mathbf{f}$ and the normalized residue $(\int_{V_p} |(\mathbf{U} + \boldsymbol{\omega} \times \mathbf{r} + \mathbf{u}_{\text{in}} - \mathbf{u}|dV/U_0V_p)$ falls below 10^{-3}.

8.2.3 Simulation conditions

Many organisms utilize techniques like ion exchange [305], [306], gas vesicles [307], and/or carbohydrate ballasting [308] for buoyancy control [286]. Hence, for this study in order to isolate the effect of stratification on the motion of a squirmer, we consider the squirmer to be neutrally buoyant, i.e., there is no net buoyancy force acting on them due to difference in the density with the background fluid. This is achieved by setting the squirmer density equal to the background fluid density at its instantaneous location. As a result, ρ_s changes as the squirmers moves. We assume the κ to be the same for the squirmer and the fluid [292], [309]. The squirmer is free to move and rotate and its translational and angular positions are calculated by integrating the translational and rotational velocities forward in time.

If we do not consider the swimmers to be neutrally buoyant, then they have a different density compared to the background fluid. This means that, they will have two main contributions which will determine their swimming speeds. 1) their self-propulsion due to the surface velocity and 2) the settling/rising motion due to the difference in density with the background fluid.

If the swimmers are close to their neutrally buoyant level in the fluid, i.e., the depth of the fluid where the fluid density is equal to the squirmer density, then we expect them to swim till they reach their neutrally buoyant level where they might either oscillate or stop or get deflected in the horizontal direction depending on their β and the stratification strength. This kind of mechanism might be leading to the accumulation of phytoplanktons in the oceans. In all these cases, they get trapped at their neutrally buoyant levels due to the reduction of their vertical swimming velocity to 0. This is similar to what happens in the case of a heavy sphere settling [299] or a drop rising [310] in a stratified fluid. Their settling/rising velocity gradually decreases and becomes 0 as they reach their neutrally buoyant levels. If the swimmers are far away from their neutrally buoyant levels, then there will be a huge difference in the fluid and swimmer density resulting in a strong heavy sphere like settling motion as the buoyancy force will dominate. But they will not attain a steady state velocity as it will decrease with time but at a slower rate than the first case. In any of these cases, we do not expect the squirmers to reach a steady velocity. We discuss more on this in Sec. 8.3.5. Hence, we consider the squirmers to be neutrally buoyant so that we can specifically study the effect of stratification on the swimmer motion.

In many real-life situations, the swimmers move in the vertical direction such that they are parallel to the direction of the stratification or gravity mainly for grazing or in the search of the sunlight during their diel cycles [311]–[313]. In addition, the direction of the motion considered in this study is one of the common situations for swimmers moving in oceans, e.g., bioconvection [314]. So, we initialize the squirmers with their initial orientations in the direction of gravity, i.e., downwards. Since the squirmers considered here are neutrally buoyant, they will exhibit the similar dynamics even if they move against the direction of gravity, i.e., upwards. We also performed a few simulations with the initial squirmer orientation perpendicular to the direction of gravity, i.e., horizontal. In this case, the squirmers move with similar speeds and exhibit the similar dynamics as they do in a homogeneous fluid. More details on the effect of the initial squirmer orientation on their dynamics is presented in Sec. 8.3.6.

8.2.4 Validation: Grid and domain independence

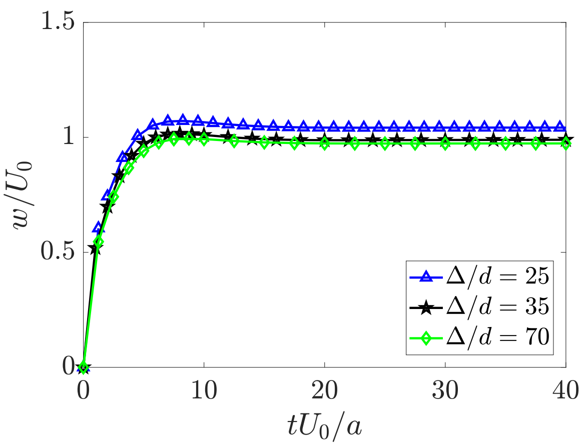

(a) Grid independence

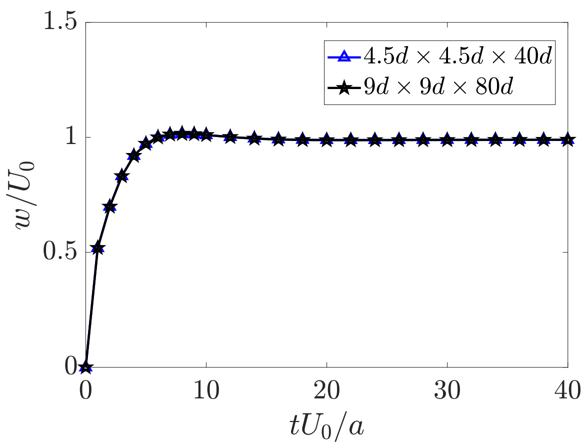

(b) Domain independence

Figure 8.2. a) Grid independence test for three different grid sizes. The plot shows z-velocity evolution for a pusher with $\beta = -1$ at $Re = 25$. b) Domain independence test for two different grid sizes. The plot shows z-velocity evolution for a pusher with $\beta = -1$ at $Re = 25$ and $Fr = 5$.

Here we present the grid and domain independence tests of the computer program utilized for this chapter. Fig. 8.2a shows the effect of three grid sizes with 70 grid points per diameter, 35 grid points per diameter and 25 grid points per diameter on the velocity evolution of a pusher with $\beta = -1$ moving at $Re = 25$. The change in the swimming speed from 25 grid points to 35 grid points is 5.2 % which reduces to 1.5 % from 35 grid points to 70 grid points per diameter. So we run all the simulations for a grid size with 35 grid points per squirmer diameter in all the cases.

Fig. 8.2b shows the effect of changing the domain size. We tested two domain sizes $4.5d \times 4.5d \times 40d$ and $9d \times 9d \times 80d$. The results are the same for both the domain sizes with less than 0.1 % deviation. Hence we run all the simulations for a domain size $9d \times 9d \times 80d$.

Additional validations can be found in [299] (for dynamics of a spherical object in a linearly stratified fluid) and [280] (for dynamics of inertial squirmers in a homogeneous fluid).

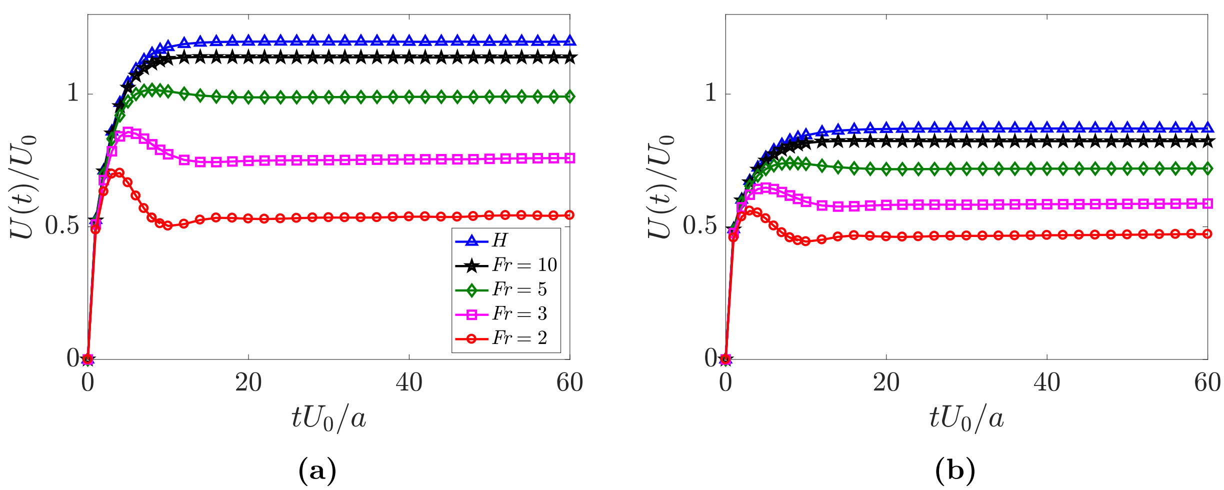

Figure 8.3. Effect of stratification on the velocity evolution of squirmers with $Re = 25$ for a a) pusher, β = -1, b) puller, β = 1. The velocity has been normalized with the steady state squirmer velocity in Stokes flow, i.e., $U_0 = 2B_1/3$ and the time has been made dimensionless with the time scale a/U_0. H = homogeneous fluid. The legends are the same for both the plots. These plots show that increasing the stratification leads to a reduction in the squirmer swimming speeds.

8.3 Results and discussion

This section presents the results for the motion of a squirmer at finite Re in a linearly stratified fluid. The velocities are normalized by the velocity scale U_0 and the time has been normalized by the time scale a/U_0. The mesh size was chosen such that there are 35 grid points across the diameter of the squirmer. We performed simulations for $Re = \rho_0 U_0 a/\mu$

ranging from 5 to 100 and for $\beta = \pm 3, \pm 1$. We vary the Froude number, $Fr = U_0/Na$ from 10 to 1 and also compare the velocities with the velocity of a squirmer in a homogeneous fluid. The Brunt–Väisälä frequency, $N = (\gamma g/\rho_0)^{1/2}$, where γ is the density gradient.

The Prandtl number, Pr for salt stratified water is 700 and for temperature stratified water it is 7. But, we set the Prandtl number Pr to be equal to 0.7. This has been done mainly to resolve the density boundary layer which scales as $O(d/\sqrt{PrRe})$ where d is the diameter of the object. This means as long as the velocity boundary layer is resolved, the density boundary layer is also well resolved. Previous studies on the effect of Pr on the settling velocity of a rigid sphere have shown that changing the Pr changes the magnitudes of the flow variables and velocity of the object, but the overall behavior and trends remain the same [299]. We also present results for $Pr = 7$ to show that this is also true for a squirmer along with grid and domain independence tests in Sec. 8.2.4.

To explain the results we present the streamlines, vorticity field and the density difference contours (isopycnals) in the frame of reference of a steadily moving squirmer. We also study the effect of stratification on the power expenditure and the mixing efficiency by a squirmer.

8.3.1 Stratification slows down the squirmer

Fig. 8.3 shows the time evolution of the swimming speed ($U(t)$ denotes the time dependent squirmer speed in the vertical or parallel to initial squirmer orientation) of a pusher and a puller with $Re = 25$ in homogeneous and stratified fluids. It has been shown that increasing the inertia leads to an increase in the swimming speed of pushers and a reduction in the swimming speeds of pullers [277], [279], [280] in a homogeneous fluid compared to their speeds in Stokes flow limits. Thus, the results plotted in Fig. 8.3 for homogeneous fluid are consistent with the previous studies [277], [279], [280]. We initialize the squirmer with a zero velocity orientated along the direction of gravity. The velocity reaches a steady state after the initial transient dynamics. The steady state squirmer velocity can be obtained by taking a time average once the transients die out. As we increase the stratification strength, i.e., reduce the Fr, we observe that the swimming speed of both pusher and puller decreases.

To quantify the effect of stratification on the the swimming speed reduction, we plot the steady state swimming speed U, scaled by the steady state velocity of the squirmers in a

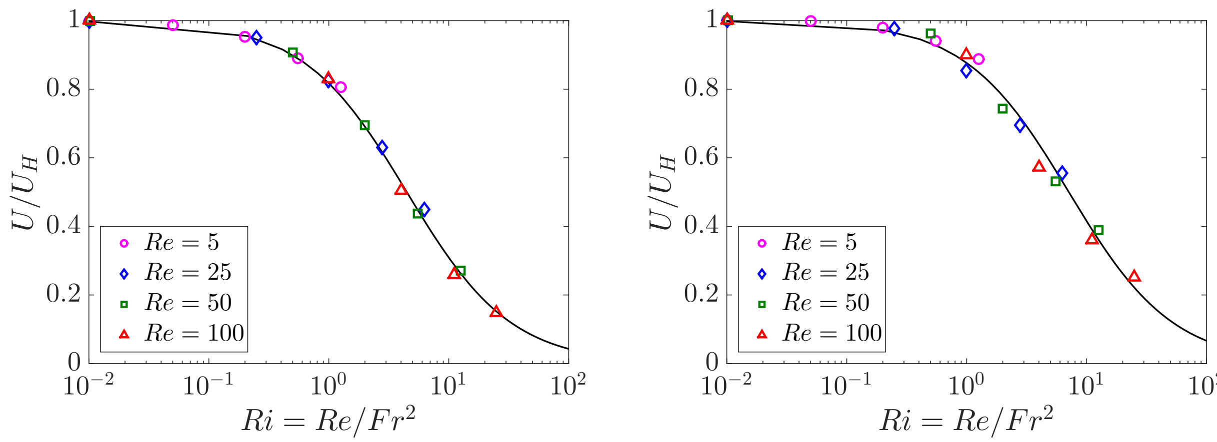

(a) **(b)**

Figure 8.4. Effect of stratification on steady state swimming speed U of a a) pusher, $\beta = -1$ ($a = b = 4.48$), b) puller, $\beta = 1$ ($a = b = 7.11$) for different Ri. The solid line represents a curve fit with $U/U_H = a/(R\mathrm{i} + b)$. The steady state state swimming speed U has been normalized with squirmer's steady state swimming speed in a homogeneous fluid (U_H) at the same Re.

homogeneous fluid at the same Re as a function of Richardson number, $R\mathrm{i} = R\mathrm{e}/Fr^2$. U is calculated by taking time-average of the squirmer velocity once it reaches a steady state, i.e., from $tU_0/a = 20 - 60$. Fig. 8.4 shows the effect of increasing the stratification on the steady velocity of a pusher and puller for different Re and Ri values. The plots indicate that for $R\mathrm{i} \approx O(1)$ the reduction in the swimming speed is about 20 % while for higher $R\mathrm{i} \approx O(10)$ the reduction is more than 50 % from their velocities in a homogeneous fluid. These results are consistent with low but finite Re (= 0.5) squirmer dynamics in a stratified fluid [293]. Please note that the squirmers reach a steady velocity only if they are stable. It has been shown that the squirmers remain steady even at high inertia if $|\beta| <= 1$ [279]. However, for $\beta > 1$, the pullers become unstable in a homogeneous fluid for $R\mathrm{e} \approx O(10)$. Hence, we present results for $|\beta| = 1$ in Fig. 8.4 as the squirmers with $|\beta| = 1$ are stable at all Re investigated in this study.

Stratification affects the motion of a pusher more than a puller which is apparent as reduction in the velocity for a pusher is more for the same Ri. Plotting the data against Ri reveals that Ri is the fundamental parameter determining the velocity of the squirmer (See

Fig. 8.4) compared to their swimming velocities for the same Re in a homogeneous fluid. We fit the data with the following equation:

$$\frac{U}{U_H} = \frac{a}{Ri + b}, \tag{8.12}$$

where a and b are the fitting constants which depend on the value of β. Thus giving us an $O(Ri^{-1})$ dependence for the swimming speed of the squirmers.

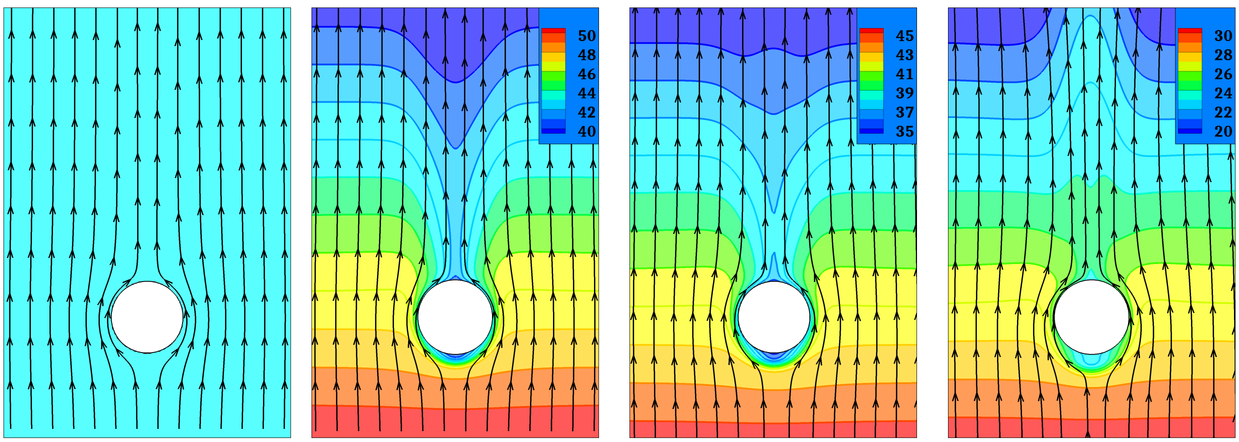

(a) $Re = 50$, $Fr \to \infty$ **(b)** $Re = 50$, $Fr = 7$ **(c)** $Re = 50$, $Fr = 5$ **(d)** $Re = 50$, $Fr = 3$

Figure 8.5. Normalized density difference ($(\rho - \rho_0)/(\gamma a)$) contours (isopycnals) for a pusher ($\beta = -3$) at different Fr. The lines with arrows are the streamlines in the frame of reference attached to the swimmer. A pusher entrains lighter density fluid in the vorticity bubble in its front. This results in a higher buoyancy force as it moves down in a heavier fluid and hence a reduction in its swimming speed. Stratification also leads to expansion of this vorticity bubble which means the vorticity generated at the pusher's surface cannot advect to the downstream as easily as it does in a homogeneous fluid. As a result, a pusher becomes unstable and the flow around it breaks axisymmetry in strong stratifications. The coordinate system is the same as in Fig. 8.1c hence not shown here.

A pusher propels forward by "pushing" the fluid on its sides to in front and behind it as shown in the cartoon in Fig. 8.1a. In a homogeneous fluid, the pusher (shown by dashed lines in Fig. 8.1a) is pushed forward by the flow field generated by itself at an earlier time (shown by solid lines in Fig. 8.1a). This results in a rise in the swimming speed of a pusher as its inertia increases in a homogeneous fluid. However, as the pusher moves in a stratified fluid, it experiences a higher resistance in maintaining the flow field around it. This is due to

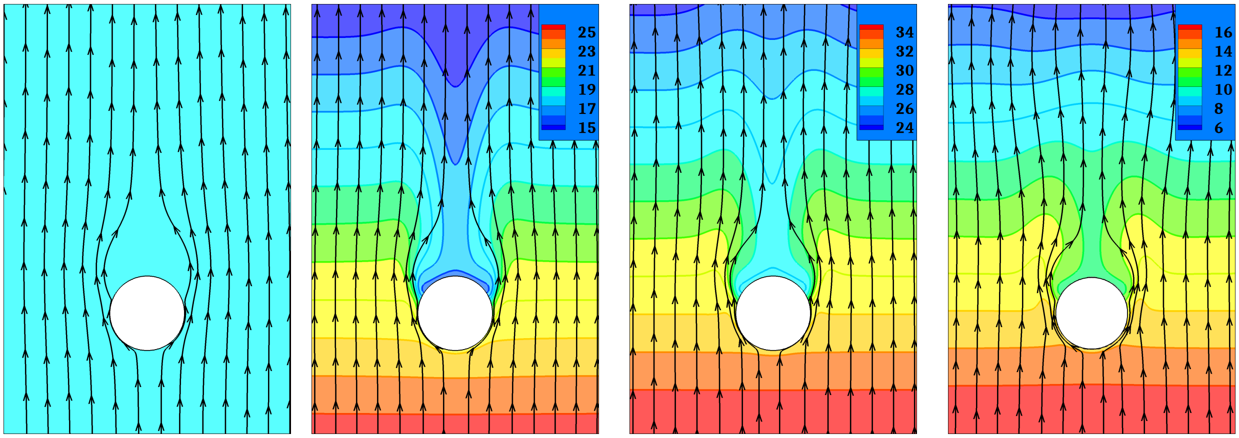

(a) $Re = 50,\ Fr \to \infty$ **(b)** $Re = 50,\ Fr = 7$ **(c)** $Re = 50,\ Fr = 5$ **(d)** $Re = 50,\ Fr = 3$

Figure 8.6. Normalized density difference ($(\rho - \rho_0)/(\gamma a)$) contours (isopycnals) for a puller ($\beta = 3$) at different Fr. The lines with arrows are the streamlines in the frame of reference attached to the swimmer. A puller entrains lighter density fluid in the vorticity bubble in its rear. This results in a higher buoyancy force as it moves down or in a heavier fluid and hence a reduction in its swimming speed. A puller also pulls the heavier fluid around it upwards as it swims. These heavier isopycnals assist the swimming of the puller as they drag the puller with them while they try to resettle to their neutrally buoyant positions. Stratification also leads to contraction of this vorticity bubble size which means the resistance to the vorticity advection to the downstream decreases as we increase stratification. As a result, a puller becomes stable and the flow around it remains axisymmetric even at high Re for a strong stratification. The coordinate system is the same as in Fig. 8.1c hence not shown here.

the fact that, it essentially needs to push the packets of fluid around it to regions where the fluid packets experience higher buoyancy forces. The fluid which the pusher pushes upwards, i.e., behind it, is heavier than the fluid it is getting pushed into, i.e., fluid at the top and vice versa for the fluid which the pusher pushes downwards.

The hindrance in maintaining the flow field around the pusher increases with increasing the stratification. This is because the exigency of the isopycnals to return to their neutrally buoyant positions as the squirmers deform them, increases with the stratification strength. The secondary flow generated due to this phenomenon directly opposes the primary flow generated by the squirmers to propel themselves. As the stratification increases, the isopycnals can return to their neutrally buoyant positions quickly, resulting in smaller isopycnal deformations and hence, offer higher resistance to the flow generated by the squirmers which reduces its swimming speed. This becomes clear by comparing the deformations in the isopycnals just behind the pusher as we increase the stratification. The hindrance to the flow field generated by the pusher is higher if the isopycnals undergo little deformations. The isopycnals with increasing stratification are plotted in Fig. 8.5. The isopycnals offer higher resistance to their deformation as the stratification increases which essentially resists the pushing of the fluid by a pusher. This is expected as the exigency of the deformed isopycnals to return to their neutrally buoyant positions increases with increasing the stratification strength. This is one of the reasons which leads to the reduction in the swimming speed of a pusher with increasing stratification as shown in Fig. 8.4a.

As the inertia of the pusher increases in a homogeneous fluid, the recirculatory region in front of and behind it shrinks leading to efficient downstream advection of the vorticity generated on its surface. As a result, its swimming speed increases with increasing the inertia in a homogeneous fluid. However, in a stratified fluid, the size of these recirculatory regions increases as we increase the stratification (see Fig. 8.6 and 8.11). In addition, the pusher entrains the lighter fluid in this recirculatory bubble in front of it. So, as the pusher moves, it has to push this blob of the lighter fluid into a heavier fluid in front of it. This results in a higher buoyancy force opposite to the motion of a pusher reducing its swimming speed. Increasing the stratification strength increases the size of this blob of the lighter fluid in front of the pusher owing to the increase in the size of the recirculatory region. This effect can be seen by comparing the size of the lighter fluid blobs in front of the pushers in Fig. 8.5b, 8.5c and 8.5d or the size of the vorticity bubbles in front of the pushers in Fig. 8.10b, 8.10c and 8.10d.

Unlike the pusher, a puller propels forward by "pulling" the fluid in front and behind its body to its sides as shown in the cartoon in Fig. 8.1b. In a homogeneous fluid, the puller (shown by dashed lines in Fig. 8.1b) is pulled back by the flow field generated by itself at an earlier time (shown by solid lines in Fig. 8.1b). In addition, the fluid flow behind the puller obstructs the downstream advection of the vorticity generated on the pullers surface with increase in the inertia of the puller. The combined impact of these effects is the reduction in the puller's velocity as its inertia increases in a homogeneous fluid. Thus, any hindrance to the flow field generate by a puller in front and behind it will result in an inefficient downstream advection of the vorticity resulting in a slower swimming puller.

Similar to a pusher in a stratified fluid, the density stratification offers a significant resistance to generate the flow field around a puller as it swims. This is because the puller has to pull the fluid packets in front and behind it from their neutrally buoyant positions to a region where the fluid packets experience a buoyancy force. E.g., the fluid which the puller pulls downwards behind it is lighter than the fluid it is getting pulled into, i.e., the fluid on the sides of the puller and vice versa for the fluid which the puller pulls upwards. Again, the hindrance to the flow field generation by a puller can be visualized in terms of the deformations of the isopycnals around a puller at various stratification strengths. The isopycnals around a puller with increasing stratification are plotted in Fig. 8.6. The deformations in the isopycnals significantly reduce with increasing the stratification strength which becomes clear by comparing the deformations of the isopycnals in the wake of the pullers in Fig. 8.6b, 8.6c and 8.6d.

A puller entrains a lighter fluid in its rear recirculatory region. Thus, a puller has to drag this lighter blob of fluid with it as it moves into the heavier fluid below it. This results in a buoyancy force on the puller in the opposite direction to its motion resulting in a reduction in its swimming speed. But unlike the case of a pusher, the size of this recirculatory region behind a puller decreases with an increase in the stratification strength. This shrinkage can be seen by comparing the size of the lighter fluid blobs behind the pullers in Fig. 8.6b, 8.6c and 8.6d or the size of the vorticity bubbles behind the pullers in Fig. 8.11b, 8.11c and 8.11d. As a result, the size of the blob of the lighter fluid that a puller has to pull with it also reduces which is opposite to what happens in the case of a pusher moving in a stratified fluid. This explains the relatively lower reduction in the swimming speed of a puller than a pusher at the same $R\mathrm{i}$.

In addition to the squirmer speed, it is also interesting to look at the far-field velocity away from the squirmers. The far-field velocity for squirmers in a homogeneous fluid at $R\mathrm{e} = 0$. i.e., in the absence of inertia decays as $|w| \approx r^{-2}$. If the squirmers posses a finite inertia, then the fluid velocity in the swimming direction of the squirmers decays as $|w| \approx r^{-3}$ [280], [315]. We observe the same far-field flow structure in the squirmer swimming direction,

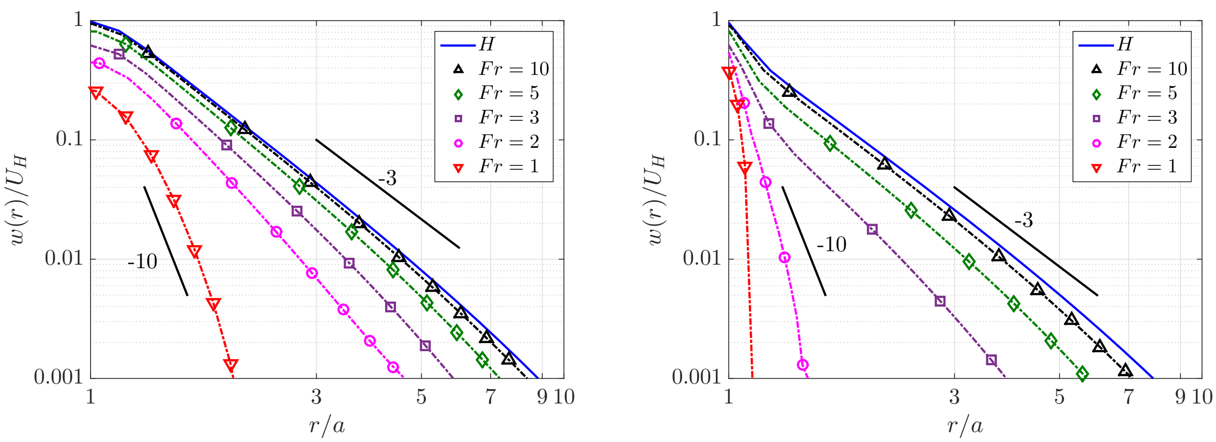

(a) **(b)**

Figure 8.7. Effect of stratification on the far-field flow structure in the swimming direction of the inertial squirmers ($Re = 25$) with increasing stratification strength. a) Pusher with $\beta = -1$. b) Puller with $\beta = 1$. Here $r/a = 1$ is at the velocity at the squirmer surface and increasing r/a gives the locations in front of the squirmers in the downward direction along their axes (shown by dash-dotted lines in Fig. 8.1). H in the legends stands for homogeneous fluid. The black solid lines are for comparison and show r^{-3} and r^{-10} decay. The velocity has been made dimensionless by the steady state squirmer speeds in a homogeneous fluid, U_H.

i.e, $|w| \approx r^{-3}$, for the squirmers moving in a homogeneous fluid with a finite inertia as shown in Fig. 8.7. Introducing stratification further hastens this decay with r from the squirmer in the swimming direction as shown in Fig. 8.7a and 8.7b for pushers and pullers, respectively. Figure 8.7 shows that the decay exponent of the far-field velocity in the swimming direction of the squirmers reduces significantly from ≈ -3 in a homogeneous fluid to ≈ -10 in a strongly stratified fluid with $Fr = 1$. These results are consistent with previous studies which show that the effect of stratification is to suppress the vertical motion of the fluid [251], [284], [299]. The velocity field decays less rapidly for a pusher as compared to a puller at higher stratification strength owing to the increase in the vorticity bubble ahead of a pusher which expands as the stratification strength increases.

8.3.2 Strong stratification stabilizes a puller but destabilizes a pusher at intermediate Re

In a homogeneous fluid, a pusher is stable at high Re in the sense that the flow around it maintains a steady axisymmetry and it does not become unsteady 3D as opposed to the flow around a puller which becomes unsteady 3D at $Re \approx O(10)$ [279], [280]. This breaking of the flow axisymmetry eventually makes the puller unstable beyond a critical Re. For the purpose of this study, we say that a squirmer is unstable once the axisymmetry of the flow around it breaks and it becomes unsteady.

A look at the flow fields around the squirmers predicts that the hydrodynamic interactions between the velocity fields induced by the inertial squirmers with their bodies is the reason behind these observations. An inertial puller (pusher) perturbed from its straight line trajectory is pushed away (pulled towards) the original trajectory due to these hydrodynamic interactions making it unstable (stable) at high Re ([280], & Fig. 8.1a, 8.1b). To gain further insight into why this is the case, we need to look at the vorticity field around a puller and a pusher. Pullers form a recirculatory region just behind them which is shown in Fig. 8.6a (streamlines are not shown inside the recirculatory region for the neatness of the plot). As we increase Re for a puller, the size of this bubble increases. At some critical Re determined by β, this bubble becomes so large that it hinders the convection of the vorticity produced on the surface of the squirmer to the downstream leading to instability and breaking the axisymmetry of the flow around the puller. On the contrary to pullers, pushers have the recirculatory region in front of them (Fig. 8.5a) and its size reduces with increasing Re. As a result, the vorticity produced on pusher's surface can be easily advected to the downstream making it eternally stable in a homogeneous fluid ([279] & Fig. 8.5a, 8.6a). We observe the same behavior for pullers and pushers with high Re in a homogeneous fluid. The puller fails to attain any steady velocity, becomes unsteady and suddenly follows a 3D motion while a pusher is always steady in a homogeneous fluid (Fig. 8.9a & 8.9b for $Fr \to \infty$).

At intermediate Re, we expect the puller to become stable at high enough stratification strengths and a pusher to be unstable at strong stratification strengths which is exactly opposite of what is observed in a homogeneous fluid. For an inertial squirmer in a stratified fluid, there are two competing effects which influence the stability of the squirmer: i) the

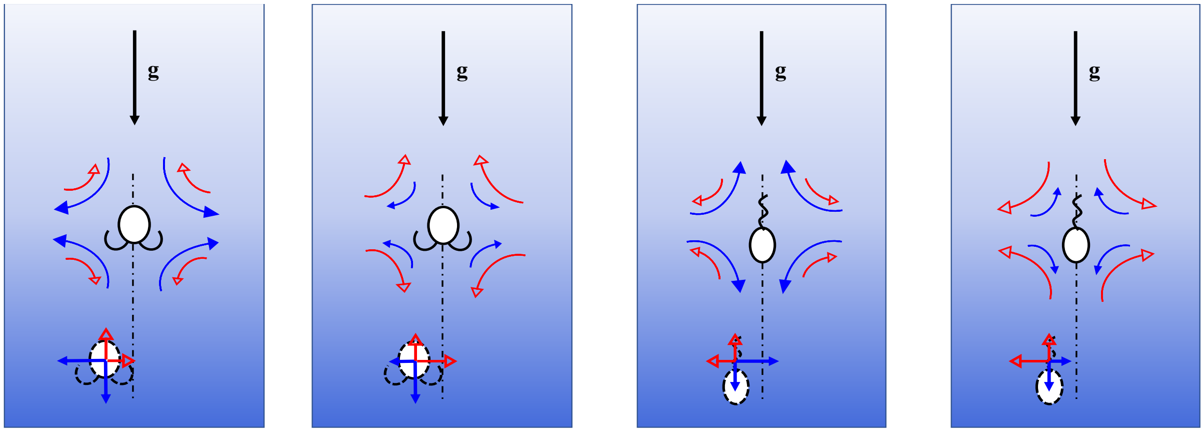

(a) Puller in weak stratification

(b) Puller in strong stratification

(c) Pusher in weak stratification

(d) Pusher in strong stratification

Figure 8.8. Competition between the inertial and the stratification effects for a puller (a, b) and a pusher (c, d) in a weak and strong stratification. Curved arrows with filled heads (blue) denote the velocity fields induced by the squirmers (i.e., inertial effect) and arrows with hollow heads (red) denote the flow field induced by the exigency of the displaced isopycnals to return to their original position (i.e., stratification effect) at an earlier time, i.e., by the squirmer shown by solid lines. Sizes of the horizontal arrows on the perturbed squirmers show the relative magnitudes of these competing effects on the squirmer at the present time, i.e., on the squirmer shown by dotted lines. The laterally perturbed squirmer (denoted by dotted outline) is either attracted towards its original trajectory (b & c, stable squirmers) or is knocked away from the original trajectory (a & d, unstable squirmers) depending on the relative strength of these competing effects. Vertical arrows show the tendency of the squirmers to propel forward (blue) and the effect of stratification which hinders the forward propulsion of the squirmers (red). The vertical arrows are just for showing the directions of the respective effects and are not scaled. The flow-field description here is approximate and is not up to scale. The coordinate system is the same as in Fig. 8.1c hence not shown here.

hydrodynamic interactions between the squirmer body and the flow field induced by its motion (inertial effect), and ii) the secondary flow generated by the exigency of the isopycnals displaced by the motion of the squirmer to resettle to their original positions (stratification effect). These two effects are competing because the flow field induced by the squirmers displaces the density stratified fluid around it in such a way that it has to go against the squirmer induced primary velocity field to return to its neutrally buoyant position creating a secondary flow, e.g., a pusher pushes the fluid around it downwards and upwards. The isopycnal that is pushed downwards (upwards) is flowing into a heavier (lighter) fluid, so as it tries to return to its original position, it has to flow opposite to the primary flow induced by the pusher.

In Fig. 8.8, we visualize the effects of the primary and the secondary flows on the squirmers by arrows showing directions of the flows with their sizes indicating the strengths of these effects. For a puller (pusher) perturbed from its initial straight line trajectory, the inertial effect tries to push it away (pull it closer) while the stratification effect tries to pull it closer to (push it away from) the original trajectory. Consequently for a particular Re, at low enough Fr, the stratification effect wins making the motion of the puller (pusher) stable (unstable). This is indeed true and can be seen easily in Fig. 8.9a and 8.9b which show that a puller which is unsteady in weak stratification becomes steady in strong stratifications and vice versa for a pusher.

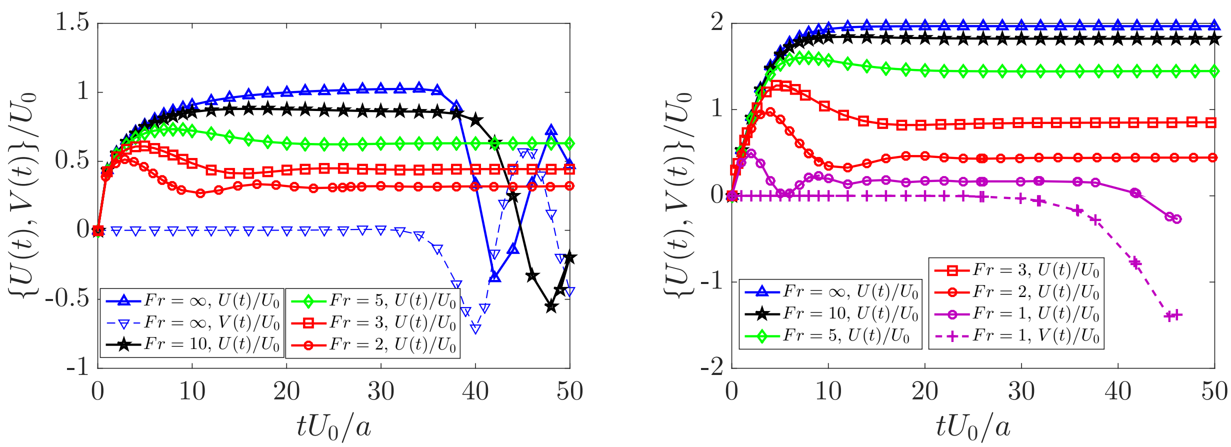

(a) $Re = 50$, $\beta = 3$ **(b)** $Re = 50$, $\beta = -3$

Figure 8.9. Effect of stratification on velocity history of squirmers. Swimming velocity evolution in vertical ($U(t)$) and horizontal direction ($V(t)$) for a a) puller with $\beta = 3$ and b) pusher with β = -3. Pullers become unstable and the flow around them becomes 3D as we increase their inertia in a homogeneous fluid. Increasing stratification makes the motion of a puller steady and stable. On the other hand, a pusher is stable and the flow around it is axisymmetric for Re as high as 1000 in a homogeneous fluid. Pushers are stable at low stratification strength, but become unstable for a strong stratification or at a large Ri. The other components of velocity remain 0 hence not shown.

Stratification affects the stability of squirmers at finite Re in interesting ways compared to the homogeneous case as discussed earlier. Pullers which are unstable in a homogeneous fluid at high Re become stable and the flow around them remains axisymmetric for a high enough stratification. A puller with $\beta = 3$ at $Re = 50$ is unstable in a homogeneous fluid and for a weak stratification ($Fr = 10$), but it becomes stable for higher stratifications ($Fr < 8$) (See Fig. 8.9a). The effect of the stratification is to reduce the size of the vorticity bubble behind the pullers. The exigency of the heavier isopycnals pulled upwards by the puller to go back to their neutrally buoyant level is the reason behind this reduction in its size. This reduction in the recirculatory bubble size with increasing stratification is apparent from Fig. 8.6 and 8.11. Thus the advection of the vorticity produced at the puller's surface improves with increasing stratification which consequently makes the puller stable.

A pusher which is always stable in a homogeneous fluid for Re as high as 1000, however becomes unstable at very strong stratification (See Fig. 8.9b) as the flow around it becomes unsteady 3D. With increasing stratification, there are two mechanisms at play: i) more rapid restoration of the disturbed isopycnals to their neutrally buoyant level, ii) more entrainment of lighter fluid in the recirculatory region. For a particular Re, as we increase the stratification, both these effects lead to increase in resistance for the vorticity advection for a pusher, eventually breaking axisymmetry of the flow around it. This is because, the size of the recirculatory region in front of a pusher increases as more lighter fluid is trapped (See Fig. 8.5). In addition, the need of the isopycnals to go back to their original level in the downstream of the pusher results in lateral expansion of the vorticity wake behind it (See Fig. 8.10).

Fig. 8.5, 8.6 and Fig. 8.10, 8.11 reveal the similarity between the flow fields generated by the motion of a bubble [310] and a rigid sphere [299] in a stratified fluid with the flow fields around pushers and pullers, respectively. This resemblance in the corresponding flow fields generated by a pusher and a puller with that of a inviscid spherical bubble and a rigid towed sphere is also observed in the case of a homogeneous fluid [279]. A rising bubble and a pusher have a mobile surface which causes the advection of the vorticity downstream. This avoids formation of any wake eddy in the downstream flow of a pusher giving it a long trailing vorticity wake which is similar to that of a rising bubble. On the other hand, the trailing

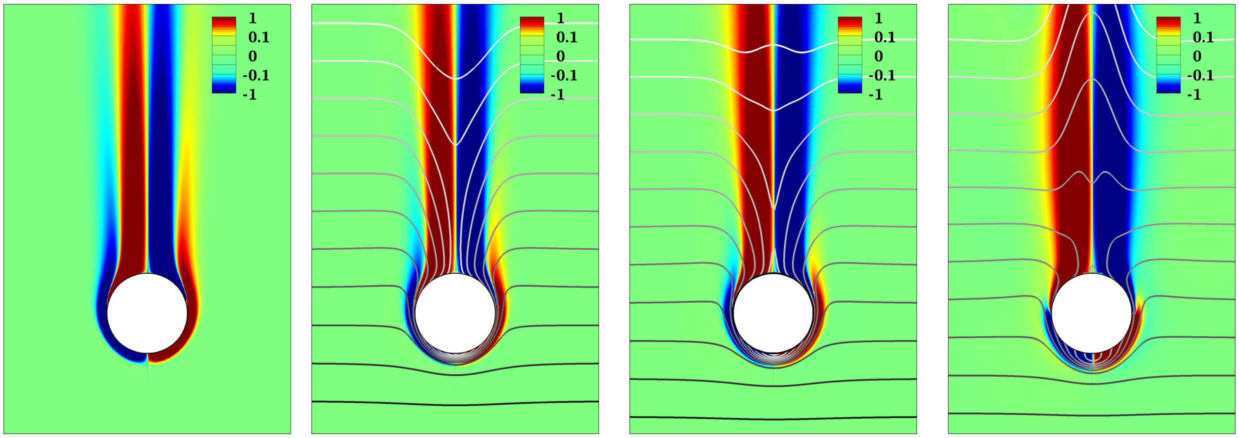

(a) $Re = 50,\ Fr \to \infty$ **(b)** $Re = 50,\ Fr = 7$ **(c)** $Re = 50,\ Fr = 5$ **(d)** $Re = 50,\ Fr = 3$

Figure 8.10. Effect of stratification on the vorticity field around a pusher with $\beta = -3$. Colorbar shows the y-vorticity value. Increasing stratification leads to accumulation of the vorticity in front of a pusher which hinders the advection of vorticity generated in the front part of a pusher to the downstream. (a) shows the vorticity advection in a homogeneous fluid and hence isopycnals are not shown. In (b), (c) and (d) the solid lines denote density differences compared to the reference density ρ_0 and normalized by γa, i.e., $\frac{\rho-\rho_0}{\gamma a}$. Spacing between the lines is 1 unit and darker shade of grey denotes higher density value. The coordinate system is the same as in Fig. 8.1c hence not shown here.

vorticity wake bubble in the case of a puller is similar to the vorticity field behind a settling rigid sphere in a stratified fluid. This is caused by the reversal of the tangential surface velocity of the pusher and is akin to the effect caused by the no-slip boundary condition on the surface of the settling sphere.

Fig. 8.12 summarizes the stable-unstable squirmer motion at all the $Re - Fr$ values explored in this study. We observe that, if a puller is stable in a homogeneous for a given Re, it remains stable in a stratified fluid too (pullers with low $|\beta|$, e.g., $\beta = 1$). However, at higher β, pullers become unstable in a homogeneous fluid for Re $O(10)$. We observed that, at high Re, the pullers are unstable in a homogeneous fluid and weak stratifications, but gradually their motion transitions to a steady state as we increase the stratification. Thus, if a puller is unstable at a particular Re in a homogeneous fluid, it remains unstable in weak stratifications for the same Re but becomes stable if stratification is sufficiently strong. But the critical stratification strength required for a puller to be stable increases with Re. For the pushers, we observed that, the instability in their motion ensues for $Fr \lessapprox 1$ for $Re > 5$

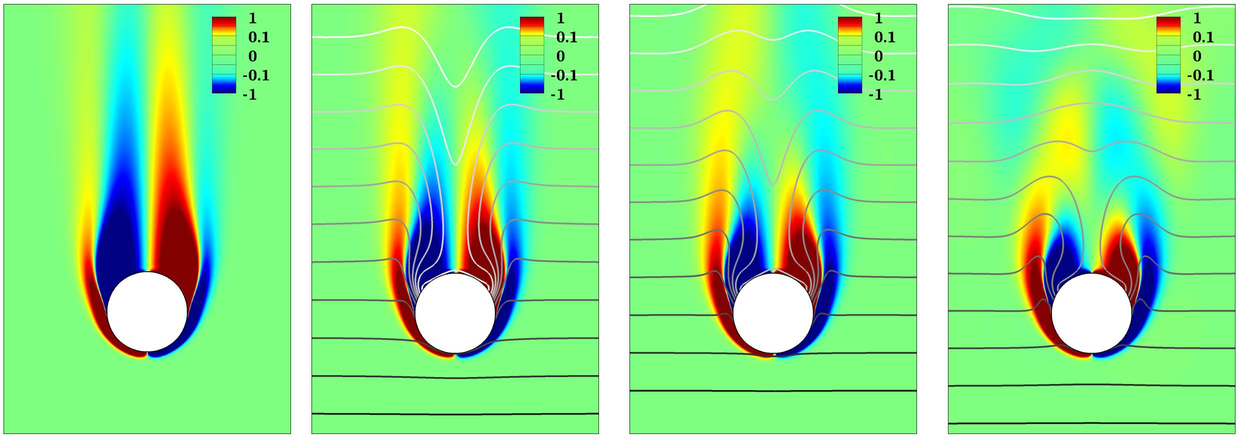

(a) $Re = 50,\ Fr \to \infty$ **(b)** $Re = 50,\ Fr = 7$ **(c)** $Re = 50,\ Fr = 5$ **(d)** $Re = 50,\ Fr = 3$

Figure 8.11. Effect of stratification on the vorticity field around a puller with $\beta = 3$. Colorbar shows the y-vorticity value. Increasing stratification leads to shrinking of the vorticity bubble behind the puller which facilitates the advection of vorticity to the downstream. (a) shows the vorticity advection in a homogeneous fluid and hence isopycnals are not shown. For (b), (c) and (d) the solid lines denote density differences compared to the reference density ρ_0 and normalized by γa, i.e., $\frac{\rho-\rho_0}{\gamma a}$. Spacing between the lines is 1 unit and darker shade of grey denotes higher density value. The coordinate system is the same as in Fig. 8.1c hence not shown here.

explored in this study. Fr gives the relative magnitude of the inertial forces with the effect of the secondary flow due to the displacement of the isopycnals. So, it is expected that as $Fr \lessapprox 1$, a pusher becomes unstable due to the increase in the relative importance of the destabilizing effects due to the density stratification. Also, the finite time required for the onset of instability from the initial time (as can be seen in Fig. 8.9) is due to the time required for the flow solver to reach a solution where initial transients in the velocity field die down. This is consistent with previous studies in a homogeneous fluid [279], [280]. The onset path/wake instabilities in a settling no-slip sphere also require a finite time which is expected as it takes some time for the flow field to develop fully [316].

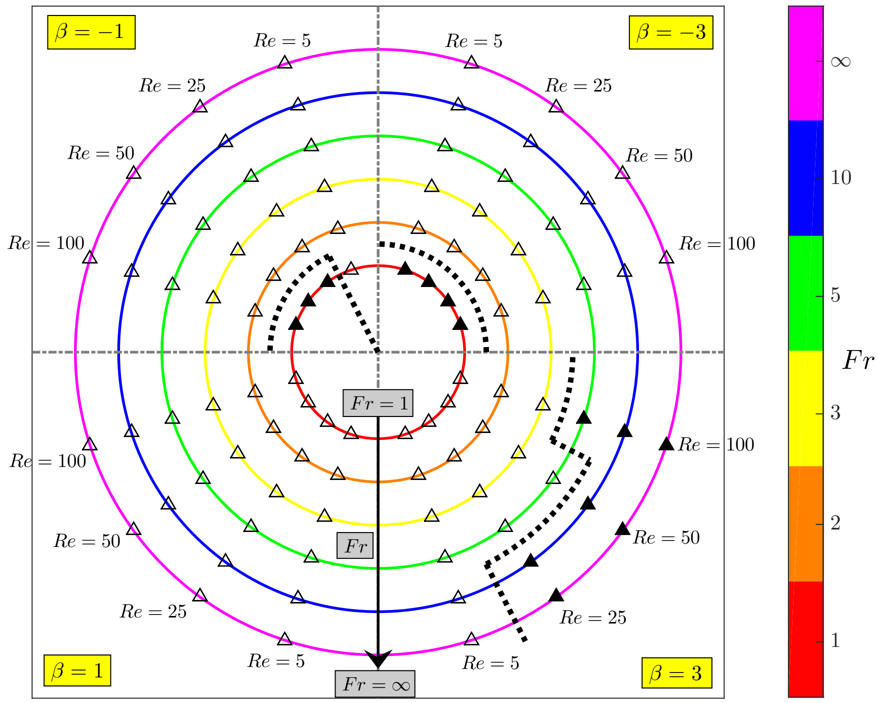

Figure 8.12. A polar phase diagram indicating the effect of stratification and inertia on the stability of the squirmers. Open symbols (△) indicate stable squirmer motion, while filled symbols (▲) indicate unstable squirmer motion. Each quarter (separated by dash-dotted lines) is for a fixed β value indicated by legends in the corners. The black dotted lines separate the stable cases from the unstable ones. Each quarter is for a fixed β squirmer. Each circle (radial direction) represents a constant Fr value which increases as we go outward. Innermost circle is the maximum stratification strength while outermost circle is for a homogeneous fluid. A fixed polar coordinate represents a fixed Re with values indicated on the outermost circle.

8.3.3 Swimming and Mixing efficiency

For a body moving in a linearly stratified fluid, the energy equation in a quasi steady state can be written as,

$$\mathcal{P} = \oint_S (\mathbf{u} \cdot \boldsymbol{\sigma}) \cdot \mathbf{n} \, dS = \int_{\Omega - \Omega_s} 2\mu \mathbf{E} : \mathbf{E} \, d\Omega - \int_{\Omega - \Omega_s} w \rho g \, d\Omega, \tag{8.13}$$

where $\boldsymbol{\sigma}$ is the stress tensor, S is the squirmer's surface, $\mathbf{n}$ is the normal unit vector to S, $\mathbf{E}$ is the strain rate tensor, ρ is the perturbation from the initial linear background density ρ_f and Ω_s is the squirmer domain, i.e., $\phi = 1$. The first term on the right hand side is the viscous dissipation (Φ) over the entire fluid domain while the second term is the rate of creation of the gravitational potential energy (ΔPE). Together, these two terms give us the energy expended by the squirmer for its locomotion in a linearly stratified fluid in a steady state. The energy expended by the squirmer for its steady state motion is dissipated in the form of mechanical energy in the surrounding fluid and hence can be calculated as in equation 8.13.

The swimming efficiency (η_{e}) of the squirmers is defined as the ratio of the power necessary to move the spherical squirmer body ($\mathcal{P}^* = 6\pi\mu U^2 a(1 + 3/8Re)$) at its swimming speed U to the power expended by the squirmer $\mathcal{P}$ [277]:

$$\eta_{\mathrm{e}} = \frac{\mathcal{P}^*}{\mathcal{P}}, \tag{8.14}$$

Fig. 8.13a shows the swimming efficiency of the squirmers in a stratified fluid at a constant $Re = 25$. Earlier studies for the motion of an inertial squirmer in a homogeneous fluid observed that a pusher is more efficient than puller [277], [279] which is also true in a stratified fluid. In addition, increasing the magnitude of $|\beta|$ results in a reduction in the swimming efficiency. The viscous dissipation as well as the gravitational potential energy generation increases with increasing $|\beta|$ resulting in a lower swimming efficiency. This is expected as the gradients in the velocity as well as the magnitude of density perturbations increase with the squirmer $|\beta|$ value. This observation is consistent with earlier studies in an inertial regime but in a homogeneous fluid [277], [279].

A pusher observes a higher reduction in its swimming velocity in a stratified with respect to its swimming velocity in a homogeneous fluid than a puller for the same Re and Fr as discussed in Sec. 8.3.1. Still, a pusher swims faster than a puller for the same Re and Fr values (see Fig. 8.3). This is due to the effective vorticity advection by the flow field around a pusher as compared to a puller. As can be seen by comparing Fig. 8.10 and 8.11, pullers have a long wake behind them which indicates the efficient vorticity advection downstream.

However, the wake becomes shorter with increasing the stratification for a puller signifying resistance to the vorticity advection downstream. This is also the reason why a pusher swims more efficiently that a puller in a stratified fluid for the same Re and Fr values. Furthermore, with increasing the stratification, the ΔPE increases by 1-2 orders of magnitude while Φ increases only slightly. Thus, as the stratification increases, more energy is expended by the squirmer in ΔPE resulting in the lowering of its swimming efficiency with increase in the stratification strength.

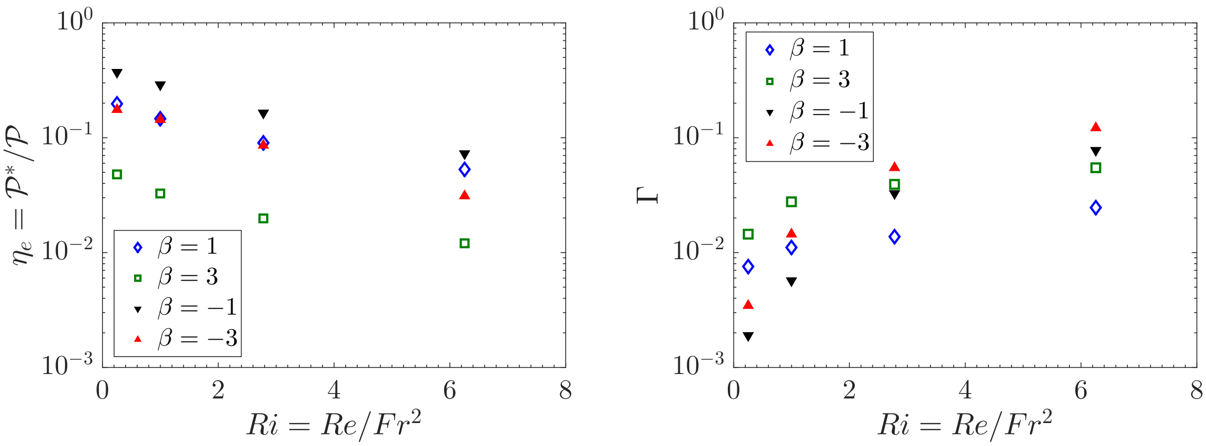

(a) **(b)**

Figure 8.13. a) Effect of stratification on the swimming efficiency of the squirmers for swimming. Here, $\mathcal{P} = 6\pi\mu U^2 a\,(1 + 3/8Re))$, which is the power required to tow the squirmer body in a homogeneous fluid at the same Re and the velocity U. b) Effect of stratification on the mixing efficiency (Γ) of squirmers. $Re = 25$ for both plots. Open symbols: pullers. Filled symbols: pushers.

The mixing efficiency (Γ), which is the ratio of the potential energy generated to the total energy expended in producing the mixing, is an important parameter to quantify the mixing generated by bodies in a stratified fluid. It can be defined as,

$$- = \frac{-\int_{\Omega-\Omega_s} w\rho g \, d\Omega}{\oint_{\Omega-\Omega_s} (\mathbf{u}\cdot\sigma)\cdot\mathbf{n}\, dS} = \frac{-\int_{\Omega-\Omega_s} w\rho g \, d\Omega}{\int_{\Omega-\Omega_s} 2\mu\mathbf{E}:\mathbf{E}\, d\Omega - \int_{\Omega-\Omega_s} w\rho g\, d\Omega}. \tag{8.15}$$

The mixing efficiency induced by organisms has been an active area of study in the recent years [292], [317]–[321]. Thus, looking at the mixing efficiency of an individual swimmer can help us in understanding the mixing produced by a school of swimmers. Fig. 8.13b gives the mixing efficiency for pushers and pullers at various Ri and shows that increasing stratification increases the mixing efficiency for both pushers and pullers. A pusher (puller) with higher magnitude of β has a larger mixing efficiency. This is obvious as a squirmer with higher $|\beta|$ has a higher velocity leading to higher vertical mass flux and hence achieves larger mixing.

The mixing efficiency induced by an individual micron size microorganism in a marine environment is $O(10^{-8})$ [322] which means in absence of swimmer inertia, its motion does not lead to any significant mixing. Wang & Ardekani (2015) [292] calculated Γ for a swarm of squirmers at finite inertia. They observed that Γ increases with Re and the squirmer concentration. They also observed that, at a lower Ri, a puller exhibits higher Γ while at a high value of Ri, a pusher has higher Γ. However, it is not clear as to why the mixing efficiency increases with increasing Ri for the swarm of squirmers. The reason for this becomes clear if we look at the mixing efficiency generated by individual squirmers in Fig. 8.13b. At low Ri (< 2), the mixing efficiency is more for a puller compared to a pusher with the same Re and β. However, at higher Ri (> 2), pusher has a higher Γ than a puller. This trend in Γ at the individual level of the squirmers is what leads to the same behavior for a swarm of squirmers.

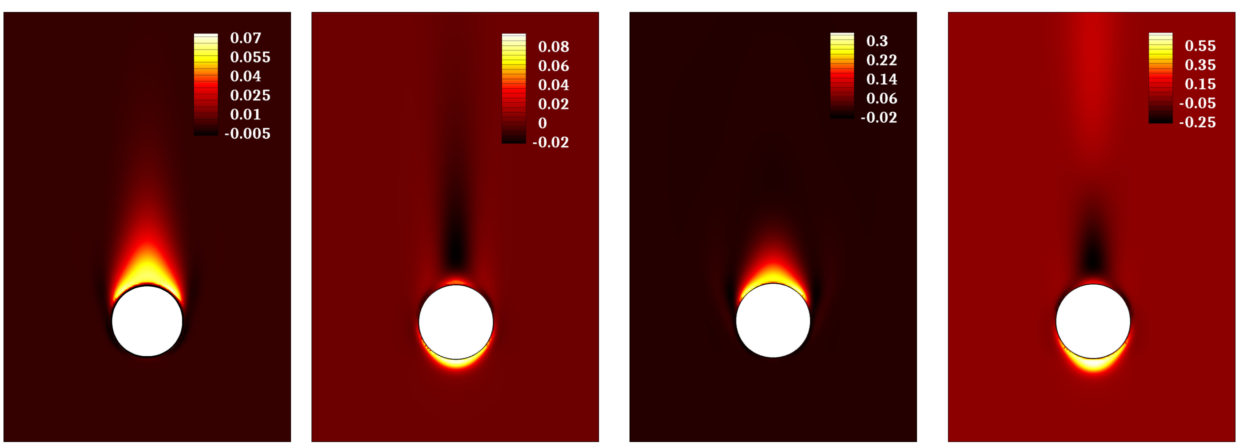

(a) $Fr = 10, \beta = 3$ **(b)** $Fr = 10.\beta = -3$ **(c)** $Fr = 3, \beta = 3$ **(d)** $Fr = 3, \beta = -3$

Figure 8.14. Effect of stratification on the gravitational potential energy generated by squirmers at low and high stratification strengths normalized by its maximum value for $Re = 25$. Potential energy is generated mainly in the recirculatory regions of pushers and pullers. The coordinate system is the same as in Fig. 8.1c hence not shown here.

As mentioned before, we observed that, with increasing the stratification, the ΔPE increases by 1-2 orders of magnitude while Φ increases only slightly. Also, the calculations show that $\Phi >> \Delta PE$. Thus, we can conclude that, it is the numerator term that governs the behavior of mixing efficiency generated by a single squirmer moving in a stratified fluid. Hence, to explain the trends in Γ, we plot the gravitational potential energy generated, i.e., the numerator term in eq. 8.15. As can be seen in Fig. 8.14, most of the gravitational potential energy is generated in the recirculatory regions of the squirmers. With increasing the stratification, the amount of ΔPE generated by a puller (can be seen by maximum ΔPE value in the contours) increases significantly but the size of its recirculatory region also decreases. However, this increase in the amount of ΔPE generated by a puller is significantly higher ($\approx$ 4 folds) than the shrinking ($\approx$ 2 folds) of its rear recirculatory region as can be seen in Fig. 8.14a and 8.14c. This results in the higher Γ at higher Ri for a puller. On the other hand, with increasing the stratification strength, the size of the recirculatory region as well as the amount of ΔPE generated by a pusher increases as can be seen from Fig. 8.14b and 8.14d. Thus, the Γ by a pusher also increases with increase in the stratification strength of the background fluid.

The switching in the relative magnitudes of Γ for a puller and a pusher for $R\text{i} > 2$ can also be explained by looking at the ΔPE contours in Fig. 8.14. At low Ri values, i.e., high Fr values (Fig. 8.14a and 8.14b), the puller generates more ΔPE compared to a pusher owing to the bigger size of its recirculatory region. However, this scenario changes completely with increasing the stratification strength. At high Ri values, i.e., low Fr values (Fig. 8.14c and 8.14d), the recirculatory region behind a puller shrinks while the recirculatory region in front of the pusher gets bigger as compared to the lower Ri case. In addition, the amount of ΔPE (can be seen by comparing the maximum ΔPE value in the contours), also increases significantly for a puller as compared to a pusher at high stratification strengths. This results in the higher Γ for a pusher than a puller at high Ri values as shown in Fig. 8.13b. We observed similar trends for other Re values investigated in this study as well.

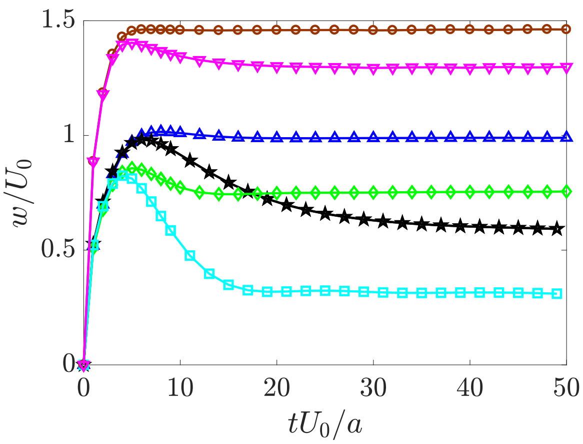

Figure 8.15. Effect of Pr on the velocity evolution of the squirmers. Changing Pr merely changes the magnitude of the velocity but the overall behavior for the velocity is the same. This observation is similar to the effect of changing Pr on a rigid sphere settling in a stratified fluid. This plot shows even at a higher Pr increasing stratification reduces the swimming speed. -O-: $Re = 5$, $Fr = 5$, $\beta = -3$, $Pr = 0.7$; -▽-: $Re = 5$, $Fr = 5$, $\beta = -3$, $Pr = 7$;-△-: $Re = 25$, $Fr = 5$, $\beta = -1$, $Pr = 0.7$; -★-: $Re = 25$, $Fr = 5$, $\beta = -1$, $Pr = 7$;-◊-: $Re = 25$, $Fr = 3$, $\beta = -1$, $Pr = 0.7$; -□-: $Re = 25$, $Fr = 3$, $\beta = -1$, $Pr = 7$;

8.3.4 Effect of Prandtl number

This study investigated the locomotion of a squirmer in a linearly stratified fluid with the fluid having a $Pr = 0.7$. This was done in order to resolve the density boundary layer without making the simulations computationally too expensive. Here we present results for $Pr = 7$ and compare them with the results for $Pr = 0.7$. It has been shown for the case of a spherical object settling in a linearly stratified fluid, changing the Pr only changes the magnitudes of the flow variables with their behavior and trends being similar [299]. We expect similar effect of changing Pr on the motion of a squirmer as well.

Fig. 8.15 shows that increasing Pr changes the magnitude of steady state swimming velocities but the overall behavior of the velocity time history is similar in both cases. The plot shows that squirmer velocity does not experience a notable change before reaching the maximum value after which it attains a smaller steady state swimming speed at higher Pr. These observations are similar to the effect of changing Pr in the case of a sphere settling in a linearly stratified fluid [299]. The effect of stratification on the swimming speed of a squirmer is similar at higher Pr, i.e., stratification reduces the swimming speed of squirmers.

8.3.5 Locomotion of non-neutrally buoyant squirmers in a stratified fluid and the validity of Boussinesq approximation

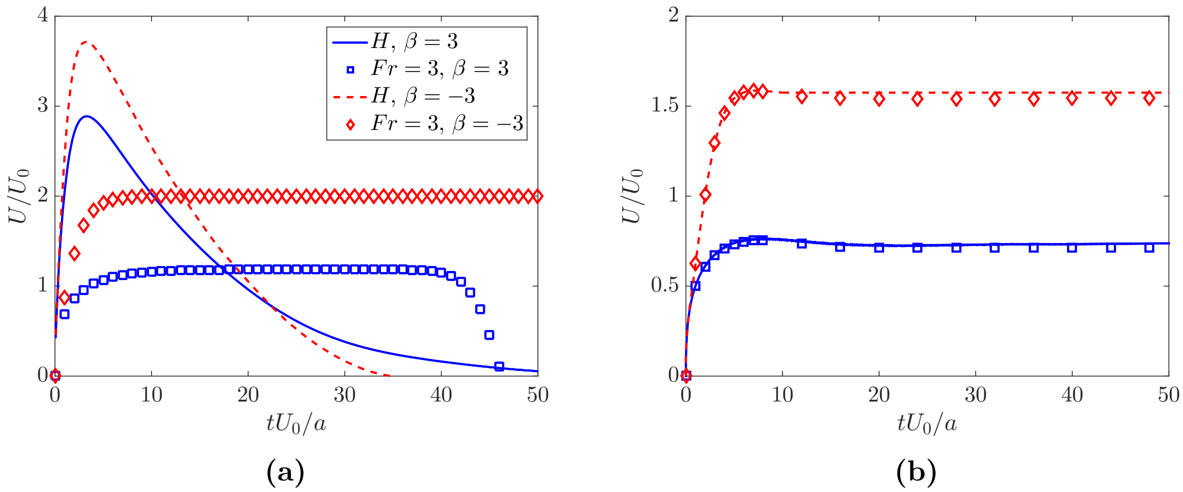

Figure 8.16. a) Swimming speed evolution of non-neutrally buoyant squirmers with $\rho_s/\rho_0 = 1.04$ with $Re = 15.6$ in a homogeneous fluid (H) and a stratified fluid with $Fr = 3$. The squirmers were initialized at a distance $40d$ above their neutrally buoyant positions (i.e., z at which $\rho(z) = \rho_s$). b) Validity of Boussinesq approximation. The plot shows the swimming speed evolution for a pusher with ($\Diamond$) and without (dashed line, $--$) the Boussinesq approximation as well as for a puller with ($\Box$) and without (solid line, $-$) the Boussinesq approximation. Here, $|\beta| = 3$, $Re = 25$ and $Fr = 5$.

In this section, we present the motion of non-neutrally buoyant squirmers and the validity of using the Boussinesq approximation in eq. 8.3. Fig. 8.16a shows the swimming speed evolution of a pusher and a puller in a homogeneous and a stratified fluid with $Fr = 3$. The squirmers are not neutrally buoyant in this plot. They have $\rho_s/\rho_0 = 1.04$. Please note that, $\rho_0 = \rho_f$ in a homogeneous fluid. As a result of this, they experience a buoyancy force in the direction of their motion due to the density difference with the background fluid. In a homogeneous fluid, this density difference leads to a higher swimming speed of the squirmers compared to their swimming speeds when $\rho_s/\rho_0 = 1$. In a stratified fluid, the squirmer velocity increases first, reaching a maximum and it decreases gradually after that to become 0 when the squirmers reach their neutrally buoyant positions.

For the results presented in this paper, we have assumed the Boussinesq approximation is valid in the Navier-Stokes equations (Eq. 8.3). The validity of using the Boussinesq approximation in the case of a settling no-slip sphere is presented in [299]. To test this assumption for squirmers as well, we present the comparison of the velocity evolution for a pusher and a puller with $|\beta| = 3$ and $Re = 25$ in a stratified fluid with $Fr = 5$ in Fig. 8.16b. The plot shows that there is only a small change in the squirmer velocity if we relax the Boussinesq approximation. The solution with the Boussinesq approximation slightly under-predicts the swimming velocity for the squirmers. These results show that the Boussinesq approximation is valid in the present study.

8.3.6 Effect of squirmer orientation

The results presented in the manuscript are for squirmers swimming downwards, i.e., parallel to the direction of the gravity and in a heavier fluid. However, in reality they might swim in various other orientations too. So, in this section, we present swimming speed evolution for squirmers with $Re = 50$ in other orientations. The other orientations considered are: 1) Opposite to the direction of gravity, or vertically upwards, 2) Perpendicular to the direction of gravity, or horizontal. In both these cases, the qualitative behavior of the squirmer swimming is similar as shown in Fig. 8.17a and 8.17b.

Fig. 8.17a shows the swimming speed evolution for a puller and a pusher with $|\beta| = 3$ and $Re = 25$ at two different Fr moving parallel to (downward) and opposite to (upward) the direction of the gravity. The swimming speed evolution is similar in both cases. The squirmer swimming speed decreases with increasing the stratification compared to its swimming speed in a homogeneous fluid even if it is moving opposite to the direction of gravity. We observe that, the squirmer swimming upward in a stratified fluid has slightly smaller velocity that the same squirmer swimming downward for the same conditions.

Fig. 8.17b shows the swimming speed evolution for a pusher and a puller with $|\beta| = 3$ and $Re = 50$ in a homogeneous fluid and a stratified fluid with two different Fr moving in a direction perpendicular to the direction of gravity, i.e., horizontal. Increasing the stratification

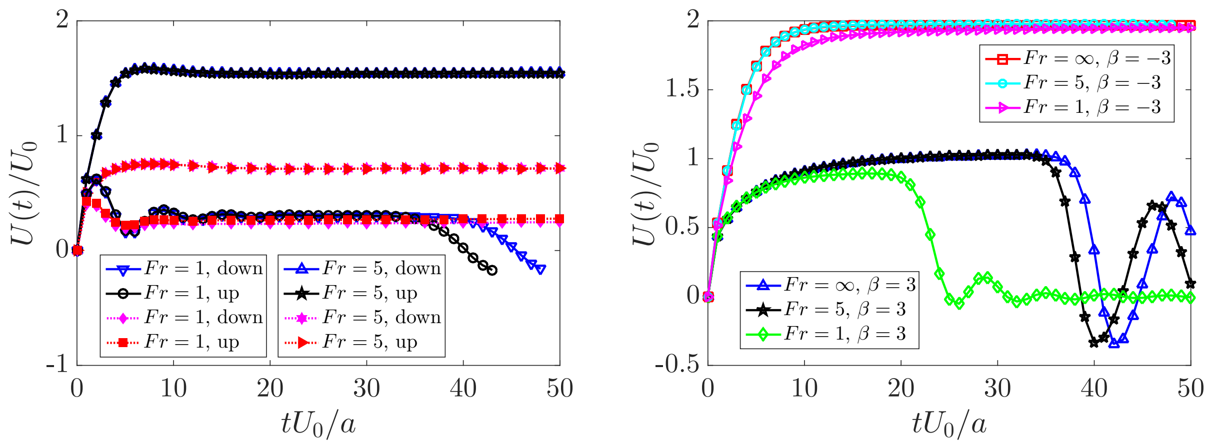

(a) **(b)**

Figure 8.17. a) Swimming speed evolution of squirmers with initial orientations vertically down (direction of gravity) and up (opposite to the direction of gravity), respectively. Here, $Re = 25$ and $|\beta| = 3$. Hollow symbols and solid lines represent pushers while filled symbols and dotted lines represent pullers. b) Swimming speed evolution of squirmers with initial orientations horizontal (perpendicular to the direction of gravity). Here, $Re = 50$ and $|\beta| = 3$. Increasing the stratification reduces the swimming speed of the squirmers but this reduction is small compared to the case when they move in the direction of gravity.

decreases the swimming speed of the squirmers compared to their speeds in a homogeneous fluid. But this reduction is small compared to the case when they move vertically. In addition, the stratification does not stabilize a puller even in a strongly stratified fluid at high Re if it moves in the horizontal direction.

9. HYDRODYNAMIC INTERACTIONS BETWEEN SWIMMING MICROORGANISMS IN A LINEARLY DENSITY STRATIFIED FLUID

9.1 Introduction

The sizes of swimming organisms span a wide range of length scales from micrometers to a few meters. Thus, depending on their size these organisms employ a variety of swimming mechanisms that take advantage of the fluid flow around them to propel themselves. In a fluid with a characteristic density ρ_0 and dynamic viscosity μ, the Reynolds number for an organism of size a and moving with a speed U_0, is defined as $\mathrm{Re} = \rho_0 U_0 a/\mu$, which is the ratio of inertial to viscous forces. At micro scales, $\mathrm{Re} \approx 0$ and the microorganisms make use of the viscous drag exerted by the fluid to move. Larger organisms like fishes and whales have a finite Re and utilize the lift generated by the accelerating fluid past them to swim.

In the recent years, researchers have devoted significant effort to investigate the collective dynamics of organisms. Dense suspensions of bacteria on scales much larger than a cell in the Stokes flow limit exhibit transient, reconstituting, high-speed jets straddled by vortex streets [323], self sustained turbulence [324], extended spatio-temporal coherent dynamics [325], and superdiffusion in short times [326]. The collective motion of the bacteria is determined by short-range pair interactions at high concentrations [324]. Even at high Re, e.g., schooling fish, flocking birds and swarming insects, the hydrodynamic interaction between the moving organisms and their detached vortical structures significantly affect the swimming (flying) efficiency [263], [327].

Many studies on the collective behavior of swimmers neglect the near-field hydrodynamic interactions and only consider the far-field interactions to simulate the dynamics of swimmer suspensions [328], [329]. But, to completely understand the collective behavior of the micro-swimmers, it is important to investigate the near-field hydrodynamics between a pair of interacting swimmers. It is well known that, in the dilute limit, micro-swimmers behave as a force dipole leading to a velocity field decaying as $1/r^2$, where r is the distance from the micro-swimmer [330]. Due to the slow decay of the induced velocity field, the pairwise interaction between two swimmers cannot be neglected even at large separations. Various experimental studies have shown the crucial role of hydrodynamic interactions between microorganisms in determining their dynamics, e.g., dancing *Volvox* [265], interacting pair of *Paramecia* [267], the formation of dynamic clusters in suspensions of motile bacteria [331] and hydrodynamic self-mediation of bacteria into two-dimensional crystals [332].

Many theoretical and numerical studies have also been conducted to investigate the hydrodynamic interactions between two model swimmers. Pullers (pulled from the front) are attracted towards each other first which leads to near contact and changes in their swimming orientations to finally separate [333], [334]. Two self-propelling bacteria by rotating helical flagella avoid each other by changing their orientations [335]. The swimmer-swimmer interaction is complex and strongly affected by their relative displacement, orientation, initial configuration and swimming stroke phase. Slight variations in these parameters lead to different scattering angles, swimming speeds and a range of different interactions, such as attraction, repulsion, or oscillation [336]–[339]. Hydrodynamic interactions between two microswimmers also lead to the the enhancement of the swimming efficiency by synchronizing the phase of two adjacent flagella [340]. However, all these studies however were performed in the Stokes regime assuming $\mathrm{Re} = 0$ without considering the effect of swimmer inertia.

For swimming microorganisms, the Re ranges from 10^{-4} for bacteria [264], 10^{-3} for *Chlamydomonas*, $0.01 - 0.1$ for *Volvox* [265], $0.1 - 1$ for freely swimming zooplankton *Daphnia magna* [266], $0.2 - 2$ for *Paramecia* depending on swimming or escaping mode [267], $O(10)$ for *Pleurobrachia*, and $20 - 150$ for copepods [268]. Thus, it is crucial to know the influence of finite inertia on the hydrodynamic interactions of two swimmers. Theoretical and computational studies on the locomotion of an individual swimmer with finite inertia [277], [279] further indicate that inertia can lead to notable differences in the swimming dynamics of swimmers. Inertia also affects the hydrodynamic interactions between swimmer pairs. Puller and pusher pairs either separate away from each other or get trapped near each other depending on their Re and swimming modes [280].

Many swimming organisms with low to intermediate Re are abundant in oceans and lakes and their motion results in intense biological activity in these aquatic bodies. Hence studying the interactions of organisms is an intriguing problem having wide implications for ocean ecology [227]. However, understanding the physics behind these phenomenon is a complex undertaking as vertical variations in water density are ubiquitous in aquatic and marine environments [211], due to gradients in temperature (thermoclines) or salinity (haloclines). These density variations with depth can manifest themselves in a gamut of environmental and oceanographic processes [218], [251], [292], [341]. Even though the stratification length scale is $O(m)$, the appropriate length scale to determine whether stratification affects the motion of the swimmers is $O(100)\ \mu m$ [284]. Marine microplankton with sizes ranging from $20 - 200\ \mu m$ are abundant in such a stratified environments along with other meso-, macro- and mega-planktonic organisms which have Re ranging from $O(0.01 - 100)$ [286]. These observations insinuate the significant role of stratification in governing the locomotion of individual organisms as well as the interaction between two close organisms in the mentioned size range.

Much like inertia, stratification also significantly affects the motion of micro-swimmers. At low Re, the vertical migration of small organisms is hydrodynamically affected due to the rapid velocity decay as well as a higher energy expenditure in stratified fluids [293], [294]. At a finite Re, stratification even leads to striking differences in the swimming speeds and stability of swimmers as compared to their motion in a homogeneous fluid [342]. The collective vertical migration of swimmers in a stratified fluid generates aggregation-scale eddies which can potentially alter the physical and bio-geo-chemical structure of the water column [226], [291], [292]. Stratification also leads to the accumulation of marine organisms like plankton [288], [289]. Thus, investigating the combined effect of inertia and stratification on the interaction between a pair of interacting swimmers is a non-trivial and interesting problem that we address in this paper.

Looking at the interactions between a pair of organisms is crucial for modeling the collective dynamics of marine organisms, e.g., migrating swimmer schools in stratified environments. To this end, we numerically investigate the effect of density stratification on the interactions between a pair of inertial swimmers. We model the swimmers using the archetypal spherical squirmer model which is explained in detail in Sec. 9.2.2. But first, we present the governing equations and the computational methodology used to solve these equations in Sec. 9.2.1. Then we discuss the findings of the simulations in Sec. 9.3.

9.2 Governing equations and computational methodology

We consider a pair of interacting squirmers moving through an incompressible Newtonian viscous fluid. The governing equations and the numerical procedure implemented to simulate the motion a pair of interacting squirmers through a linearly stratified fluid at finite Re are presented in this section. We consider a linearly density stratified fluid such that the density increases in the downward z direction and the gravity is acting in the downward z direction as shown in Fig. 9.1. The following subsections explain the governing equations and the numerical schemes used to solve them in details.

9.2.1 Flow and density fields

The fluid flow is governed by the Navier-Stokes equations for an incompressible Newtonian fluid and these equations are solved in the entire domain, Ω. We simplify the Navier-Stokes equations for a fluid flow of a density stratified fluid using the Boussinesq approximation. The resulting equations can be written as,

$$\rho_0 \frac{\mathrm{D}\mathbf{u}}{\mathrm{D}t} = -\nabla P + \mu \nabla^2 \mathbf{u} + (\rho - \bar{\rho})\mathbf{g} + \mathbf{f}, \text{ in } \boldsymbol{\Omega}, \tag{9.1}$$

$$\nabla \cdot \mathbf{u} = \mathbf{0}, \text{ in } \boldsymbol{\Omega}, \tag{9.2}$$

where t is the time, $\mathbf{u}$ is the velocity vector, P is the hydrodynamic pressure, $\mathbf{g}$ is the acceleration due to gravity, μ is the dynamic viscosity of the fluid, ρ_0 is the reference fluid density and $\bar{\rho}$ is the volumetric average of the density over the entire domain. $D(\cdot)/Dt$ is the material derivative. ρ is the local density at the grid point. We use the phase indicator function ψ which is 1 inside the squirmer and 0 outside to mark the squirmer domain. The subscript f stands for fluid and s for squirmer. $\mathbf{f}$ in equation 9.1 is the body force which accounts for fluid-solid interactions in the Distributed Lagrange Multiplier (DLM) method [295]. DLM has been widely used in the literature to simulate the motion of rigid particles and model swimmers in both homogeneous and stratified fluids [280], [292], [297]–[299].

The density field evolution is governed by the following advection-diffusion equation,

$$\frac{\mathrm{D}\rho}{\mathrm{D}t} = \kappa\nabla^2\rho, \text{ in } \Omega, \tag{9.3}$$

here κ is the diffusivity of the stratifying agent and ρ is the density field. We define Prandtl number $\mathrm{Pr} = \nu/\kappa$, which is the ratio of the momentum diffusivity to the diffusivity of the stratifying agent. We split the density into two parts: i) the initial linear background density profile, $\bar{\rho}(z)$, and ii) the density perturbation induced by the motion of the squirmers, ρ. So,

$$\rho = \bar{\rho}(z) + \rho. \tag{9.4}$$

Here, the initial density of the fluid varies linearly with depth z as $\bar{\rho}(z) = \rho_0 - \gamma(z - z_0)$, where γ is the vertical density gradient and z_0 is the location with reference density ρ_0. The stratification strength can be quantified by the Brunt–Väisälä frequency, $N = (\gamma g/\rho_0)^{1/2}$, the natural frequency of oscillation of a vertically displaced fluid parcel in a stratified fluid. Substituting eq. 9.4 in eq. 9.3 we obtain the following temporal and spatial evolution equation for the density perturbation, ρ,

$$\frac{\mathrm{D}\rho}{\mathrm{D}t} = -\mathbf{u}\cdot\nabla\bar{\rho}(z) + \kappa\nabla^2\rho, \text{ in } \Omega. \tag{9.5}$$

We solve the advection-diffusion equation for the density perturbation, ρ and add it to the initial linear density profile to calculate the density field as shown in eq. 9.4.

We use a finite volume method [300] to discretize the equations 9.1-9.2 and 9.5 on a non-uniform staggered Cartesian fixed grid. We use a second order quasi Crank-Nicolson method for temporal evolution. Convection and diffusion terms in the momentum equation have been solved using a QUICK (quadratic upstream interpolation for convective kinetics) and central-difference schemes [301], respectively. Both convection and diffusion terms in the density perturbation, ρ, equation have been discretized using the central difference scheme [292]. The numerical tool utilized for this study is based on the earlier version of PARIS [300]. We use periodic boundary conditions for velocity components and the density perturbation in all the three directions.

9.2.2 Swimmer model

Mathematically modelling the motion of a real micro-organism is an enormously convoluted undertaking. This is due to the existence of a wide variety of length scales (roughly $O(1) - O(1000)\mu m$ for common marine species), multitudes of swimming, grazing and other behaviors depending on a range of parameters relating to their environments. In addition, these organisms exhibit a vast variety of shapes which might even not be the same as individual micro-organisms change their shapes to feed, reproduce or protect themselves from predators or hostile environments. Thus, we need to make several simplifications, even for the simplest micro-organisms in order to mathematically model and analyse them [264]. Hence, by necessity, we use a reduced order squirmer model which is primitive. This model, however simple it may be, still includes important aspects of micro-organism hydrodynamics such as, it swims and has a finite size so that excluded-volume effects and hydrodynamic interactions can be analysed non-trivially.

The squirmer model [271], [272] has been widely used as a model for swimmers like *Volvox* in the literature [302]. In the earlier studies, researchers utilized the squirmer model to investigate the motion of self-propelled organisms in a viscosity dominated flow regime, i.e., Re $\to 0$. This allowed researchers to investigate various problems in a non-inertial regime, such as, the nutrient uptake by self-propelled organisms [273], the hydrodynamic interactions between two squirmers [267], rheology of suspensions of squirmers [274], mixing by swimmers [275] as well as swimming in non-Newtonian fluids [276], [343] using the squirmer model. Recently, researchers have studied the effect of finite inertia on the motion of swimmers by extending the squirmer model to low and intermediate Re number regimes [277], [279], [280], [292], [303], [304]. The squirmer model was also used to study the effect of fluid density stratification on the motion of an individual squirmer [293], [342] and the biogenic mixing induced by a swarm of swimming organisms [292] with low to intermediate Re. Thus, the squirmer model, owing to its simplicity and germane representation of the flow field generated by the self-propelling ciliary organisms, opens up a wide range of avenues for studying self-propulsion in various environmental conditions.

The squirmer self-propels by wavelike motion of its surface. The spherical squirmer model, first introduced by Lighthill [271] and later modified by Blake [272] mimics the self-propulsion produced by the coordinated beating of dense array of cilia on its surface. These axisymmetric ciliary deformations result in the radial (u_r^s) and the tangential (u_θ^s) surface velocity components in a frame of reference attached to the squirmer with radius a:

$$u_r^s|_{r=a} = \sum_{n=0}^{\infty} A_n(t) P_n(\cos\theta), \tag{9.6}$$

$$u_\theta^s|_{r=a} = \sum_{n=1}^{\infty} \frac{-2}{n(n+1)} B_n(t) P_n^1(\cos\theta), \tag{9.7}$$

respectively. Here, r is the distance from the center of the squirmer, θ is the angle measured from the direction of the locomotion, A_n and B_n are the time dependent amplitudes of ciliary deformations and P_n, P_n^1 are the associated Legendre polynomials of degree n. The swimming speed of a neutrally buoyant squirmer at $\mathrm{Re} = 0$, i.e., in a Stokes flow depends only on the first mode of each surface velocity component and is given by, $U_0 = (2B_1 - A_1)/3$. This swimming speed is independent of fluid viscosity and other swimming modes [271].

For this study we consider a reduced order squirmer which has no radial velocity and only the first two modes of the surface tangential velocity,

$$u_\theta^s(\theta) = B_1 \sin\theta + B_2 \sin\theta\cos\theta, \tag{9.8}$$

where θ is the angle with respect to the swimming direction, and B_1 and B_2 are the first two squirming modes. The ratio, $\beta = B_2/B_1$, determines whether the squirmer is neutral ($\beta = 0$) or a puller ($\beta > 0$) or a pusher ($\beta < 0$). In the Stokes flow limit, the velocity of a squirmer in an unbounded domain is $U_0 = 2B_1/3$, we use this as the velocity scale in this study. To impose the above given tangential velocity on the surface of the squirmer, we set the following divergence free velocity field inside the squirmer [303],

$$\begin{aligned} \mathbf{u}_{\text{in}} = & \left[\left(\frac{r}{a}\right)^m - \left(\frac{r}{a}\right)^{m+1} \right] \left(u_\theta^s \cot\theta + \frac{du_\theta^s}{d\theta} \right) \mathbf{e}_r \\ & + \left[(m+3)\left(\frac{r}{a}\right)^{m+1} - (m+2)\left(\frac{r}{a}\right)^m \right] u_\theta^s \mathbf{e}_\theta, \end{aligned} \tag{9.9}$$

here a is the radius of the squirmer, r is the distance from the squirmer's center, $\mathbf{e}_r$ and $\mathbf{e}_\theta$ are the unit vectors in the radial and polar directions, and m is an arbitrary integer. The simulation results do not depend on the choice of m. The squirmer velocity is calculated by solving the following equations:

$$\mathbf{U} = \frac{1}{M_s} \int_{V_s} \rho_s (\mathbf{u} - \mathbf{u}_{\text{in}}) dV, \tag{9.10}$$

$$\mathbf{I_s} \cdot \boldsymbol{\omega} = \int_{V_s} \mathbf{r} \times \rho_s (\mathbf{u} - \mathbf{u}_{\text{in}}) dV, \tag{9.11}$$

where V_s, M_s, and $\mathbf{I_s}$ are volume, mass and the moment of inertia of the squirmer. $\mathbf{U}$ and $\boldsymbol{\omega}$ are the translational and the rotational velocities of the squirmer. Finally, the force $\mathbf{f}$ is calculated by the following iterative formula:

$$\mathbf{f} = \mathbf{f}^* + \alpha \frac{\rho\psi}{\Delta t} (\mathbf{U} + \boldsymbol{\omega} \times \mathbf{r} + \mathbf{u}_{in} - \mathbf{u}), \tag{9.12}$$

where $\mathbf{f}^*$ is the force calculated in the previous iteration and α is a dimensionless factor chosen in such a way that iterations for calculating $\mathbf{f}$ converge quickly [280], [299]. Many organisms utilize techniques like gas vesicles [307], carbohydrate ballasting [308], and ion replacement [305], [306] for buoyancy control. Hence, for this study in order to isolate the effect of stratification on the motion of a squirmer, we consider the squirmer to be neutrally buoyant, i.e., the net buoyancy force acting on the squirmers due to differences in their density and the density of the fluid is zero at any instance of time. This is achieved by equating the density field inside the squirmer domain to the instantaneous background fluid density at that location ($\rho_s(\mathbf{x}, t) = \bar{\rho}(\mathbf{x}) + \rho(\mathbf{x}, t)$, where $\mathbf{x}$ is any location inside the squirmer domain). The same condition for neutral buoyancy was used for investigating the swimming dynamics of an individual squirmer with finite inertia in a stratified fluid [342]. In addition, we assume the κ to be uniform and the same for the squirmer and the background fluid [292], [309].

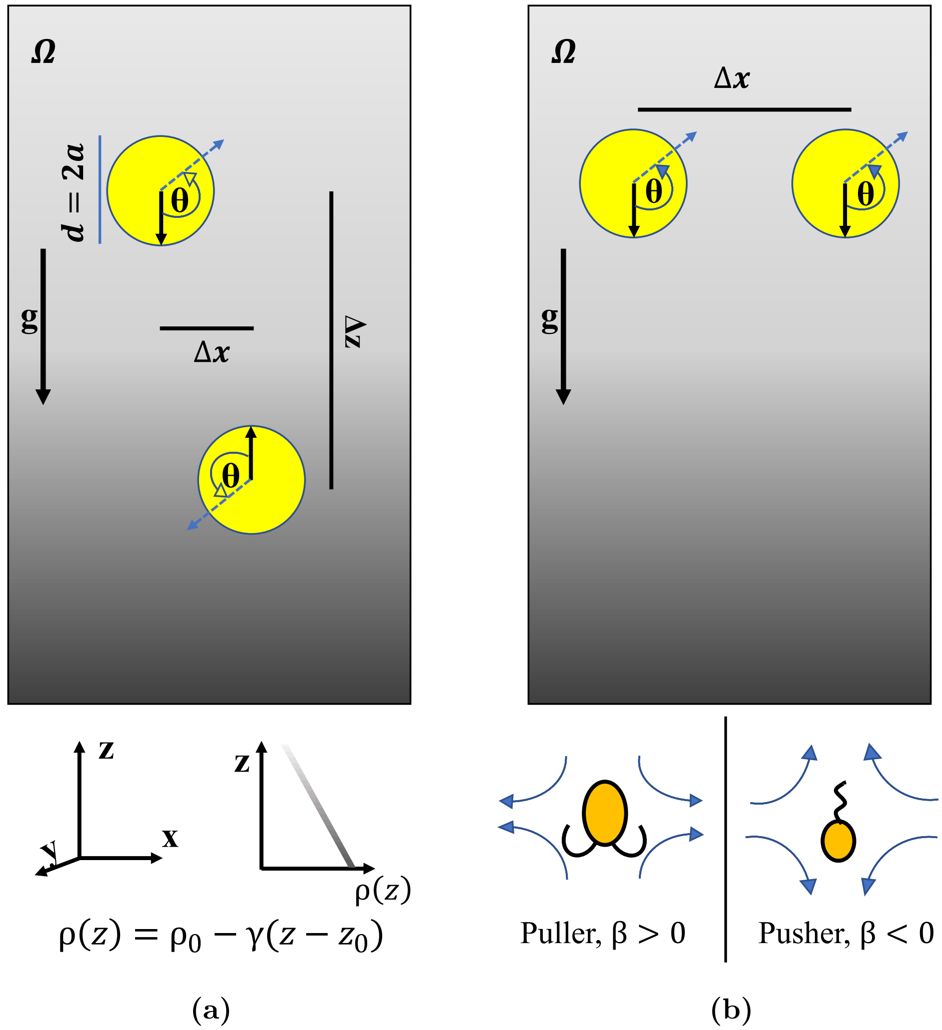

Figure 9.1. Problem schematic: a) Initial conditions for the pair of squirmers approaching each other in a linearly stratified fluid. b) Initial conditions for a pair of squirmers moving side-by-side in a stratified fluid. The cartoons at the bottom in (b) show the flow fields generated by pullers ($\beta > 0$) and pushers ($\beta < 0$) as they move. The arrows in the squirmer bodies show their initial orientations. Darker shade of grey indicates higher density.

9.2.3 Simulation conditions

We explore the interactions of two squirmers moving towards each other leading to collision and two squirmers moving in the same direction side by side. We normalize the spatial parameters with the squirmer radius a, the velocities with U_0 and the time with the time scale a/U_0. We denote the dimensionless time with T.

The first case considered is that of a pair of squirmers approaching each other in opposite directions so that they collide. In this case, the squirmers are initialized at a center to center distance Δz and Δx in the z and x directions, respectively in the plane $y = 0$. Their initial orientations are such that they are moving in opposite directions facing each other. We set $\Delta z = 8$ and $\Delta x = 1$, unless stated otherwise (see Fig. 9.1a).

In the second case, where the squirmers are moving in the same direction side by side, we initialize them at the same initial vertical location z_i, separated by a center to center distance Δx in the x direction in the plane $y = 0$. We set $\Delta x = 4$, unless mentioned otherwise (see Fig. 9.1b).

An earlier study in a homogeneous fluid considered only a colliding pair of squirmers in which the squirmers swim in opposite direction [280]. We, however, consider colliding as well as side-by-side configuration which covers squirmers moving opposite to each other as well as moving in the same direction. Also, the vertical direction is the preferred direction because in many real-life situations, the swimmers move in the vertical direction such that they are parallel to the direction of the stratification or gravity mainly for grazing or in the search of the sunlight during their diel cycles [312], [313]. In addition, the direction of the motion considered in this study is one of the common situations for swimmers moving in oceans, e.g. bioconvection [314]. So, we initialize the squirmers with their initial orientations parallel to the direction of gravity, i.e. downwards or upwards.

When the squirmers approach very close to each other, the high pressure in the thin film between the squirmers prevents any non-physical overlaps. However, a very small grid resolution is needed to resolve the thin liquid film and consequently it is computationally expensive. A repulsive force is imposed during the collision to prevent the non-physical overlap [280], [295],

$$\mathbf{F}_r = \frac{C_m}{\epsilon}\left(\frac{D - d - dr}{dr}\right)^2 \mathbf{n}, \tag{9.13}$$

where $\epsilon = 10^{-4}$ is a small positive number, D is the distance between two squirmers, $C_m = M_s U_0^2/a$ is the characteristic force, $d = 2a$ is the minimum possible distance, and dr is the force range and is set to be twice the smallest grid size Δ. The direction of the repulsive force $\mathbf{n}$ is along the squirmers' line of centers.

We carry out simulations for pushers and pullers with β = -5 and 5, respectively. The Re for the squirmers were varied between $1 - 50$. To study the effects of stratification on the interaction of two inertial squirmers, we vary the Richardson number, $\mathrm{Ri} = \rho_0 a^3 N^2/\mu U_0$, which quantifies the relative importance of the buoyancy and the viscous forces, between $0 - 10$. The domain size for this study is $40a \times 20a \times 40a$ for colliding squirmers case while the domain size is $40a \times 20a \times 80a$ for the side-by-side case. The smallest grid size was chosen such that there are around 35 grid points in one squirmer diameter, i.e., $\Delta \approx d/35$. This grid size was found to be enough to resolve both the velocity and density boundary layers around the squirmers for the chosen Re range and $\mathrm{Pr} = 0.7$. We present the grid independence tests in Sec. 9.2.4.

It should be noted that we use $\mathrm{Pr} = 0.7$ for this study rather than $\mathrm{Pr} = 7$ or $\mathrm{Pr} = 700$ which are the Pr values for a temperature stratified water and a salt stratified water, respectively. This has been done mainly to save the computational costs incurred by setting high values of Pr. In a stratified fluid, a density boundary layer is present in addition to the velocity boundary layer near the squirmer's surface. The thickness of this density boundary layer scales as $\approx O(d/\sqrt{\mathrm{RePr}})$. For accurate resolution of the flow within this boundary layer, it is necessary to have at least a few grid points in it. This imposes limitations on the maximum mesh size that can be used for the simulations. Owing to large size of the domain, using such a fine grid becomes computationally expensive. Hence, we use a smaller value for the Pr which enables us to resolve the fluid flow as well as the density field in both the boundary layer and the outside. It has been shown in previous studies that, changing the value of Pr merely changes the magnitudes of the velocities of the objects [299] and squirmers [342] moving in a stratified fluid conserving the overall qualitative trends and behaviors. We discuss more on this in Sec. 9.3.5.

9.2.4 Validation: Grid and domain independence

We present the grid independence test results in this section. Fig. 9.2 shows the trajectories for a pair of squirmers approaching each other in opposite directions for two different grid sizes. As can be seen in the figure, changing the grid size from $\Delta = d/35$ to $\Delta = d/50$ results in a negligible variation in the trajectories of the colliding squirmers. Here, Δ is the

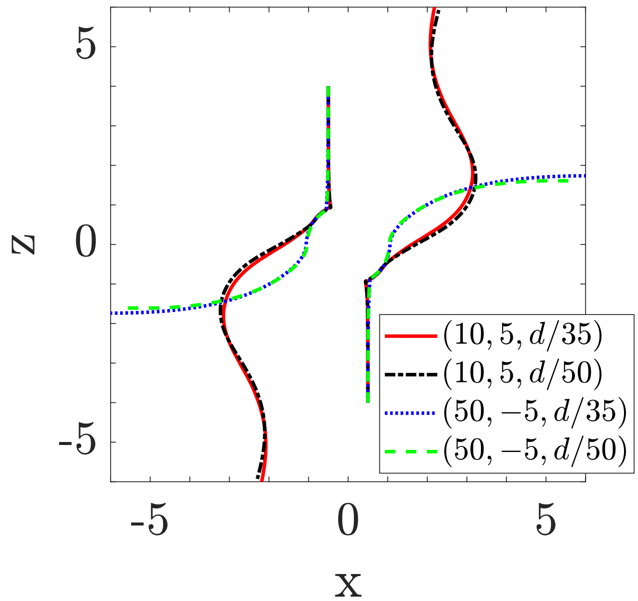

Figure 9.2. Trajectories of a pair of colliding squirmers at two different grid resolutions. Legends are for (Re, β, Δ). Here $\mathrm{Ri} = 5$ for all the cases.

smallest grid size. Hence, to save the computational cost, we carried all the simulations with $\Delta = d/35$. Further validations for the homogeneous fluid cases can be found in Ref. [280].

9.3 Results and discussion

This section presents the important results from the simulations. We also present results on the interactions of pair of inertial squirmers in a homogeneous fluid. The comparison between the trajectories of the squirmers and their velocities in the two distinct fluids allows us to investigate the effect of density stratification on the squirmer pair interactions.

9.3.1 Pairwise interactions of pullers in a stratified fluid

9.3.1.1 Pullers approaching each other

Fig. 9.3 shows the trajectories for two pullers approaching each other in opposite directions, initially oriented parallel to each other for Re = 1, 5, 10 and 50 in a homogeneous fluid and a stratified fluid with Ri = 1, 5 and 10. In the absence of any density stratification, the trajectories of the colliding pullers reveal three patterns based on the magnitude of Re.

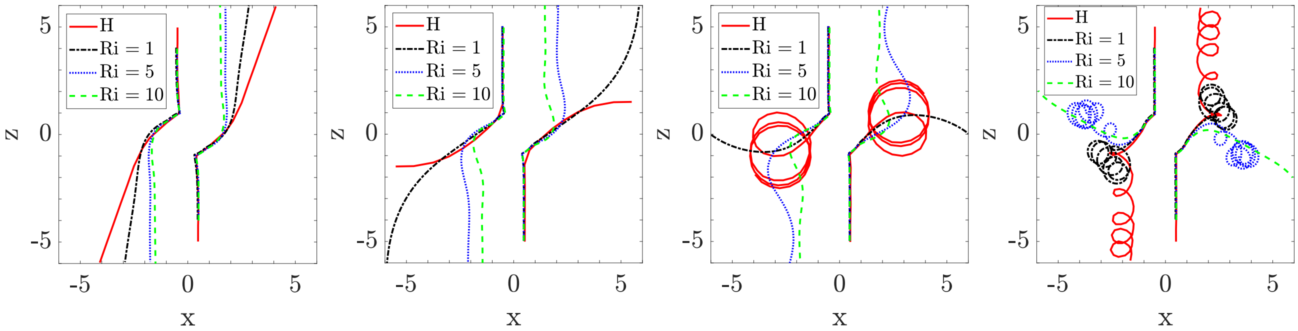

(a) Re = 1 **(b)** Re = 5 **(c)** Re = 10 **(d)** Re = 50

Figure 9.3. Trajectories for colliding pullers with $\beta = 5$ in a homogeneous and a stratified fluid with increasing stratification strengths. At low Re (1 and 5), stratification leads to reorientation of the pullers after the collision. For higher Re values (10 and 50), stratification results in the elimination of the close loop trajectories observed in a homogeneous fluid after the collision of two pullers. *H* in the legends stands for homogeneous fluid or Ri = 0.

At relatively low values of Re, i.e. 1 and 5, the pullers scatter away from each other with a positive scattering angle, ϕ, measured with respect to initial squirmer orientation. With increasing Re, i.e., from Re $= 1$ to Re $= 5$, ϕ increases from $\approx 20°$ to a value just less than $90°$. As we increase the Re further to a higher value of 10, the pullers do not escape each other after the collision, but are trapped in clockwise loops with radii $\approx 2a$. At an even higher Re $= 50$, the pullers are no longer trapped but escape with $\phi \approx 0°$ but keep on rotating in clockwise loops with diminished radii compared to Re $= 10$ case.

Introducing stratification results in distinct changes in the trajectories of the interacting pullers depending on their Re and the stratification strength, i.e., Ri. Stratification leads to reduction in the scattering angle of the squirmers after collision compared to their scattering angles in a homogeneous fluid as can be seen in Fig. 9.3a, and 9.3b. For Re $= 1$ (Fig. 9.3a), stratification reduces ϕ from $\approx 45°$ in a homogeneous fluid to $0°$ for a stratified fluid with Ri $= 10$. For Re $= 5$, ϕ reduces to $0°$ for Ri $= 10$ from $\approx 90°$ for a homogeneous fluid. Thus, at low inertia, high enough stratification leads to the reorientation of the pullers to their original orientation after the collision unlike in a homogeneous fluid.

For higher Re $= 10$, stratification leads to the elimination of the rotating motion of the pullers in clockwise loops present in a homogeneous fluid (see Fig. 9.3c). For Re $= 10$, pullers are no more hydrodynamically trapped in the presence of density stratification unlike in the

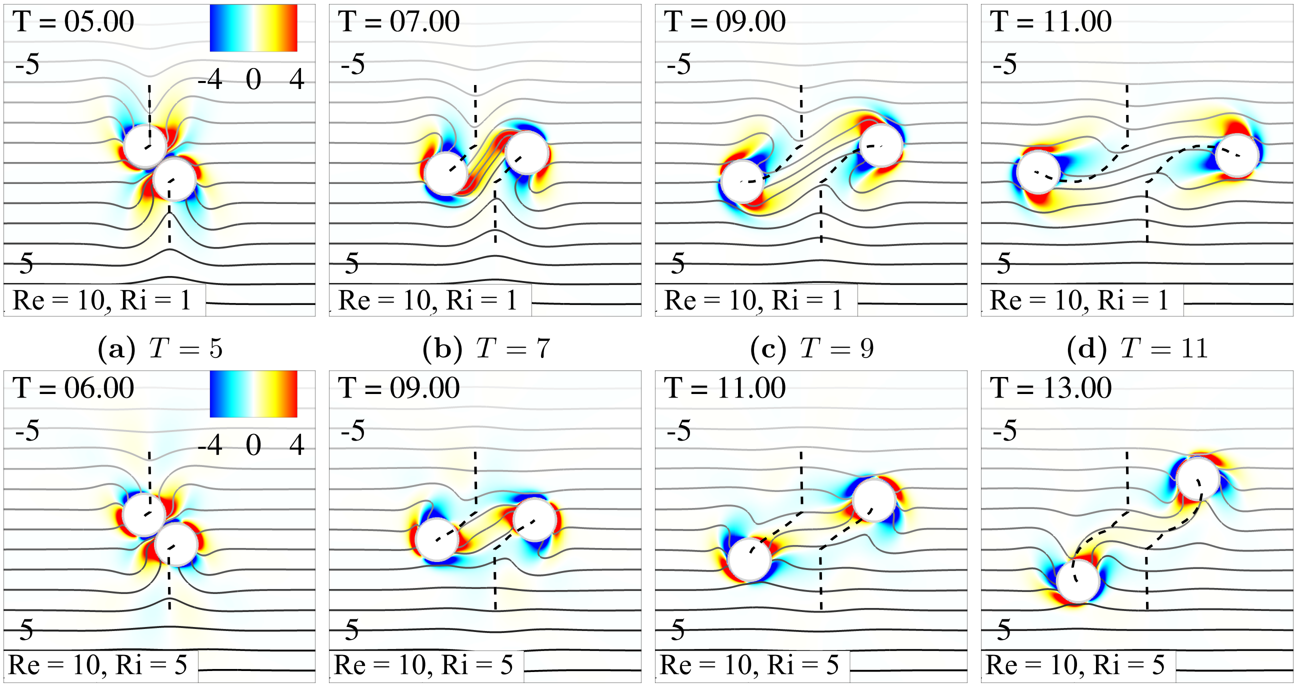

(a) $T = 5$ **(b)** $T = 7$ **(c)** $T = 9$ **(d)** $T = 11$

(e) $T = 6$ **(f)** $T = 9$ **(g)** $T = 11$ **(h)** $T = 13$

Figure 9.4. Vorticity contours and isopycnals during the collision process of two approaching pullers with Re $= 10$ at different stratification strengths, Ri $= 1$ (a,b,c,d) and 5 (e,f,g,h). These plots show the interaction between the rear vorticity bubbles and the deformed isopycnals. The need of the displaced isopycnals to return to their original levels explain the rotational motion of the pullers after the collision. The isopycnals are the normalized density differences given by $(\rho - \rho_0)/\gamma a$ and each line is 1 unit apart. Darker shade of the line color indicates a higher density value. Colorbar for the vorticity contours is presented in the plots. The dashed lines show the trajectory of the pullers. These are snapshots of the flow-field at different dimensionless times, $T = tU_0/a$, the value of which is indicated in the caption. Colorbar is only shown in the first plot of each row for the neatness of the plots. For movies see **supplementary**.

homogeneous fluid. They scatter away from each other with a positive scattering angle much like lower Re cases which decreases with an increase in the stratification strength. Again, high enough stratification strength leads to the reorientation of the pullers to their original orientation (see Fig. 9.3c). For Re $= 50$, only a high stratification results in the elimination of the clockwise loops in the trajectories of the pullers after the collision. This is clear from the trajectories of pullers with Re $= 50$ in a stratified fluid with Ri $= 10$ (Fig. 9.3d). The pullers escape from each other but with a large scattering angle which is greater than $90°$.

However, a lower stratification (Ri = 1 and 5) leads to the hydrodynamic trapping of the pullers after the collision in this case which is similar to the Re = 10 case in a homogeneous fluid.

To explain the reorientation of the pullers after the collision, the elimination of the closed loop trajectories and the prevention of the hydrodynamic trapping of the pullers we plot the vorticity contours and isopycnals at different time instances during the collision process of the pullers for two stratification strengths in Fig. 9.4. The effect of increasing the inertia (or Re) of pullers is to increase the size of the vorticity bubble in the rear part of their bodies [279]. Introducing stratification reduces the size of these recirculatory regions behind pullers [342]. The trapping of the pullers in loops after the collision in a homogeneous fluid can be explained by the interaction between the bigger recirculatory regions behind the pullers at higher Re = 10 and 50 [280]. Since stratification leads to shrinking in the size of these rear recirculatory regions, the interaction between these rear bubbles is limited at finite Ri values. This prevents the pullers to attain a constant angular velocity after the collision unlike the homogeneous case (see Fig. 9.5b). This damping of the angular velocity of the pullers after collision essentially allows the pullers to scatter away from each other without being trapped in counterclockwise loops. This point becomes clear from Fig. 9.4 where we plot the vorticity contours and isopycnals for Re = 10 in stratified fluids with different stratification strengths, Ri = 1 and Ri = 5, respectively.

As the pullers move down (up) in a stratified fluid, they trap lighter (heavier) fluid in their rear recirculatory bubbles which can be seen in terms of deformed isopycnals in Fig. 9.4. After the collision, the axisymmetry of the flow and the isopycnal deformations is broken. The interaction between the rear vorticity bubbles rotates the pullers in clockwise direction as can be seen in Fig. 9.4b. However, the tendency of the deformed isopycnals behind the pullers to return to their original positions reduces the effect of this interaction on the puller orientations (Fig. 9.4f). The counterclockwise torque due to the flow induced by need of the deformed isopycnals to return to their original positions determines the rotational motion of the pullers after the collision and leads to the reorientation of the pullers in the original orientation. This prevents them from getting trapped into loops. This is clear from the comparison of the isopycnal deformation in Fig. 9.4c and 9.4g.

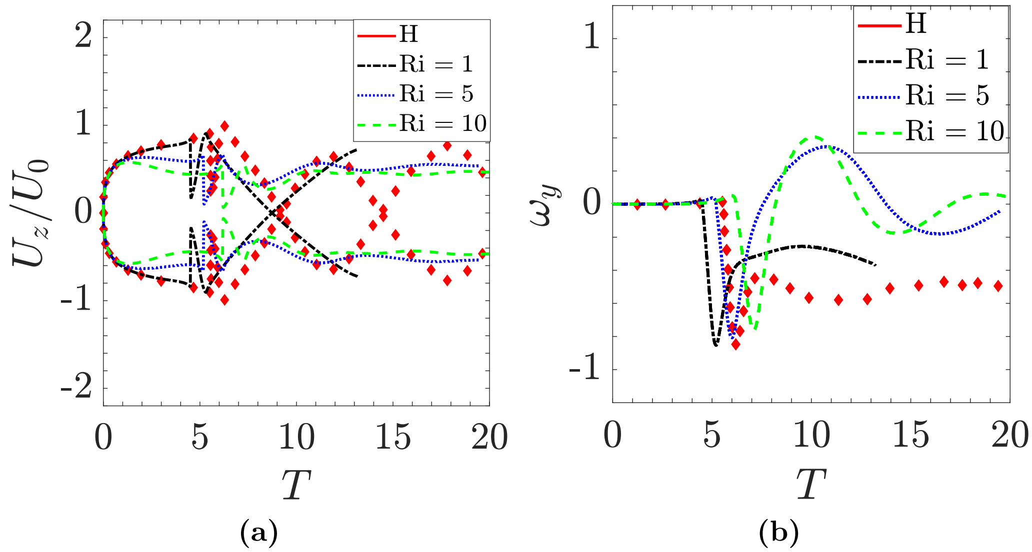

Figure 9.5. Time evolution of the a) translational velocity and the b) rotational velocity of two approaching pullers during the collision process at different Ri values for a fixed Re = 10. Stratification eliminates the oscillations in the translational velocity and prevents the pullers from attaining a constant angular velocity thus eliminating the close loop trajectories as observed in the case of a homogeneous fluid. Stratification also results in a change in the sign of the angular velocity which reorients the pullers in their original orientations after the collision at high enough Ri.

At high Ri, i.e., Ri = 5 as compared to Ri = 1, the isopycnals are less deformed indicating that the resistance to the displacement of the isopycnals due to the flow induced by the squirmers is stronger. This prevents the clockwise rotation of the pullers and reorients them. Thus, the competition between the rear vorticity bubble interactions and the tendency of deformed isopycnals to return to their original levels determines the rotational motions and the orientations of the pullers after the collision. Owing to the smaller size of the rear vorticity bubbles of pullers in a stratified fluid compared to a homogeneous fluid [342], the effect of the stratification dominates the vorticity bubble interactions between the two pullers at high Ri values. This prevents the pullers from attaining a constant angular velocity unlike in a homogeneous fluid, thus, eliminates the closed loops for Re = 10, 50 and results in the reorientation of the pullers for Re = 1, 5 and 10.

The consequences of the mentioned vorticity and isopycnal interactions on the colliding pullers can be understood from their translational and angular velocities. Velocity evolution for two approaching pullers is plotted in Fig. 9.5 for Re = 10 and various stratification strengths. Stratification leads to the elimination of the oscillations in the translational velocities of the pullers after the collision and allows them to attain a steady velocity which results in their escape from each other (Fig. 9.5a). In addition, the tendency of the displaced isopycnals to return to their neutrally buoyant levels prevent the pullers from attaining a constant angular velocity as can be seen in Fig. 9.5b. This results in the reorientation of the pullers to their original orientation.

9.3.1.2 Pullers moving side by side

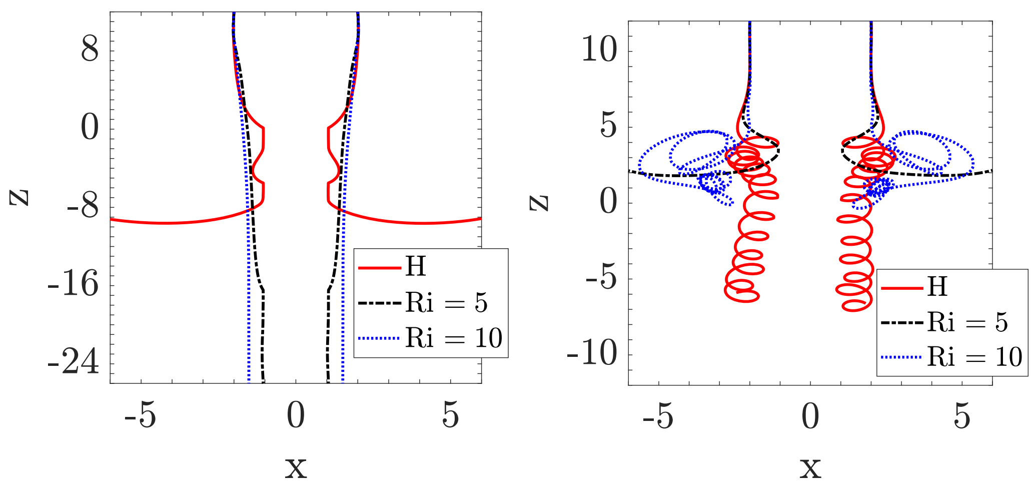

(a) Re = 10 **(b)** Re = 50

Figure 9.6. Trajectories of a pair of pullers, $\beta = 5$, moving side-by-side initially separated by a distance $4a$ in x direction at various stratification strengths. a) Re = 10, b) Re = 50. H in the legends stands for homogeneous fluid or Ri = 0.

In addition to squirmers approaching each other in the opposite directions and colliding, we also investigate the motion of a pair of squirmers moving side by side initially apart by Δx in the x-direction. Fig. 9.6 shows the trajectories of two pullers moving side by side in different stratification strengths at Re = 10 and 50. In a homogeneous fluid, pullers moving side-by-side exhibit completely disparate trajectories at Re = 10 and Re = 50. At Re = 10, the pullers are initially attracted towards each other and they come close and stick together while they move downward. They move away from each other but are pulled together after a while. They again move down together a little before being repelled away from each other and finally scatter away in the horizontal direction (see Fig. 9.6a). While for Re = 50, the pullers are slightly repelled from each other initially. But they are pulled towards each other which also leads to a torque on them making them rotate in a loop while they move down (see Fig. 9.6b). Thus, in a homogeneous fluid, a pair of pullers moving side-by-side scatter away from each other at Re = 10 while they are hydrodynamically trapped near each other in loops for Re = 50.

Introducing stratification increases the attraction between the pullers moving side-by-side at Re = 10 (see Fig. 9.6a). At Ri = 5 and 10, this increase in the attraction between the pullers increases the time that the pullers spend near each other before they collide and prevents the pullers from separating unlike in a homogeneous fluid. As a result, once the pullers collide sideways they stick together and move further down.

The significant changes in the trajectories of two pullers moving side-by-side due to stratification can also be seen at a higher Re (= 50, see Fig. 9.6b). For Ri = 5, the pullers are again hydrodynamically trapped near each other in loops but they do not move much in the downward direction. Increasing the stratification further to Ri = 10, the pullers are attracted towards each other leading to a sideways collision. However, after this collision, they are repel away from each other and scatter away in the horizontal direction, similar to what happens eventually for Re = 10 in a homogeneous fluid. This is expected as stratification leads to a reduction in the squirmer velocities. This reduces their effective Re which explains the qualitative similarities between the trajectories in the high Re-high Ri and the low Re-no stratification case.

9.3.2 Pairwise interactions of pushers in a stratified fluid

9.3.2.1 Pushers approaching each other

Fig. 9.7 shows the trajectories for two pushers approaching each other in opposite directions, initially oriented parallel to each other for Re = 1, 5, 10 and 50 in a homogeneous fluid and a stratified fluid with different Ri. In the absence of any density stratification, the trajectories of the colliding pushers reveal two patterns based on the magnitude of Re. At relatively low values of Re, i.e., 1, the pushers come to a complete stop after the collision. However, this configuration is unstable and the pushers are deflected away from the $y = 0$ plane resulting in a three-dimensional (3D) motion after the collision [280]. This behavior is common for interacting pushers for Re << 1 and is due to the instability in their two-dimensional (2D) motion once they come close to each other [333]. As we increase the Re further, the pushers escape each other after the collision with a scattering angle $\phi < 90°$. ϕ increases with increase in the inertia of the pushers with values $\approx 0°$, $\approx 30°$ and $\approx 90°$ for Re = 5, 10 and 50, respectively.

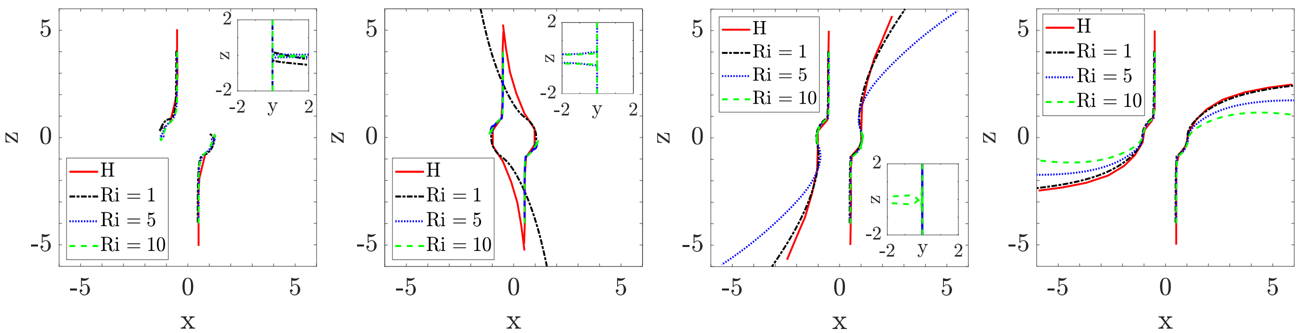

(a) Re = 1 **(b)** Re = 5 **(c)** Re = 10 **(d)** Re = 50

Figure 9.7. Trajectories for colliding pushers with $\beta = -5$ in a homogeneous and a stratified fluid with increasing stratification strengths. At low Re = 1, 5 and 10, high enough stratification leads to the stoppage of the pushers as they collide. This state is not stable and as a results the pushers are deflected away from the xz plane in the y direction. The pushers stick together as they are move in the y direction after the deflection indicating that stratification leads to hydrodynamic trapping of colliding pushers. This deflection away from the xz plane is shown in the insets in (a), (b) and (c). This instability is gradually prevented with increasing Re and the pushers no more stop or are deflected at high Re, i.e., Re = 50. H in the legends stands for homogeneous fluid.

Introducing stratification results in distinct changes in the trajectories of the interacting squirmers depending on their Re and the stratification strength, i.e., Ri. At low Re, the effect of introducing stratification on the trajectories of colliding pushers is to trap them near each other by bringing them to a complete stop. However, these states are not stable and soon the pushers leave the plane of collision, i.e., xz plane, and are deflected in the y direction. The pushers stick together as they leave the $y = 0$ plane and continue to move together in the y direction as shown in the insets of Fig. 9.7a and 9.7b. The same is true for a high enough stratification at higher Re. The pushers come to a stand-still after collision and move together in the y plane for Re $= 10$ at Ri $= 10$. Introduction of the stratification leads to the reduction in the translational velocities of the pushers which reduces their effective inertia resulting in low Re like trajectories even at high Re values.

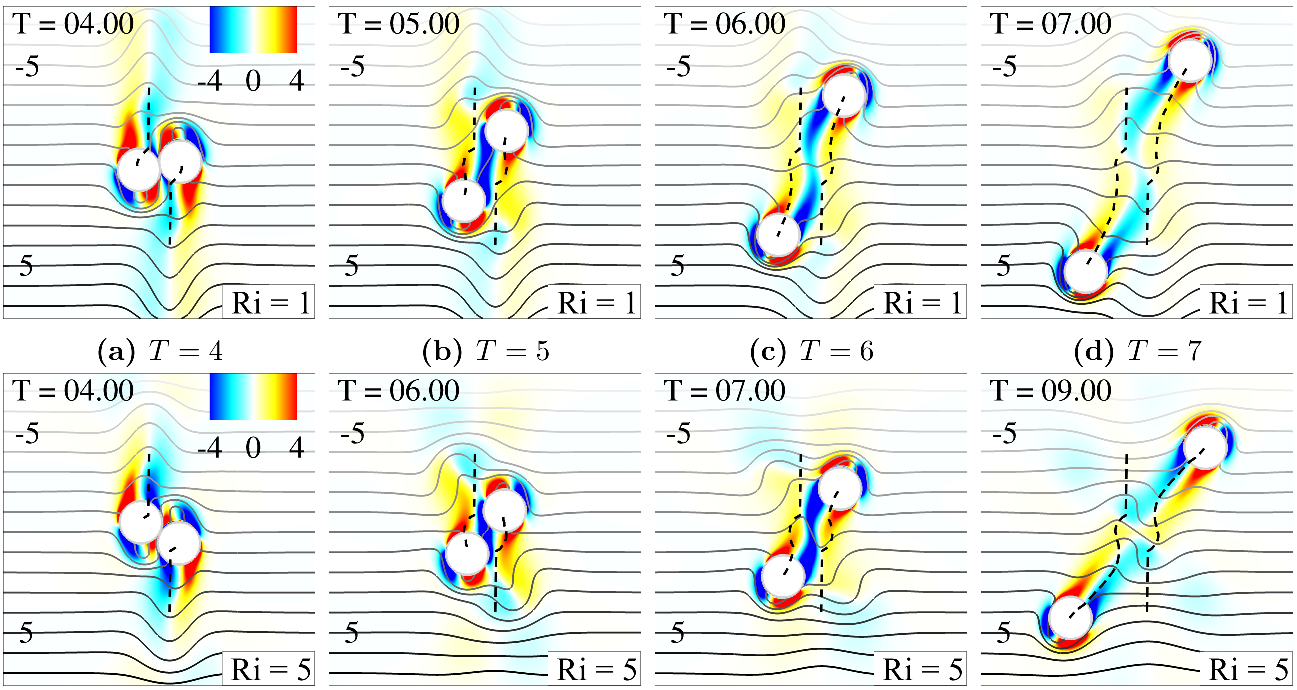

(a) $T = 4$ **(b)** $T = 5$ **(c)** $T = 6$ **(d)** $T = 7$

(e) $T = 4$ **(f)** $T = 6$ **(g)** $T = 7$ **(h)** $T = 9$

Figure 9.8. Vorticity contours and isopycnals during the collision process of two approaching pushers with Re $= 10$ at different stratification strengths, Ri $= 1$ (a,b,c,d) and 5 (e,f,g,h). These plots show the interaction between the vorticity bubbles and the deformed isopycnals. The need of the displaced isopycnals to return to their original levels determine the trajectories of the pushers after the collision. The isopycnals are the normalized density differences given by $(\rho - \rho_0)/\gamma a$ and each line is 1 unit apart. Darker line color shade indicates a higher density value. Colorbar for the vorticity contours is presented in the plots. Dashed lines indicate the pusher trajectories. These are snapshots of the flow-field at different dimensionless times, $T = tU_0/a$, the value of which is indicated in the caption. Colorbar is only shown in the first plot of each row for the neatness of the plots. For movies see **supplementary**.

For intermediate Re $= 10$ and high Re $= 50$, the effect of stratification depends on the magnitude of Ri. The trapping due to the stoppage of the pushers after the collision at low Re values and the 3D trajectories are progressively prevented at high Re values. This can be seen in Fig. 9.7c and 9.7d. At high Re and low Ri, the effect of inertia is significant compared to the effect of stratification. As a result, the pushers try to move away from each other similar to what happens in a homogeneous fluid. This can be observed for Re = 10 at Ri = 1 & 5 and Re = 50 at Ri = 1, 5 & 10 for which pushers are scattered away from each other with $\phi \approx 45°$ and 90°, respectively.

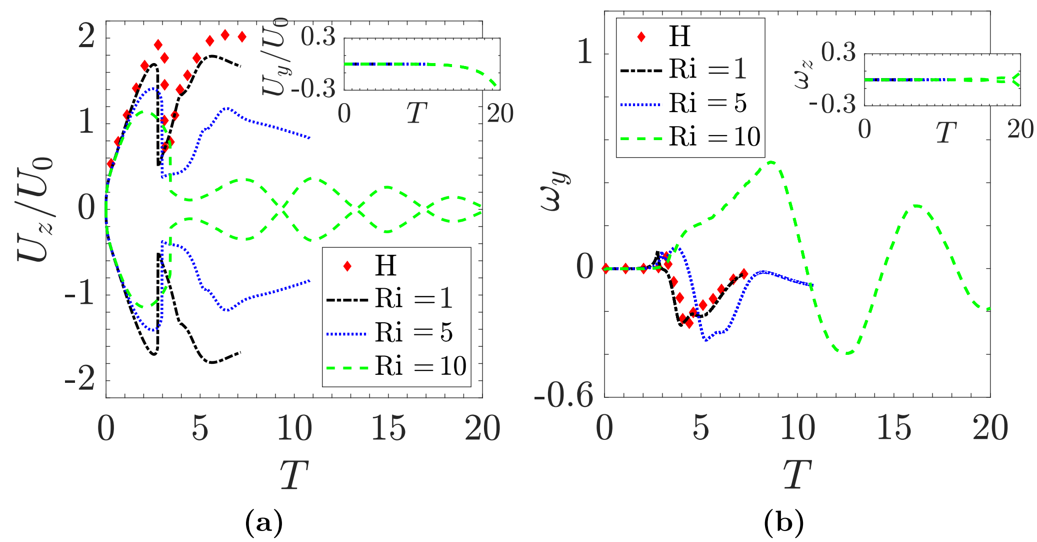

Figure 9.9. Time evolution of the a) translational velocity and the b) rotational velocity of two approaching pushers during the collision process at different Ri values for a fixed Re = 10. Stratification leads to a significant reduction in the velocities of the pushers after their collision. At a high stratification, the pushers come to almost a stop after collision and eventually are deflected away from the $y = 0$ plane which is shown by the time evolution of the y velocities of the pullers in the insets.

We plot the vorticity contours and the isopycnals in Fig. 9.8 for Re = 10 at two Ri values, viz., 1 and 5. The interaction of the pushers with the isopycnals reveal the reason behind the deflection from their trajectories in a homogeneous fluid for high Re values (10 and 50). Fig. 9.8 shows that as the pushers move forward, they displace the isopycnals behind them owing to the long vorticity trail behind them. However, as Ri increases these displaced isopycnals resist the flow induced by the pushers as they try to return to their original levels. The strength of opposition by the displaced isopycnals to their further deformation increases with Ri. E.g., for Ri = 1 (Fig. 9.8a - 9.8d) the isopycnals behind the pushers are deformed for a longer time while they return to their original levels quickly for Ri = 5 (Fig. 9.8e

- 9.8h). As a result of the interaction between rear vorticity bubbles and the flow due to the deformed isopycnals in the wake of the pushers, their y angular velocity increases (see Fig. 9.9b) and the pushers are deflected to their right.

Fig. 9.9 shows the translational and rotational velocities of the pushers at various stratification strengths for Re = 10. It can be seen from Fig. 9.9a that the translational velocities of the squirmers decrease with increasing stratification both before and after the collision. The reason for this decrease is the trapping of lighter (heavier) fluid in the recirculatory region which in the front region leading to a higher buoyancy force on them as they move in a heavier (lighter) fluid. For a high enough Ri value (e.g. Ri = 10 at Re = 10) the velocity reduction is large enough to lead to an instability which deflects them away from the $y = 0$ plane. For the cases when the collision process does not lead to an instability (e.g., Ri = 1 and 5 at Re = 10), stratification increases the magnitude of the rotational velocity of the pushers which causes the divergence in their trajectories after the collision compared to their homogeneous fluid trajectories (see Fig. 9.9b).

9.3.2.2 Pushers moving side by side

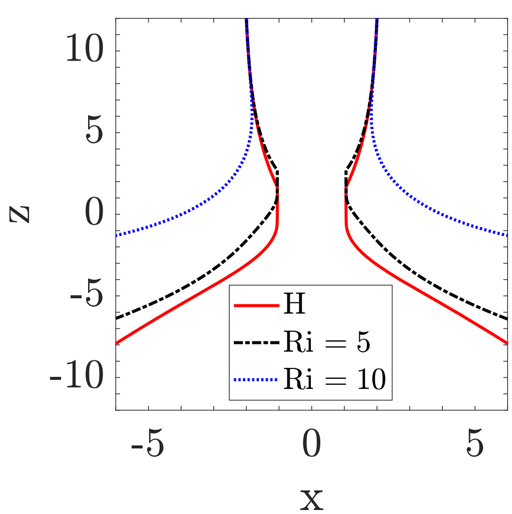

(a) Re = 10

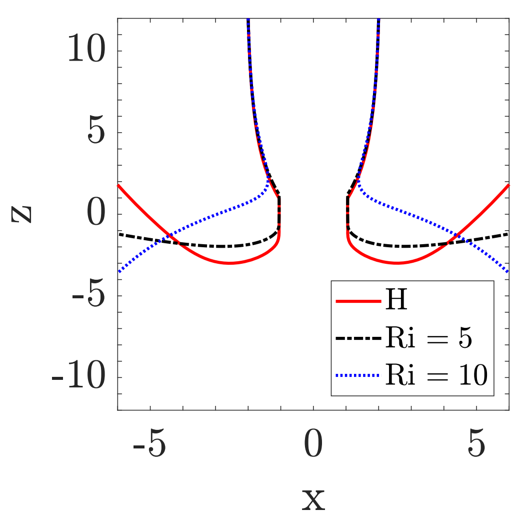

(b) Re = 50

Figure 9.10. Trajectories of a pair of pushers, $\beta = -5$, moving side-by-side initially separated by a distance $4a$ in x direction at various stratification strengths. a) Re = 10, b) Re = 50. H in the legends stands for homogeneous fluid or Ri = 0.

In contrast to a pair of pullers moving side-by-side, stratification has a limited effect on the trajectories of a pair of pushers moving side-by-side which is shown in Fig. 9.10. For all the Re values explored, i.e., 10 and 50, the pushers are initially attracted towards each other. But this attraction does not last very long and eventually they deflect away from each other. The effect of stratification is to lower the z value where the pushers first start to separate from each other. Here we measure the scattering angle as the angle the final pusher orientation makes with its initial orientation.

In a homogeneous fluid, the pushers are attracted to each other at Re = 10 and 50. As they come very close, they stick together and move down before deflecting away. Increasing the inertia of the pushers leads to an increase in their scattering angle after the deflection (see Fig. 9.10). Increasing the stratification strength hastens the process of repulsion leading to the pushers are pushed away at lower z distances from their initial positions as compared to a homogeneous fluid. At a high stratification, the pushers are pushed away from each other even before they can come very close to each other as they do in a homogeneous fluid. This is observed from the pusher trajectories at Ri = 10 for both Re values in Fig. 9.10. In addition, at Re = 50, increasing the stratification leads to a reduction in the scattering angles of the pushers. However, at Re = 10, stratification results in a slight increase in the scattering angles of the pushers. Again, there are qualitative similarities in the trajectories of the pushers at high Re-high Ri and low Re-no stratification values as we observed in the case of a pair of pullers which is due to the reduction in the effective Re of the pushers at high Ri due to the reduction in their swimming speeds.

9.3.3 Contact time

Fig. 9.11 plots the contact time for a pair of squirmers colliding with each other against Ri for various Re values explored in this study. We define contact time as the time spent by the squirmers in contact, i.e., when their center-to-center distance is less than $d + 2\Delta$ which is also the distance when the repulsive force between the squirmers is active. For the cases where the squirmers deflect away from the $y = 0$ plane, we measure contact time just before the squirmers are deflected. We observe that pushers spend more time in contact as compared to pullers for the range of parameters explored in this study. The contact time

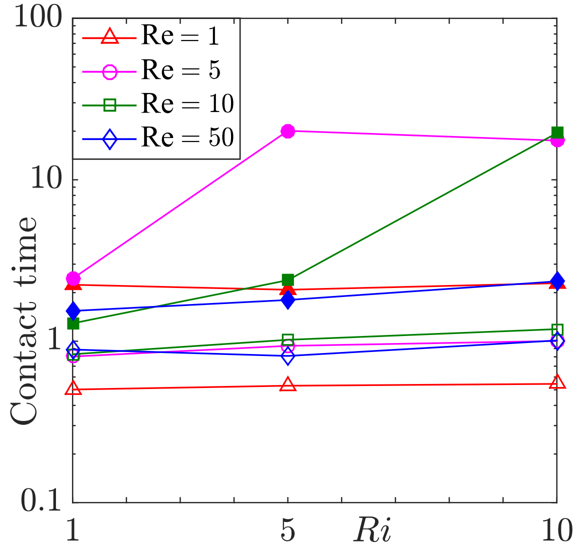

Figure 9.11. Contact time, i.e., time spent by the squirmers near (center-to-center distance ≤ 2.12) each other for colliding squirmer pairs. Hollow symbols are for pullers and filled symbols are for pushers.

increases slightly with Ri for all the cases except for pushers with Re $=5$ & 10. This is because the pushers are separated from each other at low Ri while they are trapped and deflect in the third direction at high Ri for Re $=5$ & 10.

In many real-life situations, it is beneficial to estimate the contact time of swimmers. For reproductive purposes, it is beneficial for the swimmers to spend more time on contact while they want to not be in contact with a predator and escape as soon as possible. The results thus can be used to predict the encounter time of pusher and puller swimmers to predict their success in reproduction or feeding or escaping from predators. These results show that pushers tend to spend more time in contact than pullers which increases with increasing the stratification. This can enhance their success in reproduction in stratified environments.

9.3.4 Effect of initial lateral spacing

Fig. 9.12 shows the effect of changing Δx on the trajectories of a pair of colliding squirmers for Re $=10$ and Ri $=5$. These results show that changing Δx for pullers does not change the trajectories of the pullers significantly as they are qualitatively the same. However, Δx

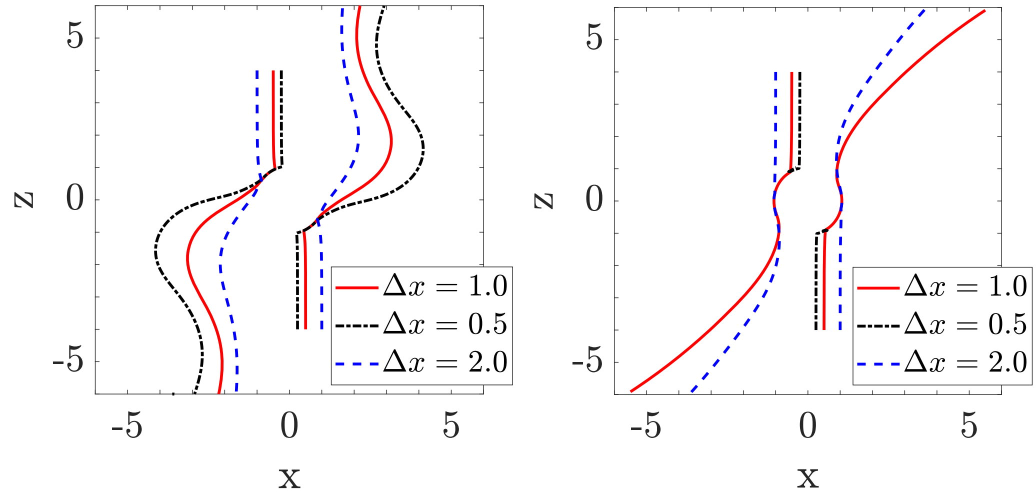

(a) Pullers, $\beta = 5$ **(b)** Pushers, $\beta = -5$

Figure 9.12. Trajectories of a pair of colliding a) pullers, $\beta = 5$ and b) pushers, $\beta = -5$ For different Δx. Re = 10 and Ri = 5.

has a significant role in determining the trajectories of colliding pushers. For $\Delta x = 1$ & 2 the pushers collide and separate from each other, while for a smaller Δx (=0.25), the pushers stop after the collision which is similar to what happens for high stratification at larger Δx. Thus, decreasing Δx simply decreases the Ri above which the instability in the colliding squirmer configuration sets in. Thus, the details of the trajectories are more closely related to the initial configuration for pushers than pullers.

9.3.5 Effect of Prandtl number

We briefly discuss the effects of varying Pr on the trajectories of colliding pair of pullers and pushers in this subsection. We assumed Pr = 0.7 for this study in order to resolve the density boundary layer. But for temperature stratified water Pr = 7 while Pr = 700 for salt stratified water. Resolving the density boundary layer ($\approx O(d/\sqrt{\text{RePr}})$) becomes computationally expensive with increasing Pr. Hence a small value of Pr was used to save the computational penalty. Changing Pr of the fluid quantitatively changes the settling velocity of a rigid sphere [299] and the swimming velocity of neutrally buoyant squirmers [342] while the qualitative trend remains the same in both these cases. Thus, changing Pr will also change the trajectories of a pair of squirmers interacting in a stratified fluid. In addition,

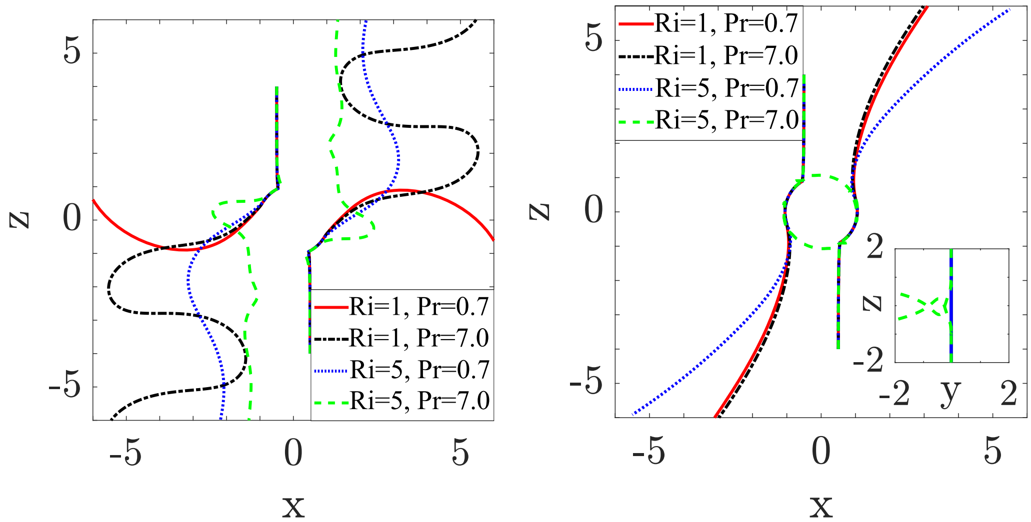

(a) Pullers, $\beta = 5$ **(b)** Pushers, $\beta = -5$

Figure 9.13. Trajectories of a pair of pushers, $\beta = -5$, moving side-by-side initially separated by a distance $4a$ in x direction at various stratification strengths. a) Re $= 10$, b) Re $= 50$. H in the legends stands for homogeneous fluid or Ri $= 0$.

the transition from one type of trajectory to the other will happen at different values of Re and Ri.

We present the trajectories of a pair of pullers and pushers colliding for two different Ri and Pr in Fig. 9.13. For a pair of colliding pullers with Re $= 10$, the pullers swim away from each other even at Pr $= 7$, however, their trajectories are different compared to Pr $= 0.7$ case. On the other hand, for pushers, the trajectories are similar for a lower Ri. But the swimmers get trapped near each other for Ri $= 5$ in the case of Pr $= 7$ unlike the case when Pr $= 0.7$. These results show that the details of the trajectories, i.e., Ri for which they separate, exact trajectories and Ri for which they get trapped near each other and deflect away from the initial plane, depend on the value of Pr. This is expected as Pr governs the size of the density boundary layer which has an important role in determining the near field interactions between swimmers.

10. ORIENTATION INSTABILITY OF SETTLING SPHEROIDS IN A LINEARLY DENSITY STRATIFIED FLUID

10.1 Introduction

Particles settling in a fluid medium under the influence of gravity has historically been a widely investigated research problem [344]–[348]. In the past few decades, researchers have devoted many efforts to understand the effects of fluid density stratification on the settling dynamics of spherical particles, mainly motivated by geophysical applications [261], [299], [349]. The most notable effect of density stratification on the motion of a spherical particle is drag enhancement. This observation has been confirmed by experiments [252], [350], [351], theory [240] and computations [352], [353]. The immediate effect of this drag enhancement is to reduce the settling velocity of a sphere falling through a stratified fluid under the influence of gravity, an effect which should therefore be considered in large-scale transport models of environmental interest [299].

Fluid stratification also modifies the flow structures around spherical particles in interesting ways. Depending on the Reynolds number of the moving particle, $Re_p = U_p D/\nu$, and the Froude number of the flow, $Fr = U_p/ND$, a variety of jet structures can be observed [354] behind a sphere with diameter D moving vertically with a velocity U_p in a stratified fluid with kinetic viscosity ν and Brunt–Väisälä frequency N. The formation of the jet influences a variety of phenomena in the oceans, such as the vertical movement of zooplankton and buoys used for ocean observation. Owing to the ubiquity of the density stratification due to salinity and/or temperature gradients in nature, e.g., in the atmosphere [216], lakes, and oceans [211], it is obvious that studying how the density stratification influences the dynamics of settling/moving particles is crucial to understand a plethora of natural phenomenon. For example, the atmospheric pollutants and pyroclastic particles [355] have sizes ranging from a few μm to a few mm with Re_p ranging from $O(0-1000)$.

In oceans, the top layer, $O \approx (1-1000)m$ deep, is associated with intense biological and ecological activities which are strongly influenced by the density stratification. The formation of algal blooms has been known to be a direct consequence of marine organisms' interactions with density stratification [211]. Stratification significantly alters the stability, interaction, and nutrient uptake of organisms [284], [293], [356], [357]. Stratification impacts carbon fluxes into the ocean by inhibiting the descent of marine snow particles (aggregates > 0.5mm in diameter) [220]. Furthermore, the vertical density stratification promotes accumulation of marine snow [220] and of phytoplankton [358]. The Re_p of these marine entities is $\approx O(0-100)$ depending on their sizes [359], [360]. The bio-convection in the oceans is an important step in the carbon cycle and is responsible for transferring about 300 million tons of carbon from the atmosphere to the oceans every year [361], [362]. These observations make it imperative to investigate the role of density stratification on the dynamics of settling particles. However, the particles/organisms which are influenced by stratification are not exactly spherical. They come in a variety of shapes [363]. The most common shapes that can be imagined are plate-like flat [364] or rod-like elongated [365]. The extra degree of freedom introduced by the anisotropy of the particle shape leads to interesting settling dynamics.

Even in a homogeneous fluid, the anisotropy of the settling particle shape leads to more convoluted phenomena like breaking of the flow axial symmetry, oscillatory settling path, and wake instability not observed for a spherical particle [366], [367]. The influence of the body degrees of freedom on the wake dynamics along with the vorticity production at the body surface can explain the wake instabilities and their consequences on the body path [368], [369]. Specifically, for oblate spheroids, four different states for the particle motion are observed for Galileo number, $Ga = \sqrt{(|\rho_r - 1|gD^3)/\nu^2}$, between 50 to 250 [369], [370] for aspect ratio, $\mathcal{AR} = 1/3$. Here g is the acceleration due to gravity and D is the diameter of a sphere with the same volume as the spheroidal particle. The transition between the four states takes place at $Ga \approx 120$, 210, and 240 for $\rho_r = 1.14$. On the other hand, the onset of secondary motions for prolate spheroids occurs at a considerably lower Ga than for an oblate spheroid. The peculiar feature of settling prolate spheroids is that they attain a terminal rotational velocity about the axis parallel to the vertical direction in which it is falling freely for $Ga > 70$ in the case of aspect ratio, $\mathcal{AR} = 3$. This behavior can be explained by the four thread-like quasi-axial vortices appearing in the wake of a prolate spheroid [369]. Recently, [371] have presented theoretical and experimental evidence of an orientation transition of a fiber due to a gravitational torque that arises above a critical Reynolds number and showed the evolution of the oblique orientation toward the broadside orientation as Re increased.

Although particle shape anisotropy leads to path and wake instabilities in the settling motion of particles in a homogeneous fluid, it does not change the steady-state settling orientations of the particles. The spheroidal particles have been observed to settle such that their long axis is always perpendicular to the settling direction [367], [369], [372], [373] for $Re_p > 0.1$. In addition, the particles reach a constant terminal velocity when falling freely in a homogeneous fluid. The terminal velocity depends on the Ga and the aspect ratio of the particles.

The settling dynamics of spherical as well as non-spherical particles is significantly altered by the presence of fluid density stratification. The first notable departure from the settling in a homogeneous fluid is the absence of a terminal velocity. This is because stratification increases the drag experienced by the settling particles which therefore reduces their settling speeds. In addition, increasing buoyancy leads to the deceleration of the particle as it approaches the neutrally buoyant position and can cause oscillations in the particle velocity depending on the strength of stratification [299].

Recently, researchers have started exploring the effects of stratification on the settling dynamics of anisotropically shaped particles in a stratified fluid. Most of the investigations are limited to disks. Experiments of a disk settling encountering a stratified two-layer fluid show that the disk reorients itself such that the long axis is perpendicular to the vertical direction while it moves through the transition layer between the two fluids [233], [374], [375]. Further, a disk settling in a linearly stratified fluid has been observed to go through three regimes as it settles. First, there is a quasi-steady state with the disk long axis perpendicular to the vertical direction. Then, there is a change in the stability for the disk orientation when it changes its orientation from long axis normal to the vertical direction (broad-side on) to long axis parallel to the vertical axis (edge-wise). Finally, the disk settles edge-wise at its neutrally buoyant position [376]. As concerns prolate spheroids, we can only mention the numerical study by [377], on the settling across a density interface. Hence, we are still far from completely understanding the settling and orientation dynamics of spheroidal shaped particles in a stratified fluid.

From a computational point of view, tracking an oblate and a prolate spheroid is similar but computationally, the simulations for prolate spheroids are more expensive. This is also true in the current numerical framework which will be discussed in the following sections. The scarcity of studies with prolate spheroids does not mean a lack of practical applications as elongated particles in a stratified fluid are routinely encountered in many industries involving suspensions of particles settling under gravity, pollutant transport in atmosphere or water, fluidized beds, and settling of marine snow or organisms in upper ocean layers. The most common shapes that can be imagined are plate-like flat [364] or rod-like elongated [365].

To gain some new understanding of the problem, we numerically simulate the free-falling motion of spheroidal particles, an oblate spheroid with an aspect ratio, $\mathcal{AR} = 1/3$ and a prolate spheroid with $\mathcal{AR} = 2$, in a linearly stratified fluid for different Ga and Fr values. The aim of this effort is to investigate the possible mechanism which leads to the orientational instability of a freely falling spheroidal object in a linearly stratified fluid.

10.2 Governing equations

We present the governing equations and the solution methodology implemented to solve them in this section. We solve the Navier-Stokes equations and the continuity equation in terms of the perturbation velocity field and calculate the perturbation flow field $\mathbf{u} = \mathbf{u} - \mathbf{U}_p$, where $\mathbf{u}$ is the fluid velocity field and $\mathbf{U}_p$ is the instantaneous particle velocity. We assume the fluid to be Newtonian and incompressible and assume the Boussinesq approximation for the density to be valid which means we can ignore density differences everywhere except in the gravitational body force term. These assumptions results in the following equations, written in the reference frame translating with the particle velocity $\mathbf{U}_p$:

$$\rho_f \left(\frac{\partial \mathbf{u}}{\partial t} + (\mathbf{u} - \mathbf{U}_p) \cdot \nabla \mathbf{u} \right) = -\nabla p + \mu \nabla^2 \mathbf{u} + \rho_f (\mathbf{g} + \mathbf{f}), \tag{10.1}$$

$$\nabla \cdot \mathbf{u} = \mathbf{0}, \tag{10.2}$$

where ρ_f is the density field, $\mathbf{U}_p$ is the instantaneous particle translational velocity, p is the pressure, μ is the fluid dynamic viscosity, $\mathbf{g}$ is the acceleration due to gravity. The additional term $\mathbf{f}$ on the right-hand-side of (10.1) accounts for the presence of particle, modelled with the immersed boundary method (IBM). This IBM force is active in the immediate vicinity of a particle to impose the no-slip and no-penetration boundary conditions indirectly. In other words, the force distribution $\mathbf{f}$ ensures that the fluid velocity at the surface is equal to the particle surface velocity ($\mathbf{U}_p + \boldsymbol{\omega}_p \times \mathbf{r}$).

The particle motion is solution of the following Newton-Euler Lagrangian equation of particle motion:

$$\rho_p V_p \frac{\mathrm{d}\mathbf{U}_p}{\mathrm{d}t} = \oint_{\partial V_p} \boldsymbol{\tau} \cdot \mathbf{n} \, \mathrm{d}A, \tag{10.3}$$

$$\frac{\mathrm{d}\left(\mathbf{I}_p \boldsymbol{\omega}_p\right)}{\mathrm{d}t} = \oint_{\partial V_p} \mathbf{r} \times (\boldsymbol{\tau} \cdot \mathbf{n}) \, \mathrm{d}A, \tag{10.4}$$

here $\mathbf{U}_p$ and $\boldsymbol{\omega}_p$ are the particle translational and angular velocities. ρ_p, V_p and $\mathbf{I}_p$ represent the particle density, particle volume and the particle moment of inertia matrix. $\mathbf{n}$ is the unit normal vector pointing outwards on the particle surface, while $\mathbf{r}$ is the position vector from the particle's center. $\boldsymbol{\tau} = -p\mathbf{I} + \mu\left(\nabla\mathbf{u} + \nabla\mathbf{u}^T\right)$ is the stress tensor and its integration on the particle surface accounts for the fluid-particle interaction.

Accounting for the inertia and Buoyancy forces of the fictitious fluid phase inside the particle volume and using IBM, Eqs. 10.3 and 10.4 are rewritten as below:

$$\rho_p V_p \frac{\mathrm{d}\mathbf{U}_p}{\mathrm{d}t} \approx -\rho_0 \sum_{l=1}^{N_L} \mathbf{F}_l \Delta V_l + \rho_0 \frac{\mathrm{d}}{\mathrm{d}t}\left(\int_{V_p} \mathbf{u} \mathrm{d}V\right) - \int_{V_p} \rho_f \mathbf{g} \mathrm{d}V + \rho_p V_p \mathbf{g} \, , \tag{10.5}$$

$$\frac{\mathrm{d}\left(\mathbf{I}_p \boldsymbol{\omega}_p\right)}{\mathrm{d}t} \approx -\rho_0 \sum_{l=1}^{N_L} \mathbf{r}_l \times \mathbf{F}_l \Delta V_l + \rho_0 \frac{\mathrm{d}}{\mathrm{d}t}\left(\int_{V_p} \mathbf{r} \times \mathbf{u} \mathrm{d}V\right) - \int_{V_p} \mathbf{r} \times \rho_f \mathbf{g} \mathrm{d}V \, , \tag{10.6}$$

where the first two terms on the right-hand-side of the equations denote the hydrodynamic force and torque F_h and T_h, respectively. The third term and the fourth term together in Eq. 10.5 indicate the buoyancy force F_b while the third term in Eq. 10.6 indicate the T_b. More details on the numerical model can be found in [378], [379].

The vertical variation in the fluid density can either be due to the vertical variation in the fluid temperature or salinity or both. For this study we consider the density stratification to arise from the fluid temperature variation. Thus, the particle sediments in a linearly density stratified fluid with the initial vertical density stratification given by $\bar{\rho}(z) = \rho_0 - \gamma z$. ρ_0 is the reference density, γ is the vertical density gradient and z is the vertical coordinate. The fluid density increases linearly in the downward z direction (gravity direction). The density variation across thermocline occurs due to the vertical variation in the temperature, since

$\rho = \rho_0 \left(1 - \beta \left(T - T_0\right)\right)$, where β is the coefficient of thermal expansion, T is the temperature field and T_0 is the reference temperature corresponding to the reference density, ρ_0. Thus, the initial temperature of the background fluid is given by, $\bar{T}(z) = T_0 + (\gamma/\beta\rho_0)z$. The energy equation for an incompressible fluid flow in the frame of reference moving with the particle can be simplified to,

$$\frac{\partial T}{\partial t} + (\mathbf{u} - \mathbf{U}_p) \cdot \nabla T = \nabla \cdot (\alpha \nabla T). \tag{10.7}$$

α is the thermal diffusivity. We split the temperature field in the linear component and the perturbation (T) as $T = \bar{T}(z) + T$. We solve for the temperature perturbation, T, and add it to the linear component to get the temperature field at any instance of time. Eq. (10.7) can be rewritten in term of the temperature perturbation field, T as follow:

$$\frac{\partial T}{\partial t} + (\mathbf{u} - \mathbf{U}_p) \cdot \nabla(\bar{T}(z) + T) = \nabla \cdot (\alpha \nabla T). \tag{10.8}$$

We set $\alpha = 0$ for the particle [299] and $\alpha = \nu/Pr$ for the fluid phase. ν is the fluid kinematic viscosity and Pr is the Prandtl number. This is equivalent to the insulating/impermeable/no-flux boundary condition on the surface of the particle [299], [353] which is also true if the stratifying agent is salt or having an adiabatic particle. We also investigate the effects of relaxing the no-flux boundary condition on the particle surface by varying α for the particle by changing the particle heat conductivity, k, in Sec. 10.3.2.4.

10.2.1 Dimensionless parameters & simulation conditions

Re-writing the equations in the non-dimensional form results in the following equations:

$$\frac{\partial \mathbf{u}}{\partial t} + ((\mathbf{u} - \mathbf{U}_p) \cdot \nabla) \mathbf{u} = -\nabla P + \frac{1}{Re} \nabla^2 \mathbf{u} + \frac{Ri}{Re} T + \mathbf{f}, \tag{10.9}$$

$$\frac{\partial T}{\partial t} + (\mathbf{u} - \mathbf{U}_p) \cdot \nabla T + \mathbf{u} \cdot \hat{e}_g = \frac{1}{\rho^* C_p^*} \nabla \cdot \left(\frac{k^*}{RePr} \nabla T \right), \tag{10.10}$$

$$\nabla \cdot \mathbf{u} = \mathbf{0}, \tag{10.11}$$

where, $\mathbf{u}$, T and P now denote dimensionless perturbations in velocity, temperature and pressure field. Temperature is normalized with the temperature difference of 1 equivalent particle diameter in the gravity direction. ρ^*, C_p^* and k^* indicate particle density, heat capacity and heat conductivity ratio (ρ_r, C_{p_r} and k_r) inside the particles and are equal to 1 in the fluid region. We investigate the sedimentation of spheroidal particles in a quiescent but linearly density stratified fluid with finite inertia. The details on the numerical algorithm to solve the governing equations and validations of the numerical tool are provided elsewhere [369], [380], [381] and hence not discussed here.

The non-dimensional parameters defining the problem are described below:

1. The Galileo number, $Ga = UD/\nu$, with the reference velocity U defined as $U = \sqrt{D|\rho_r - 1|g}$. D is the length scale corresponding to the particle size, set as the diameter of a sphere with the same volume as that of the spheroidal particle ($D = (b^2 a)^{(1/3)}$). a and b denote the polar and the equatorial radius of the spheroidal particle. Ga quantifies the relative importance of gravitational and viscous forces.

2. The particle Reynolds number, $Re_p = U_p D/\nu$, which quantifies the relative importance of the inertial and the viscous forces. Here U_p is the instantaneous particle velocity so this is a non-dimensional measure of the particle settling speed.

3. The Richardson number, $Ri = \gamma g D^3/(U\rho_0\nu) = D^3N^2/(U\nu)$, which quantifies the relative importance of buoyancy and the viscous time scales. $N = (\gamma g/\rho_0)^{1/2}$ is the Brunt–Väisälä frequency. It is the natural frequency of oscillation of a vertically displaced fluid parcel in a stratified fluid.

4. The Prandtl number, $Pr = C_p\mu/k$, defined as the ratio of momentum diffusivity to thermal diffusivity inside the fluid region.

5. The particle density ratio, indicating the ratio between the particle density and the reference density of the fluid. $\rho_r = \rho_p/\rho_0$.

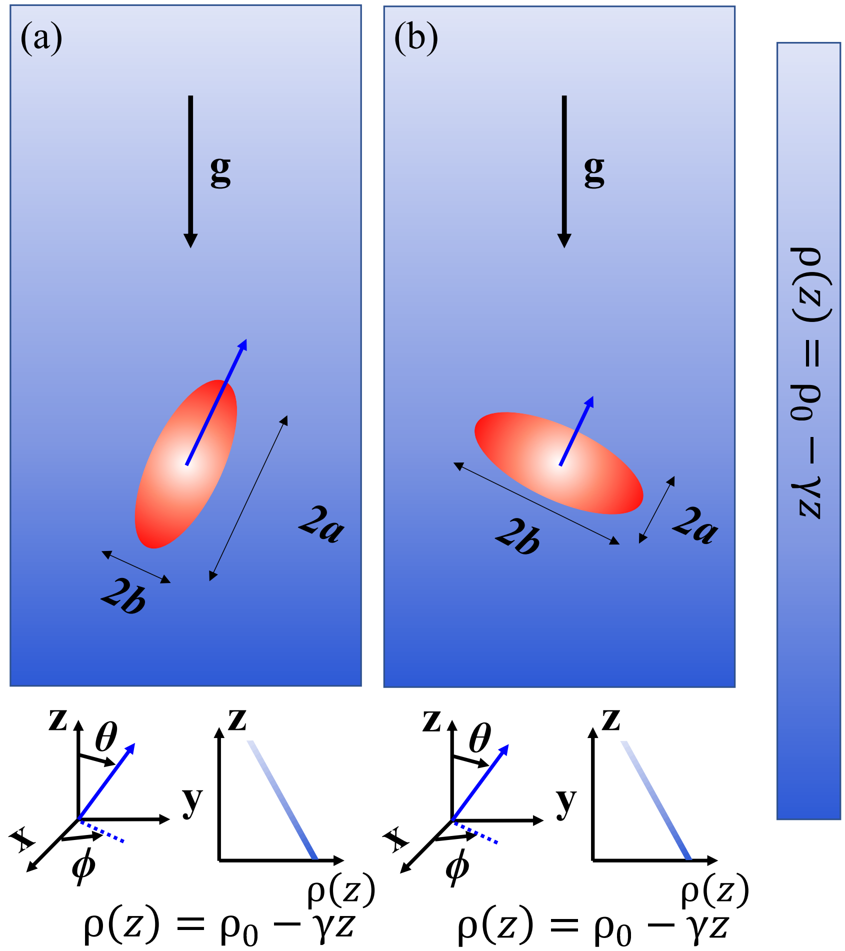

Figure 10.1. Schematic of the settling spheroidal objects in a linearly density stratified fluid. a) Oblate spheroid ($\mathcal{AR} < 1$) and b) prolate spheroid ($\mathcal{AR} > 1$). Here a and b are the semi-major and the semi-minor axis. The aspect ratio $\mathcal{AR}$ is given by a/b. For spherical particles $\mathcal{AR} = 1$. The orientation of the particle is quantified in terms of the polar angle θ and the azimuthal angle ϕ for a vector directed along the major axis of the spheroids. The coordinate system used is shown at the top of the figures.

6. The particle heat conductivity ratio, $k_r = k_p/k_f$, with subscripts $_p$ and $_f$ denoting the particle phase and the fluid phase.

7. The particle heat capacity ratio, $C_{p_r} = C_{p_p}/C_{p_f}$.

8. the particle aspect ratio, $\mathcal{AR} = a/b$.

Finally, the characteristic time scale, τ, used to make t dimensionless is chosen to be $\tau = D/U$. In eq. 10.9 and 10.10, Re is the Reynolds number which has the same definition as the Galileo number, Ga. Please note that we use Re_p to denote the instantaneous Reynolds number of the particle which changes with time and particle location. Re_p is used later for drag calculations.

We simulate the sedimenting motion of a spheroidal shaped particle in a linearly density stratified fluid using a 3D rectangular domain of size $20D \times 20D \times 80D$ ($10D \times 10D \times 40D$) for an oblate (prolate) spheroid with grid size equal to $D/32$ ($D/48$), resulting in $\approx O(10^9)$ ($\approx O(5 \times 10^8)$) grid points. We use periodic boundary conditions for the velocity field and the temperature perturbations on all the sides of the domain. We consider an oblate particle with aspect ratio, $\mathcal{AR} = a/b = 1/3$ (Fig. 10.1a) and a prolate particle with $\mathcal{AR} = a/b = 2$ (Fig. 10.1b). Since we solve the flow field in the frame translating with the particle, the particle stays at its initial position, i.e., ([10D, 10D, 20D] for an oblate spheroid and [5D, 5D, 10D] for a prolate spheroid). The domain sizes chosen ensure that there is no significant interaction between the particles and its wake for the entire parameter range explored in this study as shown in Sec. 10.2.2.

Depending on the hydrodynamic torque it experiences, the particle can rotate freely. The orientation of the spheroid is measured in terms of the polar angle θ, which is the angle made by the major axis of the spheroid with the $z-$axis as shown in Fig. 10.1. In the atmosphere, the typical value of N is $10^{-2}s^{-1}$ while in the ocean N is around $10^{-4} - 0.3s^{-1}$ depending on the strength of density stratification [382], [383]. We perform simulations for $Ga = 80 - 250$, while we vary Ri between $0 - 10$ (or $N \approx 0.04 - 0.2s^{-1}$) which are consistent with the typical value of N mentioned above. $Ri = 0$ represents a particle settling in a homogeneous fluid with a constant density. We fix the density ratio, $\rho_r = 1.14$ in all the cases. The temperature inside the particle is set similar to the surrounding fluid initially, resulting in a domain with zero temperature fluctuations at the start of the simulations.

We use $Pr = 0.7$ for all the simulation cases in this study except in Sec. 10.3.4 where we investigate the effect of changing fluid Pr. $Pr = 0.7$ corresponds to temperature stratified atmosphere, while $Pr = 7$ and $Pr = 700$ correspond to temperature stratified water and salt stratified water, respectively. In a stratified fluid, a density boundary layer is present

Table 10.1. Values of relevant parameters investigated in this study

$\mathcal{AR}$	C_{p_r}	k_r	ρ_r	Ga	$R\mathrm{i}$	Pr
1/3	1	$(0, 0.001, 1)$	1.14	$(80, 170, 210, 250)$	$0-10$	$0.7, 7.0$
2	1	$(0, 0.001, 1)$	1.14	$(80, 180)$	$0-10$	$0.7, 7.0$

in addition to the velocity boundary layer near the particle surface. The thickness of this density boundary layer scales as $\approx O(D/\sqrt{RePr})$. For accurate resolution of the flow within this boundary layer, it is necessary to have at least a few grid points in it. This imposes limitations on the maximum mesh size that can be used for the simulations. Owing to large size of the domain, using such a fine grid becomes computationally expensive. Hence, we use a smaller value for the Pr which enables us to resolve the fluid flow as well as the density field in both the boundary layer and the outside. We show in Sec. 10.3.4 (in agreement with previous studies [299]) that, changing the value of Pr merely changes the magnitudes of the velocities of the objects moving in a stratified fluid conserving the overall qualitative trends and behaviors. Finally, it should be noted that though we use the N and Pr values corresponding to a temperature stratified atmosphere and water, the density ratio chosen, i.e., $\rho_r = 1.14$ is representative of particles settling in an ocean rather than in a stratified air. A realistic ρ_r for atmospheric particles would be $\approx O(10^3)$ resulting in large inertial effects and effectively subverting any governing influence of density stratification. Hence, the simulations presented here are not intended to mimic any atmospheric phenomenon but are intended to provide crucial insights in understanding the sedimentation of individual particles/organisms through oceanic thermoclines. The motivation for the chosen value of Pr is computational convenience. Table 10.1 summarizes the values of all the relevant parameters investigated.

10.2.2 Validation: Domain size independence

In the absence of stratification, a domain with a vertical length much larger than Ga is needed to make sure that the wake does not have a strong effect on the settling of the particle by interacting with it. However, since fluid stratification suppresses the vertical motion, we

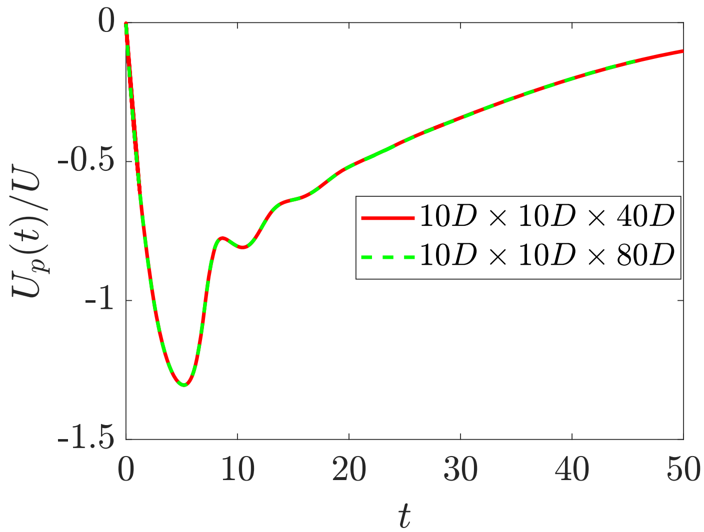

Figure 10.2. Comparison of velocity vs time for a prolate spheroid with $\mathcal{AR} = 2$ in two different domain sizes at $Ga = 180$ and $Ri = 5$. The error in the velocity using a smaller domain is negligible which means even a smaller domain gives accurate results but at a lower computational cost.

Table 10.2. Comparison of terminal Reynolds numbers, Re_t, with two different domain sizes in a homogeneous fluid, i.e., $Ri = 0$ for an oblate spheroid with $\mathcal{AR} = 1/3$ at different Ga. The values are in agreement which means there is no significant interaction between the particle wake and the particle.

Ga	Re_t $(15D \times 15D \times 125D)$	Re_t $(20D \times 20D \times 80D)$
80	55.3	56.1
170	132.1	129.6
210	165.3	166.0
250	198.5	199.8

can use a smaller vertical length for our domain. Here we show that the chosen domain sizes are big enough to make sure that the particles do not interact with their wakes for the entire range of parameters explored in this study.

We find an excellent agreement between the terminal Re attained by a settling oblate spheroid with $\mathcal{AR} = 1/3$ in a homogeneous fluid, i.e., $Ri = 0$, at different Ga in a bigger domain $(15D \times 15D \times 125D)$ and a smaller domain $(20D \times 20D \times 80D)$, used for this study) as shown in table 10.2. This proves that there is no significant interaction between the particle wake and the particle as it settles and the used domain size is enough to resolve the particle dynamics. Additionally, Fig. 10.2 shows the velocity vs time evolution for a prolate spheroid with $\mathcal{AR} = 2$ with $Ga = 180$ in a stratified fluid with $R\text{i} = 5$ in a bigger domain ($10D \times 10D \times 80D$) and a smaller domain ($10D \times 10D \times 40D$), used for this study). Again, this shows that there is no significant interaction between the particle and its wake and the domain size used for this study is enough to ensure accuracy for an affordable computational cost.

10.3 Results and discussion

The following subsections present the simulation results for settling spheroids in a stratified fluid. We present the settling velocities and orientations of the spheroids for the range of Ga and $R\text{i}$ investigated. We first present and discuss the results for an oblate spheroid followed by the results for the prolate spheroid. We compare the data from the stratified fluid case with the data from the homogeneous fluid case for better understanding the results. We use "broad-side on" to indicate an orientation of the spheroidal particles such that their broader side is horizontal, i.e., $\theta = 0°$ for an oblate spheroid and $\theta = 90°$ for a prolate spheroid. On the other hand, "edge-wise" indicates the orientation of the particles in which their broader side is perpendicular to the horizontal direction, i.e., $\theta = 90°$ for an oblate spheroid and $\theta = 0°$ for a prolate spheroid.

10.3.1 Settling dynamics of an oblate spheroid in a stratified fluid

10.3.1.1 Fluid stratification slows down and reorients a settling oblate spheroid

This subsection presents the simulation results for an oblate spheroid with $\mathcal{AR} = 1/3$ settling in a stratified fluid. The oblate spheroid starts from rest in an initially quiescent fluid. The spheroid velocity then evolves depending on the hydrodynamic and buoyancy forces acting on it as the flow evolves. We initialize the orientation of the oblate spheroid such that $\theta = 90°$ or in edge-wise orientation. In a homogeneous fluid, the oblate spheroid accelerates and attains a terminal velocity after the initial transients (which are due to the oscillations in the spheroid orientation) as shown in Fig. 10.3a. In addition, as the oblate spheroid accelerates, it topples from its initial edge-wise to a broad-side on orientation.

However, due to its inertia and periodic shading of hair-pin like vortex structures from alternate edges [369], it oscillates around the broad-side on ($\theta = 0°$) orientation. So, for $Ga = 210$, an oblate spheroid settles in an oscillatory orientation about $\theta = 0°$ as shown in Fig. 10.3b for $Ri = 0$. The oscillations are not present at lower Ga (< 120) [369].

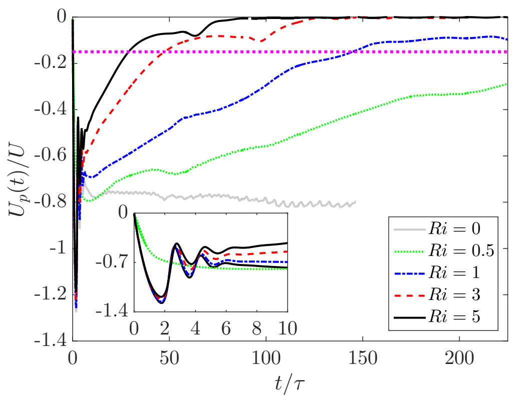

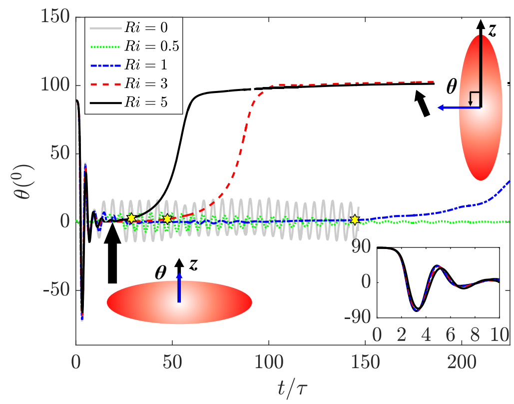

Figure 10.3. Settling dynamics of an oblate spheroid ($\mathcal{AR} = 1/3$) with $Ga = 210$ in a homogeneous fluid ($Ri = 0$) and a stratified fluid with different Ri values: a) Settling velocity evolution, b) spheroid orientation evolution versus time. The insets in both the figures show the initial oscillations with decreasing amplitudes in the velocity and orientation of the spheroid. The oblate spheroid attains a steady state terminal velocity and oscillates about broad-side on orientation in a homogeneous fluid after the initial transients. Stratification leads to a reduction in the spheroid velocity and a continuous deceleration of the spheroid velocity until it stops. The magnitude of the deceleration increases with stratification. In addition, the steady state orientation of the oblate spheroid changes from broad-side on (i.e., $\theta = 0°$) in a homogeneous fluid to edge-wise (i.e., $\theta \approx 90°$) in a stratified fluid. The transition in the orientation starts once the magnitude of the dimensionless spheroid velocity drops below a particular threshold. Here for $|U_p/U| < 0.15$. The onset of transition in the spheroid orientation is denoted by dotted horizontal line in (a) and yellow stars in (b).

Introducing density stratification in the fluid significantly changes the settling dynamics of an oblate spheroid. This is shown in Fig. 10.3 for $Ga = 210$ and various Ri as well as in Fig. 10.4 for $Ri = 3$ and various Ga values. As the oblate spheroid sediments in a stratified fluid, it moves from a region with lighter fluid into a region with heavier fluid. As a result, it experiences an increasing buoyancy force which essentially opposes its settling motion.

Hence, the particle cannot attain a steady state terminal velocity. This phenomenon is clearly depicted in Fig. 10.3a and 10.4a where the particle velocity decreases continuously after the initial transients. The suppression of the fluid flow due to the tendency of the displaced iso-density difference surfaces (isopycnals) to return to their original locations is another reason for the reduction in the particle velocity (see the detailed discussion in Sec. 10.3.1.3 and Fig. 10.9).

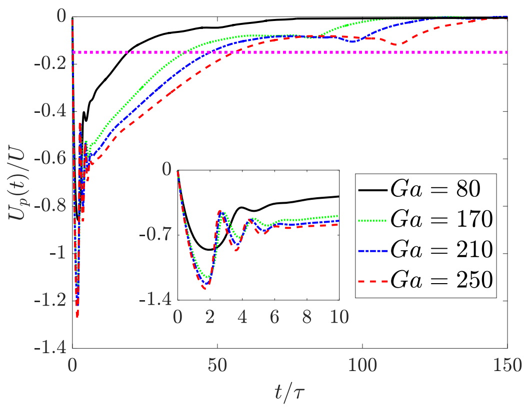

(a)

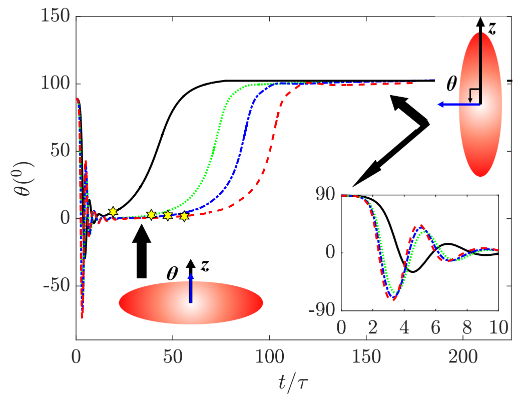

(b)

Figure 10.4. Settling dynamics of an oblate spheroid in a stratified fluid and $Ri = 3$ with different Ga values: a) Settling velocity, b) spheroid orientation evolution versus time. The insets show the initial oscillations with decreasing amplitude. The oblate spheroid attains a steady state terminal velocity and orientation (broad-side on, $\theta = 0°$) in a homogeneous fluid. Stratification leads to a reduction in the spheroid velocity and a continuous deceleration of the spheroid velocity until it stops. The magnitude of the deceleration decreases with increasing the particle inertia. In addition, the steady state orientation of the oblate spheroid changes from broad-side on (i.e., $\theta = 0°$) in a homogeneous fluid to broad-side perpendicular (i.e., $\theta \approx 90°$) in a stratified fluid. The transition in the orientation starts once the magnitude of the dimensionless spheroid velocity drops below a threshold. Here for $|U_p/U| < 0.15$. The onset of transition in the spheroid orientation is denoted by the dotted horizontal line in (a) and the yellow stars in (b).

An increase in the stratification strength of the background fluid increases the magnitude of the particle deceleration. This is expected as the magnitude of the buoyancy force experienced by the particle increases with the fluid stratification. As a result, the particle stops at earlier times for increasing Ri values as shown in Fig. 10.3a. Another consequence of this increased opposition to the settling motion is the reduction in its peak velocity when increasing the stratification as shown in Fig. 10.3a. In addition, as the Ga of the particle increases for a fixed Ri, the magnitude of deceleration decreases as shown in Fig. 10.4a. This is because of the increase in the inertia of the particle with Ga.

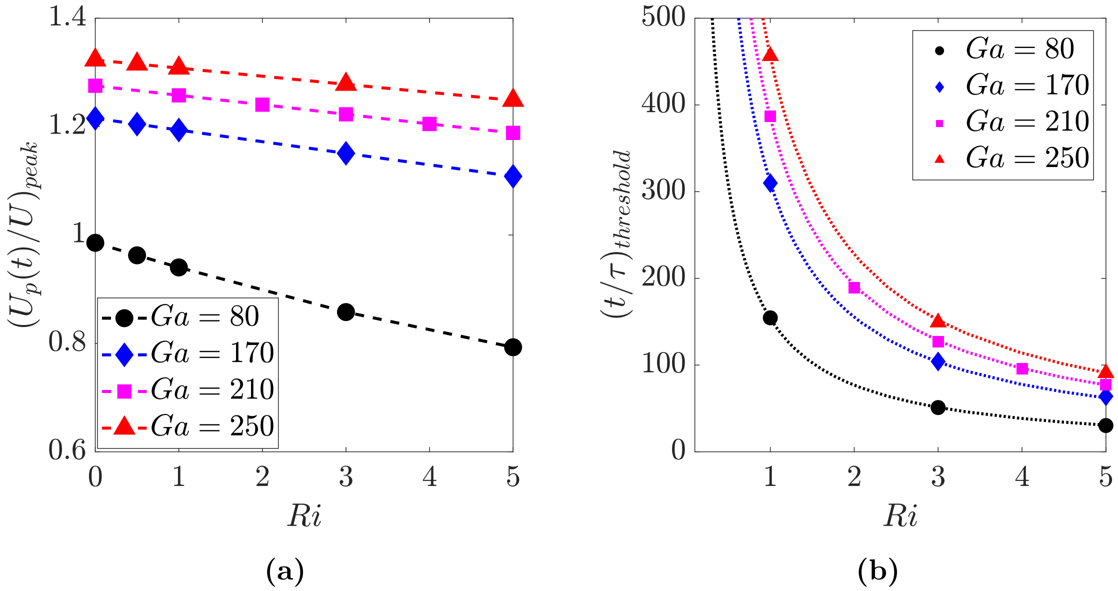

Figure 10.5. Effect of inertia and stratification strength on a) the peak velocity, $(U_p(t)/U)_{peak}$, of a settling oblate spheroid with $\mathcal{AR} = 1/3$. The peak velocity attained by the particle decreases stratification and increases with increase in particle inertia, and b) the time ($(t/\tau)_{threshold}$) at which $|U_p(t)/U| < 0.15$. The dashed line in (a) is a guide to the eye. The dotted line in (b) is the $(t/\tau)_{threshold} = A * R\text{i}^{-1}$ fit with A = 153.7, 310.5, 384.8 and 455.5 for Ga = 80, 170, 210 and 250, respectively.

A closer comparison between the time histories of the velocity and orientation reveals that, the onset of reorientation of the oblate spheroid is connected to the reduction of the settling velocity below a certain threshold. From the simulation data, we observe that, the reorientation starts once the magnitude of the dimensionless velocity of the particle falls below ≈ 0.15. This is indicated by a horizontal dashed line in the velocity evolution plots and a star in the spheroid orientation evolution plots (see Fig. 10.3 and 10.4). This observation is consistent with the experimental and numerical study on the orientation of a settling disk in a stratified fluid by [376]. Since stratification leads to a reduction in the particle velocity, an oblate spheroid eventually settles in an edge-wise orientation. This is because after a long enough time, the particle velocity goes below the threshold velocity for the onset of reorientation in a stratified fluid.

We quantify the effects of fluid density stratification on the peak velocity of the particles in Fig. 10.5a. We define the peak velocity as the maximum velocity achieved by the particles as it settles. We observe that the peak velocity decreases monotonically with the fluid stratification strength and increases with increasing Ga. Also, the relative decrease in the peak velocity for the lowest to the highest stratification strengths explored reduces with the Reynolds number. For $Ga = 80$ it decreases by $\approx 20\%$ while for $Ga = 250$ it decreases by $\approx 6\%$. This is due the increase in the strength of the inertial effects as compared to the stratification effects with increasing Ga at fixed $R\mathrm{i}$. As concluded from Fig. 10.3a and 10.4a, increasing the stratification strength or reducing the inertia of the particle moves the onset of the reorientation instability to an earlier time. Fig. 10.5b shows the effect of changing particle Ga and $R\mathrm{i}$ on the time for the onset of reorientation instability. We observe that, the time ($(t/\tau)_{threshold}$) at which particle velocity falls below the threshold velocity for the onset of reorientation instability decreases as $O(R\mathrm{i}^{-1})$.

10.3.1.2 Disappearance of oscillatory paths of settling oblate spheroid

An oblate spheroid settling in a homogeneous fluid exhibits four distinct trajectories depending on its Ga [369]. An oblate spheroid with $\mathcal{AR} = 1/3$ falls in a straight line with an axisymmetric wake for $Ga \lessapprox 120$. Increasing Ga further eliminates the axisymmetry and introduces oscillations in the settling path. The path is fully vertical with periodic oscillations for $Ga \lessapprox 210$. A weakly oblique oscillatory state motion is observed in the range $210 \lessapprox Ga \lessapprox 240$ whereas for $Ga \gtrapprox 240$ the particle path becomes chaotic with patterns of quasi-periodicity. These four states of motion can be explained by the wake instabilities behind a settling oblate spheroid [369] similar to the wake instabilities behind a settling disk [366], [384], [385].

Stratification significantly alters the settling paths of an oblate spheroid. In particular, it completely annihilates the oscillatory trajectories experienced by a settling oblate spheroid at $Ga \gtrapprox 120$ as shown in Fig. 10.6b, 10.6c, and 10.6d. Comparing the trajectories at different non-zero $R\mathrm{i}$ for various Ga in Fig. 10.6 shows that an oblate spheroid experiences a

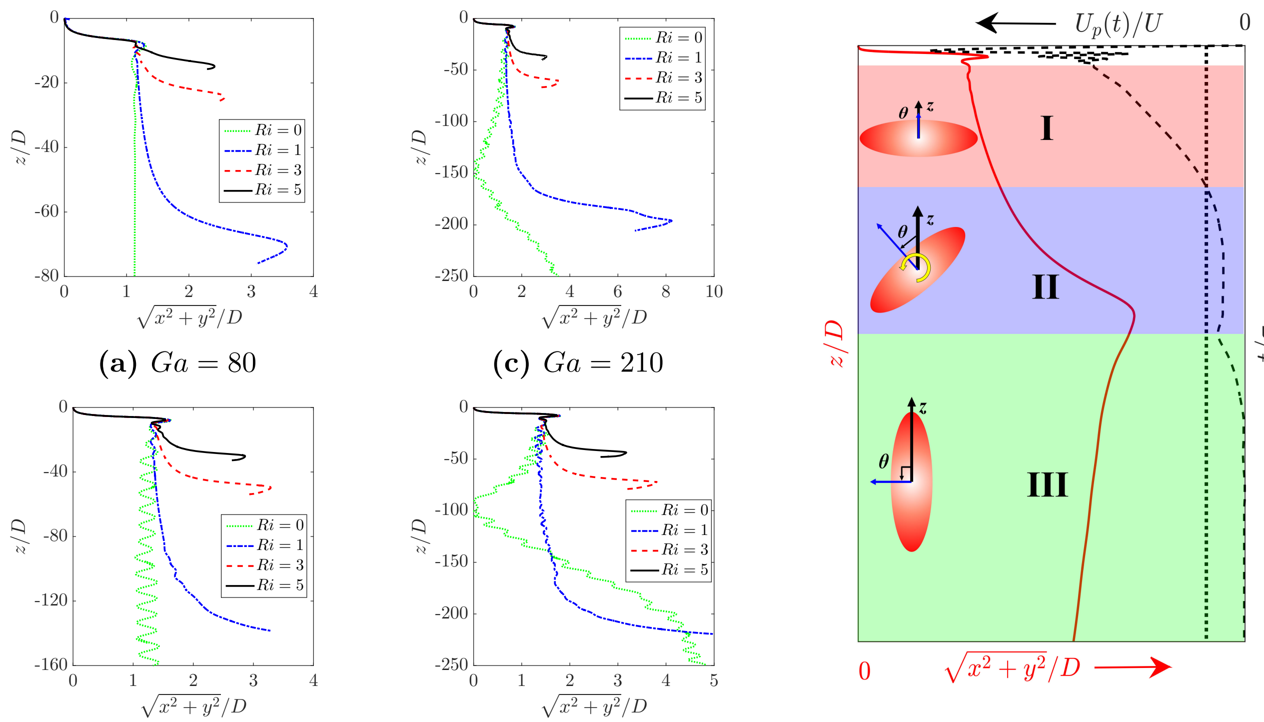

(a) $Ga = 80$ **(b)** $Ga = 170$ **(c)** $Ga = 210$ **(d)** $Ga = 250$ **(e)** Schematic

Figure 10.6. Trajectories of an oblate spheroid with $\mathcal{AR} = 1/3$ in a homogeneous and a stratified fluid for different Ga and Ri. a) $Ga = 80$, b) $Ga = 170$, c) $Ga = 210$, d) $Ga = 250$, and e) a schematic summarizing the settling velocity, particle trajectory and the orientation in the three zones identified in the settling motion of an oblate spheroid in a stratified fluid. Left vertical axis and bottom horizontal axis indicate spheroid position (solid line is the settling trajectory). Right vertical axis and top horizontal axis are for particle settling velocity vs time (dashed line is the settling velocity).

qualitatively similar trajectory (after the initial transients which will be absent if we initialize the oblate spheroid with the broad-side on orientation) irrespective of its Ga and Ri. The settling path can be divided into three regions.

Initially, as the spheroid accelerates from rest, it sediments approximately in a straight line until its velocity approaches the threshold for the reorientation onset. We call this region I. In region II, the oblate spheroid starts reorienting due to the onset of the reorientation instability. This induces a non-zero horizontal velocity component in the settling of an oblate spheroid. As a result, the particle moves in the horizontal direction, breaking the straight line motion and getting deflected in the transverse direction. This region can also be identified in the settling velocity of the oblate spheroid. The settling velocity attains a temporary plateau after it falls below the threshold for reorientation. During this time, the oblate spheroid experiences reorientation from broad-side on to edge-wise and gets deflected in the horizontal direction. This horizontal deflection has previously been observed for disks [233], [374], [376]. This region ends when the reorientation is over and the settling velocity increases momentarily as can be seen in Fig. 10.3a. Finally, in region III, as the particle comes close to its neutrally buoyant position, its velocity quickly decelerates and stops which is indicated by the reversal of the horizontal trajectory at the end of the settling path in Fig. 10.6. These settling trajectories and regions are similar to those observed for a disk in a stratified fluid [376]. However, we do not observe any change in the orientation of an oblate spheroid from edge-wise at the end of region III as observed for a disk [376]. This is most likely because of the ideal conditions in simulations as opposed to experiments. Fig. 10.6e summarizes the three regions of the settling path of an oblate spheroid in a stratified fluid along with their onset conditions on the settling velocity evolution plot.

10.3.1.3 What causes deceleration and reorientation of an oblate spheroid in a stratified fluid?

In the case of disk-like bodies settling in a homogeneous fluid, the path instabilities as described in the last subsection can be explained by the wake instabilities [366], [384], [385]. Therefore, analysing the wake vortices can provide insight into the mechanisms leading to a particular type of motion in either a homogeneous or a stratified fluid. For an oblate spheroid settling in a homogeneous fluid, a single toroidal vortex attached to the particle is initially formed. This is similar to a spherical particle moving with a steady velocity in a homogeneous fluid. As time passes, instabilities develop and the particle starts rotating around one of its major axes, normal to the direction of gravity as shown in Fig. 10.3b. As the angle of the oblate spheroid with respect to the horizontal axis increases, a part of this toroidal vortex detaches from the particle in a hairpin like structure [369]. Vortices are associated with low pressure regions than the ambient. So, as a result of the detachment of the toroidal vortex, the oblate spheroid experiences a torque due to the formation of this low pressure region behind it which directly opposes the rotation of the particle in the other

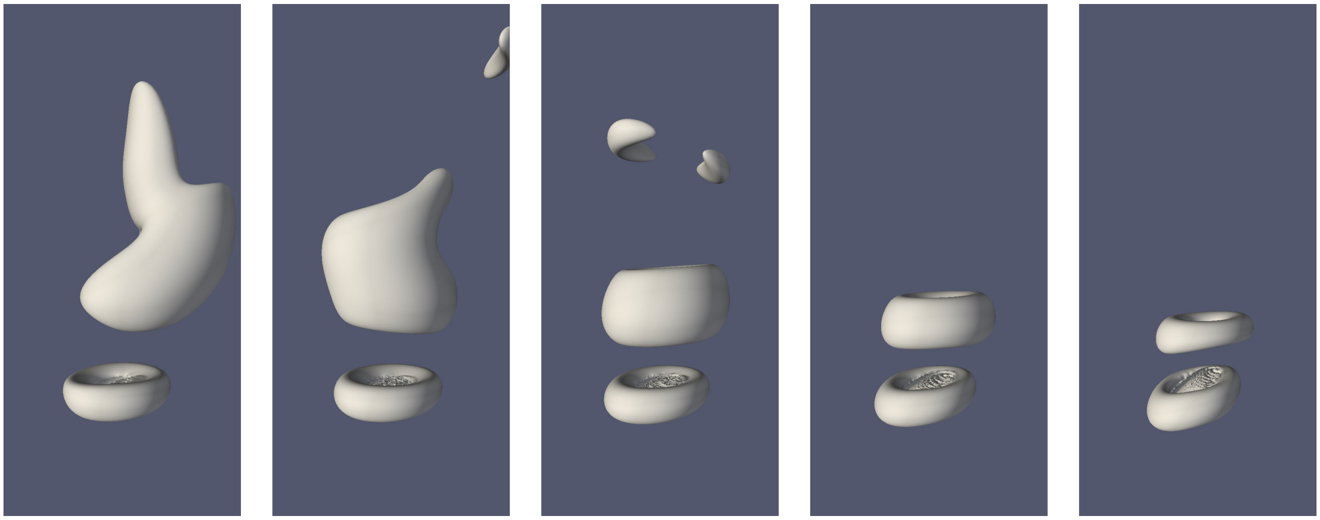

Figure 10.7. Dimensionless iso-surfaces of Q-criterion equal to 5×10^{-4} for an oblate spheroid with $\mathcal{AR} = 1/3$, $Ga = 80$ and $R\mathrm{i} = 5$ at equal time intervals of $t/\tau = 10.74$ starting from $t/\tau = 18.78$. These contours show the evolution of vortices. The vortical structures identified by the positive Q-criterion are associated with a lower pressure region behind the particle.

direction. Owing to inertia, the particle then rotates in the other direction. New hairpin vortices keep detaching from the oblate spheroid alternatively from either sides as it settles, leading to periodic changes in the orientation and oscillatory paths [369].

The situation is completely different in the case of an oblate spheroid settling in a stratified fluid. This is due to the fact that stratification suppresses the vertical motion of the fluid ([251], [284], [299] as shown by the isopycnals in Fig. 10.9) and prevents the particle from attaining any steady state speed. As a result, there is no mechanism which can lead to periodic vortex shedding as described above. Conversely, we observe two toroidal vortices, one attached to the particle and one detached from the particle, as shown in Fig. 10.7. Once the particle velocity falls below the threshold velocity for reorientation, the detached vortex is asymmetric and does not oscillate from one side to the other unlike the case of an oblate spheroid sedimenting in a homogeneous fluid. As a result, there is a consistent low pressure region behind the oblate spheroid which predominantly remains on one side. This results in a torque on the particle which reorients it until it reaches its neutrally buoyant position. Eventually, as the oblate stops, the torque acting on it also vanishes and it stops in the edge-wise orientation.

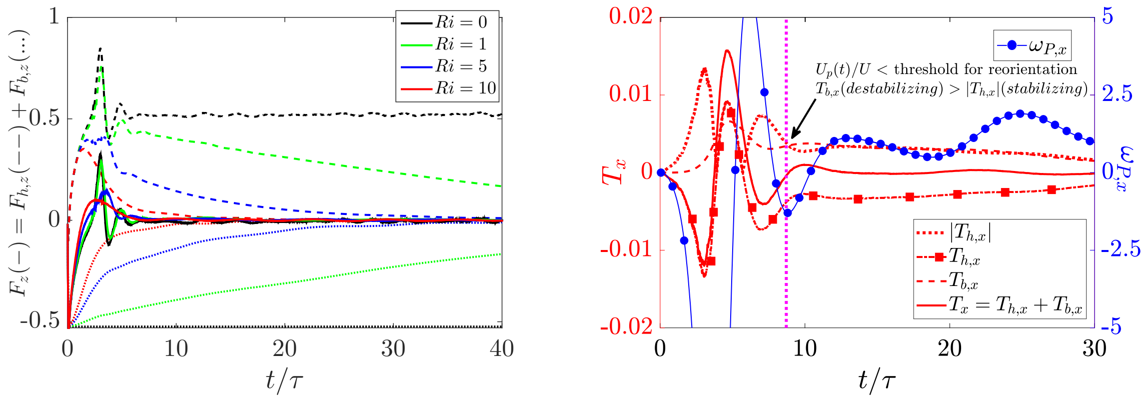

(a) **(b)**

Figure 10.8. a) Forces acting on the oblate spheroid with $Ga = 80$ as it settles in a stratified fluid with varying Ri shown with different colors. The total force (solid line) can be split into two components, the hydrodynamic component (dashed line) and the buoyancy component (dotted line). b) x-component of the torque acting on the oblate spheroid with $Ga = 80$ as it sediments in a stratified fluid with Ri $= 5$ along with the x-component of the angular velocity. The net torque (solid line) is split into two components, the hydrodynamic torque (dotted line) which tries to orient it in a broadside on orientation (hence stabilizing) and the buoyancy component (dashed-dotted line) which is destabilizing and tries to reorient it in a edgewise orientation. The reorientation starts once the magnitude of hydrodynamic torque falls below the buoyancy torque which happens when the particle velocity falls below the threshold for reorientation as discussed in Sec. 10.3.1.1.

To make this point clear, we measure the forces and torques acting on the spheroid. As shown in the methodology section, the force (torque) acting on the spheroid can be split into two components (eq. 10.5 and 10.6): 1) $\mathbf{F}_h$ ($\mathbf{T}_h$) , arising from the hydrodynamic stresses acting on the particle surface, denoted as the hydrodynamic force (hydrodynamic torque), and 2) $\mathbf{F}_b$ ($\mathbf{T}_b$), arising from the buoyancy or the density disturbance at the particle surface, denoted as the buoyancy force (buoyancy torque). The reason behind the deceleration of the spheroid and its reorientation becomes clear by looking at the z-component of the forces and the x-component of the torques acting on the spheroid shown for an oblate spheroid with $\mathcal{AR} = 1/3$, $Ga = 80$ and $R\text{i} = 5$ in Fig. 10.8.

Initially, the density difference between the particle and the local surrounding fluid results in a high buoyancy force (high $F_{b,z}$) on the spheroid resulting in its acceleration (negative F_z at the initial t/τ in Fig. 10.8a). As the spheroid accelerates, the magnitude of the

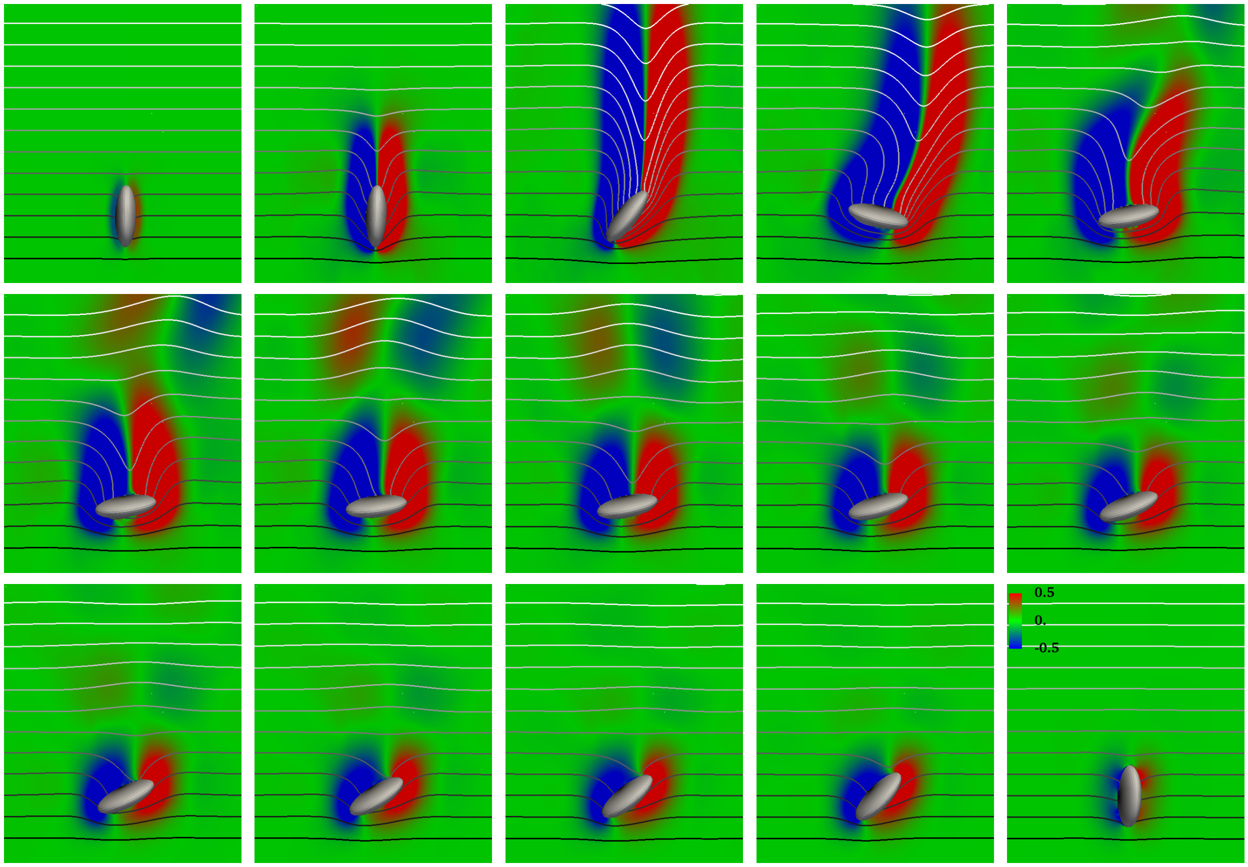

Figure 10.9. Evolution of the x-component of the dimensionless baroclinic vorticity generation term due to the mis-alignment of the density gradient vector with the direction of gravity, $\boldsymbol{\nabla}\rho_f \times \hat{\mathbf{k}}$, in the $x = 0$ plane for an oblate spheroid with $\mathcal{AR} = 1/3$, $Ga = 80$ and $Ri = 5$. For a major clarity, colorbar for the baroclinic vorticity generation is shown only in the last panel. The solid lines indicate dimensionless isopycnals or equal density lines separated by a value of 0.5. Darker shade of grey indicates a higher density. The panels are snapshots (row-wise) at specific time intervals with $t/\tau = 0$, 2.69, 8.06, 13.43, 18.8, 24.17, 29.54, 34.91, 40.28, 45.65, 51.02, 56.39, 61.76, 67.13, and 107.4. The first panel shows the initial configuration and the last shows the settling configuration after the oblate reorients in the edge-wise orientation.

hydrodynamic drag increases ($F_{h,z}$ increases) and the buoyancy force decreases in a region with increasing fluid density. Hence, the spheroid accelerates till the magnitude of the hydrodynamic drag becomes larger than the buoyancy force ($F_{h,z} > F_{b,z}$) at which point it attains the maximum velocity. The buoyancy force is unable to overcome this increasing hydrodynamic drag which leads to the deceleration of the spheroid ($F_z > 0$ meaning the net force acting on the spheroid is in the opposite direction to its motion). Eventually, as the particle reaches its neutrally buoyant position, it stops as there is no net force acting on it. In a homogeneous fluid, i.e., $Ri = 0$, the buoyancy force acting on the particle is constant, $F_{b,z} = (\rho_p - \rho_f)V_p g$ and the hydrodynamic drag balances the buoyancy force at steady state, resulting in a constant terminal velocity.

To understand the reason behind the reorientation, we plot the x-component of the torques acting on the spheroid in Fig. 10.8b. Initially, as the particle accelerates, it topples from edge-wise orientation to a broad-side orientation because of the increasing magnitude of the hydrodynamic torque ($T_{h,x}$) compared to the buoyancy torque ($T_{b,x}$). Because of inertia, $T_{h,x}$ changes sign and and the oblate oscillates about its broad-side on configuration. This is shown by the oscillating $T_{h,x}$ and $\omega_{p,x}$ in Fig. 10.8b at initial times. Meanwhile, the buoyancy torque ($T_{b,x}$) increases gradually and is always > 0, which leads to dampening of the oscillations of the oblate spheroid about the broad-side on orientation as can be seen from the diminishing magnitude of the rotational velocity in Fig. 10.8b.

The spheroid keeps oscillating about the broad-side on orientation as long as the inertial effects (or $T_{h,x}$) are stronger compared than the buoyancy effects (or $T_{b,x}$). However, as the spheroid decelerates, inertial effects start to weaken. In addition, the isopycnals resist further deformation as will be explained below. As the spheroid velocity falls below the threshold for reorientation ($U_p(t)/U < 0.15$), the destabilizing buoyancy torque dominates over the stabilizing hydrodynamic torque, i.e., $T_{b,x} > |T_{h,x}|$. This transition in the dominating torque is demarcated by a dotted vertical line in Fig. 10.8b which also corresponds to the time when $U_p(t)/U < 0.15$. As a result, the spheroid stops oscillating about the broad-side on orientation and starts to reorient to the edge-wise orientation since $T_{b,x} > |T_{h,x}|$ implies a net positive torque on the spheroid which results in a net positive rotational velocity ($\omega_{p,x} > 0$) as shown in Fig. 10.8b. In a homogeneous fluid, the buoyancy/baroclinic torque is absent. Hence, the inertia and T_h acting on the spheroid results in a broad-side on orientation at steady state. The competition between the stabilizing hydrodynamic torque and the destabilizing buoyancy torque can be understood by looking at the flow field and the isopycnals around the spheroid as it sediments, as discussed below.

The equation for the vorticity, $\boldsymbol{\omega}$, can be obtained by taking the curl of the momentum equation 10.1.

$$\rho_f \frac{D\boldsymbol{\omega}}{Dt} = (\boldsymbol{\omega} \cdot \boldsymbol{\nabla})\, \mathbf{u} + \mu \nabla^2 \boldsymbol{\omega} - g \boldsymbol{\nabla} \rho_f \times \hat{\mathbf{k}}. \tag{10.12}$$

The last term on the right hand side of equation 10.12, i.e., $\boldsymbol{\omega}_g = -g\boldsymbol{\nabla}\rho_f \times \hat{\mathbf{k}}$, is the vorticity generation due to the displacement of isopycnals caused by the settling motion of the particle. This term is also known as the baroclinic vorticity generation. This contribution arises due to the mis-alignment of the density gradient with the direction of gravity. This term will be exactly $\mathbf{0}$ in a homogeneous fluid. This contribution is thus specific to particles sedimenting in a stratified fluid as the vorticity around the particle is very different in a homogeneous and a stratified fluid [299].

We plot the x-component of the baroclinic vorticity generation, $\boldsymbol{\omega}_g$, in the yz plane around a settling oblate spheroid in Fig. 10.9. This term reveals the reason behind the onset of instability and the reorientation of an oblate spheroid in a stratified fluid. Initially this vorticity generation term is symmetric with a thin region of zero $\boldsymbol{\omega}_g$ separating regions of positive and negative baroclinic vorticity (blue and red regions in Fig. 10.9) exactly along the center-line of the spheroid. We call this the plume of zero baroclinic vorticity or "the plume" for simplicity. The plume also acts as the axis of symmetry for $\boldsymbol{\omega}_g$. We call the point at which the plume intersects the particle surface as the origin of the plume. A vertically straight plume with its origin on one of the center-lines of the oblate signifies a symmetric $\boldsymbol{\omega}_g$ around the particle.

As the particle settles and slows down, the oblate spheroid topples from an edge-wise to broad-side on orientation due to inertial effects. Since the particle is accelerating, the vorticity generation region expands as the isopycnals deform in the long wake behind the particle till it reaches the peak velocity. After reaching the peak velocity, the particle decelerates due to increasing buoyancy effects because of the tendency of the displaced isopycnals to return to their original levels as shown by evolution of isopycnals in Fig. 10.9. As a result, the region of vorticity generation shrinks. The origin of the plume shifts along the longer face of the oblate towards the other end as it oscillates about the broad-side on orientation.

As the inertial effects decrease with the particle deceleration, the oscillations of the oblate spheroid about the broad-side on orientation are dampened. The isopycnals that were deformed earlier (in the wake of the particle) do not completely return to their original form, thus opposing further deformation as the oblate particles tries to oscillate. Hence, the oscillations die out. This prevents the origin of the thin plume from shifting completely to the middle of the spheroid, thus preventing $\boldsymbol{\omega}_g$ to become symmetric. Since the origin of the plume is not at the center of the oblate, the generated vorticity field is asymmetric. The origin of the plume does not cross the center of the spheroid and remains on one side. In addition, because of the reduced inertia, there is no mechanism to keep the spheroid oscillating about the horizontal. Thus, the $\boldsymbol{\omega}_g$ distribution around the oblate remains asymmetric. This results in the onset of instability in the oblate orientation as the origin of the plume tries to return to its earlier position on the spheroid, i.e., on the edge. The net torque on the oblate spheroid slowly reorients it to the edge-wise orientation (Fig. 10.8b). The same process will occur irrespective of the initial orientation of the oblate spheroid which will eventually reorient in the edge-wise orientation.

10.3.1.4 Drag enhancement due to stratification

In the previous section, we discussed the reasons behind the decrease in the settling velocity of the particle as it settles into a heavier fluid. Here, we quantify the effect of fluid stratification by calculating the added drag due to stratification as the particle sediments. It has been shown in previous studies on spheres and disks that the stratification results in a significant additional drag on the settling particle [299], [351], [376]. The aim of this section is to provide an idea regarding the relative magnitudes of stratification induced drag and the hydrodynamic drag as particles settle in a stratified fluid. The results obtained here can be used for modeling the added stratification drag on spheroids in real-life situations such as suspensions of spheroids in a stratified fluid.

There are three main contributions to the total force acting on the particle as it settles in a stratified fluid [299]. First, the viscous and pressure forces due to the current motion of the particle (hydrodynamic drag). Second, the buoyancy force caused by the perturbations in the temperature field due to the particle motion (stratification drag). Thirdly, the combined effect from added mass and history forces which have been observed to be negligible with respect to the first two contributions for a sphere settling in a stratified fluid [299]. To calculate the stratification drag, we assume that the oblate spheroid undergoes a quasi-steady settling. This means that the buoyancy and the hydrodynamic contributions to the total force are instantaneously balanced [376]. Owing to the quasi-steady assumption we neglect the added mass and the history effects which are anyway smaller than the buoyancy and the drag force [299], [376]. The stratified drag coefficient can be defined as [351]

$$C_D^S = \frac{2\left(\rho_P/\rho(z) - 1\right) gD}{U_P^2(z)}. \tag{10.13}$$

Here $\rho(z)$ and $U_P(z)$ are the unperturbed background density and the particle velocity at the instantaneous particle location z. Hence, various dimensionless parameters also vary with z and can be written as a function of the instantaneous particle location as

$$\rho_r(z) = \rho_P/\rho(z), \tag{10.14}$$

$$Re_p(z) = \frac{|U_P(z)|D}{\nu}, \tag{10.15}$$

$$Fr(z) = \frac{|U_P(z)|}{ND}. \tag{10.16}$$

Here, $Fr(z)$ is the instantaneous Froude number which can also be written as $Fr(z) = \sqrt{Re_p(z)/Ri}$. Please note that Ri remains constant irrespective of the particle speed and location.

For spheroids in a homogeneous fluid, we use the following correlation for the drag coefficient (C_D^H) which is valid in the range $1 \leq Re_p \leq 200$ and $0.4 \leq \mathcal{AR} \leq 4$ [386]

$$C_D^H = \frac{24\mathcal{AR}^{0.49}}{Re_p(z)}\left(1.05 + 0.152 Re_p(z)^{0.687}\mathcal{AR}^{0.671}\right). \tag{10.17}$$

Fig. 10.10 presents the variation in the added drag due to stratification ($C_D^S - C_D^H$) for different stratification strengths (Fig. 10.10a) and different Ga (Fig. 10.10b). As the particle starts from rest, it accelerates initially and $Fr(z)$ increases. As the particle accelerates, the stratification drag acting on it decreases and hence $C_D^S - C_D^H$ decreases. This is expected as the inertial effects dominate in the initial phase of the settling until the particle attains

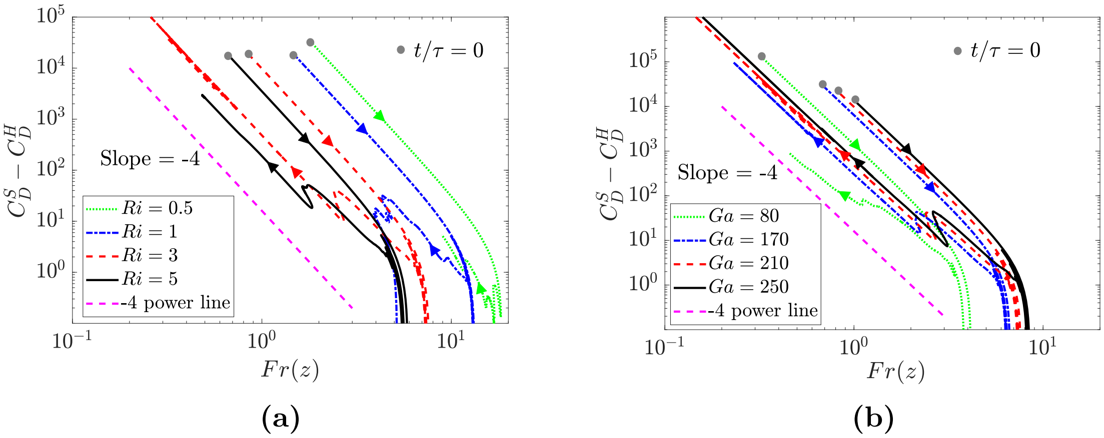

Figure 10.10. Added drag due to stratification, $C_D^S - C_D^H$, for an oblate spheroid with $\mathcal{AR} = 1/3$ as a function of the instantaneous particle Froude number, $Fr(z)$, for a) $Ga = 210$ and different stratification strengths. b) Added drag for $Ri = 3$ for different Ga. The arrows show the direction of increasing time and the filled dots show the simulation start time. The dashed pink line shows the -4 power line to indicate a $Fr(z)^{-4}$ scaling of $C_D^S - C_D^H$.

a peak velocity. Hence, $C_D^S - C_D^H$ reaches a minimum when the particle attains its peak velocity.

Once the particle reaches its peak velocity, it starts to decelerate as the buoyancy and stratification effects start to dominate over the inertial effects. As a result, the stratification drag starts to increase again. The difference, $C_D^S - C_D^H$ scales as $Fr(z)^{-4}$ as shown in Fig. 10.10 and increases with increasing Ga (Fig. 10.10b). These calculations for drag show that the stratification drag can be $1-5$ orders of magnitude higher than the hydrodynamic drag and hence it is crucial to include it in calculations for when we have suspensions of particles in a stratified fluid. The calculations show that the extra contribution to the total drag varies as Fr^{-4}, a simple expression which can be used for modeling the effect of stratification on the particle motion in practical applications.

10.3.2 Settling dynamics of a prolate spheroid in a stratified fluid

Similar to the case of an oblate spheroid, we report the simulation results on the settling dynamics of a prolate spheroid with $\mathcal{AR} = 2$ in a stratified fluid. We present the results for the settling dynamics in a homogeneous fluid as well for comparison.

10.3.2.1 Fluid stratification slows down and partially reorients a settling prolate spheroid

Fig. 10.11 shows the settling velocity of a prolate spheroid with $\mathcal{AR} = 2$ in a homogeneous and stratified fluid with different stratification strengths for $Ga = 80$ and 180. The prolate spheroid starts from rest in an initially quiescent fluid. It then accelerates to reach a maximum velocity depending on its Ga and $R\mathrm{i}$. In a homogeneous fluid, i.e., $R\mathrm{i} = 0$, the prolate spheroid reaches a terminal settling velocity as shown in Fig. 10.11a and 10.11b.

The stratification has the same effect on the settling velocity of a prolate spheroid as it has on an oblate spheroid. In particular, the stratification causes a continuous deceleration of the settling velocity after the initial transients. In addition, the settling velocity magnitude reduces with the stratification strength for prolate spheroids with same Ga. The reasons behind these observations are the same as discussed in Sec. 10.3.1.1 and are discussed briefly in Sec. 10.3.2.3 and Fig. 10.16.

To study the effect of stratification on the particle orientation, we initialize the prolate spheroid in an edge-wise orientation, i.e., $\theta = 0°$. In a homogeneous fluid, we find that, it eventually settles down in a broad-side on, i.e., $\theta = 90°$ orientation, once it attains its terminal velocity. However, similar to the case of an oblate spheroid, fluid stratification significantly changes the settling orientation as shown in Fig. 10.11c and 10.11d.

As the prolate spheroid accelerates from rest, it topples from an edge-wise orientation to a broad-side on orientation. However, this orientation is stable only in a homogeneous fluid. In a stratified fluid, once the velocity magnitude falls below a particular threshold (we find that to be ≈ 0.15), the prolate spheroid starts to reorient. But we observe that unlike an oblate spheroid, it can only reorient partially, i.e., it does not exactly go back to $\theta = 0°$. The final settling orientation depends on the stratification strength and the Reynolds number. This becomes clear when examining the final orientations at $Ga = 80$ and $Ga = 180$ for increasing stratification strengths in Fig. 10.11c and 10.11d. At low Re, i.e., $Ga = 80$, the prolate spheroid reorients almost completely at high stratification ($R\mathrm{i} = 10$) such that $\theta \approx 0°$ at the final times. However, for a lower stratification strength, i.e., $R\mathrm{i} = 5$, it reaches a final orientation of $\theta \approx 30°$. At a higher Ga, i.e., $Ga = 180$, the final orientation is $\theta \approx 22°$ and $\theta \approx 35°$ for $R\mathrm{i} = 10$ and $R\mathrm{i} = 5$, respectively. Thus, the final orientation angle increases if we

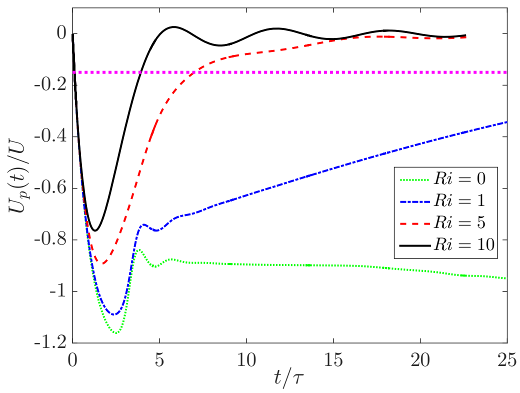

(a) Settling velocity, $Ga = 80$

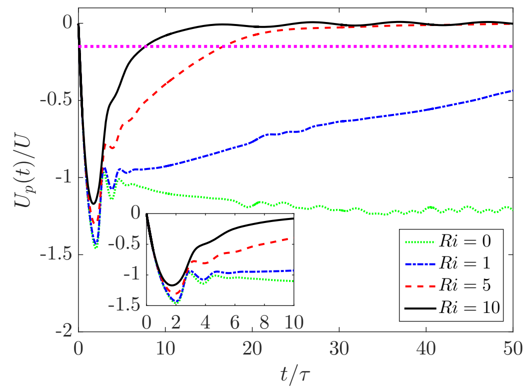

(b) Settling velocity, $Ga = 180$

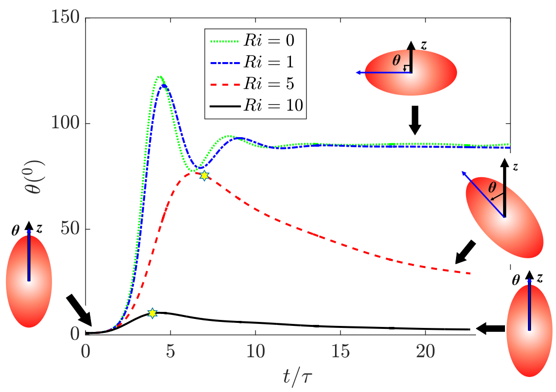

(c) Orientation, $Ga = 80$

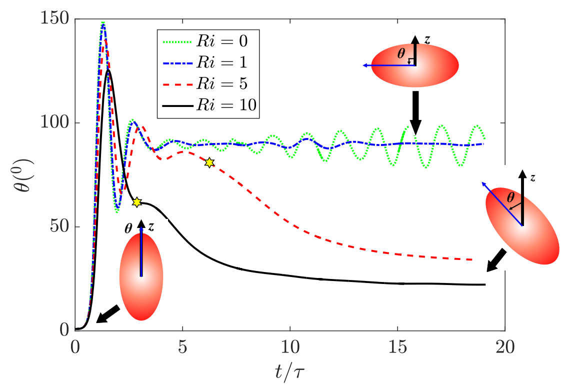

(d) Orientation, $Ga = 180$

Figure 10.11. Time evolution of the settling velocity of a prolate spheroid with $\mathcal{AR} = 2$ in a homogeneous fluid ($Ri = 0$) and a stratified fluid with different Ri: a) $Ga = 80$, b) $Ga = 180$. Evolution of the prolate orientation for $\mathcal{AR} = 2$ in a homogeneous fluid ($Ri = 0$) and a stratified fluid with different Ri: c) $Ga = 80$, d) $Ga = 180$. The inset in (b) shows the initial oscillations with decreasing amplitudes in the velocity and orientation of the spheroid. The prolate spheroid attains a steady state terminal velocity and orientation (broad-side on) in a homogeneous fluid. Stratification leads to a reduction in the spheroid velocity and a continuous deceleration of the spheroid velocity until it stops. The magnitude of the deceleration increases with stratification. The onset of reorientation given by $|U_p/U| < 0.15$ and is denoted by a dotted horizontal line in (a,b) and correspondingly by yellow stars in (c,d).

increase Ga at fixed Ri, i.e., final orientation progressively leaves the edge-wise orientation ($\theta = 0°$).

Next, we quantify the effects of fluid density stratification on the peak velocity of the prolate spheroid (see Fig. 10.12a). The results are similar to the case of an oblate spheroid. We observe that the peak velocity decreases monotonically with the fluid stratification strength and increases with increasing Ga. Also, the relative decrease in the peak velocity for the lowest to highest stratification strength explored reduces with Ga. For $Ga = 80$, it decreases by $\approx 33\%$ while for $Ga = 180$ it decreases by $\approx 18\%$. This is due to the increase of the inertial effects as compared to the stratification effects with increasing Ga for the same $R\mathrm{i}$. As shown in Fig. 10.11a and 10.11b, increasing the stratification strength or reducing the inertia of the particle results in the earlier onset of the reorientation instability. To conclude, we observe that, the time ($(t/\tau)_{threshold}$) at which the particle velocity falls below the threshold velocity for the onset of reorientation decreases as $O(R\mathrm{i}^{-1})$, see Fig. 10.12b where we display the time for the onset of the instability for different particle Reynolds number and stratifications.

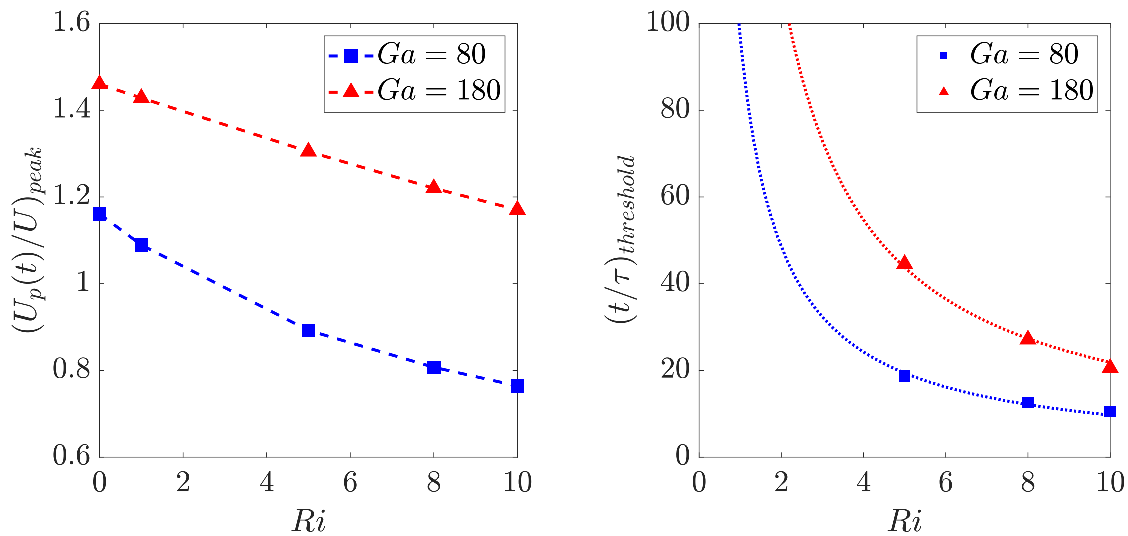

(a) **(b)**

Figure 10.12. Effect of inertia and stratification strength on a) the peak velocity, $(U_p(t)/U)_{peak}$, of a settling prolate spheroid with $\mathcal{AR} = 2$. The peak velocity attained by the particle decreases with increasing stratification and increases with particle inertia, and b) the time ($(t/\tau)_{threshold}$) at which $|U_p(t)/U| < 0.15$. The dashed line in (a) is a guide to the eye. The dotted line in (b) is the $(t/\tau)_{threshold} = A * R\mathrm{i}^{-1}$ fit with A = 97.0 and 218.8 for $Ga = 80$ and $Ga = 180$, respectively. The $O(R\mathrm{i}^{-1})$ fit in (b) is consistent with the case of an oblate spheroid in Sec. 10.3.1.1.

10.3.2.2 Settling trajectory of a prolate spheroid in a stratified fluid

Similarly to the case of an oblate spheroid, stratification suppresses the oscillatory trajectories of a prolate spheroid in a homogeneous fluid at high Ga. The settling trajectories of a prolate spheroid with $\mathcal{AR} = 2$ in a homogeneous and stratified fluid are displayed in Fig. 10.13. In a homogeneous fluid, the particle settles in a straight line at $Ga = 80$ and in an oscillatory path at $Ga = 180$. Since stratification results in a reduction of the settling velocity, the prolate spheroid stops at an earlier position as we increase the stratification strength. In addition, the oscillatory path observed for a prolate spheroid with $Ga = 180$ in a homogeneous fluid disappears in a stratified fluid.

A prolate spheroid goes through two regimes, unlike the three regimes reported above for the settling of an oblate. In the first regime, denoted by I, it oscillates about its broad-side on orientation as it settles. In this regime, the magnitude of the settling velocity is still higher than the threshold below which the spheroid starts to reorient. However, once the settling velocity drops below the threshold for the onset of reorientation, the particle starts to rotate from broad-side on to edge-wise orientation. This is regime II. Unlike an oblate spheroid which rotates quickly in regime II and settles at a final edge-wise orientation in regime III, a prolate spheroid reorients slowly in regime II. Furthermore, the prolate spheroid does not reorient completely, but attains a final oblique orientation with θ between $0°$ and $35°$. The exact value of the final θ depends on Ga and $R\mathrm{i}$ as explained before. The settling path along with the settling velocity are sketched in Fig. 10.13c.

10.3.2.3 Why does a prolate spheroid reorients partially and only has two settling paths regimes in a stratified fluid?

As for the case of an oblate spheroid, we analyse the wake vortices to gain insight into the mechanisms leading to the reorientation of a prolate spheroid. The reasons for the deceleration and the reorientation of a prolate spheroid in a stratified fluid are similar to that of an oblate spheroid as will be discussed in this subsection. For a prolate spheroid settling in a homogeneous fluid, a single vortex attached to the particle is initially observed as in the case of an oblate spheroid. As we increase Ga, this vortex grows in size. At

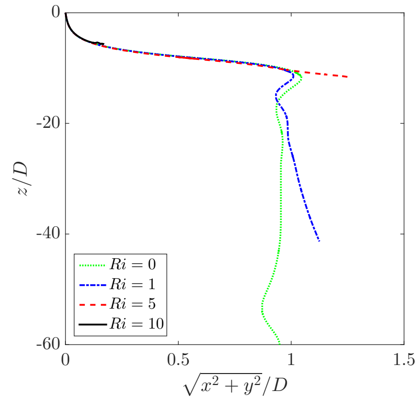

(a) $Ga = 80$

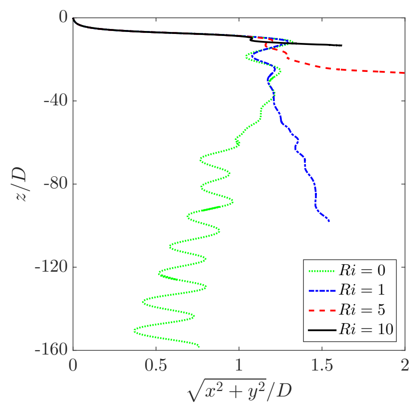

(b) $Ga = 180$

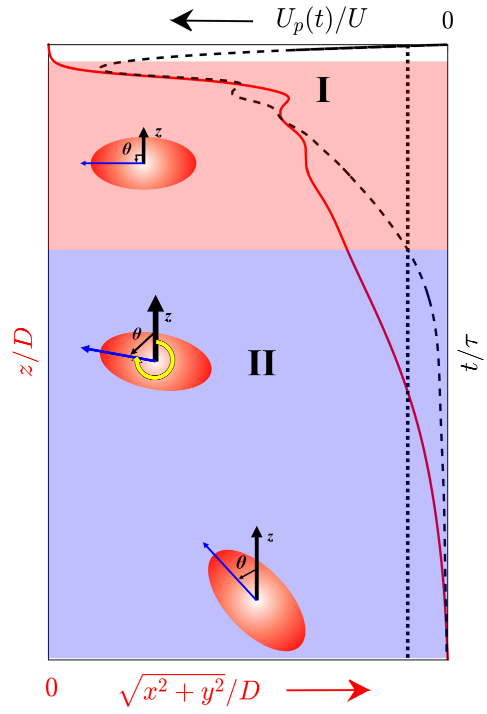

(c)

Figure 10.13. Trajectories of a prolate spheroid with $\mathcal{AR} = 2$ in a homogeneous and a stratified fluid for different Ga and Ri. a) $Ga = 80$, b) $Ga = 180$, and c) a schematic summarizing the settling velocity, particle trajectory and the orientation in the two regimes observed in the settling motion. Left vertical axis and bottom horizontal axis indicate the spheroid position (solid line is the settling trajectory). Right vertical axis and top horizontal axis display the particle settling velocity vs time (dashed line is the settling velocity).

low Ga this vortical structure is still symmetric, however, it becomes helical resulting in an instability for a prolate spheroid with $\mathcal{AR} = 3$ for $Ga > 70$. As a result, a prolate spheroid with $\mathcal{AR} = 3$ rotates about the vertical axis for $Ga > 70$ [369]. This is also clear in Fig. 10.13 as the prolate spheroid with $Ga = 80$ settles in a straight line while the prolate spheroid with $Ga = 180$ has an oscillatory path. As shown in [369] the vortical structures for a prolate spheroid in a homogeneous fluid result in a broad-side on orientation.

The situation is completely different in the case of a prolate spheroid settling in a stratified fluid. In this configuration, the stratification suppresses the vertical motion of the fluid and prevents the particle from attaining any steady state speed. In a stratified fluid, initially there is one vortex attached to the particle as shown in Fig. 10.14. As time passes, a part of this vortex detaches and remains predominantly on one side of the prolate spheroid as also shown in Fig. 10.14. As a result of this, there is a significant asymmetric low pressure region behind the prolate spheroid. This results in a torque which reorients the particle with its major axis aligned with the density gradient until it settles at its neutrally buoyant position. As discussed above, a prolate settles at an angle between 0° and 90° depending on the Reynolds number.

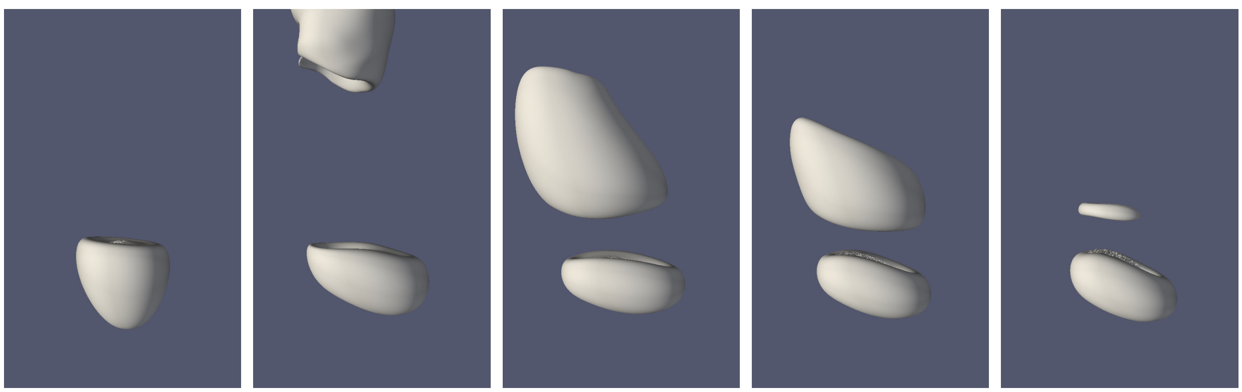

(a) **(b)** **(c)** **(d)** **(e)**

Figure 10.14. Dimensionless iso-surfaces of Q-criterion equal to 5×10^{-4} for a prolate spheroid with $\mathcal{AR} = 2$, $Ga = 80$ and $Ri = 5$ at equal time intervals of $t/\tau = 28.65$. $t/\tau = 23.87$ for the first panel. The vortical structures identified by the positive Q-criterion are associated with a lower pressure region behind the particle.

We present for forces and torques acting on the prolate spheroid in Fig. 10.15. The net force and the force components, $F_{h,z}$ and $F_{b,z}$ behave similarly to the case of an oblate spheroid discussed in Sec. 10.3.1.3. High magnitude of the buoyancy force compared to the hydrodynamic drag explains the initial acceleration of the prolate. However, the buoyancy force decreases as the prolate sediments in a region with higher fluid density causing it to slow down. The gradual increase in the magnitude of the destabilizing buoyancy torque compared to the stabilizing hydrodynamic torque as the prolate velocity decreases explains

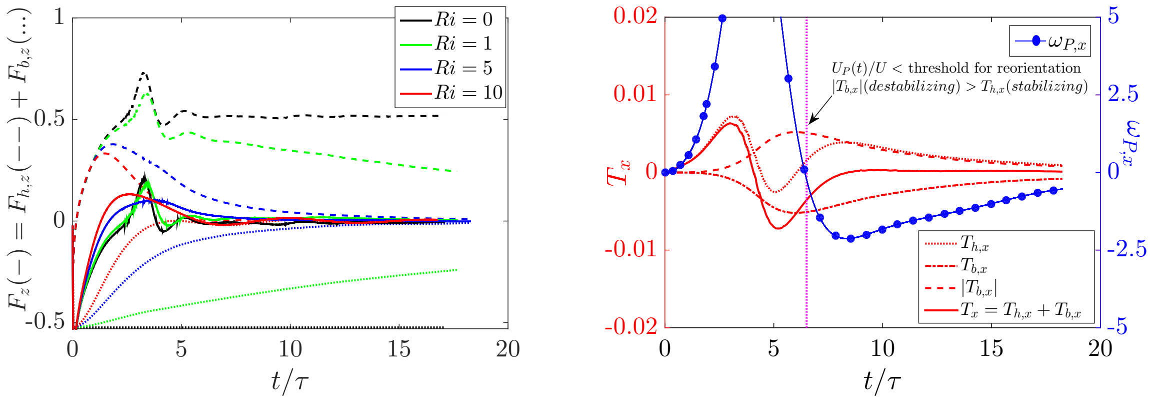

(a) **(b)**

Figure 10.15. a) Forces acting on the prolate spheroid with $Ga = 80$ as it settles in a stratified fluid for different values of Ri shown with different colors. The total force (solid line) can be split into two components, the hydrodynamic component (dashed line) and the buoyancy component (dotted line). b) x-component of the torque acting on a prolate spheroid with $Ga = 80$ as it sediments in a stratified fluid with $Ri = 5$ along with the x-component of the angular velocity. The net torque (solid line) is split into two components, the hydrodynamic torque (dotted line) which tries to orient the prolate in a broadside on orientation (hence stabilizing) and the buoyancy component (dashed-dotted line) which is destabilizing and tries to reorient the prolate edgewise. The reorientation starts once the magnitude of the hydrodynamic torque falls below the buoyancy torque which happens when the prolate velocity falls below the threshold for reorientation discussed in section. 10.3.2.1.

the onset of reorientation to the edgewise orientation below a threshold velocity as shown in Fig. 10.15b. This is similar to an oblate spheroid as shown in Fig. 10.8b. However, a difference between the oblate and prolate spheroid case is found: the partial reorientation and the absence of regime III in the settling of a prolate spheroid.

The secondary motions of the spheroids provide a hint about why the prolate spheroid does not completely reorient. An oblate spheroid oscillates about the broad-side on orientation while a prolate spheroid does not oscillate about the broad-side on orientation as it attains terminal velocity in a homogeneous fluid [369]. Hence, if the inertial effects are strong enough, they can prevent the prolate spheroid from reorienting completely. This becomes clear if we compare the evolution of the buoyancy torque on an oblate spheroid and a prolate spheroid (Fig. 10.8b and 10.15b). Once the particle velocities fall below the threshold for the

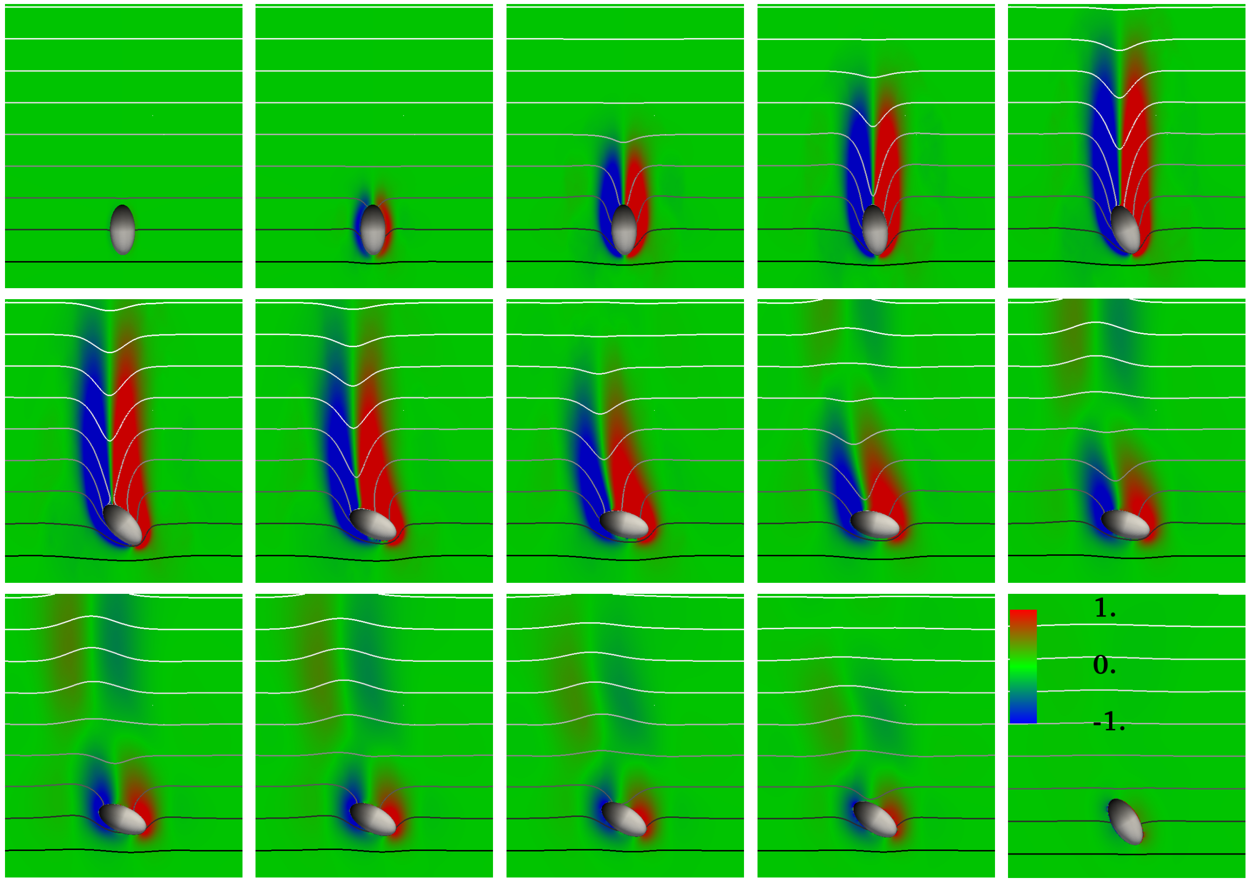

Figure 10.16. Evolution of the x-component of the dimensionless vorticity generation term due to the mis-alignment of the density gradient vector with the direction of gravity, $\boldsymbol{\nabla}\rho_f \times \hat{\mathbf{k}}$, in the $x = 0$ plane for a prolate spheroid with $\mathcal{AR} = 2$, $Ga = 80$ and $R\mathrm{i} = 5$. The solid lines indicate dimensionless isopycnals or equal density lines separated by a value of 0.5. Darker shade of grey indicates a higher density. The panels are snapshots (row-wise) at specific time intervals with $t/\tau = 0$, 4.77, 14.32, 23.87, 33.42, 42.97, 52.52, 62.07, 71.62, 81.17, 90.72, 100.27, 109.82, 119.37, and 219.65. The first panel shows the initial configuration and the last shows the settling configuration after the prolate stops.

onset of reorientation, the destabilizing buoyancy torque on an oblate spheroid dominates for a longer time (4.5 units in dimensionless time which is enough to ensure that the oblate spheroid reorients completely) as compared to a prolate spheroid (1.75 units in dimensionless time which is not enough to reorient the spheroid completely) before they balance each other as the particle velocity approaches 0. Similar observations regarding complete/partial reorientation in the limit $Re \to 0$ and $Ri \to 0$ were also made in a recent theoretical study [245] which hints at the role of the particle $\mathcal{AR}$ in determining the exact degree of reorientation.

To understand the reorientation mechanism, we again examine the x-component of the vorticity generation ($\boldsymbol{\omega}_g$) due to the deformation of the isopycnals (Fig. 10.16). The dynamics are similar to what happens in the case of an oblate spheroid settling in a stratified fluid as discussed in Sec. 10.3.1.3. The only difference is that the prolate spheroid reaches its neutrally buoyant location before it can reorient completely where it stops moving and rotating as seen in Fig. 10.11c and 10.11d.

10.3.2.4 Stratification drag on a prolate spheroid

Fig. 10.17 shows the added drag due to stratification, $C_D^S - C_D^H$ on a prolate spheroid sedimenting in a stratified fluid. The drag due to stratification behaves similarly to the case of an oblate spheroid discussed in Sec. 10.3.1.4. The stratification drag on the prolate particle decreases as it accelerates. $C_D^S - C_D^H$ is minimum when it attains a peak velocity and starts to increase again as the buoyancy/stratification effects take over inertial effects and slow it down. As in the case of an oblate spheroid, $C_D^S - C_D^H$ scales as $\approx O(Fr(z)^{-4})$.

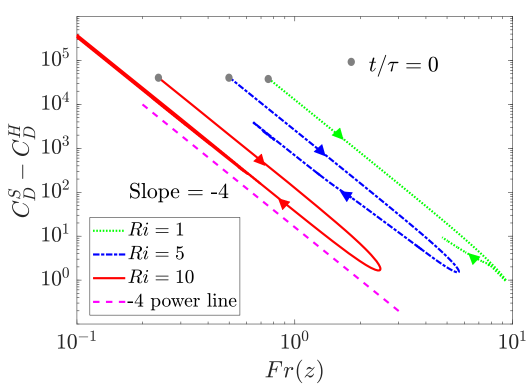

(a)

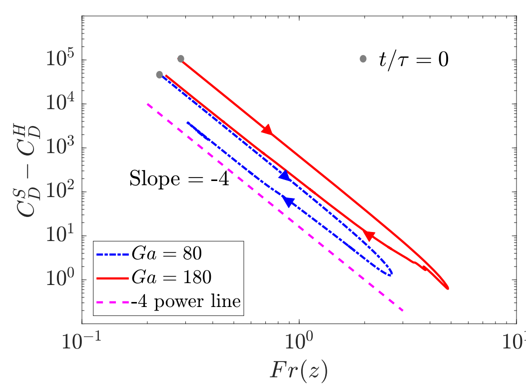

(b)

Figure 10.17. Added drag due to stratification, $C_D^S - C_D^H$, for a prolate spheroid with $\mathcal{AR} = 2$ as a function of the instantaneous particle Froude number, $Fr(z)$, for a) $Ga = 80$ and different stratification strengths. b) Added drag at $Ri = 5$ for different Ga. The arrows show the direction of increasing time and the filled dots show the simulation start time. The dashed pink line shows the -4 power line to indicate a $Fr(z)^{-4}$ scaling of $C_D^S - S_D^H$.

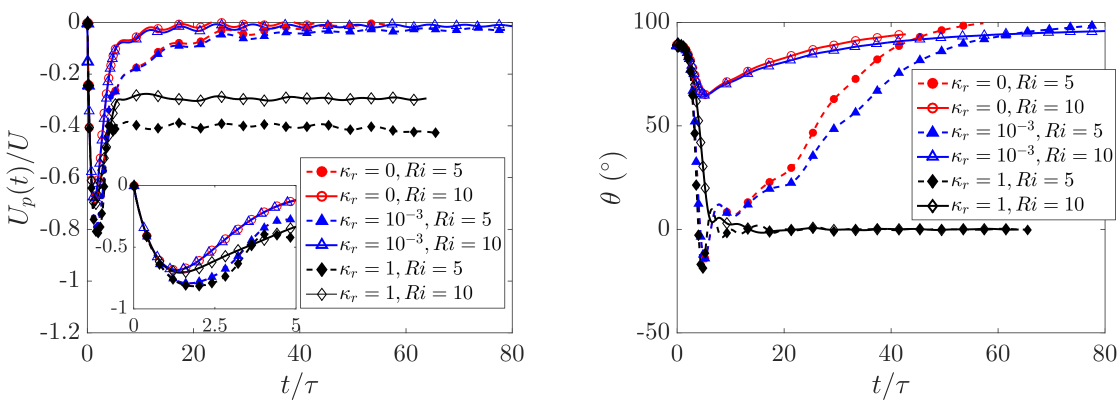

(a) **(b)**

Figure 10.18. Effect of permeability of the particle of the stratifying agent on a) the settling velocity, $U_p(t)/U$, of a settling oblate spheroid with $\mathcal{AR} = 1/3$, and b) the orientation, θ, for $Ri = 5$ & 10. $k = 0$ inside the particle means the stratifying agent cannot diffuse into/ out of the spheroid. A non-zero value for k inside the particle results in increasing the temperature and decreasing the density of the boundary layer. For a very small $k_r = 0.001$, the spheroid settling dynamics is similar to $k_r = 0$ case. However, for a high $k_r = 1$, the spheroid has a completely different settling dynamics. If the stratifying agent can diffuse inside the spheroid, then, the spheroid attains a terminal velocity and does not reorient. These results show that spheroids will reorient only in the case of salt stratified fluid or an adiabatic particle and not in a temperature stratified fluid with conductive particles.

10.3.3 The effect of heat conductivity ratio κ_r on the settling spheroid

For this study, we have chosen a no flux boundary condition on the particle surface, i.e., the stratifying agent cannot diffuse inside the particle (adiabatic/impermeable or no flux) [387] and, as a consequence, pycnoclines must be normal to the particle surface. This is the case if the stratifying agent is salt or the particle is adiabatic. In this section, we investigate the settling dynamics when the fluid and particle temperature influence each other by changing the heat conductivity ratio k_r. Fig. 10.18 shows the settling dynamics of particle having a non-zero k_r. For a small $k_r = 0.001$, the settling dynamics of an oblate spheroid is similar to the case $k_r = 0$. The velocity is slightly higher for $k_r = 0.001$. The particle accelerates initially, attaining a peak velocity after which it decelerates and stops when it reaches its neutrally buoyant position. Also, as its velocity falls below a threshold, it reorients to an edge-wise orientation. Since the flux of the stratifying agent into/out of the

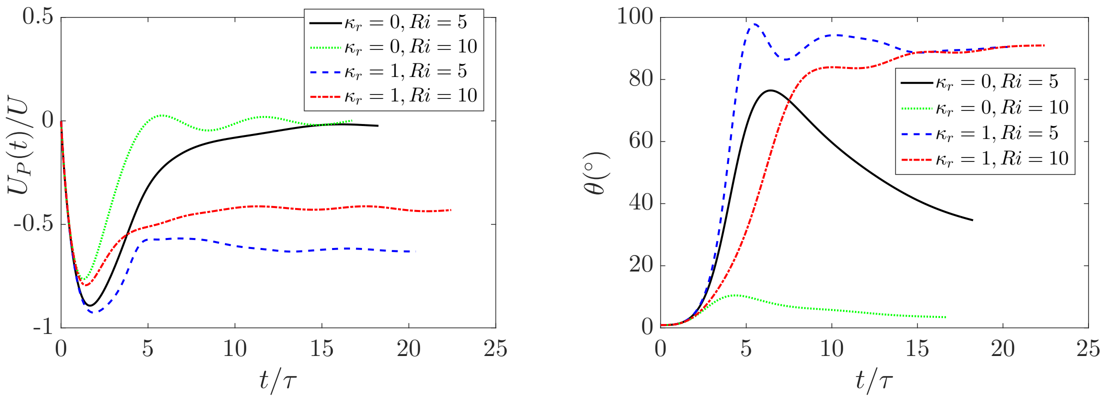

(a) **(b)**

Figure 10.19. Effect of permeability of the particle to the stratifying agent on a) the settling velocity, $U_p(t)/U$, of a settling prolate spheroid with $\mathcal{AR} = 2$, and b) the orientation, θ, for $R\mathrm{i} = 5$ & 10. $k = 0$ inside the particle means the stratifying agent cannot diffuse into the spheroid which results in no change in the density of the surrounding boundary layer. This is true in the case when the stratifying agent is salt. A non-zero value for k inside the particle results in diffusing heat to the surrounding fluid and thus decreasing the density of the boundary layer. For a high $k_r = 1$, the spheroid has a completely different settling dynamics, with the spheroid attaining a terminal velocity and not reorienting. These results show that spheroids will reorient only in the case of salt stratified fluid and not in a temperature stratified fluid with conductive particles.

particle is much slower than the settling dynamics of such small value of k_r, the surrounding fluid is not subjected to any significant heat exchange-induced density change. As for the cases studied above, the particle settles in a fluid region with increasing density, its velocity decreases as the net buoyancy force acting on it increases and the isopycnals resist their deformation. No-flux boundary condition is typical for objects settling in a temperature or a salt stratified fluid, e.g., plastics, metals, organisms, etc. [240], [299], [353], [376].

The settling dynamics changes for a high k_r value. A high k_r value implies significant heat exchanges between the two phases and results in a warmer fluid close to the particle surface. The warmer boundary layer with decreased density accelerates upwards and thus creates a downforce that prevents particles from deceleration. This scenario might occur in chemical processes, e.g. liquid fluidized beds, and marine snow settling in a temperature stratified water. For $k_r = 1$, the settling dynamics during the initial time for an oblate spheroid is similar to $k_r = 0$ case, however the particle does not keep decelerating as time passes in contrast to the case with $k_r = 0$. For a high k_r, the particle attains a terminal velocity much like in the case of an oblate spheroid settling in a homogeneous fluid. The terminal velocity, however, decreases as we increase the stratification strength as shown in fig. 10.18a. Furthermore, the oblate spheroid does not reorient to an edge-wise orientation as its velocity does not fall below the threshold for the onset of reorientation instability, but settles in a broad-side on orientation as shown in Fig. 10.18b. The same holds for a prolate spheroid as shown in Fig. 10.19. As discussed in Sec 10.3.1.3 and 10.3.2.3, $k_r = 0$ implies that the isopycnals are orthogonal to the particle surface, which creates a net torque on the spheroid. For a higher k_r value, the pycnoclines are not orthogonal to the particle surface and hence do not result in a significant destabilizing buoyancy torque, T_b, on the spheroid. Thus, we conclude that no flux boundary condition is essential to observe the reorientation of spheroids settling in a stratified fluid.

10.3.4 The effect of Prandtl number, Pr

The fluid Pr is one of the parameters that greatly influences the settling dynamics of particles in a stratified fluid. $Pr = \nu/\alpha$ quantifies the relative magnitude of momentum diffusivity and the thermal diffusivity. Previous numerical studies investigating the motion of isolated spheres in a stratified fluid concluded that changing the fluid Pr leads to quantitative changes in the settling velocity [299] and radius of downstream jet [353] but does not lead to any significant qualitative changes in the general trends and the overall behavior. We find that similar observations hold true even for spheroid shaped particles settling in a stratified fluid.

We investigate the effect of increasing the fluid Pr from 0.7 (value corresponding to a temperature stratified atmosphere) to 7 (value corresponding to a temperature stratified water) on the settling velocity and the orientation of spheroids in a stratified fluid. Fig. 10.20 show the settling velocity and orientation variations with time for an oblate ($\mathcal{AR} = 1/3$) and a prolate ($\mathcal{AR} = 2$) spheroid with fixed $Ga = 80$, $R\mathrm{i} = 5$ but for two different $Pr = 0.7$ & 7.0. The data shows that increasing the fluid Pr to 7.0 only quantitatively changes the

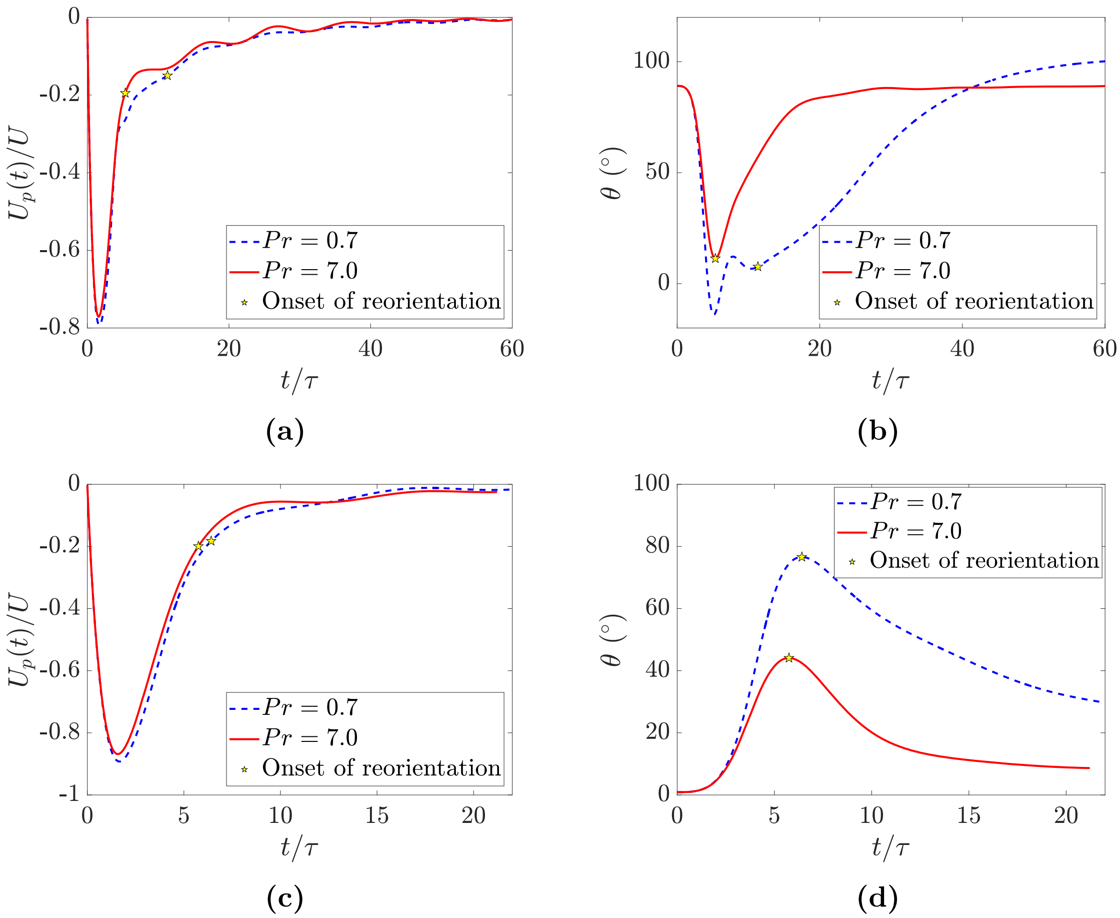

Figure 10.20. Effect of the Prandtl number, Pr, on the settling dynamics of an oblate ($\mathcal{AR} = 1/3$, (a) & (b)) and a prolate ($\mathcal{AR} = 2$, (c) & (d)) spheroid with $Ga = 80$ settling in a stratified fluid with $Ri = 5$. Here $\kappa_r = 0$. ((a), (c)) Dimensionless settling velocity vs dimensionless time. Fluid Pr quantitatively changes the settling velocity such that the settling velocity decreases with increasing Pr. However, the overall trend does not change, i.e., acceleration initially, attaining peak velocity, deceleration and finally particle stops at its neutrally buoyant level. Increasing Pr to 7 from 0.7 also increases the threshold for the onset of reorientation to $|U_p(t)/U| < 0.195$ from $|U_p(t)/U| < 0.15$, respectively. ((b), (d)) Particle orientation vs dimensionless time. Increasing the fluid Pr leads to the onset of reorientation instability at an earlier time and also reduces the time interval in which the reorientation occurs. This shows that a fluid in which the convection dominates diffusion, the influence of the fluid stratification on the spheroid settling dynamics is stronger.

particle settling velocity and its orientation with time but does not change the general trends discussed in Sec. 10.3.1.3 and 10.3.2.3 for $Pr = 0.7$.

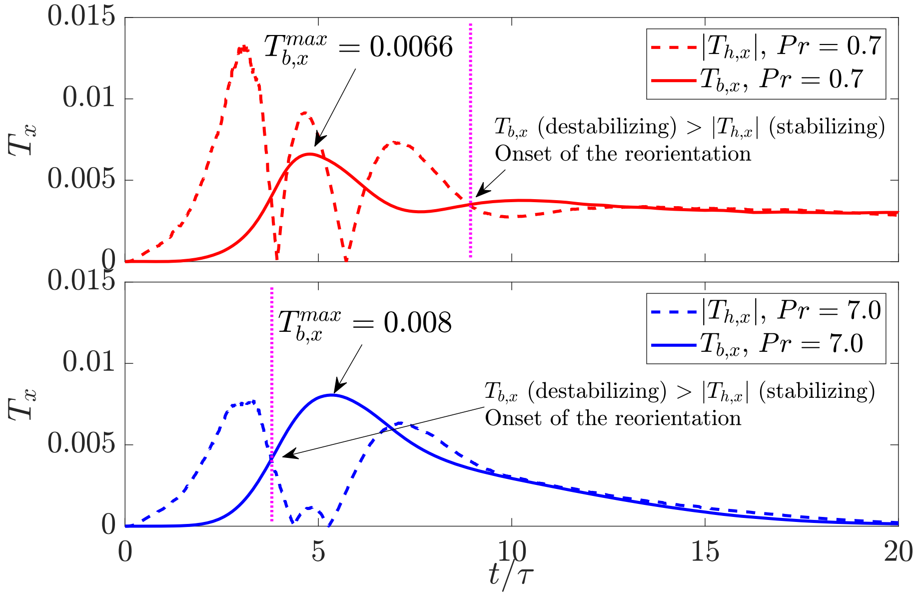

Figure 10.21. Variation in torque acting on an oblate spheroid with $Ga = 80$, $Ri = 5$ and $\mathcal{AR} = 1/3$ with time for two different Pr values. Increasing the Pr of the fluid results in a stronger and dominant buoyancy torque, T_b, on the spheroid for a fixed Ga and Ri which result in an earlier onset of the reorientation.

We observe that increasing the fluid Pr reduces the settling speed of the spheroids as in the case of spherical particles [299]. Also, the spheroids still reorient away for the broad-side on orientation once their velocity magnitude falls below a particular threshold. Interestingly, we observe that this threshold increases to $|U_p(t)/U| < 0.195$ for $Pr = 7.0$ from $|U_p(t)/U| < 0.15$ for $Pr = 0.7$ (Fig. 10.20a and 10.20c). Furthermore, increasing Pr leads to a reduction in the time, $(t/\tau)_{threshold}$, for the onset of the spheroid reorientation and the time required for its reorientation as shown in Fig. 10.20b and 10.20d. Increasing the value of Pr results in slower stratifying agent diffusion and hence increases the influence of inertial or convective effects. As a result, the density boundary layer thickness which scales as $\delta_\rho \approx D/\sqrt{RePr}$ reduces with increasing Pr. The density gradients ($\boldsymbol{\nabla}\rho_f$ as introduced in eq. 10.12) near the particle surface scale as $\approx \gamma D/\delta_\rho = \gamma\sqrt{RePr}$. Thus, with increasing Pr, the magnitude of the density gradients near the particle surface increases. This results in a stronger buoyancy torque, T_b, on the spheroid in a fluid with a higher Pr for a fixed Ga and Ri as can be seen

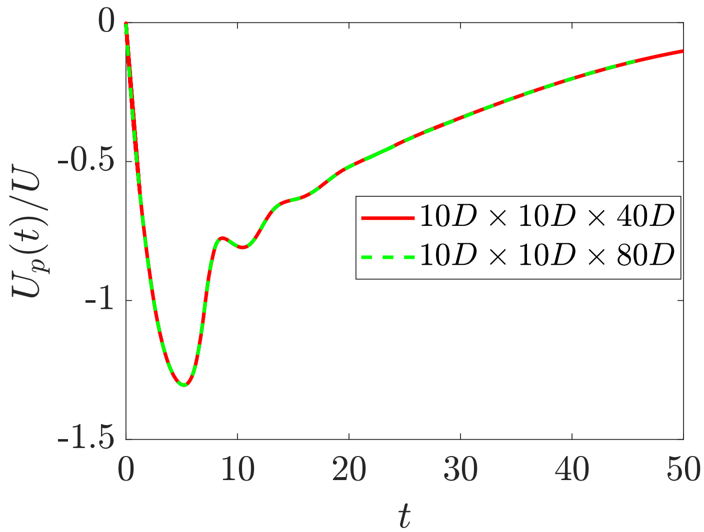

Figure 10.22. Comparison of velocity vs time for a prolate spheroid with $\mathcal{AR} = 2$ in two different domain sizes at $Ga = 180$ and $Ri = 5$. The error in the velocity using a smaller domain is negligible which means even a smaller domain gives accurate results but at a lower computational cost.

in Fig. 10.21 for an oblate spheroid. This increases the velocity threshold and also reduces $(t/\tau)_{threshold}$ for the onset of spheroid reorientation.

The results from this section prove that the basic physics behind the particle deceleration and reorientation is independent of the fluid Pr since it is rooted in the buoyancy force and torque as explained in Sec. 10.3.1.3 and 10.3.2.3. Changing Pr will change the magnitude of the buoyancy force and torque which results in a different peak velocity of the particles and a different time for the onset of the reorientation, but the particles still decelerate and reorient. Hence, the insights obtained from our study are also applicable at higher Pr like 7 for temperature stratified water or Schmidt number of order 700 for salt stratified water. Our results also show a qualitative agreement with the experiments of disks settling in a salt-stratified fluid (Schmidt number $\approx$ 700) [376] which showed that disks also decelerate as they settle and reorient which is what we observe as well.

11. CONCLUSIONS AND FUTURE WORK

Fluid density stratification hinders vertical motion in a fluid, enhances drag on objects resulting in slower settling speeds, and leads to the levitation/oscillation of objects around or before their neutrally buoyant locations depending on the flow conditions. Stratification has non-intuitive implications on the stability of vertically moving swimmers and the hydrodynamic interactions between swimmer pairs and was discussed in chapter 8 and 9, respectively.

Chapter 8 presents the findings of a direct numerical simulation study on the locomotion of a single neutrally buoyant swimmer with finite inertia in a linearly stratified fluid. For modelling the swimmer locomotion mechanism, we use the reduced squirmer model which produces propulsion by periodic deformations of an array of cilia present on its surface. The problem of self-propulsion of such a squirmer with finite inertia in a linearly stratified fluid is more complex than a squirmer moving in a homogeneous fluid. This complexity gives rise to interesting phenomena and significantly changes the motion of squirmers as compared to their movement in a homogeneous fluid.

We use the Richardson number $Ri = Re/Fr^2$ to quantify the stratification strength. We observe that, irrespective of the value of the swimming mode, β, stratification leads to reduction in the steady state swimming speed for squirmers. The reason for this is the trapping of lighter density fluids in the recirculatory regions by the pullers ($\beta > 0$) and the pushers ($\beta < 0$). This results in the buoyancy force on the squirmers in the opposite direction to their swimming motion which reduces their swimming speed. In addition, the resistance offered by the isopycnals to their deformations to the flow fields generated by the squirmers increases with increasing the stratification. This also results in the reduction of the swimming speeds of the squirmers.

Another significant deviation from the homogeneous case is regarding the stability of the squirmers. The flow around the pullers become unsteady 3D at high Re making them unstable, while pushers remaining stable for very high Re in a homogeneous fluid. The reason for this is the increasing size of the recirculatory region in the rear of the pullers with Re which hinders the vorticity advection to downstream causing the instability, while the recirculatory region in front of the pushers shrinks with increasing inertia leading to an efficient vorticity advection to the downstream making them eternally stable. The effect of stratification is exactly the opposite from the effect of inertia. Stratification leads to shrinking of the rear recirculatory bubble for a puller as a puller "pulls" heavier fluid from its sides upwards. In the exigency by these heavier isopycnals to move to their neutrally buoyant level lead to shrinking of the vorticity bubble behind the pullers. On the contrary, stratification leads to the expansion of the front recirculatory bubble of a pusher as it "pushes" lighter fluid trapped in front of it to heavier fluid. So high enough stratification makes a puller stable while a very strong stratification breaks the axisymmetry of the flow around a pusher making it unstable.

The energy calculations for a pusher and a puller show that, a pusher is more efficient at swimming in a stratified fluid as compared to a puller considering the differences in their swimming speeds. Again, the efficient advection of the vorticity to the downstream by the pushers is the reason for this trend. The mixing efficiency of the puller is higher at low Ri (< 2) while the mixing efficiency of a pusher is higher at high Ri (> 2). The reason for this is the similar trend in the generation of the gravitational potential energy by pullers and pushers in the respective Ri regimes.

These results hint towards the fascinating role of density stratification on the locomotion of the marine organisms like ciliary zooplanktons and provide possible clues for the reasons behind the preferential accumulation of larger sized planktons at pycnoclines [288]. The speed of larger organisms with higher inertia, when encounter a density jump or a strong stratification during the vertical migratory motion in oceans, significantly reduces and the energy required for the propulsion also goes up. In addition, the swimmers stray from their straight vertical trajectory and start swimming in the horizontal direction due to the onset of instability (e.g., high Re pullers in a weak stratification or a pusher in a very strong stratification). This might lead to the accumulation of the swimmers at the density interface. These mechanisms come into picture only at a finite Re. At low Re, the swimmers are always stable [279], [280] and stratification might lead to increase in their speeds, e.g., pullers [293], thus resulting in negligible accumulation which is true for smaller sized planktons [288].

Stratification also increases the mixing efficiency generated by an individual swimmer, an effect which amplifies when we consider swarms of swimmers [226], [292].

Even though these organisms dwell in a density stratified environment, most of the experimental studies on their locomotion have been done in a homogeneous fluid. More experimental studies are thus needed to investigate the effect of stratification on the motion and flow fields of individual marine organisms. In addition, real marine organisms have a wide variety of shapes, create jets as they swim and show a wide variety of other variations. Studying the effect of these variations on the swimming dynamics of organisms in a stratified fluid is also an interesting problem to investigate.

Chapter 9 investigates the hydrodynamics interaction between a pair of squirmers with finite inertia in a stratified fluid with different stratification strengths. We compare the squirmer trajectories and velocities with their trajectories and velocities in a homogeneous fluid for the same initial conditions. We present results for two types of initial configurations: 1) squirmers approaching each other in opposite directions, and 2) squirmers moving side-by-side in the vertical direction. The results presented can potentially be important in understanding the collective dynamics of microorganisms in oceans and lakes where stratification is observed.

For a pair of pullers approaching each other, stratification leads to their reorientation after the collision contrary to what happens in a homogeneous fluid. The tendency of the displaced isopycnals behind the pullers results in a torque on the pullers which reorients the pullers in their initial orientation after the collision. Stratification also leads to the elimination of the closed loop trajectories observed for colliding pullers at high Re ($= 10$ and 50) which has been explained using the flow field and the density field around the pullers during and after the collision.

A pair of pullers moving side-by-side follow complicated and distinct trajectories at different Re and Ri. In a homogeneous fluid, the pullers are repelled away from each other after initial attraction and a close contact for $Re = 10$, but they are hydrodynamically trapped near each other in loops as they move down for $Re = 50$. Again, high stratification leads to the elimination of the loops and hydrodynamic trapping deflecting the pullers away from each other even at $Re = 50$ similar to what happens for $Re = 10$ pullers in a homogeneous fluid.

A pair of pushers come to a complete stop after the collision at high Ri. However, this configuration is unstable which results in a 3D motion of the pushers away from the plane of collision. As the pushers move away from the plane of collision, they stick together. The 3D motion is gradually prevented as we increase Re and a higher Ri is required for the instability. These results indicate that in a stratified fluid, organisms might get trapped near each other and move horizontally which can lead to their accumulation in oceans [288], [289].

In a homogeneous fluid, two pushers moving side-by-side are attracted towards each other, but eventually, they scatter away from each other with a scattering angle increasing with Re. Stratification hastens the repulsion between the pullers moving side-by-side and results in a decrease in the scattering angle at high Re.

The results for contact time for the squirmers show that pushers tend to spend more time in contact with each other than pullers. Furthermore, stratification increases the contact time for the squirmers. This indicates an enhanced chance for their success in reproduction in stratified environments. We also present results for variation in the Pr of the fluid and different lateral initial separations of the squirmers. But these were limited to a few cases to save computational expenses. Logical extensions of this work are to study the effects of varying the fluid Pr, the effects of squirmer swimming mode β, effects of initial squirmer configurations, and the effects of buoyancy by relaxing the quasi-instantaneous neutral buoyancy condition on the interactions of squirmers in a stratified fluid.

The results of chapter 8 and 9 show that a strong stratification or strong inertia can destabilize the straight-line trajectory swimmers, while colliding swimmers can get trapped or deflected in horizontal directions, which increases their contact time and is better for their reproductive success. Flow induced by the swimmers decays faster in a stratified fluid, concealing them better from predators. These observations explain the hydrodynamic mechanisms behind the accumulation of phytoplankton and harmful algal blooms in oceans.

Chapter 10 probes the conditions and mechanisms behind the reorientation instability of anisotropic particles as they settle in a stratified fluid. A toroidal flow close to the particles arises due to the need for the isopycnals to be orthogonal to the rigid particle surface. This results in the reorientation instability in anisotropic particles owing to the dominance of stratification torque when the particle velocity falls below a threshold. The shapes considered are an oblate spheroid with $\mathcal{AR} = 1/3$ and a prolate spheroid with $\mathcal{AR} = 2$. We vary the Reynolds number Ga from $80 - 250$ and the Richardson number Ri from $0 - 10$ while keeping the density ratio ρ_r and Prandtl number Pr constant. The results show that the settling dynamics of spheroids is significantly different in a stratified fluid than in a homogeneous fluid.

Initially, the spheroids accelerate from rest and reach a maximum velocity. The peak velocity attained by the particles increases with their Ga while decreases monotonically when increasing the stratification. After the settling velocity attain its peak value, stratification dominates over inertia, because the inertial effects are not enough to sustain the deformation of the isopycnals once the particle reaches its peak velocity. Hence, due to the tendency of the isopycnals to return to their original positions, the fluid experiences a resistance to its motion. This results in an increased drag and hence a deceleration of the particle until it stops at its neutrally buoyant position. This evolution of the settling velocity is similar to that of a spherical particle settling in a stratified fluid.

The fluid stratification alters the orientation of the spheroids compared to their orientations in a homogeneous fluid. The fluid stratification leads to reorientation instability as the particle settling velocity falls below a threshold. For the parameters considered here, the onset of the reorientation instability occurs at $|U_p(t)/U| < 0.15$. Interestingly, the dimensionless threshold velocity for the onset of reorientation instability is found to be the same for the oblate and prolate spheroids. This value might be different for different values of the density ratio and the Prandtl number. As a result of this instability, an oblate spheroid settles with its broader side aligned with the direction of the stratification. On the other hand, a prolate spheroid reorients partially or fully depending on its Ga and settles such that its longer edge is at an angle greater than $0°$ and lower than $45°$ with the horizontal direction. This is completely opposite to what happens in a homogeneous fluid as both an oblate and a prolate spheroid settle in a broad-side on orientation. Stratification also eliminates the oscillatory path instability observed for spheroids in a homogeneous fluid. This is due to the decreasing magnitude of the inertial effects as the particle decelerates while reaching regions of higher fluid density.

The asymmetry in the low pressure region behind the spheroids due to an asymmetric wake results in the onset of the reorientation instability. This asymmetry results from the asymmetric distribution of the vorticity generation term due to the mis-alignment of the density gradient vector with the vertical direction (baroclinic vorticity generation). As a result, the destabilizing buoyancy torque, T_b, becomes dominant over the stabilizing hydrodynamic torque T_h as the spheroid velocity falls below a threshold value causing the onset of reorientation instability. We also report that the spheroids will only reorient in the case when they are impermeable to the stratifying agent ($\kappa_r << 1$) which is true in the case of a salt stratification or an adiabatic particle. If the stratifying agent can diffuse ($\kappa_r >> 0$) inside the particle, then the spheroid won't reorient and the settling dynamics is similar to that in a homogeneous fluid with stratification causing a reduction in the terminal velocity. We also find that increasing the fluid Pr from 0.7 (temperature stratified air) to 7.0 (temperature stratified water) results in a stronger and dominant T_b on the spheroids. As a results for $Pr = 7.0$, the onset of reorientation occurs at a higher velocity threshold $|U_p(t)/U| < 0.195$ and at an earlier time compared to case $Pr = 0.7$. The results presented in this paper are a first contribution to the field of settling particles in a fluid, in particular for anisotropic particles and stratified fluids. As extensions of this work, it would be interesting to investigate the behavior of particle suspensions, the effect of the aspect ratios, and also extensively quantify the effect of Pr as well as other particle shapes on the settling dynamics of particles in a stratified fluid.

Though much is known about the dynamics of spherical objects, we are just starting to investigate the dynamics of anisotropic objects in stratified fluids. The effects of stratification and particle shape anisotropy on the pair interactions and suspension dynamics are still elusive. In addition, investigating the combined effects of porosity, shape anisotropy, shear, and background turbulence can help us develop better models for predicting the transport and accumulation of marine particles in oceans. Limited numerical simulations show that changing the fluid Pr does not alter the overall qualitative behavior but affects the body dynamics quantitatively. More investigations on the role of Pr in the motion in stratified fluids can help us better understand the differences in the effects of temperature stratification vs. salinity stratification. Diffusion effects play a governing role in the accumulation and aggregation of objects in horizontal layers. More investigations are needed to understand the underlying physics and build force interaction models that could be utilized in the simulations of suspension dynamics in a stratified environment. Another interesting problem would be to probe the presence of *densitotaxis*, i.e., do swimmers have a movement preference when encountering density gradients due to factors other than nutrients?

REFERENCES

[1] R. Prasher, "Thermal interface materials: Historical perspective, status, and future directions", *Proceedings of the IEEE*, vol. 94, no. 8, pp. 1571–1586, 2006.

[2] H. Wang, D. S. Nobes, and R. Vehring, "Particle surface roughness improves colloidal stability of pressurized pharmaceutical suspensions", *Pharmaceutical research*, vol. 36, no. 3, p. 43, 2019.

[3] R. V. More and A. M. Ardekani, "Effect of roughness on the rheology of concentrated non-brownian suspensions: A numerical study", *Journal of Rheology*, vol. 64, no. 1, pp. 67–80, 2020.

[4] R. More and A. Ardekani, "Roughness induced shear thickening in frictional non-brownian suspensions: A numerical study", *Journal of Rheology*, vol. 64, no. 2, pp. 283–297, 2020.

[5] R. More and A. Ardekani, "A constitutive model for sheared dense suspensions of rough particles", *J. of Rheology*, vol. 64, no. 5, pp. 1107–1120, 2020.

[6] R. More and A. Ardekani, "Unifying disparate rate-dependent rheological regimes in non-brownian suspensions", *Physical Review E*, vol. 103, no. 6, p. 062 610, 2021.

[7] R. I. Tanner and S. Dai, "Particle roughness and rheology in noncolloidal suspensions", *Journal of Rheology*, vol. 60, no. 4, pp. 809–818, 2016.

[8] C.-P. Hsu, S. N. Ramakrishna, M. Zanini, N. D. Spencer, and L. Isa, "Roughness-dependent tribology effects on discontinuous shear thickening", *PNAS*, vol. 115, no. 20, pp. 5117–5122, 2018.

[9] L. C. Hsiao, S. Jamali, E. Glynos, P. F. Green, R. G. Larson, and M. J. Solomon, "Rheological State Diagrams for Rough Colloids in Shear Flow", *Physical Review Letters*, vol. 119, no. 15, 2017.

[10] A. Einstein, "On the theory of the brownian movement", *Ann. Phys*, vol. 19, no. 4, pp. 371–381, 1906.

[11] A. Einstein, "Berichtigung zu meiner arbeit: Eine neue bestimmung der moleküldimensionen", *Annalen der Physik*, vol. 339, no. 3, pp. 591–592, 1911.

[12] S. Kim and S. J. Karrila, *Microhydrodynamics: principles and selected applications.* Courier Corporation, N. Chelmsford, MA, 2013.

[13] G. Batchelor, "The stress system in a suspension of force-free particles", *Journal of Fluid Mechanics*, vol. 41, no. 3, pp. 545–570, 1970.

[14] J. M. Peterson and M. Fixman, "Viscosity of polymer solutions", *The Journal of Chemical Physics*, vol. 39, no. 10, pp. 2516–2523, 1963.

[15] G. Batchelor and J. Green, "The determination of the bulk stress in a suspension of spherical particles to order c 2", *Journal of Fluid Mechanics*, vol. 56, no. 3, pp. 401–427, 1972.

[16] G. Batchelor and J.-T. Green, "The hydrodynamic interaction of two small freely-moving spheres in a linear flow field", *Journal of Fluid Mechanics*, vol. 56, no. 2, pp. 375–400, 1972.

[17] F. Boyer, É. Guazzelli, and O. Pouliquen, "Unifying suspension and granular rheology", *Physical Review Letters*, vol. 107, no. 18, p. 188 301, 2011.

[18] C. Bonnoit, T. Darnige, E. Clement, and A. Lindner, "Inclined plane rheometry of a dense granular suspension", *Journal of Rheology*, vol. 54, no. 1, pp. 65–79, 2010.

[19] S. Dagois-Bohy, S. Hormozi, É. Guazzelli, and O. Pouliquen, "Rheology of dense suspensions of non-colloidal spheres in yield-stress fluids", *Journal of Fluid Mechanics*, vol. 776, R2, 2015.

[20] T. Dbouk, L. Lobry, and E. Lemaire, "Normal stresses in concentrated non-Brownian suspensions", *Journal of Fluid Mechanics*, vol. 715, pp. 239–272, 2013.

[21] G. Ovarlez, F. Bertrand, and S. Rodts, "Local determination of the constitutive law of a dense suspension of noncolloidal particles through magnetic resonance imaging", *Journal of rheology*, vol. 50, no. 3, pp. 259–292, 2006.

[22] I. E. Zarraga, D. A. Hill, and D. T. Leighton, "The characterization of the total stress of concentrated suspensions of noncolloidal spheres in Newtonian fluids", *Journal of Rheology*, vol. 185, no. 2, pp. 185–220, Mar. 2000.

[23] A. Sierou and J. Brady, "Rheology and microstructure in concentrated noncolloidal suspensions", *Journal of Rheology*, vol. 46, no. 5, pp. 1031–1056, 2002.

[24] S. Gallier, E. Lemaire, F. Peters, and L. Lobry, "Rheology of sheared suspensions of rough frictional particles", *Journal of Fluid Mechanics*, vol. 757, no. 6, pp. 514–549, 2014.

[25] R. Mari, R. Seto, J. F. Morris, and M. M. Denn, "Shear thickening, frictionless and frictional rheologies in non- Brownian suspensions", *Journal of Rheology*, vol. 58, no. 60, pp. 1693–905, 2014.

[26] J. J. Stickel and R. L. Powell, "Fluid mechanics and rheology of dense suspensions", *Annual Review of Fluid Mechanics*, vol. 37, pp. 129–149, 2005.

[27] É. Guazzelli and O. Pouliquen, "Rheology of dense granular suspensions", *Journal of Fluid Mechanics*, vol. 852, P1, 2018.

[28] J. Chong, E. Christiansen, and A. Baer, "Rheology of concentrated suspensions", *Journal of applied polymer science*, vol. 15, no. 8, pp. 2007–2021, 1971.

[29] R. Storms, B. Ramarao, and R. Weiland, "Low shear rate viscosity of bimodally dispersed suspensions", *Powder technology*, vol. 63, no. 3, pp. 247–259, 1990.

[30] R. F. Probstein, M. Sengun, and T.-C. Tseng, "Bimodal model of concentrated suspension viscosity for distributed particle sizes", *Journal of rheology*, vol. 38, no. 4, pp. 811–829, 1994.

[31] C. Chang and R. L. Powell, "Hydrodynamic transport properties of concentrated suspensions", *AIChE journal*, vol. 48, no. 11, pp. 2475–2480, 2002.

[32] I. M. Krieger and T. J. Dougherty, "A mechanism for non-newtonian flow in suspensions of rigid spheres", *Transactions of the Society of Rheology*, vol. 3, no. 1, pp. 137–152, 1959.

[33] S. H. Maron and P. E. Pierce, "Application of ree-eyring generalized flow theory to suspensions of spherical particles", *Journal of colloid science*, vol. 11, no. 1, pp. 80–95, 1956.

[34] R. Hoffman, "Discontinuous and dilatant viscosity behavior in concentrated suspensions. i. observation of a flow instability", *Transactions of the Society of Rheology*, vol. 16, no. 1, pp. 155–173, 1972.

[35] H. Barnes, "Shear-thickening ("dilatancy") in suspensions of nonaggregating solid particles dispersed in newtonian liquids", *Journal of Rheology*, vol. 33, no. 2, pp. 329–366, 1989.

[36] H. A. Barnes, "The yield stress—a review or 'π$\alpha\nu\tau\alpha$ $\rho\varepsilon\iota$'—everything flows?", *Journal of Non-Newtonian Fluid Mechanics*, vol. 81, no. 1-2, pp. 133–178, 1999.

[37] I. E. Zarraga and D. T. Leighton Jr, "Normal stress and diffusion in a dilute suspension of hard spheres undergoing simple shear", *Physics of Fluids*, vol. 13, no. 3, pp. 565–577, 2001.

[38] P. Pham, B. Metzger, and J. E. Butler, "Particle dispersion in sheared suspensions: Crucial role of solid-solid contacts", *Physics of Fluids*, vol. 27, no. 5, p. 051 701, 2015.

[39] F. Blanc, F. Peters, and E. Lemaire, “Experimental signature of the pair trajectories of rough spheres in the shear-induced microstructure in noncolloidal suspensions”, *Physical review letters*, vol. 107, no. 20, p. 208 302, 2011.

[40] A. SINGH and P. R. NOTT, “Experimental measurements of the normal stresses in sheared stokesian suspensions”, *Journal of Fluid Mechanics*, vol. 490, pp. 293–320, 2003.

[41] F. Boyer, O. Pouliquen, and É. Guazzelli, “Dense suspensions in rotating-rod flows: Normal stresses and particle migration”, *Journal of Fluid Mechanics*, vol. 686, pp. 5–25, 2011.

[42] É. Couturier, F. Boyer, O. Pouliquen, and É. Guazzelli, “Suspensions in a tilted trough: Second normal stress difference”, *Journal of Fluid Mechanics*, vol. 686, pp. 26–39, 2011.

[43] S.-C. Dai, E. Bertevas, F. Qi, and R. I. Tanner, “Viscometric functions for noncolloidal sphere suspensions with newtonian matrices”, *Journal of Rheology*, vol. 57, no. 2, pp. 493–510, 2013.

[44] J. F. Brady and G. Bossis, “Stokesian Dynamics”, *Annual Review of Fluid Mechanics*, vol. 20, no. 1, pp. 111–157, 1988.

[45] J. F. Brady and G. Bossis, “The rheology of concentrated suspensions of spheres in simple shear flow by numerical simulation”, *Journal of Fluid Mechanics*, vol. 155, pp. 105–129, 1985.

[46] E. Boek, P. V. Coveney, H. Lekkerkerker, and P. van der Schoot, “Simulating the rheology of dense colloidal suspensions using dissipative particle dynamics”, *Physical Review E*, vol. 55, no. 3, p. 3124, 1997.

[47] R. J. Hill, D. L. Koch, and A. J. Ladd, “The first effects of fluid inertia on flows in ordered and random arrays of spheres”, *Journal of Fluid Mechanics*, vol. 448, p. 213, 2001.

[48] K. Yeo and M. R. Maxey, “Dynamics of concentrated suspensions of non-colloidal particles in Couette flow”, *Journal of Fluid Mechanics*, vol. 649, pp. 205–231, 2010.

[49] R. C. Ball and J. R. Melrose, “A simulation technique for many spheres in quasi-static motion under frame-invariant pair drag and Brownian forces”, *Physica A: Statistical Mechanics and its Applications*, vol. 247, no. 1-4, pp. 444–472, 1997.

[50] M. Wyart and M. Cates, “Discontinuous shear thickening without inertia in dense non-brownian suspensions”, *Physical review letters*, vol. 112, no. 9, p. 098 302, 2014.

[51] É. Guazzelli and O. Pouliquen, “Rheology of dense granular suspensions”, *J. Fluid Mech*, vol. 852, p. 1, 2019.

[52] L. Lobry, E. Lemaire, F. Blanc, S. Gallier, and F. Peters, “Shear thinning in non-brownian suspensions explained by variable friction between particles”, *Journal of Fluid Mechanics*, vol. 860, pp. 682–710, 2019.

[53] J. R. Smart and D. T. Leighton Jr, “Measurement of the hydrodynamic surface roughness of noncolloidal spheres”, *Physics of Fluids A: Fluid Dynamics*, vol. 1, no. 1, pp. 52–60, 1989.

[54] J. Y. Moon, S. Dai, L. Chang, J. S. Lee, and R. I. Tanner, “The effect of sphere roughness on the rheology of concentrated suspensions”, *Journal of Non-Newtonian Fluid Mechanics*, vol. 223, pp. 233–239, 2015.

[55] C. Gamonpilas, J. F. Morris, and M. M. Denn, “Shear and normal stress measurements in non-brownian monodisperse and bidisperse suspensions”, *Journal of Rheology*, vol. 60, no. 2, pp. 289–296, 2016.

[56] R. Seto, R. Mari, J. F. Morris, and M. M. Denn, “Discontinuous shear thickening of frictional hard-sphere suspensions”, *Physical Review Letters*, vol. 111, no. 21, pp. 1–5, 2013.

[57] D. J. Jeffrey and Y. Onishi, “Calculations of the resistance and mobility functinos for two unequal rigid spheres in low-Reynolds number flow”, *Journal of Fluid Mechanics*, vol. 139, pp. 261–290, 1984.

[58] J. Comtet, G. Chatté, A. Niguès, L. Bocquet, A. Siria, and A. Colin, “Pairwise frictional profile between particles determines discontinuous shear thickening transition in non-colloidal suspensions”, *Nature communications*, vol. 8, p. 15 633, 2017.

[59] A. K. Townsend and H. J. Wilson, “Frictional shear thickening in suspensions: The effect of rigid asperities”, *Physics of Fluids*, vol. 29, no. 12, p. 121 607, 2017.

[60] V. Brizmer, Y. Kligerman, and I. Etsion, “Elastic–plastic spherical contact under combined normal and tangential loading in full stick”, *Tribology Letters*, vol. 25, no. 1, pp. 61–70, 2007.

[61] F. Bowden and D. Tabor, *The Friction and Lubrication of Solids*, 7. AAPT, 1951, vol. 19, pp. 428–429.

[62] S. Gallier, E. Lemaire, L. Lobry, and F. Peters, “Effect of confinement in wall-bounded non-colloidal suspensions”, *Journal of Fluid Mechanics*, vol. 799, pp. 100–127, 2016.

[63] M. M. Hilali, S. Pal, R. V. More, R. Saive, and A. M. Ardekani, “Sheared thick-film electrode materials containing silver powders with nanoscale surface asperities improve solar cell performance”, *Advanced Energy and Sustainability Research*, p. 2 100 145, 2021.

[64] D. Burnat, P. Ried, P. Holtappels, A. Heel, T. Graule, and D. Kata, “The rheology of stabilised lanthanum strontium cobaltite ferrite nanopowders in organic medium applicable as screen printed sofc cathode layers”, *Fuel Cells*, vol. 10, no. 1, pp. 156–165, 2010.

[65] J. C. Lin and C. Y. Wang, “Effect of surface properties of silver powder on the sintering of its thick-film conductor”, *Materials Chemistry and Physics*, vol. 45, no. 3, pp. 253–261, 1996.

[66] H.-W. Lin, C.-P. Chang, W.-H. Hwu, and M.-D. Ger, “The rheological behaviors of screen-printing pastes”, *Journal of Materials Processing Technology*, vol. 197, no. 1-3, pp. 284–291, 2008.

[67] S. Murakami, K. Ri, T. Itoh, N. Izu, W. Shin, K. Inukai, Y. Takahashi, and Y. Ando, “Effects of ethyl cellulose polymers on rheological properties of (La, Sr)(Ti, Fe) o3-terpineol pastes for screen printing”, *Ceramics International*, vol. 40, no. 1, pp. 1661–1666, 2014.

[68] C.-J. Hsu and J.-H. Jean, “Formulation and dispersion of nicuzn ferrite paste”, *Materials Chemistry and Physics*, vol. 78, no. 2, pp. 323–329, 2003.

[69] C. P. Hsu, R. H. Guo, C. C. Hua, C.-L. Shih, W.-T. Chen, and T.-I. Chang, “Effect of polymer binders in screen printing technique of silver pastes”, *Journal of Polymer Research*, vol. 20, no. 10, p. 277, 2013.

[70] R. Faddoul, N. Reverdy-Bruas, and A. Blayo, “Formulation and screen printing of water based conductive flake silver pastes onto green ceramic tapes for electronic applications”, *Materials Science and Engineering: B*, vol. 177, no. 13, pp. 1053–1066, 2012.

[71] S. Rane, T. Seth, G. Phatak, D. Amalnerkar, and B. Das, “Influence of surfactants treatment on silver powder and its thick films”, *Materials Letters*, vol. 57, no. 20, pp. 3096–3100, 2003.

[72] S. Rane, P. Khanna, T. Seth, G. Phatak, D. Amalnerkar, and B. Das, “Firing and processing effects on microstructure of fritted silver thick film electrode materials for solar cells”, *Materials Chemistry and Physics*, vol. 82, no. 1, pp. 237–245, 2003.

[73] H.-W. Lin, W.-H. Hwu, and M.-D. Ger, “The dispersion of silver nanoparticles with physical dispersal procedures”, *Journal of Materials Processing Technology*, vol. 206, no. 1-3, pp. 56–61, 2008.

[74] G. Guo, W. Gan, F. Xiang, J. Zhang, H. Zhou, H. Liu, and J. Luo, “Effect of dispersibility of silver powders in conductive paste on microstructure of screen-printed front contacts and electrical performance of crystalline silicon solar cells”, *Journal of Materials Science: Materials in Electronics*, vol. 22, no. 5, pp. 527–530, 2011.

[75] F. F. Lange, “Powder processing science and technology for increased reliability”, *Journal of the American Ceramic Society*, vol. 72, no. 1, pp. 3–15, 1989.

[76] J. A. Lewis, “Colloidal processing of ceramics”, *Journal of the American Ceramic Society*, vol. 83, no. 10, pp. 2341–2359, 2000.

[77] J. W. Phair, “Rheological analysis of concentrated zirconia pastes with ethyl cellulose for screen printing sofc electrolyte films”, *Journal of the American Ceramic Society*, vol. 91, no. 7, pp. 2130–2137, 2008.

[78] A. Mat, B. Timurkutluk, C. Timurkutluk, and Y. Kaplan, “Effects of ceramic based pastes on electrochemical performance of solid oxide fuel cells”, *Ceramics International*, vol. 40, no. 6, pp. 8575–8583, 2014.

[79] B. E. Taylor, J. J. Felten, S. J. Horowitz, J. R. Larry, and R. M. Rosenberg, “Advances in low cost silver-containing thick film conductors”, *Active and Passive Electronic Components*, vol. 9, no. 1, pp. 67–85, 1981.

[80] S. F. Wang, J. P. Dougherty, W. Huebner, and J. G. Pepin, “Silver-palladium thick-film conductors”, *Journal of the American Ceramic Society*, vol. 77, no. 12, pp. 3051–3072, 1994.

[81] P. Coussot and C. Ancey, “Rheophysical classification of concentrated suspensions and granular pastes”, *Physical Review E*, vol. 59, no. 4, p. 4445, 1999.

[82] A. Singh, S. Pednekar, J. Chun, M. M. Denn, and J. F. Morris, “From yielding to shear jamming in a cohesive frictional suspension”, *Physical review letters*, vol. 122, no. 9, p. 098 004, 2019.

[83] G. Chatté, J. Comtet, A. Niguès, L. Bocquet, A. Siria, G. Ducouret, F. Lequeux, N. Lenoir, G. Ovarlez, and A. Colin, “Shear thinning in non-brownian suspensions”, *Soft matter*, vol. 14, no. 6, pp. 879–893, 2018.

[84] C. Clavaud, A. Bérut, B. Metzger, and Y. Forterre, “Revealing the frictional transition in shear-thickening suspensions”, *Proceedings of the National Academy of Sciences*, vol. 114, no. 20, pp. 5147–5152, 2017.

[85] M. M. Denn and J. F. Morris, “Rheology of non-brownian suspensions”, *Annual Review of Chemical and Biomolecular Engineering*, vol. 5, pp. 203–228, 2014.

[86] A. Mahmud, J. Moon, S. Dai, R. I. Tanner, and C. Ness, “A bootstrap mechanism for non-colloidal suspension viscosity”, *Rheologica Acta*, vol. 57, no. 10, pp. 635–643, 2018.

[87] J. F. Morris, “A review of microstructure in concentrated suspensions and its implications for rheology and bulk flow”, *Rheologica Acta*, vol. 48, no. 8, pp. 909–923, 2009.

[88] R. H. Davis, Y. Zhao, K. P. Galvin, and H. J. Wilson, “Solid–solid contacts due to surface roughness and their effects on suspension behaviour”, *Philosophical Transactions of the Royal Society of London. Series A: Mathematical, Physical and Engineering Sciences*, vol. 361, no. 1806, pp. 871–894, 2003.

[89] S. Pednekar, J. Chun, and J. Morris, “Bidisperse and polydisperse suspension rheology at large solid fraction”, *Journal of Rheology*, vol. 62, no. 513, 2017.

[90] F. Tapia, S. Shaikh, J. E. Butler, O. Pouliquen, and E. Guazzelli, “Rheology of concentrated suspensions of non-colloidal rigid fibres”, *Journal of Fluid Mechanics*, vol. 827, R5, 2017.

[91] E. Bertevas, X. Fan, and R. I. Tanner, “Simulation of the rheological properties of suspensions of oblate spheroidal particles in a newtonian fluid”, *Rheologica Acta*, vol. 49, no. 1, p. 53, 2010.

[92] E. Brown, H. Zhang, N. A. Forman, B. W. Maynor, D. E. Betts, J. M. Desimone, and H. M. Jaeger, “Shear thickening and jamming in densely packed suspensions of different particle shapes”, *PHYSICAL REVIEW E*, vol. 84, p. 31 408, 2011.

[93] B. M. Guy, C. Ness, M. Hermes, L. J. Sawiak, J. Sun, and W. C. K. Poon, “Testing the Wyart-Cates model for non-Brownian shear thickening using bidisperse suspensions”, 2019.

[94] M. M. Denn, J. F. Morris, and D. Bonn, “Shear thickening in concentrated suspensions of smooth spheres in Newtonian suspending fluids”, *Soft Matter*, vol. 14, no. 2, pp. 170–184, 2018.

[95] H. J. Wilson and R. H. Davis, “Shear stress of a monolayer of rough spheres”, *Journal of Fluid Mechanics*, vol. 452, pp. 425–441, 2002.

[96] A. K. Townsend and H. J. Wilson, “Frictional shear thickening in suspensions: The effect of rigid asperities”, *Physics of Fluids*, vol. 29, no. 12, p. 121 607, 2017.

[97] M. E. Cates and M. Wyart, "Granulation and bistability in non-brownian suspensions", *Rheologica Acta*, vol. 53, no. 10-11, pp. 755–764, 2014.

[98] B. Metzger and J. E. Butler, "Irreversibility and chaos: Role of long-range hydrodynamic interactions in sheared suspensions", *Physical Review E*, vol. 82, no. 5, p. 051 406, 2010.

[99] B. Metzger, P. Pham, and J. E. Butler, "Irreversibility and chaos: Role of lubrication interactions in sheared suspensions", *Physical Review E*, vol. 87, no. 5, p. 052 304, 2013.

[100] P. Arp and S. Mason, "The kinetics of flowing dispersions: Viii. doublets of rigid spheres (theoretical)", *Journal of Colloid and Interface Science*, vol. 61, no. 1, pp. 21–43, 1977.

[101] I. Rampall, J. R. Smart, and D. T. Leighton, "The influence of surface roughness on the particle-pair distribution function of dilute suspensions of non-colloidal spheres in simple shear flow", *Journal of Fluid Mechanics*, vol. 339, pp. 1–24, 1997.

[102] F. R. DaCunha and E. J. Hinch, "Shear-induced dispersion in a dilute suspension of rough spheres", *Journal of Fluid Mechanics*, vol. 309, no. -1, p. 211, 1996.

[103] G. Drazer, J. Koplik, B. Khusid, and A. Acrivos, "Deterministic and stochastic behaviour of non-brownian spheres in sheared suspensions", *Journal of Fluid Mechanics*, vol. 460, pp. 307–335, 2002.

[104] G. Drazer, J. Koplik, B. Khusid, and A. Acrivos, "Microstructure and velocity fluctuations in sheared suspensions", *Journal of Fluid Mechanics*, vol. 511, pp. 237–263, 2004.

[105] A. Ardekani and R. Rangel, "Numerical investigation of particle–particle and particle–wall collisions in a viscous fluid", *Journal of Fluid Mechanics*, vol. 596, pp. 437–466, 2008.

[106] H. J. Wilson, "An analytic form for the pair distribution function and rheology of a dilute suspension of rough spheres in plane strain flow", *Journal of Fluid Mechanics*, vol. 534, pp. 97–114, 2005.

[107] A. Singh and P. R. Nott, "Normal stresses and microstructure in bounded sheared suspensions via Stokesian Dynamics simulations", *Journal of Fluid Mechanics*, vol. 412, pp. 279–301, 2000.

[108] P. A. Cundall and O. D. Strack, "A discrete numerical model for granular assemblies", *Geotechnique*, vol. 29, no. 1, pp. 47–65, 1979.

[109] S. Luding, "Cohesive, frictional powders: Contact models for tension", *Granular Matter*, vol. 10, no. 4, p. 235, 2008.

[110] J. Shäfer, S. Dippel, and D. Wolf, "Force schemes in simulations of granular materials", *Journal de Physique I*, vol. 6, no. 1, pp. 5–20, 1996.

[111] A. P. Shapiro and R. F. Probstein, "Random packings of spheres and fluidity limits of monodisperse and bidisperse suspensions", *Physical Review Letters*, vol. 68, no. 9, p. 1422, 1992.

[112] T. Lewis and L. Nielsen, "Viscosity of dispersed and aggregated suspensions of spheres", *Transactions of the Society of Rheology*, vol. 12, no. 3, pp. 421–443, 1968.

[113] C. S. O'hern, L. E. Silbert, A. J. Liu, and S. R. Nagel, "Jamming at zero temperature and zero applied stress: The epitome of disorder", *Physical Review E*, vol. 68, no. 1, p. 011 306, 2003.

[114] A. Lees and S. Edwards, "The computer study of transport processes under extreme conditions", *Journal of Physics C: Solid State Physics*, vol. 5, no. 15, p. 1921, 1972.

[115] F. Blanc, E. D'Ambrosio, L. Lobry, F. Peters, and E. Lemaire, "Universal scaling law in frictional non-brownian suspensions", *Physical Review Fluids*, vol. 3, no. 11, p. 114 303, 2018.

[116] A. Metzner, "Rheology of suspensions in polymeric liquids", *Journal of Rheology*, vol. 29, no. 6, pp. 739–775, 1985.

[117] A. Singh, R. Mari, M. M. Denn, and J. F. Morris, "A constitutive model for simple shear of dense frictional suspensions", *Journal of Rheology*, vol. 62, no. 2, pp. 457–468, 2018.

[118] R. V. More and A. M. Ardekani, "Effect of roughness on the rheology of concentrated non-brownian suspensions: A numerical study", *Journal of Rheology*, vol. 64, no. 1, pp. 67–80, 2019.

[119] D. Lootens, H. Van Damme, Y. Hémar, and P. Hébraud, "Dilatant flow of concentrated suspensions of rough particles", *Physical review letters*, vol. 95, no. 26, p. 268 302, 2005.

[120] J. Bender and N. J. Wagner, "Reversible shear thickening in monodisperse and bidisperse colloidal dispersions", *Journal of Rheology*, vol. 40, no. 5, pp. 899–916, 1996.

[121] E. Brown, N. A. Forman, C. S. Orellana, H. Zhang, B. W. Maynor, D. E. Betts, J. M. DeSimone, and H. M. Jaeger, "Generality of shear thickening in dense suspensions", *Nature materials*, vol. 9, no. 3, p. 220, 2010.

[122] B. Guy, M. Hermes, and W. C. Poon, "Towards a unified description of the rheology of hard-particle suspensions", *Physical review letters*, vol. 115, no. 8, p. 088 304, 2015.

[123] J. Mewis and N. J. Wagner, *Colloidal suspension rheology*. Cambridge University Press, 2012.

[124] F. Dintzis, M. Berhow, E. Bagley, Y. Wu, and F. Felker, "Shear-thickening behavior and shear-induced structure in gently solubilized starches", *Cereal chemistry*, vol. 73, no. 5, pp. 638–643, 1996.

[125] R. Williamson, "Some unusual properties of colloidal dispersions", *The Journal of Physical Chemistry*, vol. 35, no. 1, pp. 354–359, 1930.

[126] R. Williamson and W. Hecker, "Some properties of dispersions of the quicksand type", *Industrial & Engineering Chemistry*, vol. 23, no. 6, pp. 667–670, 1931.

[127] H. Freundlich and H. Röder, "Dilatancy and its relation to thixotropy", *Transactions of the Faraday Society*, vol. 34, pp. 308–316, 1938.

[128] A. Helz, "Viscosity studies of dickite suspensions", *Journal of the American Ceramic Society*, vol. 22, no. 1-12, pp. 289–301, 1939.

[129] E. da C Andrade and J. Fox, "The mechanism of dilatancy", *Proceedings of the Physical Society. Section B*, vol. 62, no. 8, p. 483, 1949.

[130] A. Metzner and M. Whitlock, "Flow behavior of concentrated (dilatant) suspensions", *Transactions of the Society of Rheology*, vol. 2, no. 1, pp. 239–254, 1958.

[131] R. Hoffman, "Discontinuous and dilatant viscosity behavior in concentrated suspensions. ii. theory and experimental tests", *Journal of Colloid and Interface Science*, vol. 46, no. 3, pp. 491–506, 1974.

[132] H. Hoffmann, H. Rehage, G. Platz, W. Schorr, H. Thurn, and W. Ulbricht, "Investigations on a detergent system with rodlike micelles", *Colloid and Polymer Science*, vol. 260, no. 11, pp. 1042–1056, 1982.

[133] N. J. Wagner and J. F. Brady, "Shear thickening in colloidal dispersions", *Physics Today*, vol. 62, no. 10, pp. 27–32, 2009.

[134] J. F. Brady and J. F. Morris, "Microstructure of strongly sheared suspensions and its impact on rheology and diffusion", *Journal of Fluid Mechanics*, vol. 348, pp. 103–139, 1997.

[135] S. Jamali, A. Boromand, N. Wagner, and J. Maia, "Microstructure and rheology of soft to rigid shear-thickening colloidal suspensions", *Journal of Rheology*, vol. 59, no. 6, pp. 1377–1395, 2015.

[136] D. P. Kalman and N. J. Wagner, "Microstructure of shear-thickening concentrated suspensions determined by flow-usans", *Rheologica acta*, vol. 48, no. 8, pp. 897–908, 2009.

[137] E. Brown and H. M. Jaeger, "Shear thickening in concentrated suspensions: Phenomenology, mechanisms and relations to jamming", *Reports on Progress in Physics*, vol. 77, no. 4, p. 046 602, 2014.

[138] N. Fernandez, R. Mani, D. Rinaldi, D. Kadau, M. Mosquet, H. Lombois-Burger, J. Cayer-Barrioz, H. J. Herrmann, N. D. Spencer, and L. Isa, "Microscopic mechanism for shear thickening of non-brownian suspensions", *Physical Review Letters*, vol. 111, no. 10, 2013.

[139] C. Heussinger, "Shear thickening in granular suspensions: Interparticle friction and dynamically correlated clusters", *Physical review E*, vol. 88, no. 5, p. 050 201, 2013.

[140] Z. Pan, H. de Cagny, M. Habibi, and D. Bonn, "Normal stresses in shear thickening granular suspensions", *Soft Matter*, vol. 13, no. 20, pp. 3734–3740, 2017.

[141] M. E. Cates and M. Wyart, "Granulation and bistability in non-Brownian suspensions", *Rheologica Acta*, vol. 53, no. 10-11, pp. 755–764, Nov. 2014.

[142] N. Y. Lin, B. M. Guy, M. Hermes, C. Ness, J. Sun, W. C. Poon, and I. Cohen, "Hydrodynamic and contact contributions to continuous shear thickening in colloidal suspensions", *Physical review letters*, vol. 115, no. 22, p. 228 304, 2015.

[143] Z. Pan, H. de Cagny, B. Weber, and D. Bonn, "S-shaped flow curves of shear thickening suspensions: Direct observation of frictional rheology", *Physical Review E*, vol. 92, no. 3, p. 032 202, 2015.

[144] J. F. Morris, "Lubricated-to-frictional shear thickening scenario in dense suspensions", *Physical Review Fluids*, vol. 3, p. 110 508, 2018.

[145] R. I. Tanner, "Aspects of non-colloidal suspension rheology", *Physics of Fluids*, vol. 30, no. 10, p. 101 301, 2018.

[146] T. Pöschel and T. Schwager, *Computational granular dynamics: models and algorithms*. Springer Science & Business Media, 2005.

[147] F. Radjaı and F. Dubois, *Discrete-element modeling of granular materials*. Wiley-Iste, 2011.

[148] S. Luding, "Cohesive, frictional powders: Contact models for tension", *Granular Matter*, vol. 10, no. 4, pp. 235–246, 2008.

[149] S. Pednekar, J. Chun, and J. F. Morris, "Bidisperse and polydisperse suspension rheology at large solid fraction", *Journal of Rheology*, vol. 62, no. 62, 2018.

[150] W. J. Frith, P. d'Haene, R. Buscall, and J. Mewis, "Shear thickening in model suspensions of sterically stabilized particles", *Journal of rheology*, vol. 40, no. 4, pp. 531–548, 1996.

[151] B. J. Maranzano and N. J. Wagner, "The effects of interparticle interactions and particle size on reversible shear thickening: Hard-sphere colloidal dispersions", *Journal of Rheology*, vol. 45, no. 5, pp. 1205–1222, 2001.

[152] B. J. Maranzano and N. J. Wagner, "The effects of particle size on reversible shear thickening of concentrated colloidal dispersions", *The Journal of chemical physics*, vol. 114, no. 23, pp. 10 514–10 527, 2001.

[153] A. Fall, A. Lemaitre, F. Bertrand, D. Bonn, and G. Ovarlez, "Shear thickening and migration in granular suspensions", *Physical review letters*, vol. 105, no. 26, p. 268 303, 2010.

[154] R. J. Larsen, J.-W. Kim, C. F. Zukoski, and D. A. Weitz, "Elasticity of dilatant particle suspensions during flow", *Physical Review E*, vol. 81, no. 1, p. 011 502, 2010.

[155] E. Brown and H. M. Jaeger, "The role of dilation and confining stresses in shear thickening of dense suspensions", *Journal of Rheology*, vol. 56, no. 4, pp. 875–923, 2012.

[156] C. D. Cwalina and N. J. Wagner, "Material properties of the shear-thickened state in concentrated near hard-sphere colloidal dispersions", *Journal of Rheology*, vol. 58, no. 4, pp. 949–967, 2014.

[157] H. Laun, "Normal stresses in extremely shear thickening polymer dispersions", *Journal of non-newtonian fluid mechanics*, vol. 54, pp. 87–108, 1994.

[158] B. K. Aral and D. M. Kalyon, "Viscoelastic material functions of noncolloidal suspensions with spherical particles", *Journal of Rheology*, vol. 41, no. 3, p. 599, 1998.

[159] M. Lee, M. Alcoutlabi, J. Magda, C. Dibble, M. Solomon, X. Shi, and G. McKenna, "The effect of the shear-thickening transition of model colloidal spheres on the sign of n 1 and on the radial pressure profile in torsional shear flows", *Journal of Rheology*, vol. 50, no. 3, pp. 293–311, 2006.

[160] J. R. Royer, D. L. Blair, and S. D. Hudson, “Rheological signature of frictional interactions in shear thickening suspensions”, *Physical review letters*, vol. 116, no. 18, p. 188 301, 2016.

[161] P. d’Haene, J. Mewis, and G. Fuller, “Scattering dichroism measurements of flow-induced structure of a shear thickening suspension”, *Journal of colloid and interface science*, vol. 156, no. 2, pp. 350–358, 1993.

[162] W. H. Boersma, J. Laven, and H. N. Stein, “Shear thickening (dilatancy) in concentrated dispersions”, *AIChE journal*, vol. 36, no. 3, pp. 321–332, 1990.

[163] D. Lootens, H. Van Damme, and P. Hébraud, “Giant stress fluctuations at the jamming transition”, *Physical review letters*, vol. 90, no. 17, p. 178 301, 2003.

[164] D. Lootens, P. Hébraud, E. Lécolier, and H. Van Damme, “Gelation, shear-thinning and shear-thickening in cement slurries”, *Oil & gas science and technology*, vol. 59, no. 1, pp. 31–40, 2004.

[165] P. Hébraud and D. Lootens, “Concentrated suspensions under flow: Shear-thickening and jamming”, *Modern Physics Letters B*, vol. 19, no. 13n14, pp. 613–624, 2005.

[166] S. Jamali and J. F. Brady, “Alternative frictional model for discontinuous shear thickening of dense suspensions: Hydrodynamics”, *Physical review letters*, vol. 123, no. 13, p. 138 002, 2019.

[167] M. Wang, S. Jamali, and J. F. Brady, “A hydrodynamic model for discontinuous shear-thickening in dense suspensions”, *Journal of Rheology*, vol. 64, no. 2, pp. 379–394, 2020.

[168] I. Bashkirtseva, A. Y. Zubarev, L. Y. Iskakova, and L. Ryashko, “On rheophysics of high-concentrated suspensions”, *Colloid journal*, vol. 71, no. 4, pp. 446–454, 2009.

[169] R. Mari, R. Seto, J. F. Morris, and M. M. Denn, “Nonmonotonic flow curves of shear thickening suspensions”, *Physical Review E*, vol. 91, no. 5, p. 052 302, 2015.

[170] M. Neuville, G. Bossis, J. Persello, O. Volkova, P. Boustingorry, and M. Mosquet, “Rheology of a gypsum suspension in the presence of different superplasticizers”, *Journal of rheology*, vol. 56, no. 2, pp. 435–451, 2012.

[171] M. Hermes, B. M. Guy, W. C. Poon, G. Poy, M. E. Cates, and M. Wyart, “Unsteady flow and particle migration in dense, non-brownian suspensions”, *Journal of Rheology*, vol. 60, no. 5, pp. 905–916, 2016.

[172] F. Peters, G. Ghigliotti, S. Gallier, F. Blanc, E. Lemaire, and L. Lobry, "Rheology of non-Brownian suspensions of rough frictional particles under shear reversal: A numerical study", *Journal of Rheology*, vol. 60, no. 4, pp. 715–732, 2016.

[173] A. Singh, C. Ness, R. Seto, J. J. de Pablo, and H. M. Jaeger, "Shear thickening and jamming of dense suspensions: The roll of friction", *arXiv preprint arXiv:2002.10996*, 2020.

[174] A. Sierou and J. F. Brady, "Accelerated stokesian dynamics simulation", *Journal of Fluid Mechanics*, vol. 118, no. 22, pp. 10 323–10 332, 2001.

[175] A. P. Shapiro and R. F. Probstein, "Random packings of spheres and fluidity limits of monodisperse and bidisperse suspensions", *Physical Review Letters*, vol. 68, no. 9, pp. 1422–1425, 1992.

[176] J. F. Morris and F. Boulay, "Curvilinear flows of noncolloidal suspensions: The role of normal stresses", *Journal of rheology*, vol. 43, no. 5, pp. 1213–1237, 1999.

[177] P. Mills and P. Snabre, "Apparent viscosity and particle pressure of a concentrated suspension of non-brownian hard spheres near the jamming transition", *The European Physical Journal E*, vol. 30, no. 3, pp. 309–316, 2009.

[178] C. D. Cwalina and N. J. Wagner, "Material properties of the shear-thickened state in concentrated near hard-sphere colloidal dispersions", *Journal of Rheology*, vol. 58, no. 4, pp. 949–967, 2014.

[179] C. Ness and J. Sun, "Shear thickening regimes of dense non-brownian suspensions", *Soft matter*, vol. 12, no. 3, pp. 914–924, 2016.

[180] E. Brown and H. M. Jaeger, "Dynamic jamming point for shear thickening suspensions", *PRL*, vol. 103, no. 8, p. 086 001, 2009.

[181] B. Guy, J. Richards, D. Hodgson, E. Blanco, and W. Poon, "Constraint-based approach to granular dispersion rheology", *Physical review letters*, vol. 121, no. 12, p. 128 001, 2018.

[182] J. R. Melrose and R. C. Ball, "Continuous shear thickening transitions in model concentrated colloids—The role of interparticle forces", *Journal of Rheology*, vol. 48, no. 5, pp. 937–960, 2004.

[183] R. L. Hoffman, "Discontinuous and dilatant viscosity behavior in concentrated suspensions III. Necessary conditions for their occurrence in viscometric flows", *Advances in Colloid and Interface Science*, vol. 17, no. 1, pp. 161–184, 1982.

[184] T. N. Phung, J. F. Brady, and G. Bossis, "Stokesian dynamics simulation of Brownian suspensions", *Journal of Fluid Mechanics*, vol. 313, pp. 181–207, 1996.

[185] J. F. Brady and D. R. Foss, "Structure, diffusion and rheology of Brownian suspensions by Stokesian Dynamics simulation", *Journal of Fluid Mechanics*, vol. 407, pp. 167–200, 2000.

[186] N. Nakajima and E. Harrell, "Rheology of pvc plastisol at instability region and beyond (proposal for super-high shear-rate coating)", *Journal of Elastomers & Plastics*, vol. 41, no. 3, pp. 277–285, 2009.

[187] D. P. Kalman, B. A. Rosen, and N. J. Wagner, "Effects of particle hardness on shear thickening colloidal suspension rheology", in *AIP Conference Proceedings*, vol. 1027, 2008, pp. 1408–1410.

[188] A. Vázquez-Quesada, R. I. Tanner, and M. Ellero, "Shear thinning of noncolloidal suspensions", *Physical review letters*, vol. 117, no. 10, p. 108 001, 2016.

[189] J. N. Israelachvili, *Intermolecular and surface forces.* Academic press, 2011.

[190] I. Szilagyi, G. Trefalt, A. Tiraferri, P. Maroni, and M. Borkovec, "Polyelectrolyte adsorption, interparticle forces, and colloidal aggregation", *Soft Matter*, vol. 10, no. 15, pp. 2479–2502, 2014.

[191] P. Richmond, "Electrical forces between particles with arbitrary fixed surface charge distributions in ionic solution", *Journal of the Chemical Society, Faraday Transactions 2: Molecular and Chemical Physics*, vol. 70, pp. 1066–1073, 1974.

[192] Richmond, "Electrical forces between particles with discrete periodic surface charge distributions in ionic solution", *Journal of the Chemical Society, Faraday Transactions 2: Molecular and Chemical Physics*, vol. 71, pp. 1154–1163, 1975.

[193] S. J. Miklavic, D. Y. Chan, L. R. White, and T. W. Healy, "Double layer forces between heterogeneous charged surfaces", *The Journal of Physical Chemistry*, vol. 98, no. 36, pp. 9022–9032, 1994.

[194] R. G. Bayer, *Mechanical wear prediction and prevention.* 1994.

[195] M. M. Maru and D. K. Tanaka, "Consideration of stribeck diagram parameters in the investigation on wear and friction behavior in lubricated sliding", *J. of the Brazilian Society of Mechanical Sciences and Engineering*, vol. 29, no. 1, pp. 55–62, 2007.

[196] I. Hutchings and P. Shipway, *Tribology: friction and wear of engineering materials.* Butterworth-Heinemann, 2017.

[197] M. J. Neale, *The tribology handbook*. Elsevier, 1995.

[198] J. J. Adler, Y. I. Rabinovich, and B. M. Moudgil, "Origins of the non-dlvo force between glass surfaces in aqueous solution", *Journal of colloid and interface science*, vol. 237, no. 2, pp. 249–258, 2001.

[199] H. Kamiya, K. Gotoh, M. Shimada, T. Uchikoshi, Y. Otani, M. Fuji, S. Matsusaka, T. Matsuyama, J. Tatami, K. Higashitani, *et al.*, "Characteristics and behavior of nanoparticles and its dispersion systems", in *Nanoparticle technology handbook*, Elsevier, 2008, pp. 113–176.

[200] Y. Diao and R. M. Espinosa-Marzal, "Molecular insight into the nanoconfined calcite–solution interface", *Proceedings of the National Academy of Sciences*, vol. 113, no. 43, pp. 12 047–12 052, 2016.

[201] D. F. Parsons, R. B. Walsh, and V. S. Craig, "Surface forces: Surface roughness in theory and experiment", *The Journal of chemical physics*, vol. 140, no. 16, p. 164 701, 2014.

[202] N. Eom, D. F. Parsons, and V. S. Craig, "Roughness in surface force measurements: Extension of dlvo theory to describe the forces between hafnia surfaces", *The Journal of Physical Chemistry B*, vol. 121, no. 26, pp. 6442–6453, 2017.

[203] M. Ramaswamy, N. Y. Lin, B. D. Leahy, C. Ness, A. M. Fiore, J. W. Swan, and I. Cohen, "How confinement-induced structures alter the contribution of hydrodynamic and short-ranged repulsion forces to the viscosity of colloidal suspensions", *PRX*, vol. 7, no. 4, p. 041 005, 2017.

[204] M. Rintoul and S. Torquato, "Computer simulations of dense hard-sphere systems", *The Journal of chemical physics*, vol. 105, no. 20, pp. 9258–9265, 1996.

[205] R. Mari, R. Seto, J. F. Morris, and M. M. Denn, "Discontinuous shear thickening in brownian suspensions by dynamic simulation", *Proceedings of the National Academy of Sciences*, vol. 112, no. 50, pp. 15 326–15 330, 2015.

[206] Y. S. Lee and N. J. Wagner, "Rheological properties and small-angle neutron scattering of a shear thickening, nanoparticle dispersion at high shear rates", *Industrial & engineering chemistry research*, vol. 45, no. 21, pp. 7015–7024, 2006.

[207] Y. S. Lee, E. D. Wetzel, and N. J. Wagner, "The ballistic impact characteristics of kevlar® woven fabrics impregnated with a colloidal shear thickening fluid", *Journal of materials science*, vol. 38, no. 13, pp. 2825–2833, 2003.

[208] E. Brown, N. Rodenberg, J. Amend, A. Mozeika, E. Steltz, M. R. Zakin, H. Lipson, and H. M. Jaeger, "Universal robotic gripper based on the jamming of granular ma-

terial", *Proceedings of the National Academy of Sciences*, vol. 107, no. 44, pp. 18 809–18 814, 2010.

[209] J. Gao, P. M. Mwasame, and N. J. Wagner, "Thermal rheology and microstructure of shear thickening suspensions of silica nanoparticles dispersed in the ionic liquid [c4mim][bf4]", *Journal of Rheology*, vol. 61, no. 3, pp. 525–535, 2017.

[210] J. S. Turner and I. H. Campbell, "Convection and mixing in magma chambers", *Earth-Science Reviews*, vol. 23, no. 4, pp. 255–352, 1986.

[211] S. MacIntyre, A. L. Alldredge, and C. C. Gotschalk, "Accumulation of marines now at density discontinuities in the water column", *Limnology and Oceanography*, vol. 40, no. 3, pp. 449–468, 1995.

[212] E. Bigg, "Atmospheric stratification revealed by twilight scattering", *Tellus*, vol. 16, no. 1, pp. 76–83, 1964.

[213] S. A. Balbus and N. Soker, "Resonant excitation of internal gravity waves in cluster cooling flows", *The Astrophysical Journal*, vol. 357, pp. 353–366, 1990.

[214] W. W. Kellogg, "Aerosols and climate", in *Interactions of Energy and Climate*, Springer, 1980, pp. 281–303.

[215] Y. Abbassi, H. Ahmadikia, and E. Baniasadi, "Prediction of pollution dispersion under urban heat island circulation for different atmospheric stratification", *Building and Environment*, vol. 168, p. 106 374, 2020.

[216] H. Fernando, S. Lee, J. Anderson, M. Princevac, E. Pardyjak, and S. Grossman-Clarke, "Urban fluid mechanics: Air circulation and contaminant dispersion in cities", *Environmental fluid mechanics*, vol. 1, no. 1, pp. 107–164, 2001.

[217] H. S. Auta, C. Emenike, and S. Fauziah, "Distribution and importance of microplastics in the marine environment: A review of the sources, fate, effects, and potential solutions", *Environment international*, vol. 102, pp. 165–176, 2017.

[218] A. L. Alldredge, T. J. Cowles, S. MacIntyre, J. E. Rines, P. L. Donaghay, C. F. Greenlaw, D. Holliday, M. M. Dekshenieks, J. M. Sullivan, and J. R. V. Zaneveld, "Occurrence and mechanisms of formation of a dramatic thin layer of marine snow in a shallow pacific fjord", *Marine Ecology Progress Series*, vol. 233, pp. 1–12, 2002.

[219] R. Lindsey, M. Scott, and R. Simmon, "What are phytoplankton", *NASA's Earth Observatory*, 2010.

[220] A. L. Alldredge and C. Gotschalk, "Direct observations of the mass flocculation of diatom blooms: Characteristics, settling velocities and formation of diatom aggre-

gates", *Deep Sea Research Part A. Oceanographic Research Papers*, vol. 36, no. 2, pp. 159–171, 1989.

[221] J. Harwood, "Mass die-offs", *Encyclopedia of Marine Mammals, edited by WF Perrin, B. Würsig, and JGM Thewissen (Academic Press, San Diego)*, pp. 724–726, 2002.

[222] K. G. Sellner, G. J. Doucette, and G. J. Kirkpatrick, "Harmful algal blooms: Causes, impacts and detection", *Journal of Industrial Microbiology and Biotechnology*, vol. 30, no. 7, pp. 383–406, 2003.

[223] T. Bewley and G. Meneghello, "Efficient coordination of swarms of sensor-laden balloons for persistent, in situ, real-time measurement of hurricane development", *Physical Review Fluids*, vol. 1, no. 6, p. 060 507, 2016.

[224] T. Jephson and P. Carlsson, "Species-and stratification-dependent diel vertical migration behaviour of three dinoflagellate species in a laboratory study", *Journal of plankton research*, vol. 31, no. 11, pp. 1353–1362, 2009.

[225] S. Wang and A. M. Ardekani, "Biogenic mixing induced by intermediate reynolds number swimming in stratified fluids", *Scientific reports*, vol. 5, p. 17 448, 2015.

[226] I. A. Houghton, J. R. Koseff, S. G. Monismith, and J. O. Dabiri, "Vertically migrating swimmers generate aggregation-scale eddies in a stratified column", *Nature*, vol. 556, no. 7702, pp. 497–500, 2018.

[227] R. Ouillon, I. Houghton, J. Dabiri, and E. Meiburg, "Active swimmers interacting with stratified fluids during collective vertical migration", *Journal of Fluid Mechanics*, vol. 902, 2020.

[228] M. Bormans and S. A. Condie, "Modelling the distribution of anabaena and melosira in a stratified river weir pool", *Hydrobiologia*, vol. 364, no. 1, pp. 3–13, 1997.

[229] J. S. Turner and J. S. Turner, *Buoyancy effects in fluids*. Cambridge university press, 1979.

[230] P. F. Linden, "The fluid mechanics of natural ventilation", *Annual review of fluid mechanics*, vol. 31, no. 1, pp. 201–238, 1999.

[231] R. V. More, M. N. Ardekani, L. Brandt, and A. M. Ardekani, "Orientation instability of settling spheroids in a linearly density-stratified fluid", *Journal of Fluid Mechanics*, vol. 929, A7, 2021.

[232] R. Dandekar, V. A. Shaik, and A. M. Ardekani, "Motion of an arbitrarily shaped particle in a density stratified fluid", *Journal of Fluid Mechanics*, vol. 890, 2020.

[233] M. M. Mrokowska, “Dynamics of thin disk settling in two-layered fluid with density transition”, *Acta Geophysica*, vol. 68, no. 4, pp. 1145–1160, 2020.

[234] M. J. Mercier, S. Wang, J. Péméja, P. Ern, and A. M. Ardekani, “Settling disks in a linearly stratified fluid”, *Journal of Fluid Mechanics*, vol. 885, 2020.

[235] J. Magnaudet and M. J. Mercier, “Particles, drops, and bubbles moving across sharp interfaces and stratified layers”, *Annual Review of Fluid Mechanics*, vol. 52, pp. 61–91, 2020.

[236] A. M. Ardekani, A. Doostmohammadi, and N. Desai, “Transport of particles, drops, and small organisms in density stratified fluids”, *Physical Review Fluids*, vol. 2, no. 10, p. 100 503, 2017.

[237] J. Zhang, M. J. Mercier, and J. Magnaudet, “Core mechanisms of drag enhancement on bodies settling in a stratified fluid”, *Journal of Fluid Mechanics*, vol. 875, pp. 622–656, 2019.

[238] A. Ardekani and R. Stocker, “Stratlets: Low reynolds number point-force solutions in a stratified fluid”, *Physical review letters*, vol. 105, no. 8, p. 084 502, 2010.

[239] I. Proudman and J. Pearson, “Expansions at small reynolds numbers for the flow past a sphere and a circular cylinder”, *Journal of Fluid Mechanics*, vol. 2, no. 3, pp. 237–262, 1957.

[240] R. Mehaddi, F. Candelier, and B. Mehlig, “Inertial drag on a sphere settling in a stratified fluid”, *Journal of Fluid Mechanics*, vol. 855, pp. 1074–1087, 2018.

[241] V. A. Shaik and A. M. Ardekani, “Drag, deformation, and drift volume associated with a drop rising in a density stratified fluid”, *Physical Review Fluids*, vol. 5, no. 1, p. 013 604, 2020.

[242] R. Camassa, C. Falcon, J. Lin, R. M. McLaughlin, and N. Mykins, “A first-principle predictive theory for a sphere falling through sharply stratified fluid at low reynolds number”, *Journal of Fluid Mechanics*, vol. 664, pp. 436–465, 2010.

[243] H. H. Arrowood, “Oil droplets rising through density-stratified fluid at low reynolds number”, Ph.D. dissertation, The University of North Carolina at Chapel Hill, 2018.

[244] R. Camassa, S. Khatri, R. M. McLaughlin, J. C. Prairie, B. White, and S. Yu, “Retention and entrainment effects: Experiments and theory for porous spheres settling in sharply stratified fluids”, *Physics of Fluids*, vol. 25, no. 8, p. 081 701, 2013.

[245] A. K. Varanasi, N. K. Marath, and G. Subramanian, "The rotation of a sedimenting spheroidal particle in a linearly stratified fluid", *Journal of Fluid Mechanics*, vol. 933, 2022.

[246] A. Doostmohammadi, S. Dabiri, and A. M. Ardekani, "A numerical study of the dynamics of a particle settling at moderate reynolds numbers in a linearly stratified fluid", *Journal of Fluid Mechanics*, vol. 750, p. 5, 2014.

[247] A. Doostmohammadi, R. Stocker, and A. M. Ardekani, "Low-reynolds-number swimming at pycnoclines", *Proceedings of the National Academy of Sciences*, vol. 109, no. 10, pp. 3856–3861, 2012.

[248] D. W. Martin and F. Blanchette, "Simulations of surfactant-laden drops rising in a density-stratified medium", *Physical Review Fluids*, vol. 2, no. 2, p. 023 602, 2017.

[249] M. Ganesh, S. Kim, and S. Dabiri, "Induced mixing in stratified fluids by rising bubbles in a thin gap", *Physical Review Fluids*, vol. 5, no. 4, p. 043 601, 2020.

[250] Q. Lin, W. Lindberg, D. Boyer, and H. Fernando, "Stratified flow past a sphere", *Journal of Fluid Mechanics*, vol. 240, pp. 315–354, 1992.

[251] R. More and S. Balasubramanian, "Mixing dynamics in double-diffusive convective stratified fluid layers", *Curr. Sci*, vol. 114, pp. 1953–1960, 2018.

[252] A. Srdić-Mitrović, N. Mohamed, and H. Fernando, "Gravitational settling of particles through density interfaces", *Journal of Fluid Mechanics*, vol. 381, pp. 175–198, 1999.

[253] S. Okino, S. Akiyama, and H. Hanazaki, "Velocity distribution around a sphere descending in a linearly stratified fluid", *Journal of Fluid Mechanics*, vol. 826, pp. 759–780, 2017.

[254] J. Chomaz, P. Bonneton, A. Butet, M. Perrier, and E. Hopfinger, "Froude number dependence of the flow separation line on a sphere towed in a stratified fluid", *Physics of Fluids A: Fluid Dynamics*, vol. 4, no. 2, pp. 254–258, 1992.

[255] H. Hanazaki, K. Kashimoto, and T. Okamura, "Jets generated by a sphere moving vertically in a stratified fluid", *Journal of fluid mechanics*, vol. 638, pp. 173–197, 2009.

[256] T. L. Mandel, L. Waldrop, M. Theillard, D. Kleckner, S. Khatri, *et al.*, "Retention of rising droplets in density stratification", *Physical Review Fluids*, vol. 5, no. 12, p. 124 803, 2020.

[257] A. G. Liu, D. Mcllroy, and M. D. Brasier, "First evidence for locomotion in the ediacara biota from the 565 ma mistaken point formation, newfoundland", *Geology*, vol. 38, no. 2, pp. 123–126, 2010.

[258] R. Baker, *Evolutionary ecology of animal migration.* Holmes & Meier Publishers, 1978.

[259] H. C. Berg, *Random walks in biology.* Princeton University Press, 1993.

[260] S. A. Isard and S. H. Gage, *Flow of Life in the Atmosphere.* Michigan State University Press, 2001.

[261] A. M. Ardekani, A. Doostmohammadi, and N. Desai, "Transport of particles, drops, and small organisms in density stratified fluids", *Physical Review Fluids*, vol. 2, no. 10, p. 100 503, 2017.

[262] S. Childress, *Mechanics of swimming and flying.* Cambridge University Press, 1981, vol. 2.

[263] B. S. Beckett, *Biology: a modern introduction.* Oxford University Press, USA, 1986.

[264] C. Brennen and H. Winet, "Fluid mechanics of propulsion by cilia and flagella", *Annual Review of Fluid Mechanics*, vol. 9, no. 1, pp. 339–398, 1977.

[265] K. Drescher, K. C. Leptos, I. Tuval, T. Ishikawa, T. J. Pedley, and R. E. Goldstein, "Dancing volvox: Hydrodynamic bound states of swimming algae", *Physical Review Letters*, vol. 102, no. 16, p. 168 101, 2009.

[266] L. N. Wickramarathna, C. Noss, and A. Lorke, "Hydrodynamic trails produced by daphnia: Size and energetics", *PloS one*, vol. 9, no. 3, 2014.

[267] T. Ishikawa and M. Hota, "Interaction of two swimming paramecia", *Journal of Experimental Biology*, vol. 209, no. 22, pp. 4452–4463, 2006.

[268] T. Kiørboe, H. Jiang, and S. P. Colin, "Danger of zooplankton feeding: The fluid signal generated by ambush-feeding copepods", *Proceedings of the Royal Society B: Biological Sciences*, vol. 277, no. 1698, pp. 3229–3237, 2010.

[269] J. Lighthill, "Flagellar hydrodynamics", *SIAM review*, vol. 18, no. 2, pp. 161–230, 1976.

[270] A. Shapere and F. Wilczek, "Efficiencies of self-propulsion at low reynolds number", *Journal of fluid mechanics*, vol. 198, pp. 587–599, 1989.

[271] M. Lighthill, "On the squirming motion of nearly spherical deformable bodies through liquids at very small reynolds numbers", *Communications on Pure and Applied Mathematics*, vol. 5, no. 2, pp. 109–118, 1952.

[272] J. R. Blake, "A spherical envelope approach to ciliary propulsion", *Journal of Fluid Mechanics*, vol. 46, no. 1, pp. 199–208, 1971.

[273] V. Magar, T. Goto, and T. Pedley, "Nutrient uptake by a self-propelled steady squirmer", *The Quarterly Journal of Mechanics and Applied Mathematics*, vol. 56, no. 1, pp. 65–91, 2003.

[274] T. Ishikawa and T. Pedley, "The rheology of a semi-dilute suspension of swimming model micro-organisms", *Journal of Fluid Mechanics*, vol. 588, pp. 399–435, 2007.

[275] J.-L. Thiffeault and S. Childress, "Stirring by swimming bodies", *Physics Letters A*, vol. 374, no. 34, pp. 3487–3490, 2010.

[276] L. Zhu, E. Lauga, and L. Brandt, "Self-propulsion in viscoelastic fluids: Pushers vs. pullers", *Physics of fluids*, vol. 24, no. 5, p. 051 902, 2012.

[277] S. Wang and A. Ardekani, "Inertial squirmer", *Physics of Fluids*, vol. 24, no. 10, p. 101 902, 2012.

[278] A. S. Khair and N. G. Chisholm, "Expansions at small reynolds numbers for the locomotion of a spherical squirmer", *Physics of Fluids*, vol. 26, no. 1, p. 011 902, 2014.

[279] N. G. Chisholm, D. Legendre, E. Lauga, and A. S. Khair, "A squirmer across reynolds numbers", *Journal of Fluid Mechanics*, vol. 796, pp. 233–256, 2016.

[280] G. Li, A. Ostace, and A. M. Ardekani, "Hydrodynamic interaction of swimming organisms in an inertial regime", *Physical Review E*, vol. 94, no. 5, pp. 1–8, 2016.

[281] B. S. Sherman, I. T. Webster, G. J. Jones, and R. L. Oliver, "Transitions between auhcoseira and anabaena dominance in a turbid river weir pool", *Limnology and oceanography*, vol. 43, no. 8, pp. 1902–1915, 1998.

[282] J. E. Cloern, B. E. Cole, R. L. Wong, and A. E. Alpine, "Temporal dynamics of estuarine phytoplankton: A case study of san francisco bay", in *Temporal Dynamics of an Estuary: San Francisco Bay*, Springer, 1985, pp. 153–176.

[283] M. Z. Jacobson and M. Z. Jacobson, *Fundamentals of atmospheric modeling*. Cambridge university press, 2005.

[284] A. Ardekani and R. Stocker, "Stratlets: Low reynolds number point-force solutions in a stratified fluid", *Physical review letters*, vol. 105, no. 8, p. 084 502, 2010.

[285] B. J. Gemmell, H. Jiang, and E. J. Buskey, "A tale of the ciliate tail: Investigation into the adaptive significance of this sub-cellular structure", *Proceedings of the Royal Society B: Biological Sciences*, vol. 282, no. 1812, p. 20 150 770, 2015.

[286] J. S. Guasto, R. Rusconi, and R. Stocker, "Fluid mechanics of planktonic microorganisms", *Annual Review of Fluid Mechanics*, vol. 44, pp. 373–400, 2012.

[287] W. Harder, "Reactions of plankton organisms to water stratification", *Limnology and Oceanography*, vol. 13, no. 1, pp. 156–168, 1968.

[288] D. Viličić, T. Legović, and V. Žutić, "Vertical distribution of phytoplankton in a stratified estuary", *Aquatic Sciences*, vol. 51, no. 1, pp. 31–46, 1989.

[289] P. Hershberger, J. Rensel, A. Matter, and F. Taub, "Vertical distribution of the chloromonad flagellate heterosigma carterae in columns: Implications for bloom development", *Canadian journal of fisheries and aquatic sciences*, vol. 54, no. 10, pp. 2228–2234, 1997.

[290] C. Noss and A. Lorke, "Zooplankton induced currents and fluxes in stratified waters", *Water Quality Research Journal of Canada*, vol. 47, no. 3-4, pp. 276–286, 2012.

[291] C. Noss and A. Lorke, "Direct observation of biomixing by vertically migrating zooplankton", *Limnology and oceanography*, vol. 59, no. 3, pp. 724–732, 2014.

[292] S. Wang and A. M. Ardekani, "Biogenic mixing induced by intermediate Reynolds number swimming in stratified fluids", *Scientific Reports*, vol. 5, 2015.

[293] A. Doostmohammadi, R. Stocker, and A. M. Ardekani, "Low-reynolds-number swimming at pycnoclines", *Proceedings of the National Academy of Sciences*, vol. 109, no. 10, pp. 3856–3861, 2012.

[294] R. Dandekar, V. A. Shaik, and A. M. Ardekani, "Swimming sheet in a density-stratified fluid", *Journal of Fluid Mechanics*, vol. 874, pp. 210–234, 2019.

[295] R. Glowinski, T.-W. Pan, T. I. Hesla, D. D. Joseph, and J. Periaux, "A fictitious domain approach to the direct numerical simulation of incompressible viscous flow past moving rigid bodies: Application to particulate flow", *Journal of Computational Physics*, vol. 169, no. 2, pp. 363–426, 2001.

[296] N. Sharma, Y. Chen, and N. A. Patankar, "A distributed lagrange multiplier based computational method for the simulation of particulate-Stokes flow", *Computer Methods in Applied Mechanics and Engineering*, vol. 194, no. 45-47, pp. 4716–4730, 2005.

[297] A. M. Ardekani, S. Dabiri, and R. H. Rangel, "Collision of multi-particle and general shape objects in a viscous fluid", *Journal of Computational Physics*, vol. 227, no. 24, pp. 10 094–10 107, 2008.

[298] A. M. Ardekani and R. H. Rangel, “Numerical investigation of particle–particle and particle–wall collisions in a viscous fluid”, *Journal of Fluid Mechanics*, vol. 596, pp. 437–466, 2008.

[299] A. Doostmohammadi, S. Dabiri, and A. M. Ardekani, “A numerical study of the dynamics of a particle settling at moderate Reynolds numbers in a linearly stratified fluid”, *Journal of Fluid Mechanics*, vol. 750, pp. 5–32, 2014.

[300] W. Aniszewski, T. Arrufat, M. Crialesi-Esposito, S. Dabiri, D. Fuster, Y. Ling, J. Lu, L. Malan, S. Pal, R. Scardovelli, and G. Tryggvason, “Parallel, robust, interface simulator (paris)”, 2019.

[301] B. P. Leonard, “A stable and accurate convective modelling procedure based on quadratic upstream interpolation”, *Computer methods in applied mechanics and engineering*, vol. 19, no. 1, pp. 59–98, 1979.

[302] T. Pedley, “Spherical squirmers: Models for swimming micro-organisms”, *IMA Journal of Applied Mathematics*, vol. 81, no. 3, pp. 488–521, 2016.

[303] G.-J. Li and A. M. Ardekani, “Hydrodynamic interaction of microswimmers near a wall”, *Physical Review E*, vol. 90, no. 1, p. 013 010, 2014.

[304] S. Wang and A. Ardekani, “Unsteady swimming of small organisms”, *Journal of Fluid Mechanics*, vol. 702, pp. 286–297, 2012.

[305] C. Boyd and D. Gradmann, “Impact of osmolytes on buoyancy of marine phytoplankton”, *Marine Biology*, vol. 141, no. 4, pp. 605–618, 2002.

[306] F. J. Sartoris, D. N. Thomas, A. Cornils, and S. B. S. Schiela, “Buoyancy and diapause in antarctic copepods: The role of ammonium accumulation”, *Limnology and oceanography*, vol. 55, no. 5, pp. 1860–1864, 2010.

[307] A. E. Walsby, “Gas vesicles.”, *Microbiology and Molecular Biology Reviews*, vol. 58, no. 1, pp. 94–144, 1994.

[308] T. A. Villareal and E. Carpenter, “Buoyancy regulation and the potential for vertical migration in the oceanic cyanobacterium trichodesmium”, *Microbial ecology*, vol. 45, no. 1, pp. 1–10, 2003.

[309] N. Sanders and J. Childress, “Ion replacement as a buoyancy mechanism in a pelagic deep-sea crustacean”, *Journal of Experimental Biology*, vol. 138, no. 1, pp. 333–343, 1988.

[310] M. Bayareh, A. Doostmohammadi, S. Dabiri, and A. Ardekani, “On the rising motion of a drop in stratified fluids”, *Physics of Fluids*, vol. 25, no. 10, p. 023 029, 2013.

[311] K. Banse, "On the vertical distribution of zooplankton in the sea", *Progress in oceanography*, vol. 2, pp. 53–125, 1964.

[312] J. Luo, P. B. Ortner, D. Forcucci, and S. R. Cummings, "Diel vertical migration of zooplankton and mesopelagic fish in the arabian sea", *Deep Sea Research Part II: Topical Studies in Oceanography*, vol. 47, no. 7-8, pp. 1451–1473, 2000.

[313] D. K. Steinberg, B. A. Van Mooy, K. O. Buesseler, P. W. Boyd, T. Kobari, and D. M. Karl, "Bacterial vs. zooplankton control of sinking particle flux in the ocean's twilight zone", *Limnology and Oceanography*, vol. 53, no. 4, pp. 1327–1338, 2008.

[314] N. Hill and T. Pedley, "Bioconvection", *Fluid Dynamics Research*, vol. 37, no. 1-2, p. 1, 2005.

[315] N. G. Chisholm and A. S. Khair, "Partial drift volume due to a self-propelled swimmer", *Physical Review Fluids*, vol. 3, no. 1, p. 014 501, 2018.

[316] M. Rahmani and A. Wachs, "Free falling and rising of spherical and angular particles", *Physics of Fluids*, vol. 26, no. 8, p. 083 301, 2014.

[317] W. K. Dewar, R. J. Bingham, R. Iverson, D. P. Nowacek, L. C. St Laurent, and P. H. Wiebe, "Does the marine biosphere mix the ocean?", *Journal of Marine Research*, vol. 64, no. 4, pp. 541–561, 2006.

[318] A. W. Visser, "Biomixing of the oceans?", *SCIENCE-NEW YORK THEN WASHINGTON-*, vol. 316, no. 5826, p. 838, 2007.

[319] K. Katija and J. O. Dabiri, "A viscosity-enhanced mechanism for biogenic ocean mixing", *Nature*, vol. 460, no. 7255, pp. 624–626, 2009.

[320] K. Katija, "Biogenic inputs to ocean mixing", *Journal of Experimental Biology*, vol. 215, no. 6, pp. 1040–1049, 2012.

[321] E. Kunze, "Biologically generated mixing in the ocean", *Annual review of marine science*, vol. 11, pp. 215–226, 2019.

[322] G. L. Wagner, W. R. Young, and E. Lauga, "Mixing by microorganisms in stratified fluids", *Journal of Marine Research*, vol. 72, no. 2, pp. 47–72, 2014.

[323] C. Dombrowski, L. Cisneros, S. Chatkaew, R. E. Goldstein, and J. O. Kessler, "Self-concentration and large-scale coherence in bacterial dynamics", *Physical review letters*, vol. 93, no. 9, p. 098 103, 2004.

[324] H. H. Wensink, J. Dunkel, S. Heidenreich, K. Drescher, R. E. Goldstein, H. Löwen, and J. M. Yeomans, "Meso-scale turbulence in living fluids", *Proceedings of the National Academy of Sciences*, vol. 109, no. 36, pp. 14 308–14 313, 2012.

[325] A. Sokolov, I. S. Aranson, J. O. Kessler, and R. E. Goldstein, "Concentration dependence of the collective dynamics of swimming bacteria", *Physical review letters*, vol. 98, no. 15, p. 158 102, 2007.

[326] X.-L. Wu and A. Libchaber, "Particle diffusion in a quasi-two-dimensional bacterial bath", *Phys. Rev. Lett.*, vol. 84, pp. 3017–3020, 13 Mar. 2000.

[327] F. E. Fish, "Kinematics of ducklings swimming in formation: Consequences of position", *Journal of Experimental Zoology*, vol. 273, no. 1, pp. 1–11, 1995.

[328] D. Saintillan and M. J. Shelley, "Orientational order and instabilities in suspensions of self-locomoting rods", *Physical review letters*, vol. 99, no. 5, p. 058 102, 2007.

[329] E. Lushi, H. Wioland, and R. E. Goldstein, "Fluid flows created by swimming bacteria drive self-organization in confined suspensions", *Proceedings of the National Academy of Sciences*, vol. 111, no. 27, pp. 9733–9738, 2014.

[330] A. T. Chwang and T. Y.-T. Wu, "Hydromechanics of low-reynolds-number flow. part 2. singularity method for stokes flows", *Journal of Fluid mechanics*, vol. 67, no. 4, pp. 787–815, 1975.

[331] X. Chen, X. Yang, M. Yang, and H. Zhang, "Dynamic clustering in suspension of motile bacteria", *EPL (Europhysics Letters)*, vol. 111, no. 5, p. 54 002, 2015.

[332] A. P. Petroff, X.-L. Wu, and A. Libchaber, "Fast-moving bacteria self-organize into active two-dimensional crystals of rotating cells", *Physical review letters*, vol. 114, no. 15, p. 158 102, 2015.

[333] T. Ishikawa, M. Simmonds, and T. J. Pedley, "Hydrodynamic interaction of two swimming model micro-organisms", *Journal of Fluid Mechanics*, vol. 568, pp. 119–160, 2006.

[334] I. O. Götze and G. Gompper, "Mesoscale simulations of hydrodynamic squirmer interactions", *Physical Review E*, vol. 82, no. 4, p. 041 921, 2010.

[335] T. Ishikawa, G. Sekiya, Y. Imai, and T. Yamaguchi, "Hydrodynamic interactions between two swimming bacteria", *Biophysical journal*, vol. 93, no. 6, pp. 2217–2225, 2007.

[336] G. Alexander, C. Pooley, and J. Yeomans, "Scattering of low-reynolds-number swimmers", *Physical Review E*, vol. 78, no. 4, p. 045 302, 2008.

[337] A. Furukawa, D. Marenduzzo, and M. E. Cates, “Activity-induced clustering in model dumbbell swimmers: The role of hydrodynamic interactions”, *Physical Review E*, vol. 90, no. 2, p. 022 303, 2014.

[338] R. Maniyeri and S. Kang, “Hydrodynamic interaction between two swimming bacterial flagella in a viscous fluid–a numerical study using an immersed boundary method”, *Progress in Computational Fluid Dynamics, an International Journal*, vol. 14, no. 6, pp. 375–385, 2014.

[339] C. Pooley, G. Alexander, and J. Yeomans, “Hydrodynamic interaction between two swimmers at low reynolds number”, *Physical review letters*, vol. 99, no. 22, p. 228 103, 2007.

[340] G. J. Elfring and E. Lauga, “Hydrodynamic phase locking of swimming microorganisms”, *Physical review letters*, vol. 103, no. 8, p. 088 101, 2009.

[341] H. Yamazaki and K. D. Squires, “Comparison of oceanic turbulence and copepod swimming”, *Marine Ecology Progress Series*, vol. 144, pp. 299–301, 1996.

[342] R. V. More and A. M. Ardekani, “Motion of an inertial squirmer in a density stratified fluid”, *Journal of Fluid Mechanics*, vol. under review, pp. –, 2020.

[343] G.-J. Li, A. Karimi, and A. M. Ardekani, “Effect of solid boundaries on swimming dynamics of microorganisms in a viscoelastic fluid”, *Rheologica acta*, vol. 53, no. 12, pp. 911–926, 2014.

[344] J. Boussinesq, “Sur la résistance qu’oppose... soient négligeables”, *CR Acad. Sci*, 1985.

[345] A. B. Basset, *A treatise on hydrodynamics: with numerous examples.* Deighton, Bell and Company, 1888, vol. 2.

[346] R. Gatignol *et al.*, “The faxén formulae for a rigid particle in an unsteady non-uniform stokes flow”, 1983.

[347] M. R. Maxey and J. J. Riley, “Equation of motion for a small rigid sphere in a nonuniform flow”, *The Physics of Fluids*, vol. 26, no. 4, pp. 883–889, 1983.

[348] J. Magnaudet, “The forces acting on bubbles and rigid particles”, in *ASME Fluids Engineering Division Summer Meeting, FEDSM*, vol. 97, 1997, pp. 22–26.

[349] J. Magnaudet and M. J. Mercier, “Particles, Drops, and Bubbles Moving Across Sharp Interfaces and Stratified Layers”, 2019.

[350] K. E. Lofquist and L. P. Purtell, “Drag on a sphere moving horizontally through a stratified liquid”, *Journal of Fluid Mechanics*, vol. 148, pp. 271–284, 1984.

[351] K. Y. Yick, C. R. Torres, T. Peacock, and R. Stocker, "Enhanced drag of a sphere settling in a stratified fluid at small reynolds numbers", *Journal of Fluid Mechanics*, vol. 632, pp. 49–68, 2009.

[352] C. R. Torres, H. HANAZAKI, J. OCHOA, J. Castillo, and M. Van Woert, "Flow past a sphere moving vertically in a stratified diffusive fluid", *Journal of Fluid Mechanics*, vol. 417, pp. 211–236, 2000.

[353] H. Hanazaki, K. Konishi, and T. Okamura, "Schmidt-number effects on the flow past a sphere moving vertically in a stratified diffusive fluid", *Physics of Fluids*, vol. 21, no. 2, p. 026 602, 2009.

[354] H. Hanazaki, K. Kashimoto, and T. Okamura, "Jets generated by a sphere moving vertically in a stratified fluid", *Journal of fluid mechanics*, vol. 638, pp. 173–197, 2009.

[355] R. Cas and J. Wright, "Volcanic successions: Ancient and modern", *Allen and Unin, London*, 1987.

[356] R. V. More and A. M. Ardekani, "Hydrodynamic interactions between swimming microorganisms in a linearly density stratified fluid (under review)", *Physical Review E*, 2020.

[357] R. V. More and A. M. Ardekani, "Motion of an inertial squirmer in a density stratified fluid", *Journal of Fluid Mechanics*, vol. 905, 2020.

[358] J. Cloern, "Temporal dynamics and ecological significance of salinity stratification in an estuary (south san-francisco bay, usa)", *Oceanologica Acta*, vol. 7, no. 1, pp. 137–141, 1984.

[359] T. Naganuma, "Calanoid copepods: Linking lower-higher trophic levels by linking lower-higher reynolds numbers", *Marine ecology progress series. Oldendorf*, vol. 136, no. 1, pp. 311–313, 1996.

[360] A. B. Bochdansky, M. A. Clouse, and G. J. Herndl, "Dragon kings of the deep sea: Marine particles deviate markedly from the common number-size spectrum", *Scientific reports*, vol. 6, no. 1, pp. 1–7, 2016.

[361] S. A. Henson, R. Sanders, E. Madsen, P. J. Morris, F. Le Moigne, and G. D. Quartly, "A reduced estimate of the strength of the ocean's biological carbon pump", *Geophysical Research Letters*, vol. 38, no. 4, 2011.

[362] R. Stone, *The invisible hand behind a vast carbon reservoir*, 2010.

[363] I. Morris, *Physiological ecology of phytoplankton*, 1980.

[364] R. Gibson, R. Atkinson, and J. Gordon, “Inherent optical properties of non-spherical marine-like particles from theory to observation”, *Oceanography and marine biology: an annual review*, vol. 45, pp. 1–38, 2007.

[365] R. Bainbridge, “The size, shape and density of marine phytoplankton concentrations”, *Biological Reviews*, vol. 32, no. 1, pp. 91–115, 1957.

[366] P. Ern, F. Risso, D. Fabre, and J. Magnaudet, “Wake-induced oscillatory paths of bodies freely rising or falling in fluids”, *Annual Review of Fluid Mechanics*, vol. 44, pp. 97–121, 2012.

[367] P. C. Fernandes, F. Risso, P. Ern, and J. Magnaudet, “Oscillatory motion and wake instability of freely rising axisymmetric bodies”, *Journal of Fluid Mechanics*, vol. 573, pp. 479–502, 2007.

[368] K. Namkoong, J. Y. Yoo, and H. G. Choi, “Numerical analysis of two-dimensional motion of a freely falling circular cylinder in an infinite fluid”, *Journal of Fluid Mechanics*, vol. 604, pp. 33–53, 2008.

[369] M. N. Ardekani, P. Costa, W. P. Breugem, and L. Brandt, “Numerical study of the sedimentation of spheroidal particles”, *International Journal of Multiphase Flow*, vol. 87, pp. 16–34, 2016.

[370] M. Chrust, “Etude numérique de la chute libre d’objets axisymétriques dans un fluide newtonien”, Ph.D. dissertation, Strasbourg, 2012.

[371] A. Roy, R. J. Hamati, L. Tierney, D. L. Koch, and G. A. Voth, “Inertial torques and a symmetry breaking orientational transition in the sedimentation of slender fibres”, *Journal of Fluid Mechanics*, vol. 875, pp. 576–596, 2019.

[372] J. Feng, H. H. Hu, and D. D. Joseph, “Direct simulation of initial value problems for the motion of solid bodies in a newtonian fluid part 1. sedimentation”, *Journal of Fluid Mechanics*, vol. 261, pp. 95–134, 1994.

[373] P. C. Fernandes, P. Ern, F. Risso, and J. Magnaudet, “Dynamics of axisymmetric bodies rising along a zigzag path”, *Journal of Fluid Mechanics*, vol. 606, pp. 209–223, 2008.

[374] M. M. Mrokowska, “Stratification-induced reorientation of disk settling through ambient density transition”, *Scientific reports*, vol. 8, no. 1, pp. 1–12, 2018.

[375] M. M. Mrokowska, “Influence of pycnocline on settling behaviour of non-spherical particle and wake evolution”, *Scientific reports*, vol. 10, no. 1, pp. 1–14, 2020.

[376] M. Mercier, S. Wang, J. Péméja, P. Ern, and A. Ardekani, "Settling disks in a linearly stratified fluid", *Journal of Fluid Mechanics*, vol. 885, 2020.

[377] A. Doostmohammadi and A. Ardekani, "Reorientation of elongated particles at density interfaces", *Physical Review E*, vol. 90, no. 3, p. 033 013, 2014.

[378] M. N. Ardekani, O. Abouali, F. Picano, and L. Brandt, "Heat transfer in laminar couette flow laden with rigid spherical particles", *Journal of Fluid Mechanics*, vol. 834, pp. 308–334, 2018.

[379] M. Majlesara, O. Abouali, R. Kamali, M. N. Ardekani, and L. Brandt, "Numerical study of hot and cold spheroidal particles in a viscous fluid", *International Journal of Heat and Mass Transfer*, vol. 149, p. 119 206, 2020.

[380] M. N. Ardekani, L. A. Asmar, F. Picano, and L. Brandt, "Numerical study of heat transfer in laminar and turbulent pipe flow with finite-size spherical particles", *International Journal of Heat and Fluid Flow*, vol. 71, pp. 189–199, 2018.

[381] M. N. Ardekani, "Numerical study of transport phenomena in particle suspensions", Ph.D. dissertation, KTH Royal Institute of Technology, 2019.

[382] S. Wüst, M. Bittner, J.-H. Yee, M. G. Mlynczak, and J. M. Russel III, "Variability of the brunt-väisälä frequency at the oh* layer height", 2017.

[383] W. R. Geyer, M. E. Scully, and D. K. Ralston, "Quantifying vertical mixing in estuaries", *Environmental fluid mechanics*, vol. 8, no. 5-6, pp. 495–509, 2008.

[384] J. Magnaudet and G. Mougin, "Wake instability of a fixed spheroidal bubble", *Journal of Fluid Mechanics*, vol. 572, p. 311, 2007.

[385] B. Yang and A. Prosperetti, "Linear stability of the flow past a spheroidal bubble", *Journal of Fluid Mechanics*, vol. 582, p. 53, 2007.

[386] N. Kishore and S. Gu, "Momentum and heat transfer phenomena of spheroid particles at moderate reynolds and prandtl numbers", *International Journal of Heat and Mass Transfer*, vol. 54, no. 11-12, pp. 2595–2601, 2011.

[387] A. Doostmohammadi and A. Ardekani, "Suspension of solid particles in a density stratified fluid", *Physics of Fluids*, vol. 27, no. 2, p. 023 302, 2015.

VITA

Purdue University, West Lafayette, Indiana, USA Aug 2017 - Feb 2022

- Ph.D. and M.S. in Mechanical Engineering
- Advisor: Prof. Arezoo Ardekani, Complex flows lab
- Committee: Prof. Osman Basaran, Prof. Ivan Christov, Prof. Jun Chen

Indian Institute of Technology Bombay, Mumbai, India Jul 2013 - May 2017

- B.Tech. in Mechanical Engineering (Honors) and in Computer Science & Engineering (Minor)
- Advisor: Prof. Sridhar Balasubramanian, Geophysical and Multiphase flows lab
- Junior Scientist/Engineer offer from Indian Space Research Organization (ISRO)

University of Florida, Gainesville, Florida, USA May 2016 - Jul 2016

- Visiting researcher, Center for Compressible Multiphase Turbulence
- Advisor: Prof. S. Balachandar

Sorbonne University (erstwhile UPMC), Paris, France May 2015 - Jul 2015

- Visiting researcher, Institut Jean Le Rond D'alembert
- Advisor: Prof. Corrado Maurini

PUBLICATION(S)

1. **More, R. V.** and Ardekani, A. M., Effect of roughness on the rheology of concentrated non-Brownian suspensions: A numerical study. *Journal of Rheology*, 64(1), pp.67-80, 2020.

2. **More, R. V.** and Ardekani, A. M., Roughness induced shear thickening in frictional non-Brownian suspensions: A numerical study. *Journal of Rheology*, 64(2), pp. 283-297, 2020 (**Invited article**, special issue on "the Physics of Dense Suspensions.").

3. **More, R. V.** and Ardekani, A. M., A constitutive model for sheared dense suspensions of rough particles. *Journal of Rheology*, 64(5), pp. 1108-1120, 2020.

4. **More, R. V.** and Ardekani, A. M., Unifying disparate rate-dependent rheological regimes in non-Brownian suspensions. *Physical Review E*, 103(6), p.062610, 2021.

5. **More, R. V.** and Ardekani, A. M., Motion of an inertial squirmer in a density stratified fluid. *Journal of Fluid Mechanics*, 905, A9, 2020.

6. **More, R. V.** and Ardekani, A. M., Hydrodynamic Interactions between swimming micro-organisms in a linearly density stratified fluid. *Physical Review E*, 103(1), p.013109, 2021.

7. **More, R. V.**, Ardekani, M., Brandt, L., Ardekani, A. M., Orientation instability of settling spheroids in a linearly density stratified fluid. *Journal of Fluid Mechanics*, 929, A7, 2021.

8. **More, R. V.**, Zhang, A., Dabiri, S., Ardekani A. M., Mixing control in therapeutic samples using Schlieren. *International Journal of Pharmaceutics*, 609, 121096, 2021.

9. Hilali, M. M., Pal, S., **More, R. V.**, Saive, R. and Ardekani, A. M., Sheared Thick-Film Electrode Materials Containing Silver Powders with Nanoscale Surface-Asperities Improve Solar Cell Performance. *Advanced Energy and Sustainability Research*, 2100145, 2021.